Applications of Resonance Raman and Fourier Transform Infrared Microspectroscopy in Malaria Research

by

Grant Thomas Webster, B.Sc. (Hons.),
Department of Chemistry, Monash University

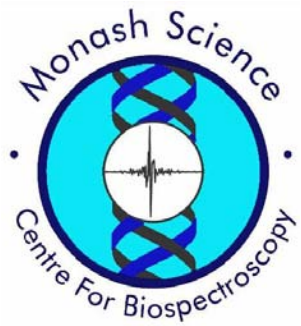

A dissertation submitted in accordance with the requirements for the Degree of Doctor of Philosophy

April, 2009

To Mum and Dad

"For all the sacrifices you made for me"

"The only way of finding the limits of the possible is by going beyond them into the impossible."

Sir Arthur C. Clarke

COPYRIGHT NOTICES

Notice 1

Under the Copyright Act 1968, this thesis must be used only under the normal conditions of scholarly fair dealing. In particular no results or conclusions should be extracted from it, nor should it be copied or closely paraphrased in whole or in part without the written consent of the author. Proper written acknowledgement should be made for any assistance obtained from this thesis.

Notice 2

I certify that I have made all reasonable efforts to secure copyright permissions for third-party content included in this thesis and have not knowingly added copyright content to my work without the owner's permission.

Table of Contents

Chapter 2

Biospectroscopy Theory and Data Analysis

Chapter 3

FTIR Spectroscopic Analysis of Malaria Infected Erythrocytes

Chapter 4

Raman Spectroscopic Analysis of Malaria Infected Erythrocytes

Chapter 5

Raman Spectroscopic Analysis of Supramolecular Interactions in Haem Aggregates

Chapter 6

Conclusions and Future Directions

Summary

This thesis investigates applications of Raman and FTIR microspectroscopy in malaria research. It was found that the use of biospectroscopy was able to generate significant new insights into discriminating lifecycle stages of the malaria parasite, detecting structural changes in malaria pigment and understanding the effects of chloroquine on supramolecular interactions in malaria pigment and its precursors. This dissertation is presented in the "thesis by publication" format, with the three results and discussion chapters (Chapters 3, 4 and 5) comprised of either published, accepted or submitted manuscripts.

The first chapter provides a general introduction to malaria, with particular emphasis on the *Plasmodium falciparum* drug resistant strain of malaria parasite. This chapter also introduces the different models of quinoline drug binding that are likely to occur within the digestive vacuole (DV) of the parasite, as well as introducing the various macromolecules that are present within infected erythrocytes. The second chapter discusses relevant biospectroscopy theory and introduces the data analysis techniques used in the application of Raman and FTIR spectroscopy to malaria research.

The third chapter describes FTIR spectroscopic investigations, focusing on discriminating the different intra-erythrocytic lifecycle stages (i.e. ring, trophozoite and schizont stage) of the malaria parasite by observing the specific lipid composition of each stage. In addition, haemozoin growth within the digestive vacuole (DV) of the parasite was observed using FTIR spectroscopy.

As part of a larger study, the relevant section in the second manuscript of this chapter (**II**) builds upon the above findings by describing how the use of FTIR-ATR and Raman spectroscopy allows for direct observation of physical changes related to quinoline drug attachment in synthetic malaria pigment (β-haematin). The FTIR-ATR

spectra show the effect of quinoline drug binding on β-haematin by revealing changes in the surface propionic acid groups (1744 cm^{-1}).

The fourth chapter describes investigations that used resonance Raman spectroscopy to detect haemozoin (malaria pigment) and the structural changes that occur in haemozoin in infected erythrocytes after chloroquine (CQ) treatment. Raman spectra show that CQ binds via π-π interactions between adjacent and oriented porphyrins, thereby disrupting the haemozoin aggregate and reducing excitonic interactions between adjacent Fe(III)PPIX units.

The final chapter explains how resonance Raman in combination with UV-Visible spectroscopy can reveal the effects of varying concentrations of Fe(III)PPIX and CQ on excitonic interactions in solution and on the extent of supramolecular interactions in malaria pigment and other related haem aggregates. Resonance Raman spectra of haematin and haemin solutions are reported for 413 nm and 514 nm wavelengths. Enhancement of A_{1g} modes (1569 cm^{-1} and 1370 cm^{-1}) and B_{1g} modes (1124 cm^{-1} and 755 cm^{-1}) as a function of increased concentration are observed when irradiating with 514 nm laser excitation but not 413 nm.

This wavelength dependent enhancement can be rationalised by considering an excitonic coupling mechanism. As the concentration of haematin increases there is an increased probability of supramolecular interactions occurring between Fe(III)PPIX units.

This study provides new insight into the nature of excitonic coupling through supramolecular and other concerted interactions and may have important implications in understanding energy transfer processes in haem systems.

Papers Included In This Thesis

This thesis is based on the following papers, referred to in the text by Roman numerals **I-IV**:

I. **"Discriminating the different stages of the malaria parasites intra-erythrocytic life cycle using synchrotron FTIR-microspectroscopy"**
Webster, G. T.; de Villiers, K.; Egan, T. J.; Deed, S.; Tilley, L.; Tobin, M.; Bambery, K.; McNaughton, D.; Wood, B. R. *J. Anal. Chem.* **2009**, 81, 2516-2524

II. **"Crystal nucleation, growth, and morphology of the synthetic malaria pigment β-haematin and the effect thereon by quinoline additives: The malaria pigment as a target of various antimalarial drugs"**
Solomonov, I.; Osipova, M.; Feldman, Y.; Baehtz, C.; Kjaer, K.; Robinson, I. K.; Webster, G. T.; McNaughton, D.; Wood, B. R. Weissbuch, I., Leiserowitz, L. *JACS* **2007**, 129, 2615-2627

III. **"Resonance Raman can detect structural changes in haemozoin (malaria pigment) following incubation with chloroquine in infected erythrocytes"**
Webster, G. T.; Deed, S.; Tilley, L.; McNaughton, D.; Wood, B. R. *FEBS Lett.* **2008**, 582, 1087-1092

IV. **"Resonance Raman microscopy in combination with partial dark-field microscopy lights up a new path in malaria"**
Wood, B. R.; Hermelink, A.; Lasch, P.; Bambery. K. R.; Webster, G. T.; Asghari-Khiavi, M.; Cooke, B. M.; Deed, S.; Naumann, D.; McNaughton, D. *Analyst.* **2009,** DOI: 10.1039/b822603b (accepted)

V. **"Aggregated Enhanced Raman Scattering in Fe(III)PPIX solutions: the effects of concentration and chloroquine on excitonic interactions"**
Webster, G. T.; McNaughton, D.; Wood, B. R. *J. Phys. Chem. B*. **2009** (accepted)

VI. **"Supramolecular interactions play an integral role in the Near-Infrared Raman "Excitonic" enhancement observed in malaria pigment and other related haem aggregates"**
Puntharod, R.; Webster, G. T.; Asghari-Khiavi, M.; Bambery, K, R.; Safinejad, F.; Haller, K. J.; Wood, B. R. *JACS* **2009** (submitted)

Monash University

Monash Research Graduate School

Declaration for thesis based or partially based on conjointly published or unpublished work

General Declaration

In accordance with Monash University Doctorate Regulation 17/ Doctor of Philosophy and Master of Philosophy (MPhil) regulations the following declarations are made:

I hereby declare that this thesis contains no material which has been accepted for the award of any other degree or diploma at any university or equivalent institution and that, to the best of my knowledge and belief, this thesis contains no material previously published or written by another person, except where due reference is made in the text of the thesis.

This thesis includes five original papers published in peer reviewed journals and one paper currently under review for publication. The core theme of the thesis is "Applications of resonance Raman and FTIR microspectroscopy in malaria research". The ideas, development and writing up of papers I, III and V in the thesis were the principal responsibility of myself, the candidate, working within the School of Chemistry under the supervision of Prof. Don McNaughton and Dr. Bayden Wood.

The inclusion of co-authors reflects the fact that the work came from active collaboration between researchers and acknowledges input into team-based research. The publications involving ORTEP molecular modeling were carried out, and the data treated, by Ratchadaporn Puntharod. Prof. Kenneth Haller assisted with reviewing manuscript VI. Dr. Keith Bambery was a post doctoral fellow in the group of Prof. Don McNaughton and assisted in the calculation of an artificial neural network (ANN) and the reviewing of the relevant manuscripts. When required, work involving the culturing of cells was carried out by Ms Samantha Deed and Prof. Leann Tilley. Ms Feryal Safinejad and Mr Mehdi Asghari-Khiavi assisted with molecular calculations and with the reviewing of the relevant manuscript (VI).

In papers I, III, V and VI my contribution to the work involved the following: all other laboratory work, FTIR, Raman and UV-visible experiments, Principal Components Analysis (PCA), synthesis of μ-oxo dimers, analysis and interpretation of results and writing the manuscripts. For paper II, my contribution to the work involved the relevant FTIR and Raman experiments within the paper. For paper IV, the experimental work was undertaken by Dr. Bayden Wood as a continuation of the experiments based on results from papers I and III. My contribution to paper IV involved the interpretation of results and proof reading of this manuscript.

Paper	Publication Title	Publication Status	Nature and extent of candidate's contribution
I	Discriminating the different stages of the malaria parasite's intra-erythrocytic life cycle using synchrotron FTIR-microspectroscopy	Published	Experimental design, interpretation of results, writing of the manuscript
II	Crystal nucleation, growth, and morphology of the synthetic malaria pigment β-haematin and the effect thereon by quinoline additives: The malaria pigment as a target of various antimalarial drugs	Published	Experimental design of relevant Raman section, interpretation of results, proof reading the manuscript
III	Resonance Raman can detect structural changes in haemozoin (malaria pigment) following incubation with chloroquine in infected erythrocytes	Published	Experimental design, interpretation of results, writing of the manuscript
IV	Resonance Raman microscopy in combination with partial dark-field microscopy lights up a new path in malaria	Accepted	Interpretation of results, proof reading the manuscript
V	Aggregated Enhanced Raman Scattering in Fe(III)PPIX solutions: the effects of concentration and chloroquine on excitonic interactions	Accepted	Experimental design, interpretation of results, writing of the manuscript
VI	Supramolecular interactions play an integral role in the Near-Infrared Raman "Excitonic" enhancement observed in malaria pigment and other related haem aggregates	Submitted	Experimental design, interpretation of results, drafting of manuscript

I have not renumbered sections of submitted or published papers in order to generate a consistent presentation within the thesis.

Signed: .....[redacted].....

Date: 17/04/09

Acknowledgements

I am grateful to the many people who have helped me in the production of this dissertation. In particular, my distinguished supervisors Prof. Don McNaughton and Dr Bayden Wood. Thank you Don for giving me this terrific opportunity to further my knowledge in the field of biospectroscopy as well as being a great role model and an expert spectroscopist, which motivated me to excel. To Bayden, thank you for your patience and support and for providing essential supervision and practical assistance throughout the project. Your encouragement, inspirational words and thirst for research was my driving force throughout my candidature.

I would also like to acknowledge the following people. Prof. Leann Tilley and her team in the Biochemistry Department at LaTrobe University in Bundoora with special thanks to Samantha Deed for culturing, inoculating and fixing the malarial infected blood cells. Dr Mark Tobin and Dr Ljiljana Puskar for their technical support at the Australian Synchrotron FTIR beamline. Finlay Shanks for technical support at Monash. Dr Keith Bambery, for proof reading Chapter 2 and whose friendship, support and scientific knowledge made my time at Monash fly past. Don McGilvery and Michael Bock for computer maintenance. To the third year chemistry lab technicians Bruce Dobney and Gordana Kitanovic for their continual support and help over the years.

To all my biospectroscopy friends, especially those that lived in the „fish bowl' office at some point in time during my candidature, Mot Sekine, Dr Pimm Vongsvivut, Mahta Zazabeti, Rahda Maganti, Ben Wong, Aim Puntharod, Dr Katherine de Villiers, Dr Torsten Frosch, Mehdi Asghari-khiavi, Chris Medcraft and Alex Kehridakis for their support, laughter and stories as well as the science discussed, which helped relieve stress.

To all my friends, words cannot express how much I appreciate the support you have given me throughout the duration of my Ph.D. Special thanks must be given to those friends whose patience, endurance and direct support guided me through this process. In particular, Paul Zubrinich, Melanie Thewlis, Ben Quinlivan, Mark Heeney, Aidan Keatley, Liam Apelgren, Cam Apelgren, Damien Seisun, Daniel Moodie, David Coggins and Michael Cromie, with a special thanks to Melanie Thewlis for proof reading the entire manuscript. Also thanks to Steve Morton for photography and printing.

I would also like to thank all the friends I have met throughout the Chemistry Department and others who have assisted in some way, albeit indirectly, to the result of this dissertation in particular Michael Blair, Bianca van Leirop, Rachel Lagatos, Dr Matthew Belousoff, Nadia Spiccia, Mandy Lee, Dr Matze Hilder, Jacinta Baker, Dr Kevin Fraser, Dr David Lupton, Dr Clint Woodward, Ruth Oliver, Dr Chris Thompson, Dr Phil Heraud, Dr Evan Robertson, Sally Caine and Danielle Martin with a special thanks to Dr David Lupton for proof reading Chapter 1 of the thesis. Also, to Dr Kevin Fraser for help with formatting and printing of the thesis.

Finally, I wish to thank my family, in particular my brothers Craig and Leigh who were genuinely interested in my progress throughout my candidature and who gave me love and support, especially during these recent years. Thank you to Mum and Dad for making numerous sacrifices and supporting me through the difficult times that I encountered throughout the duration of my candidature. Thank you for your unconditional love, support, care and guidance and for teaching me the rules of life.

Glossary

Adiabatic theorem	This theorem is an important concept in quantum mechanics. In this thesis the adiabatic state refers to one in which the Born-Oppenheimer approximation holds true.
***β*-haematin**	The synthetic equivalent of haemozoin.
Born-Oppenheimer approximation	The Born-Oppenheimer approximation allows the total wavefunction of the molecule to be broken into its electronic and nuclear (vibrational and rotational) components. This approximation states that a molecule's total wavefunction is equal to the product of its electronic and nuclear wavefunctions.
Digestive vacuole	A small cavity in the cytoplasm of a cell (protozoan) surrounded by a single membrane which contains water, food or metabolic waste.
Dispersion forces	Also known as London–van der Waals forces. It is the weak intermolecular non-covalent force found between all molecules and arises from the induced dipole of one molecule generating an electric field that polarizes another molecule to induce an instantaneous dipole. Larger molecules generally exhibit stronger dispersion forces.[1]
Erythrocyte	A cell containing large amounts of haemoglobin and specialized for oxygen transport; a mature red blood cell.[2]

Exciton	A superposition of collective excited states which describes an excitation in terms of a traveling-wave packet of excitation energy with different wavelengths and amplitudes that reinforce each other at a given position within the molecule.[3]
Haem	A prosthetic group that consists of an iron atom contained in the centre of a heterocyclic porphyrin ring.
Haematin	The monomeric precursor of haemozoin. The Fe centre of the haem group has a hydroxyl functional group ligand attached.
Haemozoin	Also known as malaria pigment. A metabolic waste product (biomineral) formed by the catabolism of haemoglobin by the *Plasmodium falciparum* malaria parasite. Haemozoin is made up of haem groups that form an array of dimers linked by the propionate side chain of an adjacent haem to the Fe centre of another haem unit found in the *Plasmodium falciparum* parasite's digestive vacuole. This array is further linked by hydrogen bonding.
Loadings	A term used in Principal Components Analysis (PCA) to describe variables responsible for having the largest variability in the spectra or dataset
Nonadiabatic transitions	A phenomenon that constitutes a fundamental mechanism of state changes in dynamical processes in physics, chemistry and biology. In this thesis, it refers to any transition state undergone by a molecule in which the Born-Oppenheimer approximation does not hold true.

Scores	A term used in Principal Components Analysis (PCA) to describe spectra in multi-dimensional space.
Supramolecular forces	Is a collection of concerted weak non-covalent interactions between molecules. These include hydrogen bonding, metal coordinations, van der Waal's interactions, π-π interactions and electrostatic effects.
Trophozoite	A sporozoan in the active feeding stage of its lifecycle.[4]

References

(1) Atkins, P. W. *Physical Chemistry*, 5 ed.; Oxford University Press: UK, 1994.

(2) Lehninger, A.; Nelson, D. L.; Cox, M. M. *Principles of Biochemistry*, 3 ed.; Worth Publishers: New York, 2000.

(3) Kasha, M. *Radiat. Res.* **1963**, *20*, 55-71.

(4) Slater, A. F. G.; Swiggard, W. J.; Orton, B. R.; Flitter, W. D.; Goldberg, D.E.; Cerami, A.; Henderson, G. B. *Proc. Natl. Acad. Sci. USA* **1991**, *88*, 325-329.

Notation

A	Absorbance
c	Speed of light
$\boldsymbol{\alpha}$	Polarizability
λ	Wavelength
v	Vibrational quantum number
$\bar{\nu}$	Wavenumber value
ν	Frequency
v	Stretching mode
δ	Deformation mode
γ	Out-of-plane vibrational mode
c	Concentration
E	Energy
g	Gerade
u	Ungerade
h	Planck's constant
$\hbar$	$h/2\pi$
I_s	Intensity of Raman scattered photons
m_1 and m_2	Mass of atoms 1 and 2
μ	Reduced mass
N	Number of atoms
$\boldsymbol{Q}$	Normal coordinate
S_0	Ground electronic state

S_1	Excited electronic state
Hz	Hertz
k	Force constant
R	Amino acid side chain
F	Restoring Force
x	Displacement Force
E_v	Vibrational energy
$\boldsymbol{M_e}$	Transition dipole moment
$\|\boldsymbol{i}\rangle$	Initial vibrational wave function
$\|\boldsymbol{v}\rangle$	Intermediate vibrational wave function
$\|\boldsymbol{j}\rangle$	Final vibrational wave function
Γ_v	Represents the life time of the excited state
P	Depolarization ratio
Γ	Irreducible representation
$\boldsymbol{R}$	Rotational tensor
$\boldsymbol{T}$	Translational tensor
$\boldsymbol{K}$	Total wave vector
I	Interferogram
d_p	Depth of penetration
ϑ_c	Critical angle
n_1	Refractive index of the internal reflection element
n_2	Refractive index of the sample
n_{21}	Ratio of the refractive index of the less dense medium divided by that of the denser medium

d_{jk}	D-value
r_{jk}	Pearson's correlation coefficient
$\bar{y}_j, \bar{y}_k$	Mean absorbance values of the *j*-th and *k*-th spectra, respectively.

Abbreviations

1˚	Primary
2˚	Secondary
3˚	Tertiary
4˚	Quaternary
AERS	Aggregated Enhanced Raman Scattering
ATP	Adenosine Triphosphate
ATR	Attenuated Total Reflectance
ANN	Artificial Neural Network
AQ	Amodiaquine
CCD	Charge Coupled Device
CD	Circular Dichroism
CO	Carbon Monoxide
CT	Charge Transfer
CQ	Chloroquine
dHb	Deoxyhaemoglobin
DFT	Density Functional Theory
DNA	Deoxyribonucleic Acid
DV	Digestive Vacuole
EMSC	Extended Multiplicative Scatter Correction
EtOH	Ethanol
FPA	Focal Plane Array
FTC	Flow-Through-Cell
FTIR	Fourier Transform Infrared

FWHH	Full Width Half Height
Hb	Haemoglobin
HbO_2	Oxygenated Haemoglobin
HeNe	Helium Neon
Hz	Haemozoin
iRBC	Infected Red Blood Cell
IRE	Internal Reflection Element
LASER	Light Amplification by Stimulated Emission of Radiation
LB	Lipid Body
LDA	Linear Discriminant Analysis
LDMS	Laser Desorption Mass Spectrometry
MCT	Mercury-Cadmium-Telluride
MIR	Mid Infrared
MSC	Multiplicative Scatter Correction
NIR	Near Infrared
NO	Nitric Oxide
OEP	Octaethylporphyrin
OPD	Optical Path Difference
PBS	Phosphate Buffered Saline
PC	Principal Component
PCA	Principal Components Analysis
PCC	Pearson's Correlation Coefficient
PCh	Phosphotidylcholine
Pf	*Plasmodium falciparum*

PCR	Polymerase Chain Reaction
PPIX	ProtoporphyrinIX
Q	Quinine
RBC	Red Blood Cell
RDT	Rapid Diagnostic Test
r.p.m.	revolutions per minute
RNA	Ribonucleic Acid
RR	Resonance Raman
RRS	Resonance Raman Scattering
RSD	Residual Standard Deviation
SERRS	Surface Enhanced Resonance Raman Scattering
SERS	Surface Enhanced Raman Scattering
SIMCA	Soft Independent Modelling by Class Analogy
S/N	Signal to Noise
TAG	Triacylglycerol
TD	Transition Dipole
THz	Terahertz
TPP	Tetraphenylporphyrin
UV	Ultraviolet
UV-Vis	Ultraviolet-Visible
v/v	volume per volume

Chapter 1

An Introduction to Malaria

1.1 BRIEF HISTORY OF MALARIA

In April 1993, fossil investigation into haematophagous insects at La Toca mine, located between the cities of Puerto Plata and Santiago de los Caballeros in the northern portion of the Dominican Republic, retrieved an amber fossil containing a perfectly preserved *Culex* mosquito infected with malaria parasites. This provided one of the earliest examples of fossil evidence of malaria, dating the existence of the genus *Plasmodium ca* 30 million years.[1] Malaria is one of the oldest and most resilient diseases humans have ever faced and may have been a human pathogen for the entire history of our species.[2] It is now generally accepted that malaria spread from our primate ancestors in Africa and coevolved with humans, since close relatives of human malaria parasites are present in chimpanzees, our closest evolutionary relations.[3] Symptoms of malaria have been recorded by physicians in every literate society from China in *ca* 2700 BC to European physicians in the 19th century.[4] The earliest detailed accounts are from Hippocrates in the 5th century BC. Thereafter, an increasing number of references to the disease in Greece, the Roman empire and throughout Europe become apparent.[3]

The disease was first spread throughout tropical and sub-tropical climates by human migration in Afro-Eurasia during the 15th century and then to the Americas and Australasia by explorers, missionaries and slaves. It became clear over this period that malaria was associated with marsh and swamp areas and so was called “ague” or “marsh fever”. The term malaria originates from the Italian word *mala aria*, which literally translates to “bad air”, and dates to Giovanni Maria Lancisi’s 1717 speculation that malaria is contracted from the poisonous vapours of swamps. Although physicians may have suspected that malaria symptoms resulted from the bite of certain insects, it

wasn't until 1880 that the source of these malarial symptoms was discovered. It was French army doctor Charles Louis Alphonse Laveran (1845–1922) who made the first significant scientific breakthrough in the study of malaria by observing, for the first time, parasites inside the red blood cells of patients suffering from malaria. From these findings, he proposed that the disease was caused by a protozoan. The protozoan was named *Plasmodium* by the Italian scientists Ettore Marchiafava and Angelo Celli. Then, in 1898, British doctor Sir Ronald Ross (1857–1932) discovered while working in Calcutta that malaria is transmitted by mosquitoes. He achieved this by proving certain species of mosquito transmit malaria to birds and then isolating the malaria parasite in the salivary glands of mosquitoes that contained blood from infected birds.

1.2 MALARIA ENDEMICITY

Based on its endemic occurrence in tropical and sub-tropical climates, malaria is one of the most serious parasitic diseases ever to have beset the human race. Today, human malaria is known to be a widespread tropical disease caused by the *Plasmodium* sporozoan and transmitted by the female *Anopheles* mosquito. Malaria is responsible for a combined mortality rate of more than 1 million deaths per annum with some 300–500 million people affected by the disease every year.[5,6] Additionally, there are more than 100 species of *Plasmodium* which can infect various animals such as birds, reptiles and other mammals.

In 1886, Golgi observed that some patients infected with malaria displayed a 72 hour cycle of symptoms, while others displayed a 48 hour cycle.[7] Golgi theorised that this differing periodicity was due to differences in the length of the lifecycles of the infecting malarial parasites. He came to the conclusion that more than one species of

parasite can cause malaria in humans. Today, we know that humans can be infected by one or more of the following main species of *Plasmodium*:

- *Plasmodium falciparum* (*Pf*), found commonly worldwide in tropical and sub-tropical climates, but most prevalent in sub-Saharan Africa due to a minimum tolerable temperature environment of *ca* 21˚C.[8] It is the most virulent and deadly species and can develop resistance to drug treatment.[9]
- *Plasmodium vivax* is the most common strain of malaria found in Asia, Latin America and in some parts of Africa due to it's tolerance of a wider range of temperatures.[8] It infects an estimated 70–80 million people annually and causing acute and febrile disease, but rarely death.[10]
- *Plasmodium ovale* is endemic mostly to West Africa and the islands of the western Pacific. It is morphologically and biologically similar to *P.vivax*, but is quite rare and less dangerous.[11]
- *Plasmodium malariae* is the least common of all the strains and is found mostly in sub-Saharan Africa, Southeast Asia, parts of Indonesia and many of the islands of the west Pacific. Unlike the other strains, which have a 48 hour intra-erythrocytic lifecycle, this species of parasite has a 72 hour lifecycle. This causes a longer lasting infection, which can sometimes last a lifetime.[12]

Malaria is currently endemic in areas of the Americas and many parts of Asia and Africa due to the *Plasmodium falciparum's* growing resistance against anti-malarial drugs such as chloroquine (Figure 1.1).[6] In sub-Saharan Africa alone 85–90% of deaths from malaria occur in children under 5 years and child mortality from cerebral malaria is approximately 20%.[13,14] Of the children that survive malaria, 10% are left with severe neurological defects. Pregnant women are also vulnerable. In areas of low transmission,

malaria infection during pregnancy can lead to the death of the mother, abortion of the foetus or stillbirth.[5] In high transmission areas, placental infection with *Plasmodium falciparum* may occur especially in early pregnancy. This impairs placental function resulting in a low birth weight and therefore increased infant mortality rates since infant survival is sensitive to even the smallest change in birth weight.[5] Malaria is more common in rural areas than in cities. However, it has been well documented that malaria vectors can adapt to urban areas[15] and local transmission has been observed in many African cities although the risk is lower in the larger cities.[16,17]

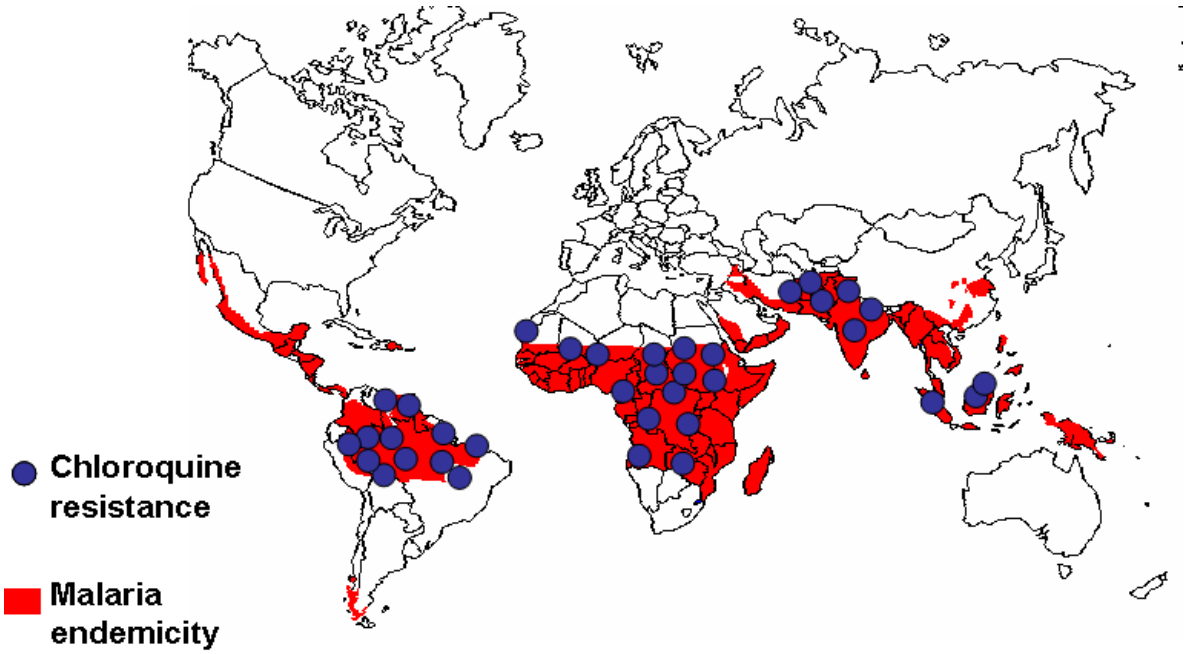

Figure 1.1: *Plasmodium falciparum* endemicity distribution within the global limits of risk and antimalarial resistance to chloroquine drug. (Modified from reference)[6]

1.3 SYMPTOMS

Symptoms of malaria often resemble those of common viral infections; this can lead to a delay in diagnosis.[18] There are a number of clinical symptoms of malaria infection. Primarily these are due to the rupturing of erythrocytes resulting from

schizonts undergoing continual nuclear division. The typical symptoms of *Plasmodium falciparum* infection are cyclical occurrence of fever (>92% of cases), chills (>79%), headaches (70%) and diaphoresis (>64%)[19] lasting 4-6 hours, and occurring every 36-48 hours. Other common symptoms include dizziness, joint pain, abdominal pain, nausea, vomiting and mild diarrhea.[20] Severe malaria symptoms are almost exclusively caused by *Plasmodium falciparum* and usually arise 6-14 days after infection. The consequences usually include coma and death if untreated.[20] Enlarged spleen and liver, severe headaches, cerebral ischemia, hypoglycemia and renal failure may occur. Developmental impairments have been observed in children who have suffered episodes of severe malaria.[21] Furthermore, cerebral malaria can cause neurological damage and can cause widespread anaemia among children experiencing rapid brain development.[22,23]

1.4 THE *Plasmodium falciparum* LIFECYCLE

Figure 1.2 depicts the *Plasmodium falciparum* intra-erythrocytic life cycle. The malarial infection commences when an infected female *Anopheles* mosquito carrying sporozoites bites a person to feed. In this process, it injects sporozoites into the bloodstream. Within an hour, sporozoites invade hepatocytes (liver cells) within the liver and begin to differentiate to form new spores known as exo-erythrocytic merozoites. This process is termed tissue schizogony.[20] The merozoites leave the liver and rupture their host cell, releasing merozoites into the blood that infect red blood cells (RBCs), thus beginning the intra-erythrocytic stage of the *Pf*-parasite's lifecycle. It is during this asexual blood stage, after the merozoites have left the liver and begun to invade and grow inside RBCs, that disease symptoms occur.[24] Once merozoites have invaded erythrocytes, they develop into vacuolated uninucleated early trophozoites,

which have a ring shape morphology (ring stage).[20] The parasite then grows into the mature trophozoite.

The trophozoites then begin to divide in a process known as blood schizogony, forming schizonts (schizont stage), which consist of many daughter merozoites.[20] The mature schizont contains several thousand daughter merozoites that cause the infected RBCs to lyse. The daughter merozoites then invade other erythrocytes to begin a new cycle of schizogony. The duration of each cycle in *Plasmodium falciparum* is about 48 hours.

After several cycles, some of the merozoites can develop into male or female gametocytes within RBCs. These cause no symptoms in humans, but are taken in by *Anopheles* mosquitoes when they take their next blood meal from an infected human. The gametocytes fuse in the vector's gut, where they develop into ookinetes that penetrate the gut lining and produce an oocyst inside the outer gut lining of the mosquito. New sporozoites develop inside the oocyst, causing it to rupture and release sporozoites that migrate to the vector's salivary gland. The sporozoites are then injected into the blood of a new human host and the cycle is repeated.

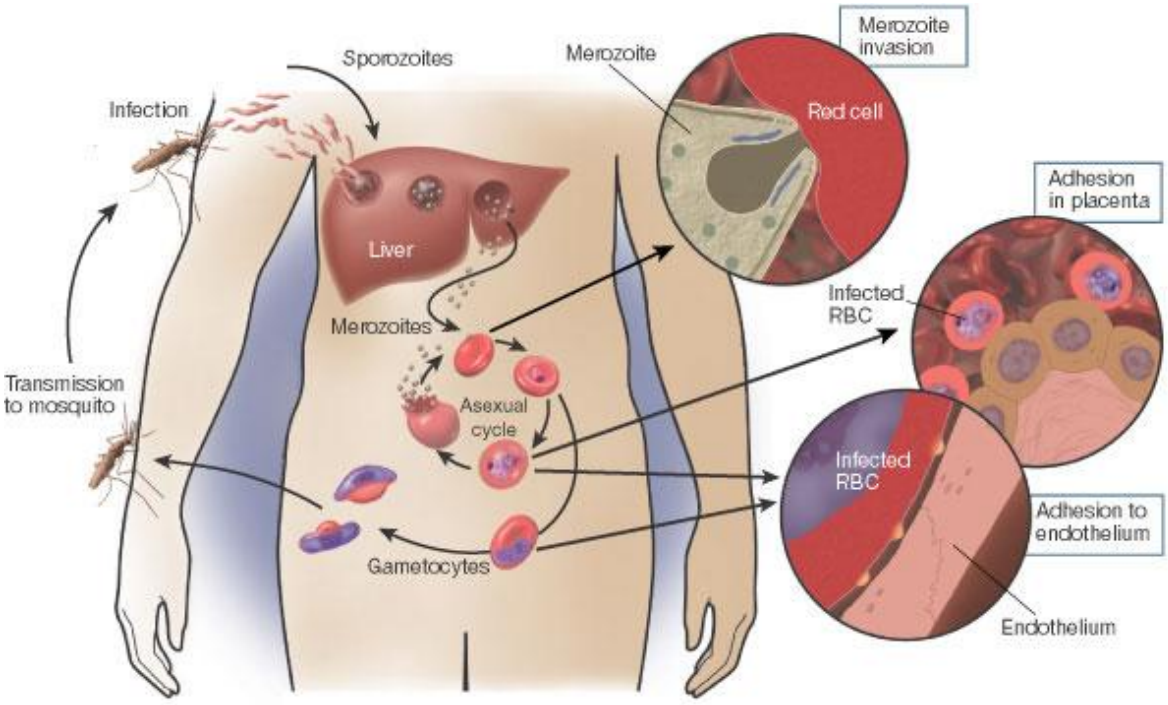

Figure 1.2: *Plasmodium* lifecycle. (Modified from reference)[24]

1.5 ANTIMALARIAL DRUG TARGET SITE

There are many drug target sites located within the malarial parasite at different stages of development. However, the drug target site of particular interest to this project is the digestive vacuole (DV) of the parasite depicted in Figure 1.3. The DV is composed of particular constituents that render it more suitable to analysis through the use of Raman spectroscopy than other organelles or drug target sites. It is documented that a mature human erythrocyte contains *ca* 310–350 mg/mL haemoglobin, which equates to a concentration of *ca* 20 mM.[25] During the trophozoite phase the parasite ingests RBC cytoplasm via a cytosome and transports it to the DV by transport vesicles. The parasite digests up to 80% of erythrocyte haemoglobin[26] to short peptides by plasmepsins, falcipains and falcilysin in its DV.[27-29] These peptides are exported from the DV to the parasite's cytoplasm and are further degraded into amino acids by

aminopeptidases[30] such as the *Plasmodium falciparum* M17 leucyl aminopeptidase (*Pf*LAP).[31]

The pH of the DV is estimated at 4.8[32] allowing toxic free haem units known as iron-protoporphyrin IX (FePPIX) released upon haemoglobin digestion to be oxidised to Fe(III)PPIX.[33] This consequently generates *ca* 0.5 M equivalence of H_2O_2.[34] It has been proposed that to neutralise the toxicity of peroxides the parasite eliminates H_2O_2 through catalase activity, thus forming H_2O and O_2.[35] Toxic FePPIX represents only 3–5% of the total DV volume.[36] If toxic FePPIX in the DV was not oxidised its concentration was allowed to accumulate to 300–500 mM then the high concentration of toxic FePPIX would cause the parasite membranes to lyse and therefore kill the parasite.[34] It is the presence of Fe(III)PPIX molecules that allows the DV to be analysed by Raman spectroscopy as these molecules are large Raman scatterers.

In aqueous solution Fe(III)PPIX is thought to dimerise to form a π–π dimer, which is transported to a lipid body (LB) also known as a lipid nanosphere. Within the lipid nanosphere the Fe(III)PPIX-OH/H_2O (haematin) π-π dimer forms with the axial ligands H_2O/OH^- directed outwards.[37] This is a haemozoin precursor which is converted to the haemozoin dimer by displacement of the axial ligands of Fe(III)PPIX-OH/H_2O. The haemozoin dimer then assembles to form the insoluble biomineral known as haemozoin (malaria pigment).[38] Through use of high resolution powder diffraction techniques, Pagola *et al.*[38] determined that *β*-haematin $(Fe(III)PPIX)_2$ is a spectroscopically identical synthetic analogue of haemozoin as depicted in Figure 1.4. It is an array of dimers linked through reciprocal iron-carboxylate bonds to one of the propionate side chains. This array of dimers is linked together by hydrogen bonds to form chains as a result of the absence of competing hydrogen bonding to the solvent within the lipid body.

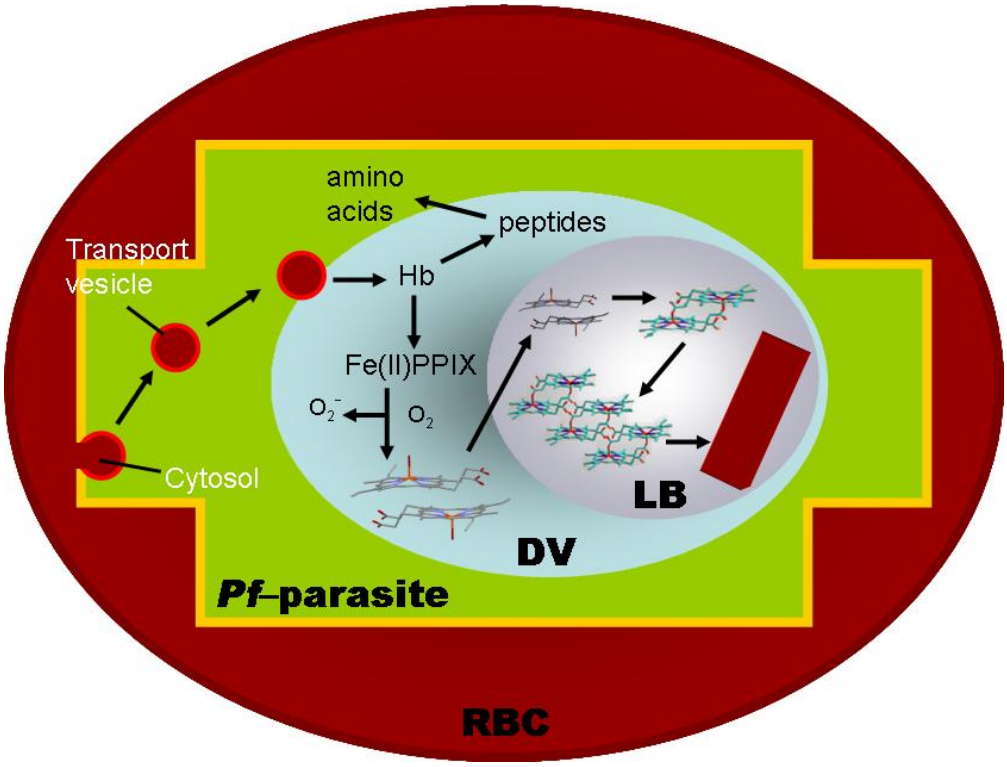

Figure 1.3: Digestive vacuole (DV) drug target site and process of haemozoin formation in *Plasmodium falciparum*. (Modified from reference)[33]

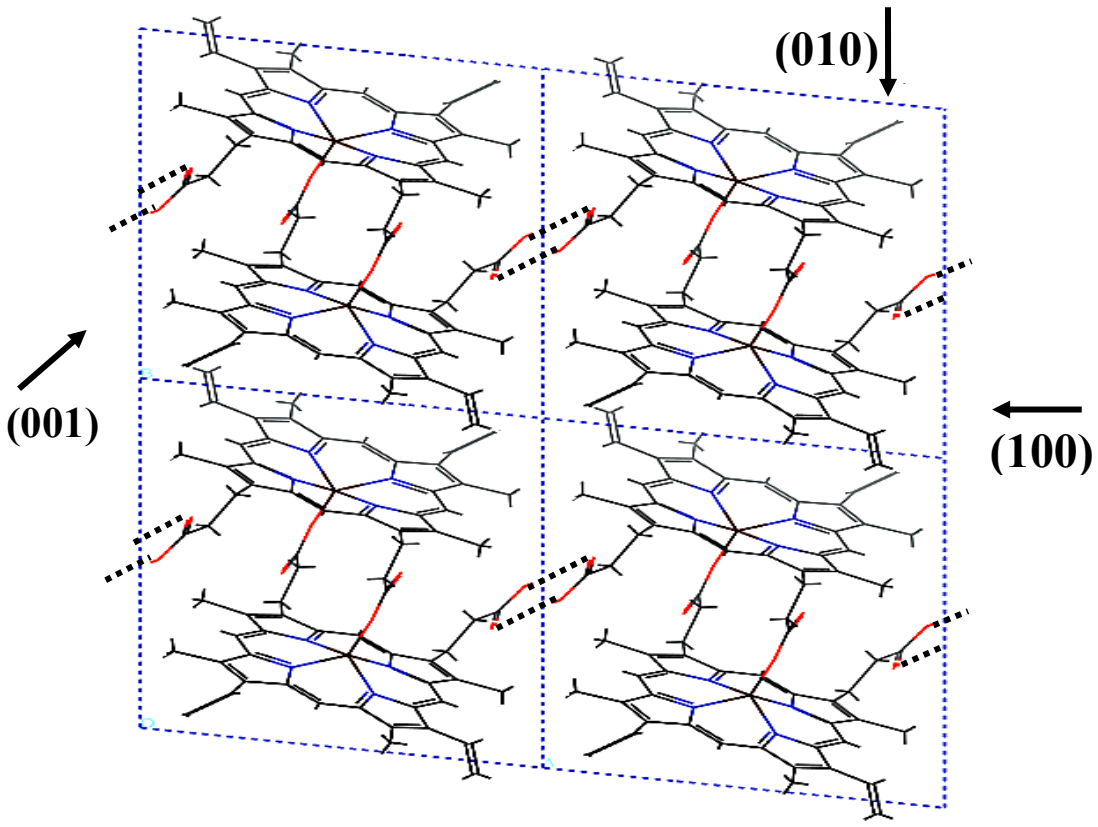

Figure 1.4: Haemozoin (β-haematin) packing structure. (Modified from reference)[38]

1.6 QUINOLINE DRUGS AND CHLOROQUINE RESISTANCE

Quinoline antimalarial drugs such as chloroquine (CQ) are derived from quinine. Quinine is found in the bark of the *cinchona* tree, which was first imported into Europe from Peru for antimalarial use in the 17th century.[39] However, it wasn't until the early 19th century that quinine was extracted from the bark, isolated, and named by French chemists Pierre Joseph Pelletier and Joseph Bienaime` Caventou.[40] Synthetic 4-aminoquinoline drugs (Figure 1.5), particularly chloroquine and later amodiaquine,[41,42] have been developed to have a low cost and a low dosage requirement for effective treatment. In comparison, quinine has limitations associated with its potential toxicity due to the high dosage required over a period of extended drug administration.

Chloroquine is regarded as one of the most important antimalarial agents in history. Loeb *et al.*[43] recommended that it be made available for the prophylaxis of all blood stage human malaria infections. In the late 1950s the World Health Organisation (WHO) initiated a project to globally eradicate the malarial parasite.[44] It was estimated by Coatney[45] that from 1960 to 1962 the U.S. International Cooperation Administration alone bought and distributed approximately 300 million tablets of chloroquine. Due to the enormous amounts of chloroquine distributed, the parasite populations worldwide were subjected to an intense selection pressure for survival in the presence of the antimalarial agent.[46]

Chloroquine resistance was first detected in South America in the following 1959, then in South East Asia the following year,[46] as resistant strains of the *Pf*-parasite evolved. Krogstad *et al.*[47] discovered that CQ-resistant *Pf*-parasites efflux chloroquine from their digestive vacuoles at *ca* 40 times the rate of CQ-sensitive *Pf*-parasites, hence decreasing the accumulation of drug at its target site. In addition, CQ-resistant parasites

are thought to have a lower transport activity of drug to the DV than CQ-sensitive parasites. They therefore have a reduced affinity for CQ where import of the drug is mediated by a *Plasmodium falciparum* Na^+/H^+ exchanger.[48] Nevertheless, chloroquine, in combination with other antimalarial drugs, remains widely prescribed in the treatment of malaria worldwide.

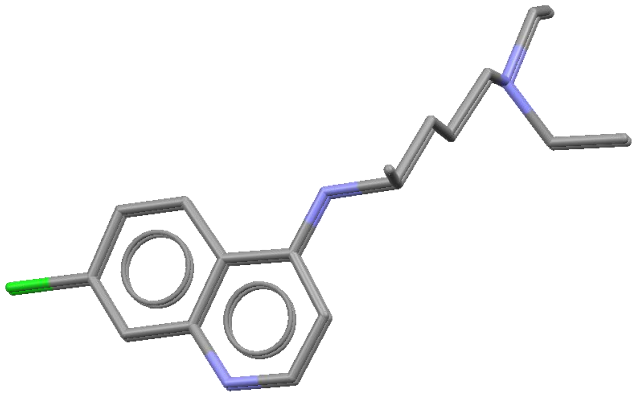

Chloroquine

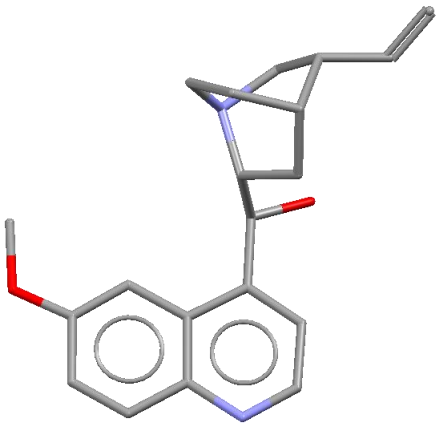

Quinine

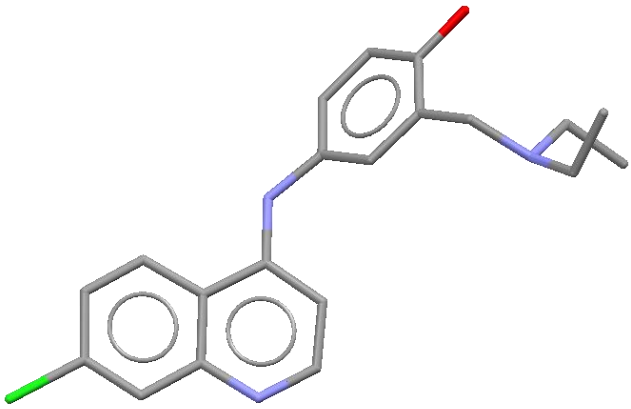

Amodiaquine

Figure 1.5: Chemical structures of quinoline-containing antimalarial drugs referred to in the text.

1.7 DRUG BINDING MODELS

Quinoline drugs such as chloroquine (CQ) are potent blood schizonticides and are effective against the intra-erythrocytic trophozoite parasite, the stage in the lifecycle of the parasite in which haemoglobin is degraded. Chloroquine enters the *Pf*-infected RBC and accumulates in the parasite's digestive vacuole (DV) by diffusion. The accumulation of CQ in the DV is largely due to the mechanism of „ion trapping' as a result of pH differential between the DV and the RBC cytoplasm as depicted by Figure 1.6. The pK_a for the quinoline N of CQ is *ca* 8.1 and it follows from the Henderson-Hasselbalch[49] equation (Equation 1.1) that at physiological pH *ca* 17% is calculated to be deprotonated. The concentration of deprotonated CQ decreases to *ca* 0.05 M at the DV pH of 4.8. This indicates that deprotonated CQ is more membrane permeable than protonated CQ and therefore protonated CQ accumulates down the pH gradient where it is trapped inside the DV.[42] The high concentration of CQ in the DV is thought to inhibit the formation of haemozoin.

$$pH = pK_a + \log_{10}\left(\frac{[Q^-]}{[HQ]}\right) \qquad \textbf{(1.1)}$$

The site of action of CQ is believed to be the free haem generated in the DV of the parasite after degradation of haemoglobin. CQ is thought to form a complex with free haem and prevent its polymerisation into haemozoin by detoxification in the DV.[50] Chou *et al*.[50] showed that the CQ-Fe(III)PPIX complex was toxic to the malarial parasite in the same way as free Fe(PPIX).

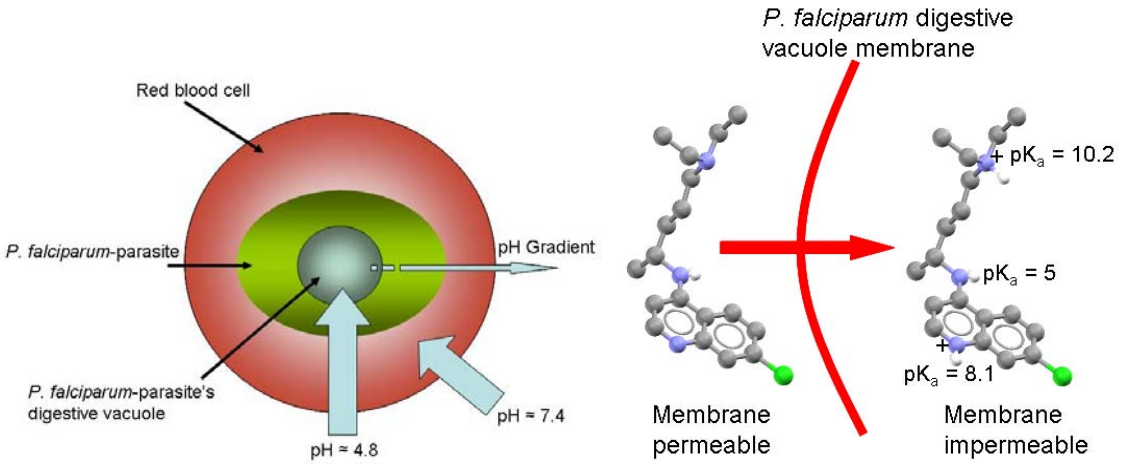

Figure 1.6: Proposed mechanism of chloroquine permeability across the digestive vacuole membrane in a *Plasmodium falciparum*-infected red blood cell. (Modified from reference)[42]

There are three models for the binding of antimalarial drugs to the haem aggregate. The first involves an intercalation of the quinoline ring of CQ between porphyrin rings within a crevice at the corrugated surface of haemozoin. CQ binds to the surface through the vinyl and methyl groups located on haemozoin (β-haematin). This suggests that binding is chiral specific as shown in Figure 1.7. The binding can disrupt or cap the growth of the aggregate in one direction. The intercalation of quinoline rings between the porphyrin rings of haemozoin is further anchored by a salt bridge between the tertiary amine of CQ and a surface-exposed carboxylate group on the growing (001) haemozoin (β-haematin) crystal face.[49]

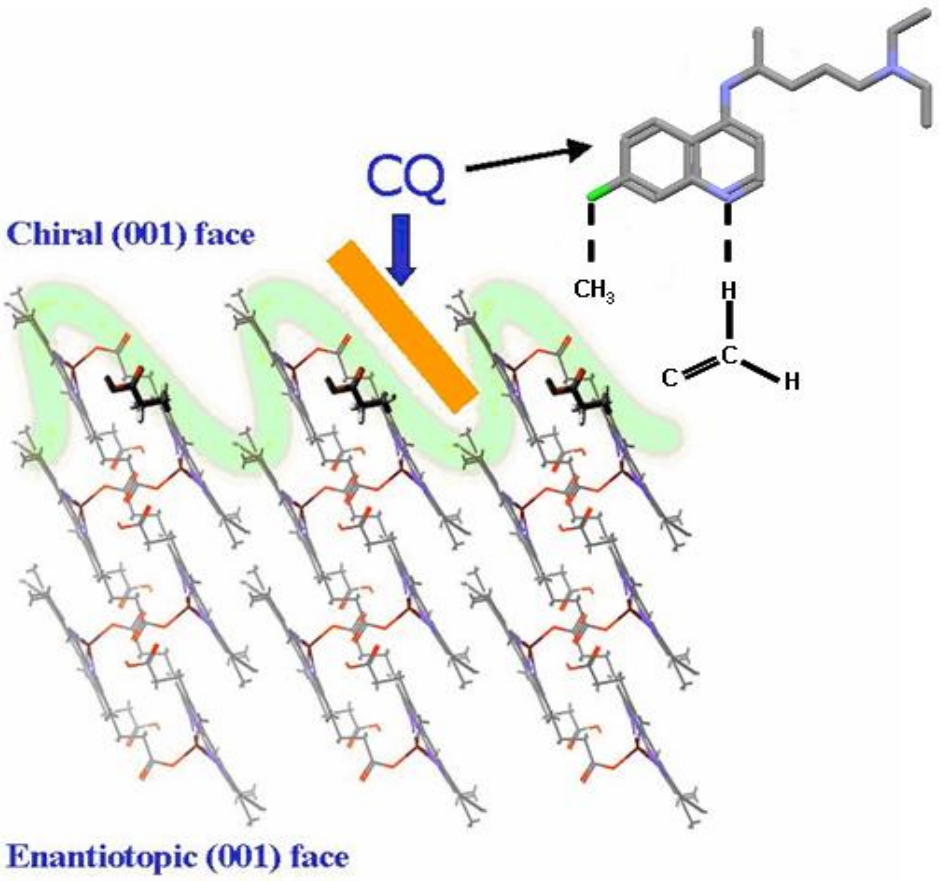

Figure 1.7: Proposed model for binding of CQ to the corrugated surface of β-haematin. (Modified from reference)[49]

Another proposed model for quinoline bioactivity is inhibition of the aggregation of Fe(III)PPIX as a result of quinoline forming a non-covalent attachment to the face of the aggregate through π-π interactions. This caps the formation of haemozoin and terminates chain extension[51] as shown in Figure 1.8.

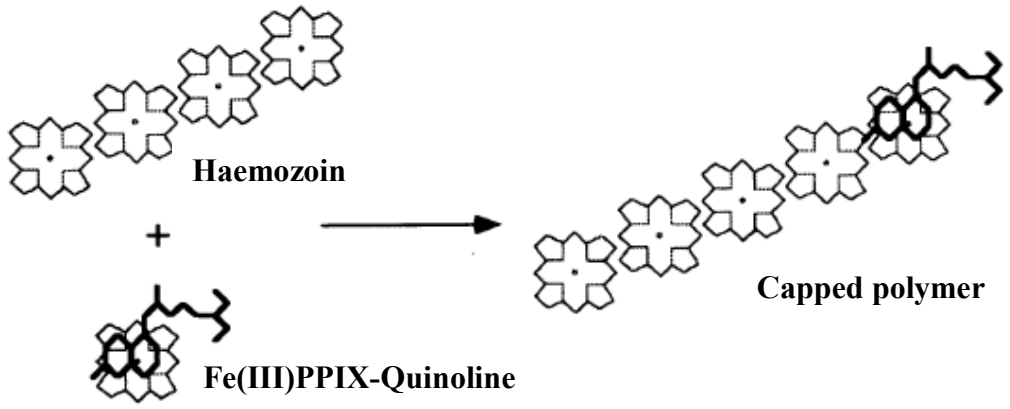

Figure 1.8: Proposed model for drug binding via a sandwich complex to the Fe(III)PPIX aggregate. (Modified from reference)[51]

Finally, the third mechanism of quinoline activity involves binding mainly to the μ-oxo dimer form of haematin rather than the monomeric form via π-π interactions. This leads to a reduction in the availability of monomeric haematin for polymerisation into malaria pigment, as the haematin dimerisation equilibrium is shifted to the μ-oxo dimer when the quinoline drugs are bound as shown in Figure 1.9.[52] It should be noted however that the existence of the μ-oxo dimer form of haematin under the conditions of the digestive vacuole has been questioned.[53]

The common feature of all three models is that they predict an increase in free haem within the digestive food vacuole. As noted above, free haem is toxic to the parasite, as it causes the DV membrane to lyse and death to ensue. These models provide a further rational for investigating the DV as they predict that the accumulation of CQ in the DV is the primary reason for the drug's efficacy. By achieving a greater understanding of the mechanisms of CQ drug attachment, it is hoped that new antimalarial drugs may be developed that can overcome the growing problem of CQ resistance in *Plasmodium falciparum* parasites.

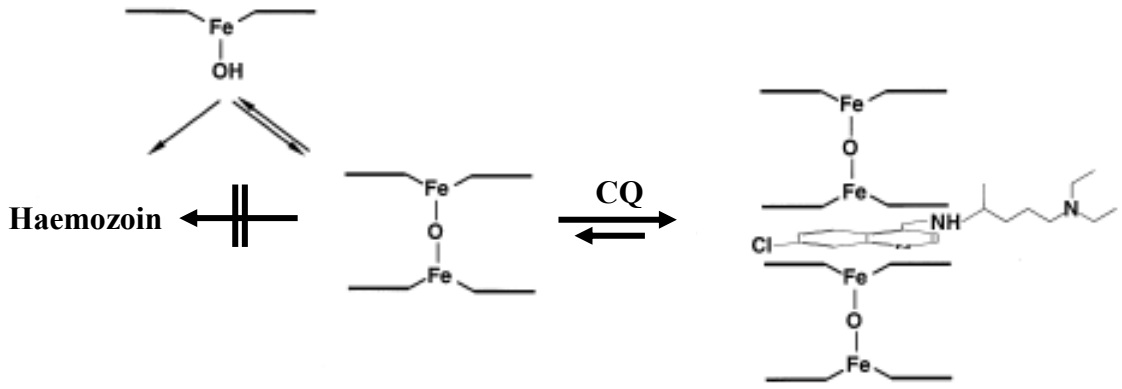

Figure 1.9: Proposed model for drug binding non-covalently between two haematin μ-oxo dimer molecules. (Modified from reference)[52]

1.8 DIAGNOSTIC TECHNIQUES

Several diagnostic techniques are employed for malaria detection. These include fluorescence microscopy,[54-58] PCR-based assays,[58-60] serological (dipstick) antigen detection,[58,61-63] flow cytometry[58,64] and Laser Desorption Mass spectrometry (LDMS).[65] Hitherto, the potential of vibrational spectroscopic techniques as malaria diagnostics has not been exploited, which is surprising given the important role the technique has played in understanding the molecular and electronic structure of β-haematin and haemozoin.[4,66,67,68] In an early study by Slater *et al.*[69] Fourier-transform infrared (FTIR) spectroscopy was used to identify vibrational modes specifically associated with the propionate groups that link the haem groups together in the haem dimeric array.[69] Initial resonance Raman studies by Ong *et al.*[70,71] demonstrated the potential of Raman spectroscopy to detect haemozoin in fixed cells. Using Resonance Raman (RR) spectroscopy Wood *et al.*[72] observed dramatic band enhancement of specific vibrational modes of haemozoin using near-IR excitation wavelengths. This enhancement could be used to identify and image haemozoin within the DV of single infected functional cells.[73] More recently this technique has been applied to investigate

the interaction of chloroquine based antimalarial drugs with haemozoin and *β*-haematin.[53,74]

Since the discovery of the malaria parasite in 1880, bright-field microscopy has been the standard tool for malaria diagnosis. The main advantage of the technique is its ability to quantify and identify the parasite at different stages of the parasite's lifecycle. This information makes it possible to determine a treatment regime specific to individual patient. However, microscopy also has several disadvantages. The major critiques are that it is subjective and requires experienced personnel to make the diagnosis.

Rapid diagnostic tests (RDTs), also known as "dipsticks", provide an alternative to microscopy. RDTs make use of a captured antibody and a conjugated detection antibody to detect the malarial antigen in blood samples. The advantages of this approach include the rapid turnaround time and the simplicity of use, which allow clinicians to make on-the-spot diagnoses. However, it is not possible at this time to quantify infected parasites with RDTs, which is a major disadvantage as knowledge of parasite numbers often determines the therapeutic approach. In addition, although their sensitivity is good at 40 parasites/μL of blood, the cost of dipsticks has limited their use in the developing world where these tests are needed.

LDMS is able to detect haemozoin to a sensitivity of 100–1,000 parasites/μL of blood, roughly similar to routine microscopy. However, the technique relies on the presence of haemozoin and therefore early ring stages of the parasite escape detection with this approach. Raman microscopy also shows potential as a diagnostic for malaria. However, like LDMS it currently relies on the detection of haemozoin in the cells and consequently at present the technique has only been shown to detect later stages of the parasite's lifecycle.

While several resonance Raman studies[70-72,75] have been implemented to detect and monitor the formation of haemozoin in erythrocytes, to date the diagnostic potential of FTIR spectroscopy has not been investigated. FTIR has the advantage of being more sensitive to the lipid moieties than Raman spectroscopy, thereby potentially enabling detection of parasites prior to trophozoite formation. In addition, the lipid bands are very weak when shorter excitation wavelength lasers are applied and high Raman excitation laser power can photo-degrade the cell. Furthermore, the synchrotron FTIR microscope has the advantage of taking high signal-to-noise (S/N) ratio spectra in 1 minute compared to 10-30 minutes when recording a Raman map using a conventional Raman microscope. Moreover, to record a map of thousands of cells using a conventional FTIR imaging microscope with a focal plane array (FPA) detector would take only 1-3 minutes compared to many hours when using a Raman microscope.

1.9 THE PRINCIPAL MACROMOLECULES WITHIN INFECTED ERYTHROCYTES

This dissertation principally reports on the potential of FTIR and Raman microspectroscopy as complimentary techniques in the detection of *Plasmodium falciparum*-parasites in functional erythrocytes. Secondly, it explores the potential of these techniques to further our understanding of malaria detection and treatment. FTIR and Raman microspectroscopy can be used to investigate chemical changes that occur within infected erythrocytes. FTIR is useful for distinguishing between the various stages of the *Pf*-parasite development based on lipid signal, while the Raman technique is useful for detecting the haemozoin commonly found in parasites in the trophozoite stage. A central aim is to spectroscopically detect changes in the concentration and

structure of macromolecules including proteins, lipids and the haem moieties present in malaria infected cells. Several studies have investigated the vibrational modes of the above macromolecules. However, there is still an element of conjecture on some band assignments, especially that of whole RBCs because there are a number of superimposed bands present in the spectrum, particularly in the IR spectrum.

In addition, there are many factors that influence band position. These include the methods, solutions and conditions used to prepare the samples, the instrumental parameters and the type of mathematical processing applied to manipulate the recorded spectra.

The above factors may render precise band assignment to a particular vibrational mode difficult, but it is feasible to give a general assignment of a vibrational mode to a wavenumber range. Also the extensive range of literature available on vibrational spectroscopy of macromolecules and whole RBCs facilitates the task of band assignment. The following subsections give a summary of the function, structure and spectroscopy of the principal macromolecular components of concern in this work.

1.9.1 PROTEINS

Peptides and proteins made of amino acids are linear polymers linked together by peptide bonds between the carboxyl and amino group of adjacent amino acid residues as seen in Figure 1.20.

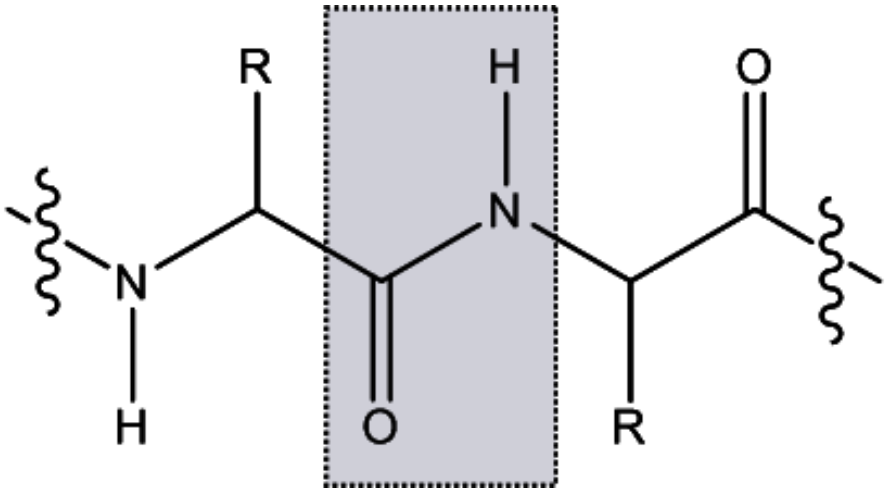

Figure 1.20: The peptide bond (highlighted) links amino acids together to form peptides and polypeptides/proteins.

The primary (1°) structure of a protein or peptide is the sequence of amino acids, which is in turn determined by its DNA template via the genetic code. The secondary (2°) structure is the three-dimensional folding of the amino acid chain that determines the protein function. In 1951, Linus Pauling and coworkers[76] discovered the α-helices and β-pleated sheets as shown in Figure 1.21, which has been found to be important in saturating all the hydrogen bond donors and acceptors in the peptide backbone. Other forms of secondary structure include coil, β-turn and random structures. The tertiary (3°) structure is observed when folding of the secondary structure produces a compact globular protein, which is often defined by the overall fold and three-dimensional arrangement of the protein. The quaternary (4°) structure refers to the interaction between subunits of large protein assemblies and often consists of more than one amino acid chain.

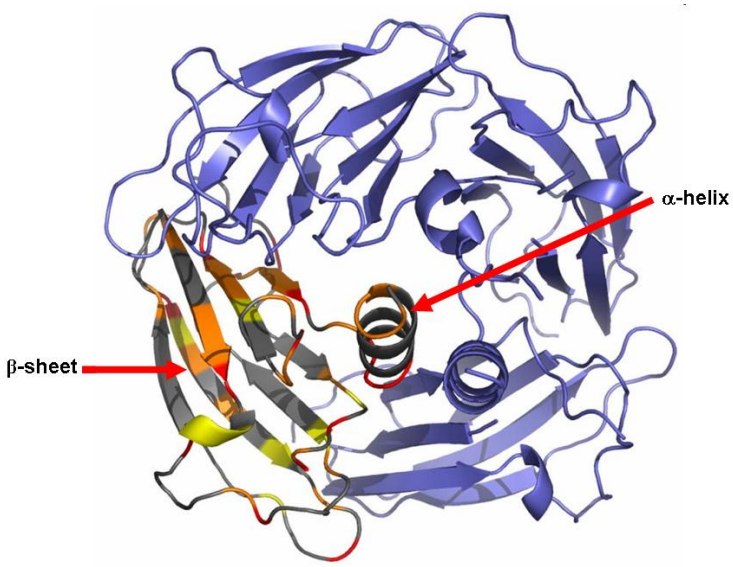

Figure 1.21: α-helical and β-pleated sheet secondary structures of protein structures. (Modified from reference)[77]

1.9.1.1 Haemoglobin

Haemoglobin is an example of a globular protein where the α-helix (*ca* 70%) is bent and folded to form a compact molecule with four quaternary subunits each of which contains a haem prosthetic group. Haemoglobin has many forms; the two most commonly known include oxy-haemoglobin and deoxy-haemoglobin. In the oxygenated state, the Fe atom is in a ferrous low spin state (S = ½) within the porphyrin plane and binds to dioxygen.[78] In the deoxygenated state, the Fe atom is in a ferric high spin state (S = 2) and is translocated *ca* 0.4 Å out of the porphyrin plane as shown in Figure 1.22.[79]

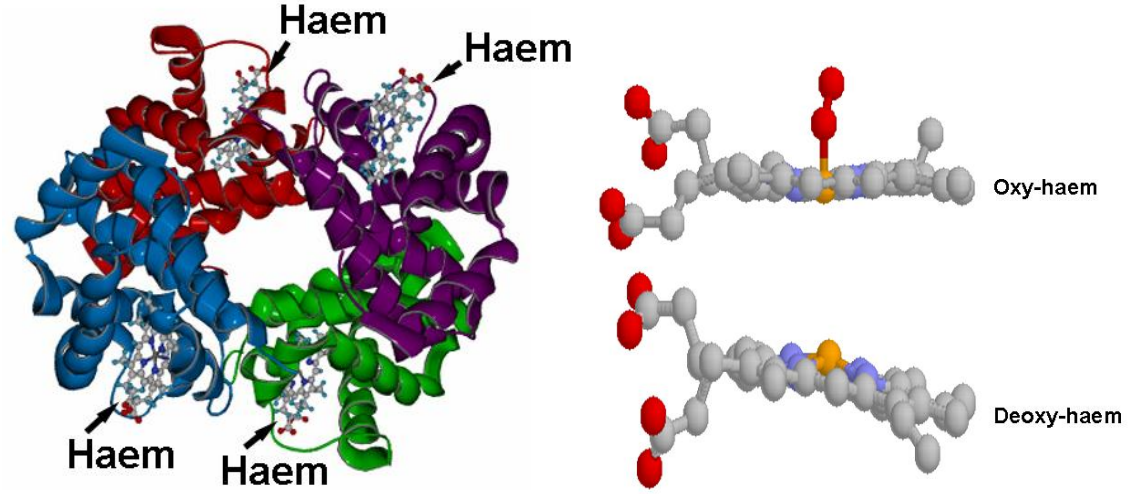

Figure 1.22: LEFT The quaternary structure of haemoglobin (Modified from reference)[80], **RIGHT** Representations of the sixth ligand binding position in Oxy/Deoxy-haem units of haemoglobin. (Modified from reference)[78] **NOTE**: The imidozole ring of the F8 histidine residue in the fifth ligand binding position is excluded from the representation on the right**.**

IR spectroscopy is a highly sensitive technique for the investigation of secondary protein structure and the detection of amide bond vibrations. IR band assignments of 2° protein structure are given in Table 1.1. The amide vibrations (Table 1.2) are influenced by the difference in H-bonding and the geometry of the 2° structures. The degree of IR spectral overlap in the position of various 2° structure IR bands, as seen in Table 1.1, makes it difficult to assign precise vibrational bands. X-ray emission/absorption spectroscopy and circular dichroism (CD), as well as the use of deuterated and non-deuterated solvents,[81] are analytical techniques that help elucidate these spectral bands.

Table 1.1: IR band assignments of different secondary protein structure. (Modified from reference)[81]

(2°) structure	Wavenumber (cm^{-1})	Band strength
α helices	1660-1620 (*as*), 1300-1250 (*s*)	*m-s*
β-pleated sheet	1695-1660 (*as*), 1255-1220 (*s*)	*w-m-s*
β-turns	1695-1615 (*as*), 1295-1270 (*s*)	*w-m-s*
coils	1670-1640 (*as*), 1294-1240 (*s*)	*w-m-s*
random structures	1650-1640 (*as*), 1294-1240 (*s*)	*w-m-s*

NOTE: *w* = WEAK, *m* = MEDIUM, *s* = STRONG, *as* = ASYMMETRIC, *s* = SYMMETRIC, *v*= STRETCH.

Table 1.2: IR band assignments of Amide vibrational modes. (Modified from reference)[82]

Name	Wavenumber (cm^{-1})	Band strength	Assignment
Amide A	3300-3250	*w-m-s*	ν(N-H)
Amide I	1700-1600	*s*	ν(C=O), ν(C-N), $\delta_{\text{in plane}}$(C-N)
Amide II	1600-1500	*m-s*	ν(N-H), $\delta_{\text{in plane}}$(C-N)
Amide III	1350-1200	*w*	$\delta_{\text{in plane}}$(N-H), ν(C-N), δ(C-H), δ(N-H)
Amide IV	750-630	*w*	δ(O=C-N)
Amide V	750-700	*w*	$\delta_{\text{out of plane}}$(N-H), δ_{torsion}(C-N)
Amide VI	*ca* 600	*w*	$\delta_{\text{out of plane}}$(C=O)

NOTE: *w* = WEAK, *m* = MEDIUM, *s* = STRONG, *v*= STRETCH, δ= DEFORMATION.

1.9.1.2 Haem moieties

Haem is derived from an organic ring structure known as protoporphyrin, to which an iron atom is bound in the center of the porphyrin as seen in Figure 1.23. The iron atom has six coordination bonds, four to nitrogen atoms that are part of the porphyrin ring system and two perpendicular to the porphyrin. Haem is found in a number of oxygen transporting proteins such as haemoglobin and myoglobin as well as in proteins responsible for energy transfer reactions such as cytochromes. Its primary function in haemoglobin is to carry molecular oxygen (O_2) since oxygen is poorly soluble in aqueous solutions and cannot be carried to tissues in sufficient quantity if it is simply dissolved in blood serum. When oxygen binds, this changes the electronic properties of the haem iron, which accounts for the change in colour from purple/blue (deoxy-haemoglobin) to red (oxy-haemoglobin). Other ligands have a higher affinity than O_2 for binding to the coordination sites of iron that are perpendicular to the porphyrin, such as carbon monoxide (CO) and nitric oxide (NO).

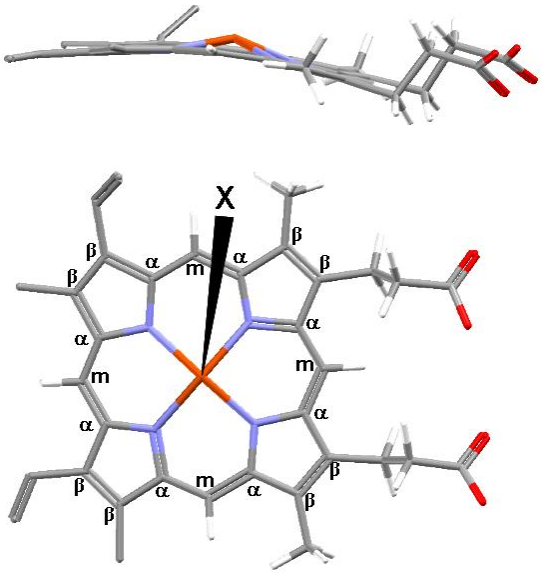

Figure 1.23: Chemical structure of Fe(III)PPIX moiety. **Above** = side view, **Below** = face view. **NOTE:** X = Cl/OH (haemin/haematin).

This study focuses on using resonance Raman spectroscopy as a tool to study porphyrin moieties, including haems and other metallo-porphyrins.[83] Because of the intrinsic symmetry and chromophoric structure of iron(III)-protoporphyrin IX (Fe(III)PPIX) molecules such as haemin (Fe(III)PPIX-Cl)) and haematin (Fe(III)PPIX-OH)) a strong Raman scattering occurs upon excitation of these molecules at many wavelengths. Haem units (Fe(III)PPIX) are also found in abundance within the digestive vacuole (DV) of the malaria parasite in infected RBCs in the form of haemozoin (malaria pigment), as discussed previously. The high sensitivity of Raman spectroscopy to haem structures confers an advantage over FTIR in directly monitoring formation and inhibition of haemozoin.

1.9.2 LIPIDS

Lipids are molecules that have a strong propensity to associate with one another through non-covalent forces[84] and are characterised by having a hydrophilic head group and a hydrophobic tail group. Biological lipids are insoluble in water and tend to aggregate due to the non-covalent bonding. The major types of lipids are simple fatty acids, triglycerides, phospholipids, sphingolipids, sterols (such as cholesterol), carotenoids and prostaglandins.

Fatty acids consist of a carboxylic acid head group with a long unbranched aliphatic tail. The long hydrocarbon tail is either saturated with hydrogens or unsaturated (containing double bonds). They are found in natural fats and oils and as a component of membrane phospholipids and glycolipids. Fatty acids are generated by the hydrolysis of the ester linkages in triglycerides liberating glycerol and the fatty acid.

Triglycerides (also termed triacylglycerols (TAGs) or neutral fats) are composed of three fatty acids each in ester linkage with a single glycerol molecule as shown in Figure 1.24. This results in the polar hydroxyls of glycerol and the polar carboxylates of the fatty acids being bound in the ester linkages, which causes TAGs to be nonpolar. TAGs have a significant advantage over polysaccharides (such as glycogen and starch) as a source of stored fuel. Stored TAGs are easily hydrolysed by enzymes (lipases) found in lysosomes to give fatty acids and glycerol; the former are further broken down after they are carried to target tissues via the bloodstream.

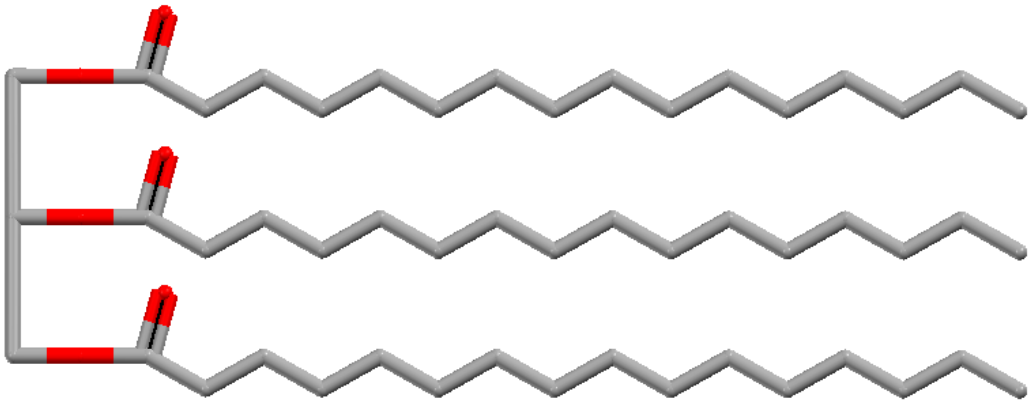

Figure 1.24: Chemical structure of TAG (tristearin).

Other common lipids in biological systems are sphingolipids, which are found most commonly as sphingomyelins (ceramide phosphocholines) in the nervous tissue and brain of humans and are important in the normal functioning of the nervous system. Sterols (such as cholesterol) are present in the cell membranes of most eukaryotic cells and play important roles in the synthesis of biological molecules, including bile acids, vitamin D, cortisol and sex hormones such as estrogen and testosterone. Carotenoids are lipid-soluble photosynthetic pigments made up of isoprene units[85] and function to absorb photons (light energy) for use in photosynthesis, while protecting chlorophyll

from photo-degeneration. Prostaglandins are lipid-soluble, hormone-like regulatory molecules containing a five-carbon ring originating from the chain of arachidonic acid.[85] They act as mediators and have complex effects on metabolism.

Phosphoglycerides are the major class of phospholipids and are the main component of biological membranes. Phospholipids are found in myelin sheaths surrounding axons and are found as granules in blood platelets (thrombocytes). In biospectroscopy, phospholipids are most commonly studied in the form of phospholipid membrane bilayers. Phosphoglycerides are glycerol-based phospholipids and are derived from glycerol-3-phosphate. They are characterised by a phosphate head group attached in a glycerol unit to two acyl chains. In general, they contain a C_{16} or C_{18} saturated fatty acid at C-2 and a C_{18} to C_{20} unsaturated fatty acid at C-3 as depicted in Figure 1.25.[85]

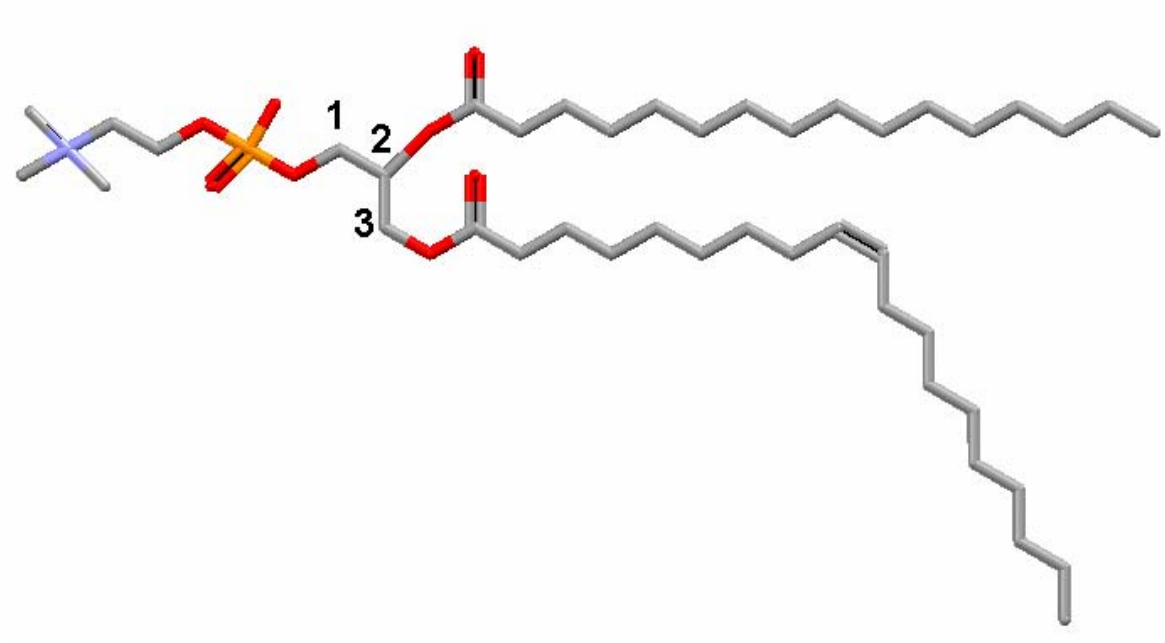

Figure 1.25: Chemical structure of phosphoglyceride (phosphatidylcholine).

The *cis* stereochemistry of the alkene in the unsaturated fatty acid chain causes the chain to kink and when packed in a parallel fashion to form extended membrane sheets, the fluid mosaic property of the membrane is increased (Figure 1.26). Phospholipids do not cross the membrane but rather move in lateral directions along the membrane while proteins never rotate in the membrane and remain in a fairly fixed position.

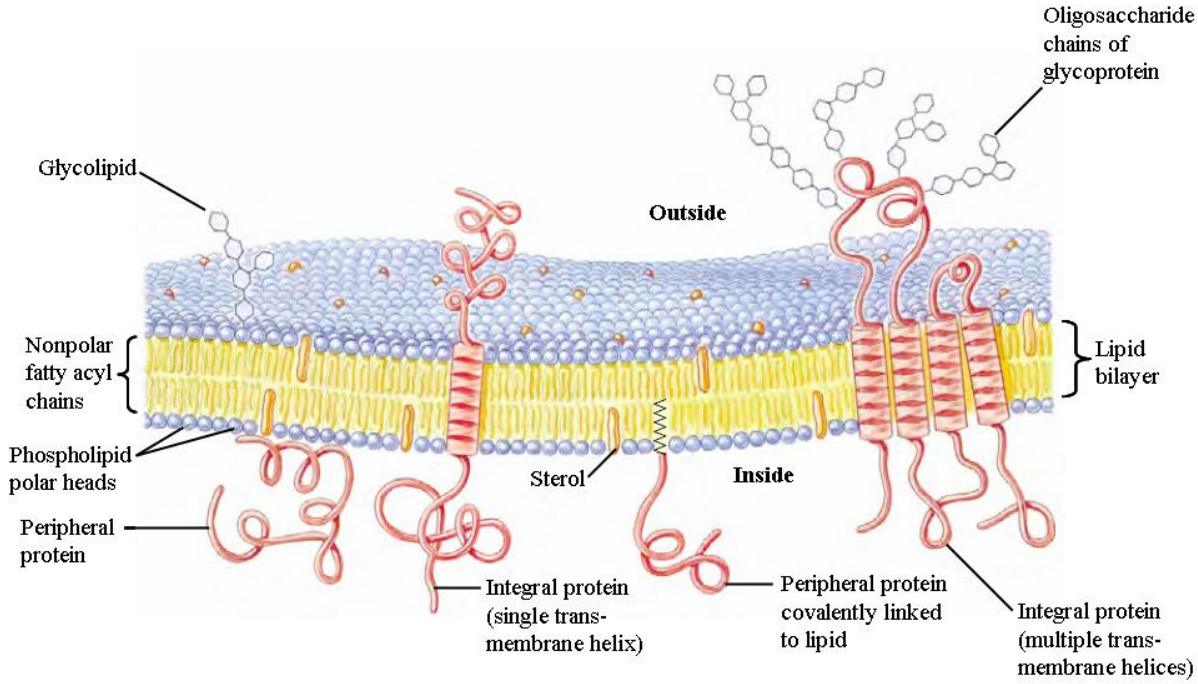

Figure 1.26: Fluid mosaic model for phospholipid bilayer membrane model. (Modified from reference)[85]

The vibrational assignment of phospholipids and TAGs is based on a number of infrared studies that have investigated model lipids and biological membranes.[86-88] Table 1.3 shows IR band assignments for lipids based on liposomes composed of a single lipid species,[89] spectroscopic studies on xenografts[90] and phospholipid phase transitions in model and biological membranes.[87,91]

Table 1.3: IR band assignments of phospholipids.

Wavenumber (cm^{-1})	Assignment
2956	$\nu_{as}(CH_3)$acyl chain lipids[90]
2922	$\nu_{as}(CH_2)$acyl chain lipids[90]
2874	$\nu_{s}(CH_3)$ acyl chain lipids[90]
2852	$\nu_{s}(CH_2)$ acyl chain lipids[90]
1474–1520	$\delta(CH_2)$ scissoring[87,91]
1228	$\nu_{as}(PO_2^-)$[89]
1085	$\nu_{s}(PO_2^-)$[89]

NOTE: ν= STRETCH, δ= DEFORMATION.

1.10 RESEARCH AIMS

Resonance Raman and FTIR spectroscopy can be used to investigate the interactions of quinoline antimalarial drugs in *Plasmodium falciparum* infected erythrocytes. The first section of this dissertation (Chapter 3) presents the intrinsic value of using synchrotron FTIR microspectroscopy to detect specific lipid and haemozoin marker bands in fixed single malaria infected cells at different stages of the intra-erythrocytic life cycle of the parasite. Chapter 4 details a resonance Raman spectroscopic investigation detecting structural changes in haemozoin following incubation with chloroquine in infected erythrocytes. The effect of supramolecular interactions in near-IR Raman excitonic enhancement observed in malaria pigment and other haem complexes are presented and discussed in Chapter 4. Chapter 5 examines aggregated enhanced Raman scattering in Fe(III)PPIX solutions and focuses on the effects of differing concentrations of Fe(III)PPIX units, with and without CQ presence,

on excitonic interactions, in an effort to monitor antimalarial drug interactions and determine the effectiveness of potential antimalarial compounds on Fe(III)PPIX. Chapter 6 discusses the major conclusions and possible future directions for research in this field.

1.11 REFERENCES

(1) Poinar, G. J. *Syst. Parasitol.* **2005**, *61*, 47-52.

(2) Joy, D. A.; Feng, X.; Mu, J.; Furuya, T.; Chotivanich, K.; Krettli, A. U.; Ho, M.; Wang, A.; White, N. J.; Suh, E.; Beerli, P.; Su, X-z. *Science* **2003**, *300*, 318-321.

(3) Martin, M. J.; Rayner, J. C.; Gagneux, P.; Barnwell, J. W.; Varki, A. *Proc. Natl. Acad. Sci. USA*. **2005**, *102*, 12819-12824.

(4) Cox, F. E. G. *Clin. Microbiol. Rev.* **2002**, *15*, 595-612.

(5) Greenwood, B.; Mutabingwa, T. *Nature* **2002**, *415*, 670-672.

(6) Ridley, R. G. *Nature* **2002**, *415*, 686-693.

(7) Golgi, C. *Arch. Sci. Med.* **1886**, *10*, 109-135.

(8) Mu, J.; Joy, D. A.; Duan, J.; Huang, Y.; Carlton, J.; Walker, J.; Barnwell, J.; Beerli, P.; Charleston, M. A.; Pybus, O. G.; Su, X-z. *Mol. Biol. Evol.* **2005**, *22*, 1686-1693.

(9) Layne, P. S. *Principles of infectious disease epidemiology.* ; UCLA: Los Angeles, 2004.

(10) Yazdani, S. S.; Mukherjee, P.; Chauhan, V. S.; Chitnis, C. E. *Curr. Mol. Med.* **2006**, *6*, 187-203.

(11) Baird, K. J.; Hoffman, S. L. *Clin. Infect. Dis.* **2004**, *39*, 1336-1345.

(12) Collins, W. E.; Jeffery, G. M. *Clin. Microbiol. Rev.* **2007**, *20*, 579-592.

(13) Snow, R. W.; Guerra, C. A.; Noor, A. M.; Myint, H. Y.; Hay, S. I. *Nature* **2005**, *7030*, 214-217.

(14) Holding, P. A.; Snow, R. W. *Am. J. Trop. Med. Hyg.* **2001**, *64*, 68-75.

(15) Chinery, W. A. *J. Trop. Med. Hyg.* **1984**, *87*, 75-81.

(16) Robert, V.; Macintyre, K.; Keating, J.; Trape, J. F.; Duchemin, J. B.; Warren, M.; Beier, J. C. *Am. J. Trop. Med. Hyg.* **2003**, *68*, 169-176.

(17) Keiser, J.; Utzinger, J.; de Castro, M. C.; Smith, T.; Tanner, M.; Singer, B. *Am. J. Trop. Med. Hyg.* **2004**, *71*, 118-127.

(18) Murphy, G. S.; Oldfield, E. C. III. *Infec. Dis. Clin. North Am.* **1996**, *10*, 747-775.

(19) Genton, B.; D' Acremont, V. *Travelers' malaria*; BC Decker, 2001.

(20) Trampuz, A.; Jereb, M.; Muzlovic, I.; Prabhu, R. M. *Crit. Care* **2003**, *7*, 315-323.

(21) Carter, J. A.; Ross, A. J.; Neville, B. G.; Obiero, E.; Katana, K.; Mung'ala-Odera, V.; Lees, J. A.; Newton, C. R. *Trop. Med. Int. Health* **2005**, *10*, 3-10.

(22) Boivin, M. J. *J. Dev. Behav. Pediatr.* **2002**, *23*, 353-364.

(23) Holding, P. A.; Snow, R. W. *Am. J. Trop. Med. Hyg.* **2001**, *64*, 68-75.

(24) Miller, L. H.; Baruch, D. I.; Marsh, K.; Doumbo, K. *Nature* **2002**, *415*, 673-679.

(25) Hellerstein, S.; Spees, L.; Surapathana, W. O. *J. Lab. Clin. Med.* **1970**, *76*, 10-24.

(26) Francis, S.; Sullivan, D. J. J.; Goldberg, D. *Annu. Rev. Microbiol.* **1997**, *51*, 97-123.

(27) Banerjee, R.; Liu, J.; Beatty, W.; Pelosof, L.; Klemba, M.; Goldberg, D. E. *Proc. Natl. Acad. Sci. USA.* **2002**, *99*, 990-995.

(28) Rosenthal, P. J.; Sijwali, P. S.; Singh, A.; Shenai, B. R. *Curr. Pharm. Des.* **2002**, *8*, 1659-1672.

(29) Eggleson, K. K.; Duffin, K. L.; Goldberg, D. E. *J. Biol. Chem.* **1999**, *274*, 32411-32417.

(30) Gavigan, C. S.; Dalton, J. P.; Bell, A. *Mol. Biochem. Parasitol.* **2001**, *117*, 37-48.

(31) Stack, C. M.; Lowther, J.; Cunningham, E.; Donnelly, S.; Gardiner, D. L.; Trenholme, K. R.; Skinner-Adams, T. S.; Teuscher, F.; Grembecka, J.; Mucha, A.; Kafarski, P.; Lua, L.; Bell, A.; Dalton, J. P. *J. Biol. Chem.* **2006**, *282*, 2069-2080.

(32) Hayward, R.; Saliba, K. J.; Kirk, K. *J. Cell Sci.* **2006**, *119*, 1016-1025.

(33) Egan, J. T. *Mol. Biochem. Parasitol.* **2008**, *157*, 127-136.

(34) Wright, A. D.; Wang, H.; Gurrath, M.; Konig, G. M.; Kocak, G.; Neumann, G.; Loria, P.; Foley, M.; Tilley, L. *J. Med. Chem.* **2001**, *44*, 873-885.

(35) Atamna, H.; Ginsburg, H. *Mol. Biochem. Parasitol.* **1993**, *61*, 231-241.

(36) Yayon, A.; Timberg, R.; Friedman, S.; Ginsburg, H. *J. Protozool.* **1984**, *31*, 367-372.

(37) de Villiers, K. A.; Kaschula, C. H.; Egan, T. J.; Marques, H. M. *J. Biol. Inorg. Chem.* **2007**, *12*, 101-117.

(38) Pagola, S.; Stephens, P. W.; Bohle, D. S.; Kosar, A. D.; Madsen, S. K. *Nature* **2000**, *404*, 307-310.

(39) Kaufman, T. S.; Ruveda, E. A. *Angew. Chem. Int. Ed. Eng.* **2005**, *44*, 854-885.

(40) Kyle, R. A.; Shampe, M. A. *JAMA* **1974**, *229*, 462.

(41) Ridley, R. G.; Hudson, A. T. *Exp. Opin. Ther. Patents* **1998**, *8*, 121-136.

(42) O' Neill, P.; Bray, P.; Hawley, S.; Ward, S.; Park, B. *Pharmacol. Ther.* **1998**, *77*, 29-58.

(43) Loeb, R. F.; Clark, W. M.; Coatney, G. R.; Coggeshall, L. T.; Dieuaide, F. R.; Dochez, A. R.; Hakansson, E. G.; Marshall, E. K.; Marvel, C. S.; McCoy, O. R.;

Sapero, J. J.; Sebrell, W. H.; Shannon, J. A.; Carden, G. A. *JAMA* **1946**, *10*, 1069-1070.

(44) Peters, W. *Chemotherapy and Drug Resistance in Malaria, Vols I and II*; Academic Press: London, 1987.

(45) Coatney, G. R. *Am. J. Trop. Med. Hyg.* **1963**, *12*, 121-128.

(46) Slater, A. F. G. *Pharmac. Ther.* **1993**, *57*, 203-235.

(47) Krogstad, D. J.; Gluzman, I. Y.; Kyle, D. E.; Oduola, A. M. J.; Martin, S. K.; Milhous, W. K.; Schlesinger, P. H. *Science* **1987**, *238*, 1283-1285.

(48) Sanchez, C. P.; Wünsch, S.; Lanzer, M. *J. Biol. Chem.* **1997**, *272*, 2652-2658.

(49) Buller, R.; Peterson, M. L.; Almarsson, O.; Leiserowitz, L. *Cryst. Growth Des.* **2002**, *2*, 553-562.

(50) Chou, A. C.; Chevli, R.; Fitch, C. D. *Biochemistry* **1980**, *19*, 1543-1549.

(51) Sullivan, D. J. J.; Gluzman, I. Y.; Russel, D. G.; Goldberg, D. E. *Proc. Natl. Acad. Sci. USA.* **1996**, *93*, 11865-11870.

(52) Dorn, A.; Vippagunta, S. R.; Matile, H.; Jacquet, C.; Vennerstrom, J. L.; Ridley, R. G. *Biochem. Pharmacol.* **1998**, *55*, 727-736.

(53) Frosch, T.; Kustner, B.; Schlucker, S.; Szeghalmi, A.; Schmitt, M.; Kiefer, W.; Popp, J. *J. Raman Spectrosc.* **2004**, *35*, 819-821.

(54) Richards, D. F.; Hunter, D. T.; Janis, B. *Am. J. Clin. Pathol.* **1969**, *51*, 280-283.

(55) Sodeman, T. M. *Am. J. Trop. Med. Hyg.* **1970**, *19*, 40-42.

(56) Shute, G. T.; Sodeman, T. M. *Bull. W.H.O.* **1973**, *48*, 591-596.

(57) Makler, M. T.; Ries, L. K.; Ries, J.; Horton, R. J.; Hinrichs, D. J. *Am. J. Trop. Med. Hyg.* **1991**, *44*, 11-16.

(58) Hanscheid, T. *Clin. Lab. Haem.* **1999**, *21*, 235-245.

(59) Humar, A.; Ohrt, C.; Harrington, M. A.; Pillai, D.; Kain, K. C. *Am. J. Trop. Med. Hyg.* **1997**, *56*, 44-48.

(60) Humar, A.; Harrington, M. A.; Kain, K. C. *Trans. R. Soc. Trop. Med. Hyg.* **1997**, *91*, 406-409.

(61) Makler, M. T.; Palmer, C. J.; Ager, A. L. *Ann. Trop. Med. Parasitol* **1998**, *92*, 419-433.

(62) Shiff, C. J.; Minjas, J. N.; Premji, Z. *Parasitol. Today* **1994**, *10*, 494-495.

(63) Garcia, M.; Kirimoama, S.; Marlborough, D.; Leafasia, J.; Rieckmann, K. H. *Lancet.* **1996**, *347*, 1549.

(64) van Vianen, P. H.; van Engen, A.; Thaithong, S.; van der Keur, M.; Tanke, H. J.; van der Kaay, H. J.; Mons, B.; Janse, C. J. *Cytometry* **1996**, *14*, 276-280.

(65) Demirev, P. A.; Feldman, A. B.; Kongkasuriyachai, D.; Scholl, P.; Sullivan, D. J. J.; Kumar, N. *Anal. Chem.* **2002**, *74*, 3262-3266.

(66) Brémard, C.; Girerd. P.; Kowalewski, P.; Merlin, J. C.; Moreau, S. *App. Spectrosc.* **1993**, *47*, 1837-1842.

(67) Bohle, D. S.; Conklin, B. J.; Cox, D.; Madsen, S. K.; Paulson, S.; Stephens, P. W.; Yee, G. T. *Am. Chem. Soc. Symp. Ser.* **1994**, *572*, 497-515.

(68) Wood, B. R.; McNaughton, D. *Exp. Rev. Proteom.* **2006**, *3*, 525-544.

(69) Slater, A. F. G.; Swiggard, W. J.; Orton, B. R.; Flitter, W. D.; Goldberg, D. E.; Cerami, A.; Henderson, G. B. *Proc. Natl. Acad. Sci. USA.* **1991**, *88*, 325-329.

(70) Ong, C. W.; Shen, Z. X.; Ang, K. K. H.; Kara, U. A. K.; Tang, J. *Appl. Spectrosc.* **2002**, *56*, 1126-1131.

(71) Ong, C. W.; Shen, Z. X.; Ang, K. K. H.; Kara, U. A. K.; Tang, S. H. *Appl. Spectrosc.* **1999**, *53*, 1097-1101

(72) Wood, B. R.; Langford, S. J.; Cooke, B. M.; Lim, J.; Glenister, F. K.; Duriska, M.; Unthank, J. K.; McNaughton, D. *J. Am. Chem. Soc.* **2004**, *126*, 9233-9239.

(73) Wood, B. R.; Tait, B.; McNaughton, D. *Appl. Spectrosc.* **2000**, *54*, 353-359.

(74) Cîntă -Pînzaru S, P. N.; Küstner, B.; Schlücker, S.; Schmitt, M.; Frosch, T.; Faber, J. H.; Bringmann, G.; Popp, J. *J. Raman Spectrosc.* **2006**, *37*, 326-334.

(75) Bonifacio, A.; Finaurini, S.; Krafft, C.; Parapini, S.; Taramelli, D.; Sergo, V. *Anal. Bioanal. Chem.* **2008**, *392*, 1277-1282.

(76) Pauling, P.; Corey, R. B.; Branson, H. R. *Proc. Nat. Acad. Sci. USA.* **1951**, *37*, 205-211.

(77) Vogeley, L.; Trivedi, V. D.; Sineshchekov, O. A.; Spudich, E. N.; Spudich, J. L.; Luecke, H. *J. Mol. Biol.* **2007**, *367*, 741-751.

(78) O' Malley, P. D., Ed. *New Developments in Sickle Cell Disease*; Nova Science Publishers, Inc.: New York, 2006.

(79) Fermi, G.; Perutz, M. F.; Shannan, B.; Fourme, R. *J. Mol. Biol.* **1984**, *175*, 154-174.

(80) Haen, P. J. *Principles of Hematology*; Wm. C. Brown Publishers: Dubuque IA, 1995.

(81) Singh, B. R. *Infrared Analysis of Peptides and Proteins, Principles and Applications*; American Chemical Society: Massachusetts, 2000.

(82) Wood, B. R., Monash University, Clayton, 1998.

(83) Spiro, T. G.; Li, X-Y. In *Biological Applications of Raman Spectroscopy*; Spiro, T. G., Ed.; Wiley: New York, 1988; Vol. 3.

(84) Mathews, C. K.; van Holde, K. J. *Biochemistry*; The Benjamin/Cummings Publishing Company: Redwood, USA, 1990.

(85) Lehninger, A.; Nelson, D. L.; Cox, M. M. *Principles of Biochemistry*, 3 ed.; Worth Publishers: New York, 2000.

(86) Astbury, W. T.; Dalgliesh, C. E.; Darmon, S. E.; Sutherland, G. B. B. M. *Nature* **1948**, *162*, 596-600.

(87) Mantsch, H. H.; McElhaney, R. N. *Chem. Phys. Lipid* **1991**, *57*, 213-226.

(88) Hübner, W.; Mantsch, H. H.; Paltauf, F.; Hauser, H. *Biochem.* **1994**, *33*, 320-326.

(89) Jackson, M.; Mantsch, H. H. *Spectrochim. Acta.* **1993**, *15*, 53-69.

(90) Fabian, H.; Jackson, M.; Murphy, L.; Watson, P. H.; Fichtner, I.; Mantsch, H. H. *Biospectroscopy* **1995**, *1*, 37-45.

(91) Wong, P. T. T.; Siminovitch, D. J.; Mantsch, H. H. *Biochim. Biophys. Acta.* **1988**, *947*, 139-171.

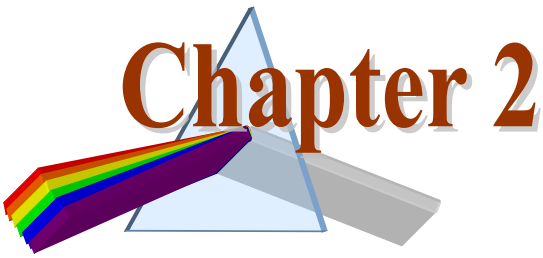

Biospectroscopy Theory and Data Analysis

2.1 SPECTROSCOPY

In the 1800s, spectroscopy referred to the interaction of matter with visible light dispersed by a prism according to its wavelength. In recent years, this definition has been broadened to include a wider range of the electromagnetic spectrum (Figure 2.1).

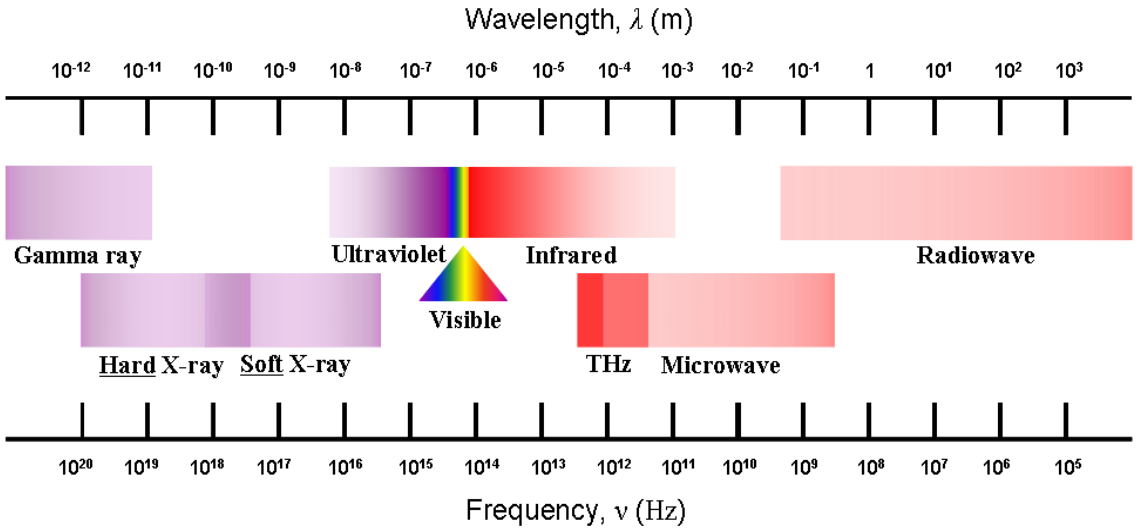

Figure 2.1: The electromagnetic spectrum

Changes in the energy of atoms and molecules as they transition between distinct energy levels cause them to emit or absorb electromagnetic radiation. Different energy transitions result in different frequencies of electromagnetic radiation. The premise of spectroscopy is to irradiate a given sample with a select portion of the electromagnetic spectrum in order to observe the interaction of radiation with the sample. The extent of absorption and emission of photons creates distinctive molecular signatures depending on the composition of the sample. Every molecule has a distinctive pattern of absorption and emission of radiation. By observing this pattern researchers are able to gain an understanding of the molecular composition of the sample and in some cases the energy transitions taking place.

Several spectroscopic techniques are employed to probe different transitions within atoms and molecules. These include X-ray emission/absorption and ultraviolet (UV) and visible spectroscopy to analyse electronic transitions; Raman and infrared (IR) spectroscopy to detect vibrational transitions; high resolution IR to probe vibration-rotation transitions; and microwave spectroscopy to investigate rotational transitions. Beyond that, Nuclear Magnetic Resonance (NMR) and Electron Paramagnetic Resonance (EPR) respectively probe nuclear and electron spin in a magnetic field.

This study utilises resonance Raman, Fourier Transform Infrared (FTIR) and UV-Visible spectroscopic techniques as potential diagnostic tools in malaria research. Taken together, these spectroscopic techniques are able to detect vibrational and electronic transitions which render them the most appropriate tools for identifying biochemical changes. Their potential as diagnostic tools lies in their ability to detect the biochemical changes that accompany the morphological variation that generally follows from disease or physiological modification in a sample.[1]

A detailed description of Raman and FTIR biospectroscopy theory follows.

2.2 BASIC THEORY OF VIBRATIONAL SPECTROSCOPY

A molecular vibration occurs when atoms in a molecule are in periodic motion relative to the constant translational and rotational motion of the entire molecule. Thus, the vibrational frequency is the frequency of the periodic motion. For a molecule with N atoms, there are $3N - 6$ vibrational modes for non-linear molecules and $3N - 5$ for linear molecules. Hence, when the number of atoms increases and consequently the number of corresponding vibrational modes increases, describing the molecular vibrations of any given molecule become increasingly difficult.

A simple model of a diatomic molecule comprising two atoms of mass m_1 and m_2 linked by a spring with zero mass that obeys Hooke's Law (Equation 2.1) is used to approximate the frequency of the oscillation in accordance with the law of simple harmonic motion.

$$F = -kx \tag{2.1}$$

where F (in N) is the *restoring force*. The force constant is represented by k (in Nm^{-1}) and depends upon the strength of the bond (spring). The displacement is given by x (in m) and the frequency (Hz) of the oscillation is given by:

$$\nu = \frac{1}{2\pi}\sqrt{\frac{k}{\mu}} \tag{2.2}$$

where μ (in kg) is the reduced mass and is defined as:

$$\mu = \frac{m_1 m_2}{m_1 + m_2} \tag{2.3}$$

The IR spectrum is a plot of the amount of radiation absorbed (or transmitted) as a function of wavenumber (cm^{-1}), where the wavenumber ($\bar{\nu}$) is given by:

$$\bar{\nu} = \frac{1}{\lambda} \tag{2.4}$$

where, λ is wavelength (in cm).

A simple diatomic molecule can be treated as a harmonic oscillator to solve the Schrödinger wave equation to give the discrete vibrational energy levels:

$$E_v = \left(v + \frac{1}{2}\right)\frac{h}{2\pi}\sqrt{\frac{k}{\mu}} \quad \textbf{(2.5)}$$

where h is Plank's constant and v is the *vibrational quantum number*, which must take only positive integer values (including zero).

The description of a molecular vibration between two atoms based on the harmonic oscillator is useful but overly simplistic. One flaw is that it describes the number of vibrational energy levels as being infinite as the bond length approaches zero. It does not model the effects of Coulombic repulsion between two nuclei, which produces a force in the same direction as the restoring force. In addition, the harmonic curve cannot predict the interatomic distance at which dissociation of the molecule occurs.

In contrast, the anharmonic model leads to two types of derivations which overcome some of the flaws in the harmonic model. First, the potential energy (E) between discrete vibrational energy levels becomes smaller, as v increases and the selection rule for the vibrational energy levels (where, $\Delta v = \pm 1$) is relaxed. Consequently, transitions of $\Delta v = \pm 2$ or 3 are also allowed. Such transitions give rise to *overtone* bands at approximately two or three times the frequency of the fundamental band. Secondly, an input of energy can simultaneously excite two different fundamental vibrational modes to produce a *combination* band. At lower vibrational energy levels, the harmonic curve closely approximates the anharmonic curve. However, unlike the harmonic model, the anharmonic model can be used to predict the interatomic distance where dissociation of the molecule occurs.

The vibrational motions are divided into two basic categories, *stretching* and *bending*. A continuous change in the interatomic distance along the axis of the bond

between two atoms results in a stretching vibration. A bending (deformation) vibration is characterised by a change in angle between two bonds. There are four types of deformation modes. These are *scissoring*, *wagging*, *rocking* and *twisting*.

The relative positions of atoms in a molecule fluctuate continuously due to the different types of molecular vibrations. Consequently, particular vibrational modes of complex molecules can be localised to specific bonds or groupings, leading to the concept of characteristic group frequencies. Some functional groups of interest to this work and observed in IR spectra include:

- C-O (*ca* 1209 cm^{-1}) and C=O vibrations (*ca* 1662 cm^{-1}) from the propionate linkage and the carbonyl stretching mode of haemozoin respectively.[2] When coordination between the carboxylate side chain of one haem to the Fe centre of another haem is unidentate, one of the C-O bonds is predicted to have double bond character and therefore give rise to C=O stretching absorption between 1700-1600 cm^{-1} in the mid-IR region.[2]
- The amide I and II modes from proteins in RBCs give an IR band positioned at *ca* 1650 cm^{-1} and *ca* 1545 cm^{-1}.
- The ester carbonyl bands from lipids in cells are positioned at *ca* 1744 cm^{-1}.
- Asymmetric methyl and methylene stretching vibrations from lipids in cells are positioned at *ca* 2956 cm^{-1} and *ca* 2922 cm^{-1} respectively.
- Symmetric methyl and methylene stretching vibrations from lipids in cells are positioned at *ca* 2874 cm^{-1} and *ca* 2852 cm^{-1} respectively.

For the specific porphyrin modes observed in the Raman spectrum, refer to Table 2.3.

2.3 BASIC THEORY OF RAMAN SPECTROSCOPY

2.3.1 RAMAN SPECTROSCOPY

In 1928 Chandrasekhara Venkata Raman discovered that certain molecules tend to scatter small portions of visible wavelength radiation inelastically, and that the chemical structure of the molecule responsible for the scattering affects the degree of the shift in wavelength. The intensity of Raman scattered photons (I_s) is inversely proportional to the 4th power of the wavelength (λ) of the incident photons and directly proportional to the square of the polarizability (α) given below:

$$I_s \propto \frac{\alpha^2}{\lambda^4} \tag{2.6}$$

There are two types of scattering, namely elastic and inelastic. Inelastic, or Raman, scattering mechanisms are known as Stokes and anti-Stokes and are depicted in Figure 2.2. Stokes scattering involves photons having energy $E_0 = hv_0$ that interacts with molecules in their electronic and vibrational ground state and excites the molecules into a virtual state. The virtual state is located anywhere between the electronic ground state (S_0) and electronic excited state (S_1). The molecules relax from the virtual state to a vibrational level in the electronic ground state that is higher than the initial level. In doing so, they emit scattered photons. The wavelength of Stokes scattered light is red shifted compared to the excitation light ($hv_0 > hv_S$).

In contrast to Stokes scattering, anti-Stokes scattering involves molecules in excited vibrational states within the electronic ground state being excited to a virtual state upon irradiation with monochromatic light as shown in Figure 2.2. From the

virtual state, the molecules relax to the ground vibrational state energy level. Thus, the molecule emits scattered photons with increased energy. The wavelength of anti-Stokes scattered light is blue shifted compared to the excitation light ($h\nu_0 < h\nu_{aS}$). Although anti-Stokes scattering can produce a Raman signal, it is less intense than the corresponding Stokes signal. This is because the Botlzmann distribution proposes that the probability of the molecule occupying an excited vibrational state is less than that of it occupying a ground vibrational state. For this reason, only the Stokes spectrum is generally used.

The Raman effect gives rise to both Stokes and anti-Stokes scattering. This occurs when a photon of the incident beam induces a dipole moment within the molecule. This entails a brief distortion of electrons scattered around the molecule or functional group, causing the molecule to temporarily become polarized. This dipole moment disappears upon reemission of the radiation as the molecule relaxes to its ground vibrational state.[3]

In contrast to inelastic Raman scattering, elastic Rayleigh scattering involves a molecule emitting scattered photons with no net change in energy. Therefore the molecule returns to the same vibrational state after excitation to a virtual state, as shown in Figure 2.2.

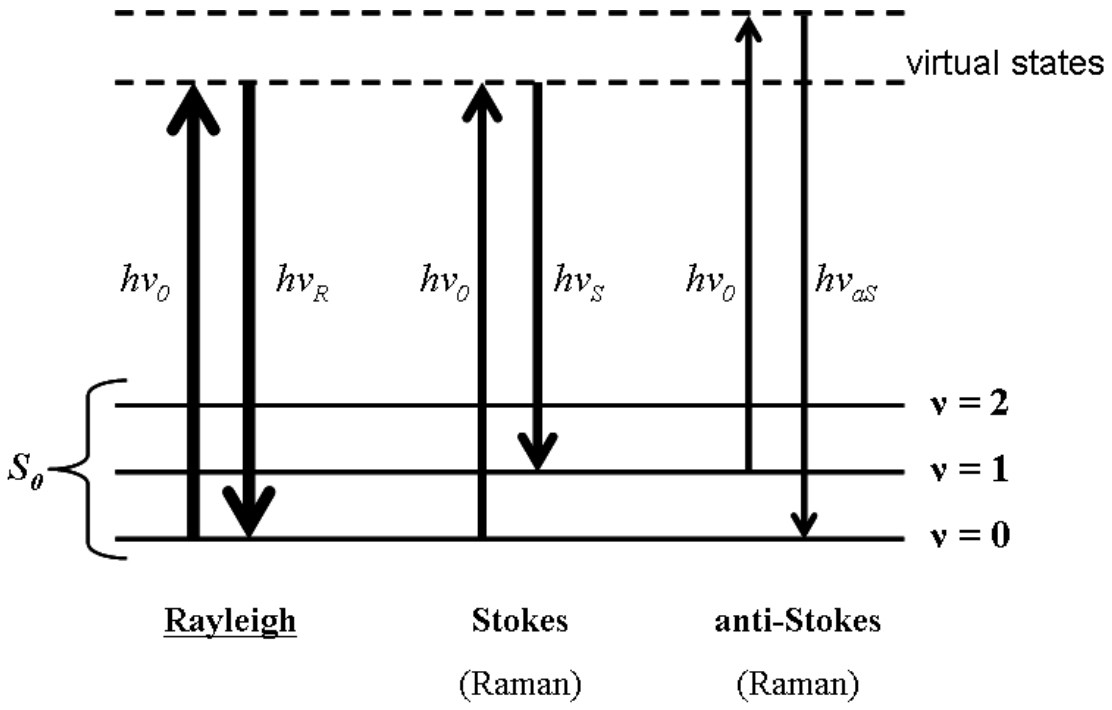

Figure 2.2: Energy schemes for Rayleigh and Raman (Stokes and anti-Stokes) scattering processes.

Raman spectroscopy measures the difference in wavelength between the incident beam and inelastically scattered radiation and the resultant spectrum has a wavenumber shift (Raman shift) axis equivalent to the mid-infrared region.[4] Figure 2.3 displays the mechanics of the Raman instrument and illustrates that the laser beam is directed through the instrument via a set of mirrors, which pass the laser beam through a condenser optic and into a beam expander, moulding the laser line into a useful laser shape and size. The laser beam then reflects off the (Edge/Notch) filter, which acts as a beam-splitter, and enters the microscope. There, it excites molecules in the sample from the electronic ground state to a virtual state. Following remission of the radiation, all Stokes, anti-Stokes and Rayleigh scattered photons travel back to the filter. The Rayleigh line is removed if the notch filter is used and the Rayleigh and anti-Stokes lines are removed if the edge filter is in place. The resulting photons are selectively reflected via the grating and are then reflected on to the Charge Coupled Device (CCD)

detector, which typically contain *ca* 2000 columns and 800 rows of pixels with an area of each pixel being *ca* 15 µm × 15 µm where they are captured.

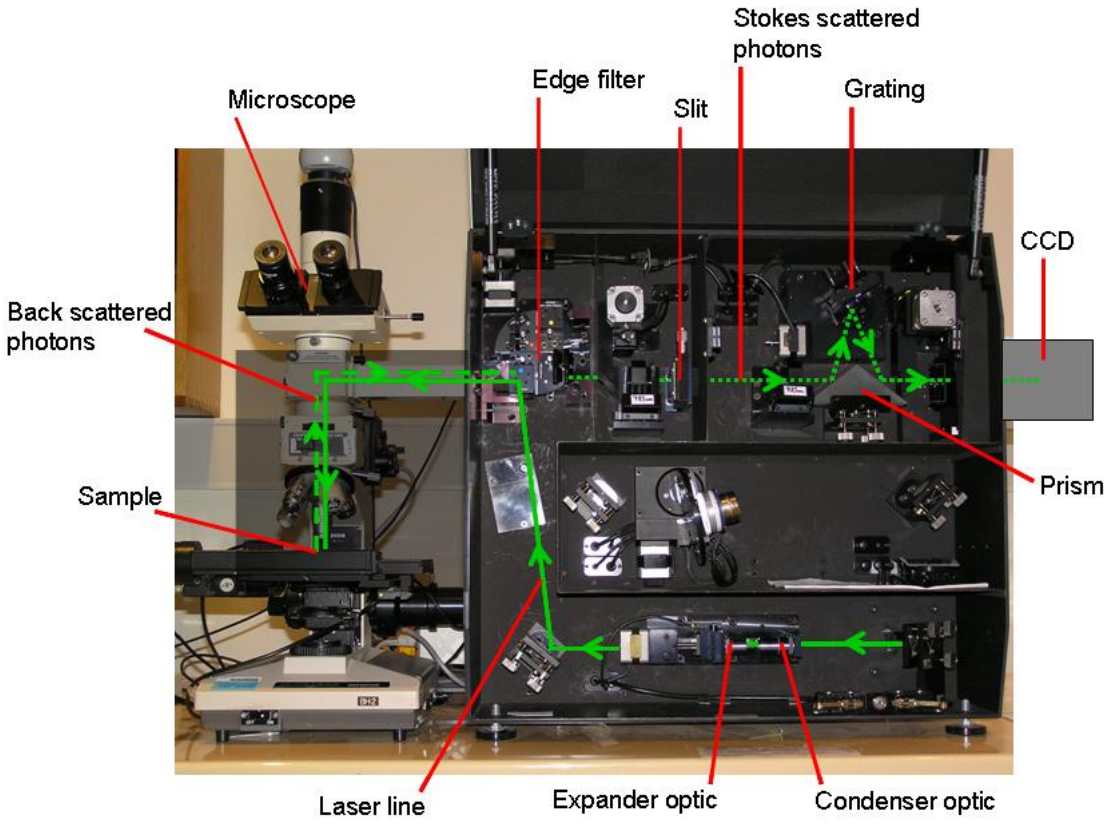

Figure 2.3: Image of the Raman instrument showing the beam-path with an edge filter in place.

There are two significant advantages to using Raman spectroscopy as a bioanalysis tool in malaria research. First, it allows analysis of aqueous solutions, as water molecules are weak Raman scatterers. Second, molecules containing haem groups tend to be strong Raman scatterers.

2.3.2 RESONANCE RAMAN SPECTROSCOPY

2.3.2.1 Scattering mechanisms

Resonance Raman refers to a phenomenon in which Raman line intensities are greatly enhanced by exciting molecules at (resonance) or close to (pre-resonance) the wavelengths at which molecules undergo electronic transitions (Figure 2.4). The enhancement of Raman peaks can be 10^2 to 10^6 orders of magnitude greater than normal Raman scattering.[3] By tuning into different electronic absorption bands, vibrational modes can be selectively enhanced. The technique was used systematically by Spiro *et al.*[5, 6] to investigate structural changes in haem proteins.

It should be noted that a significant drawback of resonance Raman spectroscopy is the potential for interference by fluorescence. Fluorescence occurs at the same time as Raman scattering and poses major problems in recording quality Raman spectra by swamping the signal of weak bands. Stokes scattering is more susceptible to interference from fluorescence than anti-Stokes. Resonance Raman scattering is more prone to problems of fluorescence due to electrons being excited into the electronic excited state as shown in Figure 2.4. However, the problem of fluorescence is minimised when analysing metallo-porphyrin molecules, such as haems, due to their large Raman cross-section giving rise to intense Raman bands and minimal intrinsic auto-fluorescence. In fact, fluorescence did not present an obstacle to obtaining Raman spectra at any stage of this project.

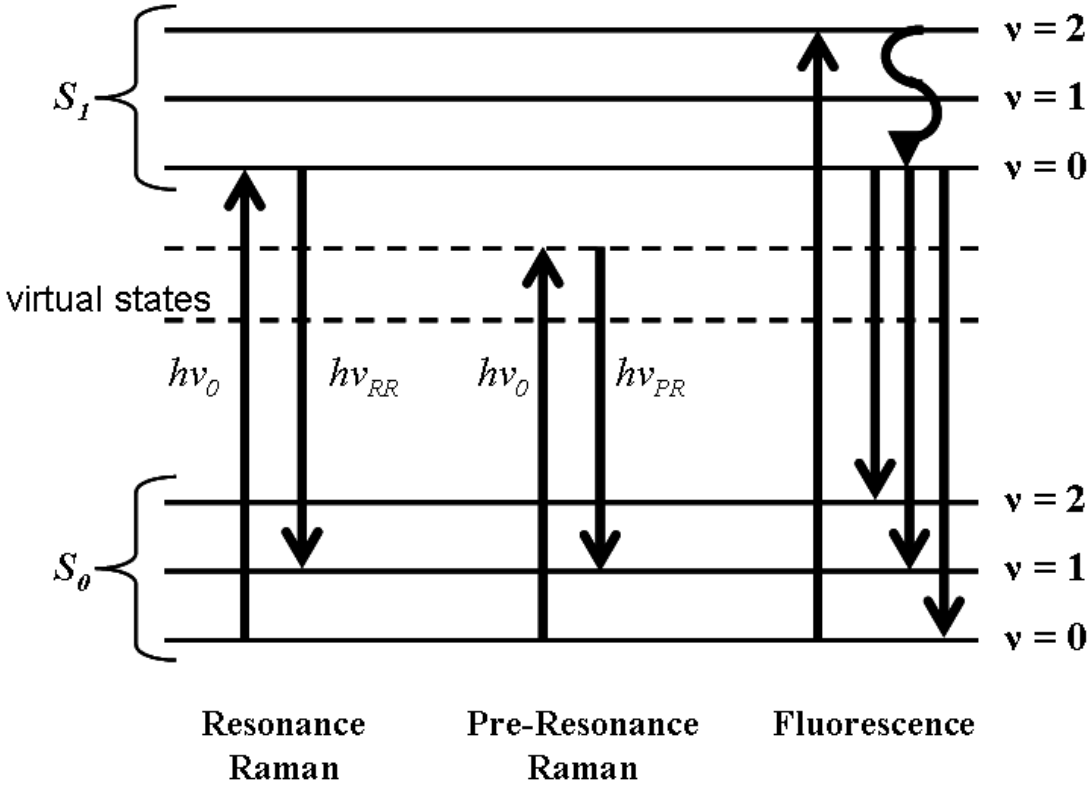

Figure 2.4: Energy schemes for resonance Raman, pre-resonance Raman and fluorescence scattering.

2.3.2.2 Theoretical perspective

The large band enhancement observed in the Raman spectra when exciting molecules in the vicinity of electronic transitions may be modeled by the Kramers-Heisenberg equation.[7-14] The Kramers-Heisenberg equation demonstrates that when the frequency of the excitation laser approaches the transition frequency of the sampled molecule, the polarizability of that molecule is large. This polarizability leads to the molecule becoming a larger Raman scatterer because the extent of electron dissociation from the nucleus is increased. The Kramers-Heisenberg equation is based on second order perturbation theory and is shown in Equation 2.7 below:

$$(\alpha_{\rho\sigma})_{gf} = \frac{1}{h}\sum_{e}\frac{\langle f|\mu_\rho|e\rangle\langle e|\mu_\sigma|g\rangle}{\nu_{eg}-\nu_0+i\Gamma_e}+\frac{\langle f|\mu_\sigma|e\rangle\langle e|\mu_\rho|g\rangle}{\nu_{ef}+\nu_0+i\Gamma_e} \quad \textbf{(2.7)}$$

where h is Planck's constant, $\boldsymbol{\mu_\rho}$ and $\boldsymbol{\mu_\sigma}$ are dipole moment operators, $|\boldsymbol{g}\rangle$ and $\langle \boldsymbol{f}|$ are the initial and final state wave functions, $|\boldsymbol{e}\rangle$ is the excited state wave function, Γ_e represents the half-width life time of the excited state, ν_{eg} and ν_{ef} are transition frequencies.

As ν_0 approaches ν_{eg}, the denominator of one of the terms in the first summation becomes very small, so that summation becomes very large. This increases the value of $(\alpha_{\rho\sigma})_{gf}$ and is therefore responsible for enhanced Raman peaks.

The Kramers-Heisenberg equation demonstrates polarizability in terms of the electronic component of a molecule's wave function. The Born-Oppenheimer approximation allows us to understand the relationship of the electronic and vibrational components of a molecule's total wave function. The approximation permits us to make the following substitution:

$$\langle \boldsymbol{f}|\boldsymbol{\mu}|\boldsymbol{e}\rangle = \langle \boldsymbol{j}|\boldsymbol{M_e}|\boldsymbol{v}\rangle \text{ and } \langle \boldsymbol{e}|\boldsymbol{\mu}|\boldsymbol{g}\rangle = \langle \boldsymbol{v}|\boldsymbol{M_e}|\boldsymbol{i}\rangle \quad \textbf{(2.8)}$$

where $|\boldsymbol{i}\rangle$ and $\langle \boldsymbol{j}|$ are the initial and final wave functions of the ground electronic state, $|\boldsymbol{v}\rangle$ is the vibrational wave function of the excited electronic state $\boldsymbol{e}$ and $\boldsymbol{M_e}$ is the transition dipole moment between $\boldsymbol{g}$ and $\boldsymbol{e}$.

This substitution makes it possible to demonstrate the polarizability of a molecule in terms of the vibrational component of its total wave function. Therefore, Raman spectra can be interpreted to give insight into the molecular signature of a given molecule based on its vibrational energy.

Furthermore, the term $\boldsymbol{M_e}$ may be expanded to give the Taylor's series:

$$\boldsymbol{M_e} = \boldsymbol{M_e^0} + \left(\frac{\partial \boldsymbol{\mu}}{\partial \boldsymbol{Q}}\right)^1 \boldsymbol{Q} + ..., \tag{2.9}$$

where $\boldsymbol{Q}$ represents the normal coordinate operator.

By elaborating on the dipole moment operator ($\boldsymbol{M_e}$), the Taylor's series is able to provide more nuanced insight into the nature of the vibrational wave function that occurs upon irradiation of a molecule. In other words, the Taylor's series allows the dipole moment to be understood in greater detail. The especial value of the first two terms in the Taylor's series, once expanded, lies in its ability to provide insight into type A and type B resonance Raman scattering, as outlined in the following section.

The theoretical perspective presented in this section demonstrates that through use of the Kramers-Heisenberg equation, the Born-Oppenheimer approximation and the expansion of the first two terms in the Taylor's series, resonance Raman spectra can be interpreted to give qualitative information about the vibrational modes of irradiated molecules.

2.3.2.3 Type A and type B scattering

There are two important types of resonance Raman scattering. These are described as type A and type B scattering. The equations which describe these types of scattering were determined by Tang and Albrecht,[15] and are named *A*-term and *B*-term respectively. These terms were expanded from part of the Taylor's series (Equation 2.9) to provide insight into the relationship between vibrational Raman intensities and excited-state structure.

In type A scattering, or Franck-Condon scattering, only totally symmetric modes are enhanced. This is achieved by using a laser excitation wavelength that displays little configuration interaction between neighbouring electronic excited states.[16] These modes are enhanced because their atomic displacements occur along molecular coordinates that vary between ground and excited states. The intense scattering is achieved by the overlap of wave functions, which involves a transition from a region of high electron density in the ground state to a region in the excited state where the wave function can contain significant electron density once populated.

In describing type A scattering, the first term in the expansion of the Taylor's series, the *A*-term, is used. The *A*-term represents the scattering amplitude, which is directly proportional to the strength of the electronic transition and inversely proportional to its bandwidth. The *A*-term depends on the square of the transition dipole moment ($\boldsymbol{M}_e$) and the sum of the Franck-Condon (FC) integral products $\langle \boldsymbol{j}|\boldsymbol{v}\rangle\langle \boldsymbol{v}|\boldsymbol{i}\rangle$ as shown in Equation 2.10.

$$A = (\boldsymbol{M}_e)^2 \frac{1}{\hbar} \sum_{v} \frac{\langle \boldsymbol{j}|\boldsymbol{v}\rangle\langle \boldsymbol{v}|\boldsymbol{i}\rangle}{\Delta\nu_v + i\Gamma_v} \qquad \textbf{(2.10)}$$

$$B = \boldsymbol{M}_e \left(\frac{\partial \boldsymbol{M}_e}{\partial \boldsymbol{Q}} \right) \frac{1}{\hbar} \sum_{v} \frac{\langle \boldsymbol{j}|\boldsymbol{Q}|\boldsymbol{v}\rangle\langle \boldsymbol{v}|\boldsymbol{i}\rangle + \langle \boldsymbol{j}|\boldsymbol{v}\rangle\langle \boldsymbol{v}|\boldsymbol{Q}|\boldsymbol{i}\rangle}{\Delta \nu_v + i\Gamma_v} \qquad \textbf{(2.11)}$$

where $|\boldsymbol{i}\rangle$ and $|\boldsymbol{j}\rangle$ are the initial and final vibrational wave functions of the ground electronic state, $\boldsymbol{Q}$ represents the normal coordinate operator, $|\boldsymbol{v}\rangle$ represents the intermediate vibrational wave function in the resonant excited state.[17] The difference between the frequency of laser excitation and frequency of the vibration in the excited state v is represented by $\Delta \nu_v$. Γ_v is the half-width of the vibrational wave function for the excited state and represents the life time of the excited state, and $\hbar$ is $h/2\pi$ (h, Plank's constant).[16]

Equation 2.10 shows that when the frequency of the laser matches the energy required to promote the molecule into the vibronic excited state, $\Delta \nu_v$ approaches zero and the denominator of the *A*-term reduces to Γ_v. Hence, during resonant conditions the *A*-term becomes large due to the denominator being very small, resulting in increased polarizability and greater Raman scattering.

In contrast, type B scattering is achieved by using laser excitation wavelengths that are in the vicinity of electronic transitions that give rise to the enhancement of non-totally symmetric modes. This is caused by the vibronic coupling of two transitions, which allows the normal coordinate operator ($\boldsymbol{Q}$) to help mix these two excited state transitions.

Type B scattering is represented by the second term in the expansion of the Taylor's series, *B*-term. The *B*-term represents the scattering amplitude and is dependent on two factors. First, the derivative of the normal coordinates ($\boldsymbol{Q}$) with respect to the

transition dipole ($\boldsymbol{M_e}$), and the extent the normal coordinate perturbs the excited state structure.[18] Second, the normal coordinate ($\boldsymbol{Q}$), usually a low frequency non-totally symmetric mode, that couples the electronic excited states, giving rise to the sum of the maximum overlap of wave function integrals between the initial, intermediate and final states over all the vibrational states (Equation 2.11).

Type B enhancement is only strong from the zero to first vibronic states of the excited electronic state. In contrast, there is no limit to the excited vibronic states that may occur during type A enhancement. This means that overtones are allowed by the *A*-term mechanism.[19]

2.3.2.4 Adiabatic and nonadiabatic effects

Type A and Type B scattering is modeled by expanding the first two terms of the Taylor's series. As demonstrated in preceding sections, the applicability of the Taylor's series to interpreting Raman spectra is dependant on the Born-Oppenheimer approximation being true. In quantum mechanics, molecular states for which the Born-Oppenheimer approximation holds true are referred to as adiabatic states and are understood as stable states.[20] Nonadiabatic transitions, in which a molecule passes through a state in which the Born-Oppenheimer approximation does not hold true, were assumed in the past to be relatively rare.[20] Today it is known that nonadiabatic transitions are a common feature of molecular systems.[20] Given the ubiquity of nonadiabatic transitions, it can be assumed that in any given system, a certain percentage of the molecules will be in a nonadiabatic state at any one time.[20]

This assumption implies that any irradiated sample will contain molecules that are in a nonadiabaic state. As the Born-Oppenheimer approximation does not hold true

for these states, these molecules will create scattering effects that are not in accordance with the results predicted by the expansion of the Taylor's series.[20] This is because the Taylor's series assumes the Born-Oppenheimer approximation is true. The resonance Raman spectra are created by the polarizability of molecules in a sample. This means a Raman spectrum directly reflects the electronic wave function of the sampled molecule. The Born-Oppenheimer approximation permits deductions about the molecule's vibronic activity to be made from this information. If the Born-Oppenheimer approximation does not hold true for a particular molecule, then it is not possible to make deductions about its vibronic activity from the evidence of its polarizability.

Conversely, it follows that the use of resonance Raman techniques to selectively enhance vibrational modes will lead to molecules in nonadiabatic states undergoing enhanced polarizability of a different nature than that undergone by molecules in an adiabatic state.[6] Hence, scattering from these molecules may seem to present in the Raman spectra as enhancement of vibrational modes other than those predicted by the expansion of the Taylor's series.[20] Not all nonadiabatic transitions present in Raman spectra. However, one particular type of nonadiabatic transition does present and hence will be considered in more detail below.

2.3.2.5 Jahn-Teller distortion

One nonadiabatic transition which can have an observable effect on the spectra obtained from resonance Raman scattering is the Jahn-Teller distortion. The Jahn-Teller distortion occurs when a nonlinear molecule enters an electronically degenerate state. This state is an example of a nonadiabatic state in which the Born-Oppenheimer equation is not true. This electronically degenerate state is unstable and hence the

molecule undergoes a geometrical distortion to remove the degeneracy.[21] The geometry of the molecule changes into a new equilibrium position of lower symmetry, and therefore lower nuclear energy. Hence, it may be demonstrated that the Jahn-Teller distortion is an example of a nonadiabatic transition.[22]

Jahn-Teller distortion may present in resonance Raman spectra as polarizability that is not predicted by the expansion of the Taylor's series. This is because the excitation laser can cause molecules in an electronically degenerate ground state to be promoted to an electronically degenerate excited state. This leads to the molecule producing a strong Raman scatter. However, because the excited state is electronically degenerate, the polarizability of the molecule is of a different nature to the polarizability of a molecule in an adiabatic excited state. Hence, molecules undergoing a Jahn-Teller distortion at the time of irradiation may present in the spectra as enhanced Raman bands that are not predicted by the expansion of the Taylor's series. Under other conditions the presence of the Jahn-Teller distortion can result in rotated or inverse polarization in a Raman scatter.[16] As the percentage of molecules undergoing a Jahn-Teller distortion at any one time is very small, the impact on the spectra is minimal. The distortion did not obscure the Raman bands in the spectra that were of relevance to this project, as will be discussed in the following section.

2.3.3 RESONANCE RAMAN SPECTROSCOPY OF HAEM DERIVATIVES

This section examines the type A and type B scattering and the Jahn-Teller distortion that is evident in resonance Raman spectra of haem derivatives. Type A scattering is evident for haem derivatives when they are irradiated with an excitation

laser that has a wavelength of *ca* 400 nm. The UV-Visible spectral profile displays an intense band known as the B band or Soret band in the vicinity of this wavelength. Type B scattering is evident for haem derivatives in two weaker bands called Q_0 and Q_v. The excitation laser that produces these bands has a wavelength that lies between 500 nm and 600 nm.[23]

The intensity of the absorbance bands can be explained by Gouterman's four orbital model as depicted in Figure 2.5.[23] This model was developed to describe the UV-Visible spectral profile of nickel(II)-octaethylporphyrin (Ni(II)OEP). It is generally accepted that this model, allowing for some differences in band shape, can account for the spectral profile of other metallo-porphyrins. In Gouterman's model, the highest occupied molecular orbitals (HOMO) have nearly the same energy allowing the two π-π orbital excitations 1 and 2 to interact. The transition dipoles (TD) add up to give the intense Soret band and nearly cancel for the weaker Q_0 band. Approximately 10% intensity is regained for the Q band transition via vibronic mixing with the Soret band leading to the Q_v side band.

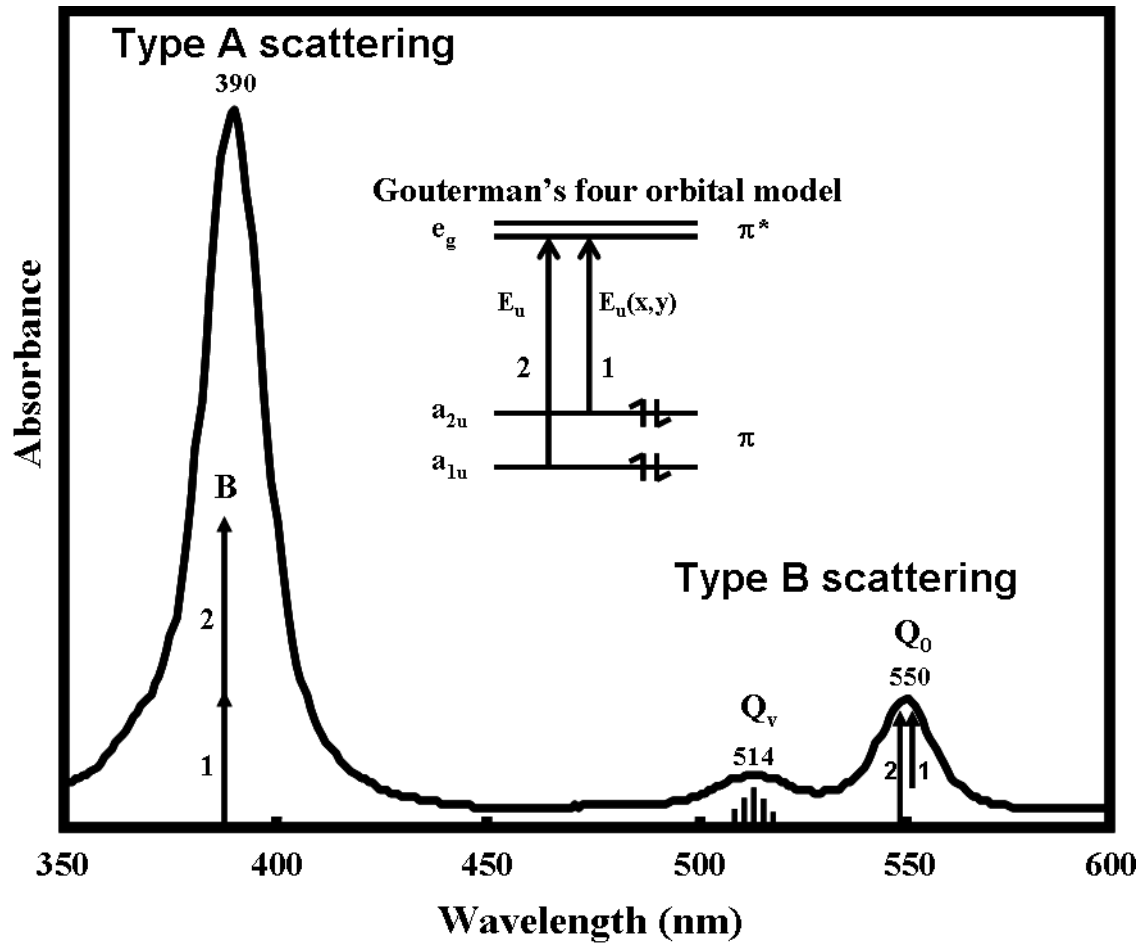

Figure 2.5: Resonance enhancement of the metallo-porphyrin (Ni(II)OEP). (Modified from reference)[16]

Since the excited states generated by the absorption in the Soret and Q bands are of E_u symmetry, the allowed symmetries of the mixing vibrations are:

$$E_u \times E_u = A_{1g} + A_{2g} + B_{1g} + B_{2g}$$

The vibrational symmetries result in depolarization ratios (ρ) of less than 0.75 for totally symmetric (A_{1g}) modes of the porphyrin ring in Fe(III)PPIX molecules.

The depolarization ratio is dependent upon the symmetry of the vibrations responsible for scattering and provides information about the structure of molecules.[3] It can be obtained experimentally by inserting a polarizer between the sample and the monochromator. Perpendicular polarized light ($I_\perp$) and parallel polarized light ($I_\parallel$) can

be separated from each other depending on the type of polarizer (parallel or perpendicular) in place. The depolarization ratio is defined as $\rho = I_{\perp} / I_{\parallel}$.[3]

2.3.3.1 Helping mode behaviour

Shelnutt *et al.*[24] describe another phenomenon known as "helping mode behavior" which can also explain the intensity of vibrational modes when irradiating metallo-porphyrin molecules with laser excitation wavelengths in the vicinity of the Q bands. Previous studies show that a high frequency A_{1g} vibrational mode can strongly "help" a low frequency vibrational mode, usually an axial ligand mode. Burke *et al.*[25] observed this phenomenon in iron-tetraphenylporphyrin μ-oxo dimers $(Fe(TPP)]_2O$), where this "helping mode behavior" occurs due to the motion of the nitrogen and iron atoms. In $(Fe(TPP)]_2O$) the high spin Fe(III) atom is *ca* 0.08 Å longer than the unconstrained radius of the circle of pyrrole nitrogen atoms.[26] Motion of the iron atom into the circle is made easier if the nitrogen atoms simultaneously move outward. This therefore provides a mechanism of coupling the low frequency (Fe-N) mode to the high frequency (pyrrole ring breathing) mode to produce Raman band enhancement in the vicinity of the Q bands.

2.3.3.2 Jahn-Teller distortion in haem derivatives

The presence of evidence for the Jahn-Teller distortion in Raman spectra of haem derivatives is dependent upon the configuration interaction between the $a_{1u} \rightarrow e_g$ and $a_{2u} \rightarrow e_g$ orbital excitations.[16] In molecules in which the a_{1u} and a_{2u} orbitals are degenerate, the Jahn-Teller distortion is not visible in the Raman spectra. This is because upon excitation with a laser that has a wavelength that lies within either the B

band or the Q band, the molecule creates a Raman scatter that is indistinguishable from that created by a molecule in an adiabatic state.[16] However, if the two orbitals have different energies then evidence of Jahn-Teller distortion is evident in Raman spectra.

In haem derivatives, the presence of Jahn-Teller distortion in a sample irradiated to produce A_{2g} modes can rotate the polarization plane of scattered light by 90°. This is caused by the coupling of the *x* and *y* components of the B transition to the *y* and *x* components of the Q transition respectively. This produces anomalous polarization.[22] The depolarization ratios ($\rho > 0.75$) from bands attributed to A_{2g} vibrations are created by the inverse polarization of Raman scattering, first demonstrated experimentally by Spiro and Strekas.[22] It is possible to observe Jahn-Teller distortion in a sample irradiated to produce B_{1g} and B_{2g} symmetry modes. The depolarization ratio of $\rho = 0.75$ from bands attributed to B_{1g} and B_{2g} vibrations is created because the excited state of the irradiated molecule is electronically degenerate (E_u).[22] The impact of Jahn-Teller distortions on Raman spectra obtained from haem derivatives is so slight that it did not need to be considered in the interpretation of the Raman spectra obtained throughout this project.

2.3.4 GROUP THEORY FOR HAEMS

Knowledge of the symmetry of haems allows for a more discerning exploitation of resonance Raman techniques. This is because knowledge of the symmetry of haems, in combination with knowledge of its UV-Visible spectral profile, allows the researcher to target particular electronic transition states for excitation which in turn enables greater understanding of the supramolecular forces that are present in the sample.

The treatment of symmetry in molecules has been adapted from mathematical group theory. The molecular symmetry of molecules allows for their classification and can be used to predict a molecule's chemical properties, such as the presence or absence of a dipole moment or allowed spectroscopic transitions. Strictly considered, ferric high spin haems such as Fe(III)PPIX monomers, Fe(III)PPIX μ-oxo dimers, β-haematin and haemozoin have C_{4v} point group symmetry because the Fe atom is translocated *ca* 0.5 Å out of the porphyrin plane as shown in Figure 2.6.[27] However, these molecules by convention have been treated as having D_{4h} symmetry. This project follows this convention; however as the D_{4h} symmetry is an idealised model there will be vibrational modes that are observed in the actual Raman spectra which are not present in the spectra of molecules with D_{4h} symmetry and therefore must be attributed to the molecule's actual C_{4v} symmetry.

The main differences observed between C_{4v} symmetry shown in Figure 2.6 and D_{4h} symmetry shown in Figure 2.7 of these haem molecules is the presence of a σ_h mirror plane in the D_{4h} model that is perpendicular to the C_4 principal axis of rotation. This plane is not present in the C_{4v} model. In addition, there is no C_2 axis of rotation perpendicular to the principal C_4 axis in the C_{4v} model.

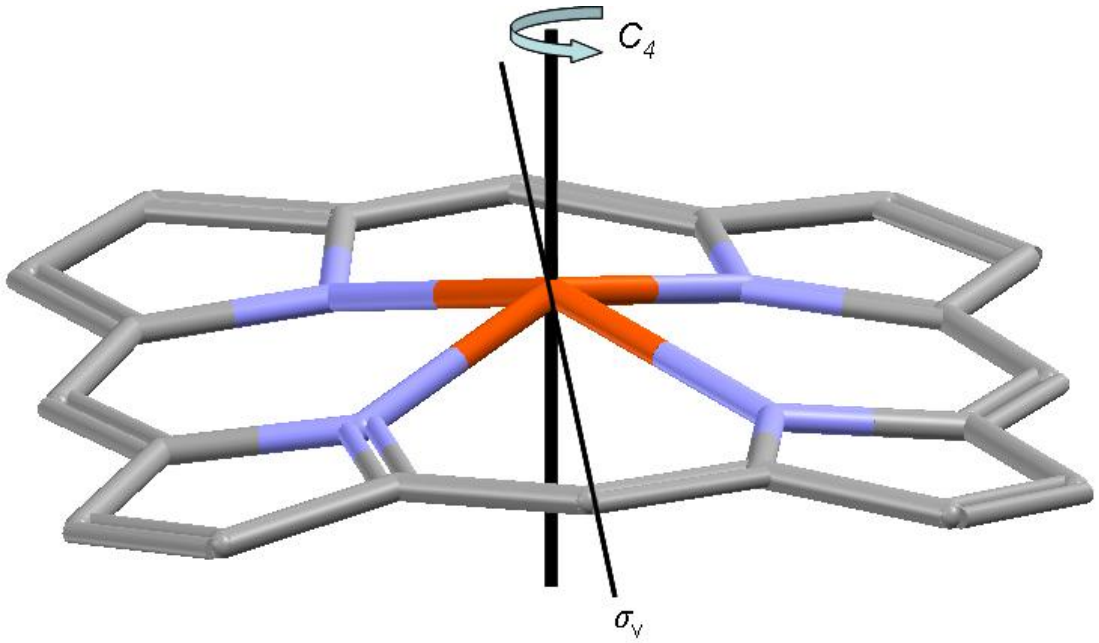

Figure 2.6: The defining axes of Fe(PPIX) C_{4v} point group showing the C_4 principal axis of rotation and a σ_v mirror plane.

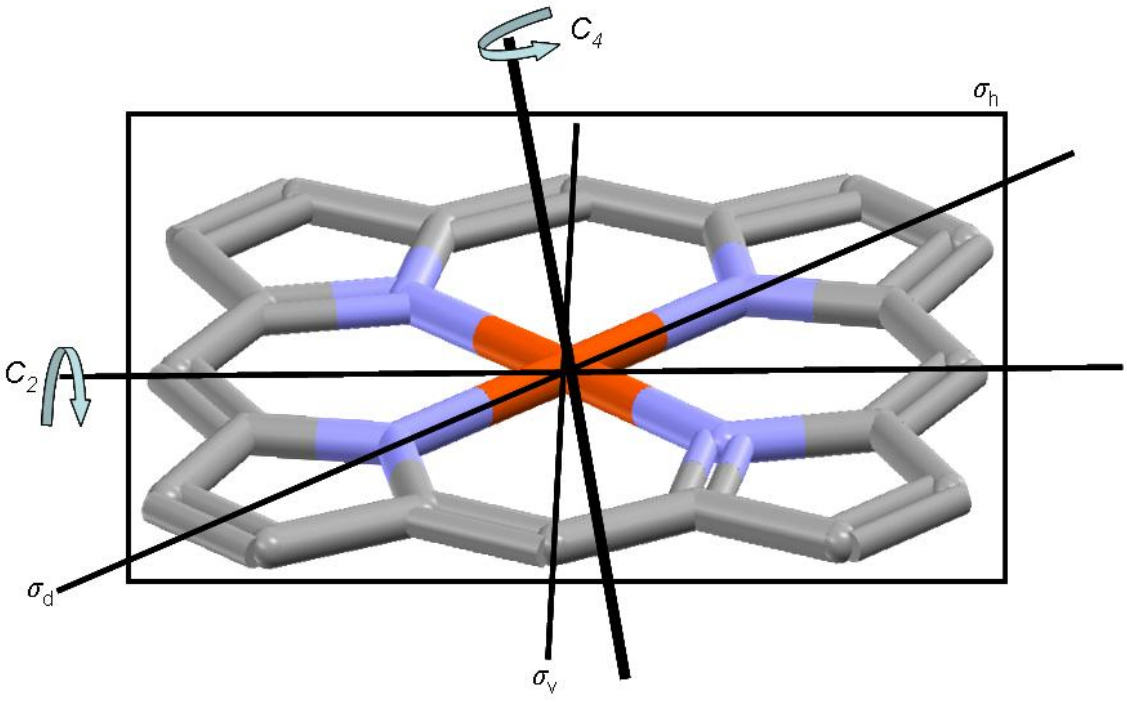

Figure 2.7: The defining axes of Fe(PPIX) D_{4h} point group showing the C_2 axis of rotation that is perpendicular to the C_n (C_4) Principal axis and a σ_d, σ_v and σ_h mirror plane.

The following tables compare the Raman active modes and IR active modes observed in the spectra for molecules with C_{4v} and D_{4h} symmetry.

Table 2.1: D_{4h} point group character table

Point group — Symmetry operations

D_{4h}	I	$2C_4$	C_2	$2C'_2$	$2C''_2$	i	$2S_4$	σ_h	$2\sigma_v$	$2\sigma_d$		
A_{1g}	1	1	1	1	1	1	1	1	1	1		$\alpha_{xx} + \alpha_{yy}$, α_{zz}
A_{2g}	1	1	1	-1	-1	1	1	1	-1	-1	R_z	
B_{1g}	1	-1	1	1	-1	1	-1	1	1	-1		$\alpha_{xx} - \alpha_{yy}$
B_{2g}	1	-1	1	-1	1	1	-1	1	-1	1		α_{xy}
E_g	2	0	-2	0	0	2	0	-2	0	0	(R_x, R_y)	$(\alpha_{xz}, \alpha_{yz})$
A_{1u}	1	1	1	1	1	-1	-1	-1	-1	-1		
A_{2u}	1	1	1	-1	-1	-1	-1	-1	1	1	T_z	
B_{1u}	1	-1	1	1	-1	-1	1	-1	-1	1		
B_{2u}	1	-1	1	-1	1	-1	1	-1	1	-1		
E_u	2	0	-2	0	0	-2	0	2	0	0	(T_x, T_y)	

Γ

NOTE: ***R*** = rotational tensor, ***T*** = translational tensor, Γ = irreducible representation

The following modes are calculated for the D_{4h} molecule observed in Figure 2.7. It is assumed that the molecule has 25 atoms with no side chains or hydrogens attached.

$$\text{Raman active modes} = 6A_{1g} + 6B_{1g} + 6B_{2g} + 5E_g$$

Although there are 28 total vibrations that are Raman active, only 23 Raman bands are observed due to the overlapping of bands from E_g modes.

$$\text{IR active modes} = 6A_{2u} + 12E_u$$

Although there are 28 total vibrations that are IR active, only 12 IR bands are observed due to the overlapping of bands from E_u modes.

Table 2.2: C_{4v} point group character table

Point group	Symmetry operations						
	C_{4v}	I	$2C_4$	C_2	$2\sigma_v$	$2\sigma_d$	
Γ	A_1	1	1	1	1	1	T_z $\alpha_{xx} + \alpha_{yy}$, α_{zz}
	A_2	1	1	1	-1	-1	R_z
	B_1	1	-1	1	1	-1	$\alpha_{xx} - \alpha_{yy}$
	B_2	1	-1	1	-1	1	α_{xy}
	E	2	0	-2	0	0	(T_x,T_y), (R_x,R_y) $(\alpha_{xz}, \alpha_{yz})$

NOTE: ***R*** = rotational tensor, ***T*** = translational tensor, Γ = irreducible representation

The following modes are calculated for the C_{4v} molecule observed in Figure 2.6. It is assumed that the molecule has 25 atoms with no side chains, hydrogens or axial ligand attached.

$$\text{Raman active modes} = 10A_1 + 9B_1 + 9B_2 + 17E$$

Although there are 62 total vibrations that are Raman active, only 45 Raman bands are observed due to the overlapping of bands from E_g modes.

$$\text{IR active modes} = 10A_1 + 17E$$

Although there are 44 total vibrations that are IR active, only 27 IR bands are observed due to the overlapping of bands from E_u modes.

There is a significant difference in the number of Raman active and IR active modes when C_{4v} and D_{4h} molecules are compared if both molecules are assumed to have the same number of atoms. In particular, due to the actual C_{4v} symmetry of the haem molecules analysed in this project, there are no A_{2u} IR modes present in the spectra even

though they are assigned for the D_{4h} idealised molecule. In contrast, haem molecules with C_{4v} symmetry display E_u active modes which are not present in molecules with D_{4h} symmetry.

In addition, because the calculation of Raman and IR active modes assumed a molecule with no side chain, hydrogen or axial ligand attachments, the actual IR spectra will display IR active modes that are not predicted by the preceding calculations. This is because these attachments themselves undergo net changes in their dipole moment, which are then evident in the IR spectra. However, the bands produced by these attachments are weak in the Raman spectra.

Table 2.3 show Raman band assignments for Fe(III)PPIX based on β-haematin (synthetic haemozoin) studies using 782 nm laser excitation. The Abe *et al.*[28] notation scheme was adopted to assign the normal modes based on the idealised D_{4h} symmetry of the porphyrin skeleton from Ni(II)OEP. However, due to the Fe atom being translocated *ca* 0.5 Å out of the porphyrin plane[27] for Fe(III)PPIX molecules, as previously mentioned, the effective symmetry is in fact C_{4v}.

The D_{4h} point group table displays that E_u symmetry modes are Raman inactive. However, this mode is observed in Table 2.3 because the actual C_{4v} symmetry of Fe(III)PPIX molecules allows these modes to be Raman active. The γ symbol is used to designate out-of-plane modes of which there are a number of categories, including (1) out-of-plane wagging modes, (2) tilting, and (3) internal folding of the pyrrole rings.

Table 2.3: Raman band assignments, local coordinates and symmetry terms for β-haematin using 782 nm excitation. (Modified from reference)[29]

Raman shift (cm^{-1})	Assignment	Symmetry term	Local Coordinate
1623	ν_{10}	B_{1g}	$\nu(C_\alpha C_m)_{asym}$
1589	ν_{37}	E_u	$\nu(C_\alpha C_m)_{asym}$
1572	ν_2	A_{1g}	$\nu(C_\beta C_\beta)$
1552	ν_{11}	B_{1g}	$\nu(C_\beta C_\beta)$
1530	ν_{38}	E_u	$\nu(C_\beta C_\beta)$
1497	ν_3	A_{1g}	$\nu(C_\alpha C_m)_{sym}$
1430	ν_{40}	E_u	$\nu(C_\alpha C_m)_{sym}$
1398	ν_{29}	B_{2g}	ν(pyrrole quarter-ring)
1377	ν_4	A_{1g}	ν(pyrrole half-ring)$_{sym}$
1338	ν_{41}	E_u	ν(pyrrole half-ring)$_{sym}$
1308	ν_{21}	A_{2g}	$\delta(C_mH)$
1241	ν_{42}	E_u	$\delta(C_mH)$
1219	ν_{13}	B_{1g}	$\delta(C_mH)$
1215	$\nu_5 + \nu_{18}$	-	$\delta(C_mH)$
1171	ν_{30}	B_{2g}	ν(pyrrole half-ring)$_{asym}$
1145	ν_{14}	B_{1g}	$\nu(C_\beta C_1)_{sym}$
1121	ν_{22}	A_{2g}	$\nu(C_\alpha N)$
1090	-	-	$\gamma(=C_\beta H_2)_{sym}$
1002	ν_{45}	E_u	$\nu(C_\beta$-methyl stretch)
975	ν_{46}	E_u	δ(pyrrole deform)$_{asym}$
940	ν_{32}	B_{2g}	$\gamma(C_aH=)$
821	γ_{10}	B_{1u}	$\gamma(C_mH)$
796	ν_6	A_{1g}	ν(pyrrole breathing)
753	ν_{15}	B_{1g}	ν(pyrrole breathing)
725	γ_5	A_{2u}	pyrrole fold$_{sym}$
710	γ_{15}	B_{2u}	pyrrole fold$_{asym}$
678	ν_7	A_{1g}	δ(pyrrole deform)$_{sym}$
406	-	-	$\delta(C_\alpha C_\beta C_m)$
365	γ_6	A_{2u}	pyrrole tilt
345	ν_8	A_{1g}	ν(Fe-N)
321	ν_{51}	E_u	$\delta(C_\beta$-$C_1)$

NOTE: ν = in-plane stretch, δ = deformation, γ = out-of-plane stretch.

2.3.5 EXCITONIC INTERACTIONS

Both type A and type B Raman scattering mechanisms act as excellent models to explain the resonance Raman spectra in the case of dilute solutions. However, the above model does not hold for aggregated solids. In aggregated systems, atypical enhancement of totally symmetric vibrational modes in molecules can be observed in resonance Raman spectra when using a laser that is in resonance with particular electronic transitions. This atypical enhancement can be explained by excitonic interactions.

The exciton theory was developed in the 1930s by Frenkel and Wannier.[30-32] The exciton model was originally based on the quantum mechanical precept that electronic energy is distributed throughout the aggregate by π-π interactions between induced transition dipole moments.[33] Today, the electronic energy is thought to be distributed throughout the aggregate via supramolecular interactions.

According to the Frenkel and Wannier models, each excited electronic state is "in resonance" with excited states localised at other points in the lattice.[34] Frenkel modeled these running states of excitation using the concept of "excitons", which represent delocalised units of excitation.[34] Electronic states in this case are linear combinations of localised excitations each belonging to a wave vector $\boldsymbol{K}$ in the reciprocal lattice.[34] The Wannier model of excitons posits them as a conduction-band electron and a valence-band hole, which travels through the crystal lattice in a state of total wave vector $\boldsymbol{K}$.[34]

Studies by Kasha[35] define a molecular exciton as a resonance interaction between the excited states of loosely bound molecular aggregates. The relevant aggregates include molecular crystals, non-conjugated polymers and molecular dimers and trimers. He described the excitation of molecular aggregates either in terms of

locally excited states producing a collective excitation, or as a superposition of these collective excited states which allows description of the excitation in terms of a traveling-wave packet of excitation energy known as the exciton.[35] This exciton is the result of the superposition of traveling waves of different wavelengths and amplitudes that reinforce each other at a given position as depicted in Figure 2.8.

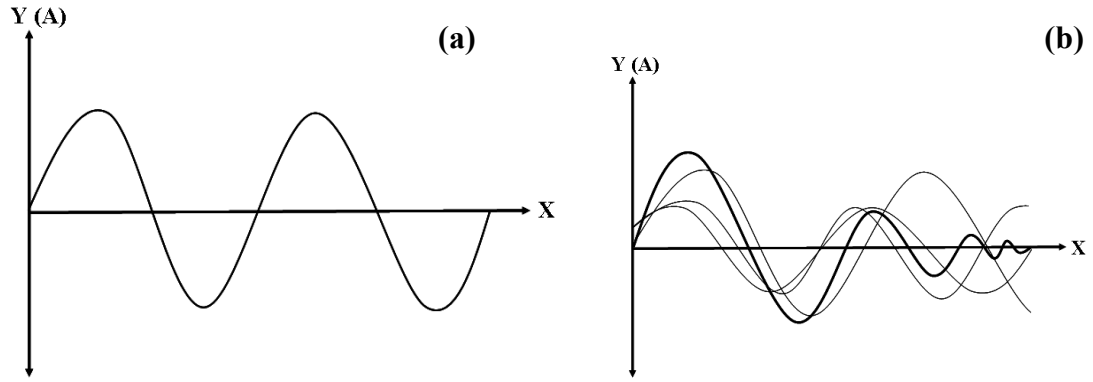

Figure 2.8: (a) An electron wave traveling with specific velocity in the x direction. **(b)** Superposition of waves of different wavelengths reinforcing each other near x = 0. (Modified from reference)[36]

2.3.6 AGGREGATED ENHANCED RAMAN SCATTERING

The existence of supramolecular excitonic interactions means that characterisation of vibrational modes based on amplitudes of individual atomic displacements in a single crystal is inaccurate.[34] As resonance Raman spectra are measurements of the polarizability of sampled molecules, electronic interactions that occur in molecular aggregates are observable in Raman spectra.

The interpretation of Raman spectra as evidence of vibrational motion is based on the Born-Oppenheimer approximation of the relationship between electronic and vibrational wave functions. This approximation describes the total wave function of a single molecule, not molecular aggregates. Hence, the presence of excitonic interactions must be considered when analysing spectra obtained from molecular aggregates.

In these cases, the possibility must be contemplated that not all evidence of electronic excitation can be read as evidence of vibrational motion. Instead, through excitonic coupling, the electronic states of a molecular aggregate are split into a broad band of states with different geometries, energies, and oscillator strengths. The extent of this coupling affects the intensity of the Raman signal for particular wavelengths.[29]

Enhancement of Raman bands in spectra of aggregated systems that is not consistent with type A and type B scattering is referred to as Aggregated Enhanced Raman Scattering (AERS). AERS results from an increased size effect, whereby the Raman signal is enhanced by the greater number of molecular interactions occurring in the system,[13] and from the impact of excitonic coupling.

Evidence of AERS was first observed by Akins,[37] who detected unusual scattering in the form of enhancement of certain vibrational modes in small aggregates of covalently linked porphyrin arrays and cyanine dyes absorbed onto surfaces. He observed simultaneous type A and type B scattering in these aggregates. He developed the concept of AERS to explain his findings. He argued that the enhancement he detected was due to both an increased size effect and to excitonic interactions.

The unusual polarizability observed by Akins can be modeled by the following equation (Equation 2.12).

$$\alpha = A + B \qquad \textbf{(2.12)}$$

AERS has relevance to the study of haem molecules. Previous studies[38] have shown that electrons move throughout an array of porphyrins via supramolecular interactions, which enables a superposition of states that results in what is essentially an

electronic band of states. Wood *et al.*[39] demonstrated enhancement occurring in β-haematin and haemozoin at near IR excitation wavelengths. They were able to utilise this enhancement to generate Raman images of haemozoin within the food vacuole of a living parasite.

In this work, the AERS model is used to present evidence of aggregation in Fe(III)PPIX solutions based on an intensity increase observed for totally symmetric (A_{1g}) modes as a function of concentration. It is demonstrated that this phenomenon is excitation wavelength dependent. This dissertation describes the excitonic coupling mechanism as being the primary mechanism that accounts for atypical enhancement of A_{1g} vibrational modes in haemozoin and its pre-cursor molecules when using an excitation laser that is off resonance with the Soret band.

Strong enhancement of totally symmetric vibrational modes in haemozoin and its pre-cursors and other Fe(III)PPIX molecules, in particular the ν_4 vibrational mode (electron density marker band), is observed when irradiating the sample molecule at near-IR wavelengths and at wavelengths in the vicinity of the Q bands. Previous studies[29] have shown this atypical enhancement occurs when using an 830 nm excitation wavelength laser. This enhancement is odd because one would expect to observe these vibrational modes being enhanced when using a laser that is in resonance with the Soret band (413 nm), as predicted by type A scattering.

However, the atypical enhancement can be explained by excitonic coupling, which splits the electronic states into a broad band of states. Previous studies[40-42] show covalently *meso-meso*-linked Cu(II)[40,41] and Zn(II)[42] porphyrin arrays display strong excitonic interactions and distinct splitting of the Soret band, which results in atypical Raman scattering patterns. These act as good metallo-porphyrin models for understanding excitonic interactions that can occur in the haem systems, such as

haemozoin and its pre-cursor molecules, which are studied in this dissertation. It is argued that owing to the C_{4v} effective symmetry of ferric high spin systems, most of the totally symmetric vibrational modes along the z-axis of the porphyrin involve z-polarized electronic transitions (Figure 2.9), which create the atypical Raman enhancement profiles observed in the spectra.

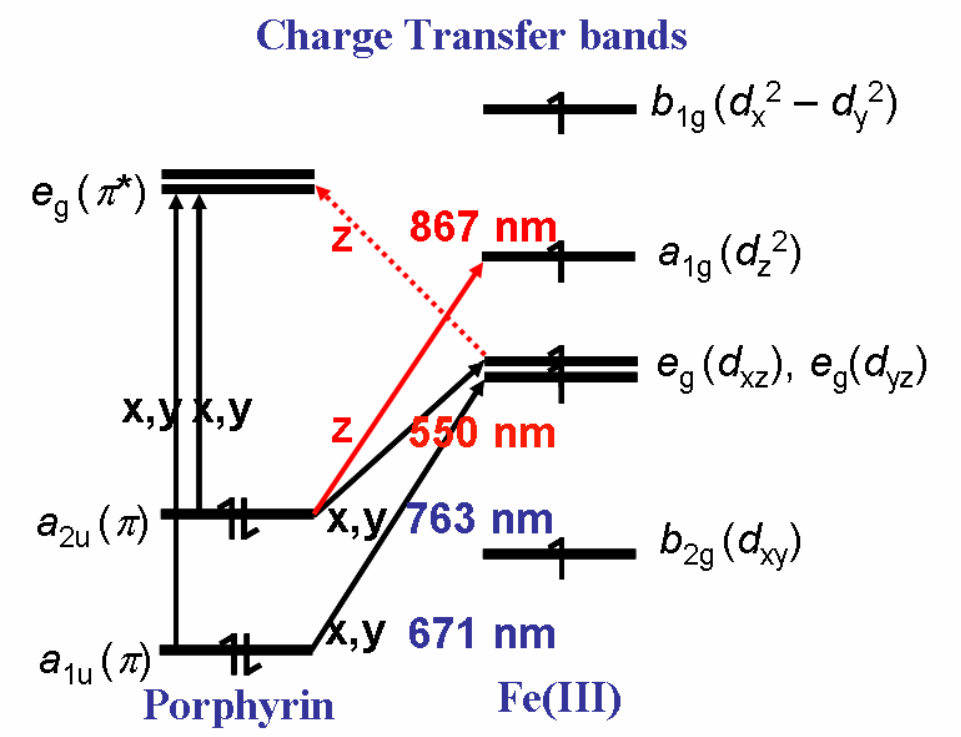

Figure 2.9: A molecular orbital diagram for the allowed transitions involving Fe(III) and porphyrin orbitals for Fe(PPIX) based on calculations by Zerner *et al.*[43] (Modified from reference)[29]

2.4 INFRARED SPECTROSCOPY

Infrared (IR) spectroscopy can be used in conjunction with Raman spectroscopy to identify particular functional groups and compare their structure. They are in fact complementary techniques, as Raman is a scattering technique and IR is an absorption technique. Infrared absorption occurs when a vibrational mode of a molecule has a net change in its dipole moment, in which radiation of the same frequency as a vibrational

mode of the molecule interacts with it, causing a net transfer of energy to take place and promoting it to an excited vibrational state as shown in Figure 2.10.[3] The magnitude of the dipole moment is determined by the charge differential and the distance between two charged centres. This dissertation focuses on the molecular vibrations that are detectable within the mid-IR region (4000-200 cm^{-1}) of the electromagnetic spectrum.

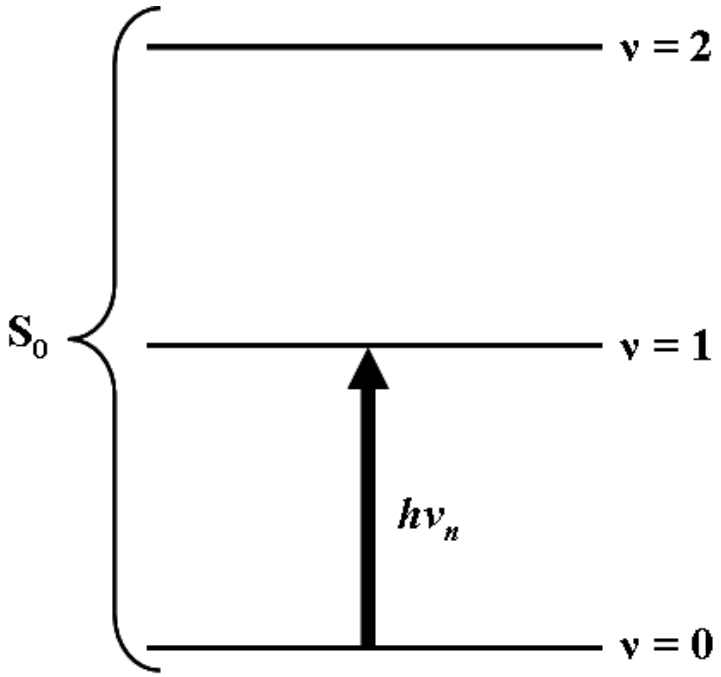

Figure 2.10: Energy scheme for IR absorption.

2.4.1 FTIR SPECTROMETER

One instrument used to analyse the absorption of IR light by molecules in a sample is the Fourier Transform Infrared (FTIR) spectrometer. The heart of the FTIR spectrometer is the Michelson interferometer, which consists of the following components: a globar light source, collimating mirrors, a beam-splitter, a fixed mirror, a moving mirror, sample holder and a detector in the form shown in Figure 2.11.

The functioning of a conventional FTIR spectrometer involves the emission of IR radiation from a globar light source, which travels to a collimating mirror. The

collimating mirror converts the expanding beam to a parallel beam. The radiation then passes through a beam-splitter, following which *ca* 50% of the IR radiation is transmitted to a fixed mirror and *ca* 50% is reflected to a movable mirror. When the radiation is reflected by the two mirrors, both wave-trains recombine at the beam-splitter. The resulting wave-train is then directed through the sample and onto a refocusing mirror, from which the focused radiation travels to a detector, such as a mercury cadmium telluride (MCT) detector. The recombination of the wave-trains causes constructive and destructive interference producing an interferogram (I vs. OPD), where I is the intensity of the combined IR beams and OPD is the optical path difference.[36] The interferogram is then converted by Fourier transformation from a time domain (interferogram (I vs. OPD)) to a frequency or wavenumber domain (IR spectrum (I vs. wavenumber, [cm^{-1}])).

There are three main advantages of FTIR over dispersive IR spectrometers. First, the multiplex advantage arises from the ability of the detector to simultaneously access all frequencies generated by the radiation source. In contrast, a dispersive IR spectrometer can only access a small portion of the spectral region at any given time. Second, the Jaquinot advantage arises because FTIR spectrometers have a larger circular aperture with fewer optical elements and no slits to attenuate the radiation. Consequently, the amount of monochromatic light passing through an FTIR spectrometer is much greater than that in dispersive instruments. Third, the Connes advantage refers to the potential for using FTIR to obtain spectra with greater wavenumber (cm^{-1}) stability compared to that obtained from dispersive instruments. This is achieved by using a Helium-Neon (HeNe) laser to act as an internal reference for each interferogram.[44]

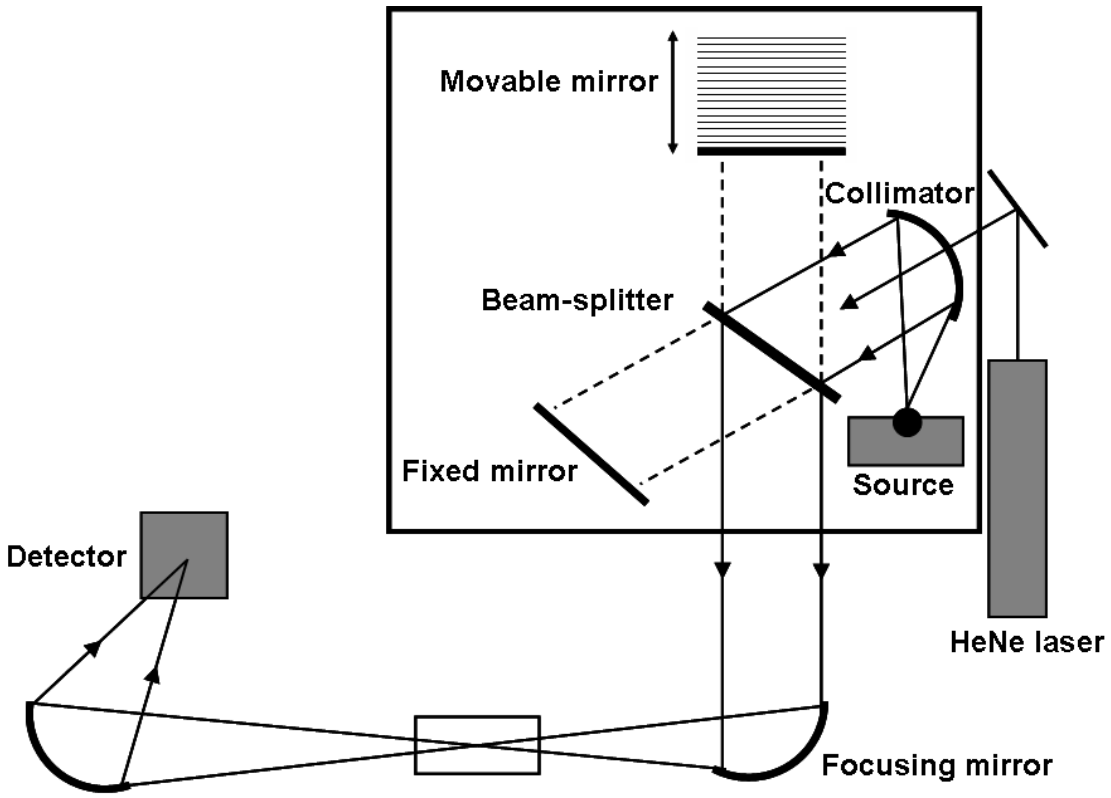

Figure 2.11: Schematic diagram of the Michelson interferometer

2.4.2 THE FTIR MICROSCOPE

The FTIR spectrometer is coupled to an FTIR microscope which enables the IR radiation to focus at the sample. The Varian Stingray FTIR microscope system (600 UMA) combines two optical systems: the FTIR spectrometer and a stereo optical microscope. The optical microscope magnifies a visible light image of the sample by 150× and utilises a knife-edge aperture enabling the researcher to target particular regions of interest in the sample for IR analysis. When a sample is in focus on the stage, its image in visible light can be observed through the optical microscope. The IR light path focuses the image onto the detector.

The microscope employs a Cassegrain objective which functions optically like a lens, but has the advantage of consisting of mirrors that focus both the visible and IR

light to the same point. Figure 2.12 shows the beam-path in a FTIR microscope that contains both a Cassegrain objective and Cassegrain condenser setup.

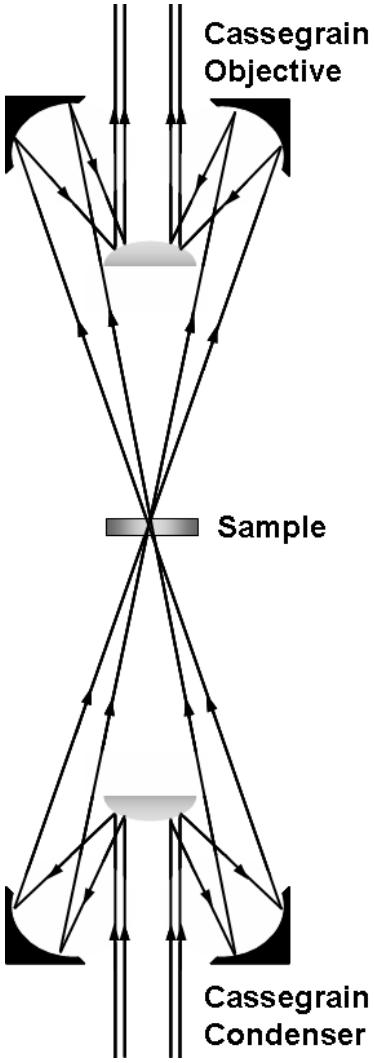

Figure 2.12: Geometrical arrangement of FTIR microscope optics with Cassegrain objective and Cassegrain condenser (Modified from reference)[45]

2.4.3 FOCAL PLANE ARRAY SPECTROSCOPY

FTIR measurements were performed using a Varian Stingray FTIR microscope system (600 UMA) equipped with a liquid nitrogen cooled HgCdTe (MCT) 64 × 64 pixel Focal Plane Array (FPA) detector with a 15× IR Cassegrain objective. The FPA

has the advantage of rapid measurement time and ready accessibility. The 64 × 64 pixel FPA detector generates 4096 FTIR spectra simultaneously. The spectra collected across the entire pixel array were added together to generate an average spectrum with a very high S/N ratio.

In light of this project however, a weakness of the FPA-FTIR system when analysing biological samples, in particular infected erythrocytes, is that it is not practicable to obtain high quality spectra of individual cells. This is because IR light from a globar source is applied over a whole population of cells at once and spectra are measured as a two-dimensional image. In addition, due to the inherent limitation to brightness of a globar source and the numerical aperture of the Cassegrain objective, a spatial resolution closer to *ca* 9-10 μm is achieved rather than the 5.5 μm that might be expected from the pixel size. Thus, there is the possibility that spectra from more than one cell can be captured onto a single pixel on the FPA detector.

2.4.4 SYNCHROTRON FTIR SPECTROSCOPY

In contrast to FPA-FTIR spectroscopy, synchrotron FTIR spectroscopy has the ability to analyse single erythrocytes. The intrinsic value of using synchrotron light to analyse erythrocytes of *ca* 6 – 8 μm in size is that a synchrotron light source is 100 – 1000 times brighter than a conventional globar source. The spatial resolution of a synchrotron source is $\lambda/2$ and so it is theoretically possible to record spectra using a 4 × 4 μm aperture down to a wavenumber value of 1250 cm^{-1}.[46] However, the combination of the high flux of coherent photons and the confocal nature of the FTIR microscope allows spectra to be recorded with excellent S/N ratio using a 4 × 4 μm aperture down to 1000 cm^{-1}. The disadvantage of a synchrotron source is the long

measurement time to obtain a single spectrum in comparison to an FTIR instrument equipped with a FPA detector.

2.4.5 ATTENUATED TOTAL REFLECTANCE

Attenuated Total Reflectance (ATR), also known as Internal Reflection Spectroscopy (IRS), is an ideal technique for studying compounds that are difficult to study by conventional IR spectroscopy because of sample thickness or opacity, which causes saturation in the spectrum.

Refraction occurs when a beam of radiation is passed through two different media, where the first medium is denser than the second. As the angle of incidence is increased, a resultant increased portion of incident light is also reflected. Internal reflection occurs when the angle of incidence is taken beyond the critical angle (ϑ_c). The critical angle is defined as:

$$\vartheta_c = \sin^{-1}(n_{21}) \text{ where, } n_{21} = n_2/n_1 \qquad \textbf{(2.13)}$$

where n_1 is the refractive index of the internal reflection element (IRE) and n_2 is the refractive index of the sample.[3,44]

The depth of penetration (d_p) achieved is dependent on three factors; these include wavelength, the material's refractive index and the angle of the incident beam with respect to the interface.[3,44]

The depth of penetration is defined as:

$$d_p = (\lambda_1) / \left[2\pi\left(\sin^2\vartheta - n_{21}^2\right)^{1/2}\right] \qquad \textbf{(2.14)}$$

where $\lambda_1 = \lambda / n_1$ is the wavelength in the denser medium. Furthermore, the sensitivity of

ATR spectra are dependent on the degree of contact between the sample and the internal reflection element.[44] A beam of radiation is passed through a sample that is in direct contact with an IRE to produce ATR spectra. The IRE used in this project is diamond.

Since the sample is simply placed in direct contact with the ATR crystal, an advantage of using the technique is that it requires little or no sample preparation. Figure 2.13 displays a single pass IRE configuration used in this project.

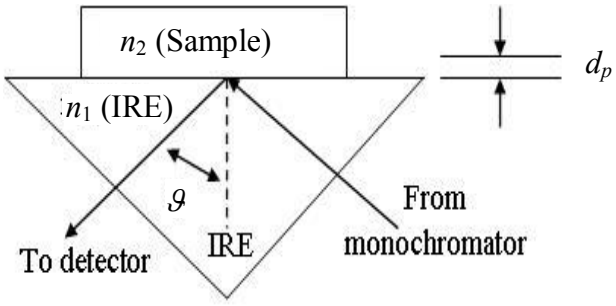

Figure 2.13: Schematic diagram of a single pass IRE configuration

2.5 MATHEMATICAL PRE-PROCESSING OF SPECTRAL DATA

A number of mathematical pre-processing techniques used in biospectroscopy were employed in this project. These techniques were employed to best observe for biochemical changes that are present in the sample. The pre-processing of spectral data allows the researcher to directly compare spectra by maintaining consistency and reproducibility in their pre-processing methods. In addition, pre-processing permits the removal of erroneous spectra that can arise from physical effects present in the sample as discussed in the following sections.

2.5.1 NORMALISATION AND BASELINE CORRECTION

Normalisation is used in biospectroscopy to reduce baseline effects in spectra by compensating for irregularities in sample variation such as sample thickness. This process is applied to ensure all data have approximately the same scaling to obtain an even distribution of the variances and the average values. There are commonly two types of normalisation processes used in this dissertation.

First, the min/max normalisation procedure involves highlighting a peak that has little variation in band intensity to include both the maximum of the peak and the minimum on either side of the peak for spectra in any given dataset. The Raman band commonly chosen to normalise spectra of haem molecules is from the ν_{10} $\nu(C_\alpha C_m)_{asym}$ B_{1g} vibrational mode positioned at *ca* 1625 cm^{-1} because there is little variation in peak intensity. The whole spectrum at every point is normalised against the intensity of this band and the relative band intensities of particular Raman bands can then be determined by dividing the intensity of a selected band by the intensity of the band that has a normalised integrated area under its peak. The band chosen to normalise IR spectra of RBCs was the amide I band because it is the strongest band in the spectrum.

Second, vector normalisation is used for FTIR spectra of infected and uninfected RBCs. The process of vector normalisation involves first calculating the average y-value (IR absorbance) of the spectrum, and then subtracting it from the spectrum so that the mean value of the spectrum is rescaled to y = 0. Second, the sum of squares for all y-values is then calculated and the spectrum is divided by the square root of this sum. The integrated intensity of the squared vector normalised spectrum is then equal to 1. The second process of vector normalisation results in all spectra having the same value

for the integrated area, which effectively corrects for variation in sample optical path length.

Baseline correction can also be applied to Raman and FTIR spectra to reduce the effects of variation in infected and uninfected RBCs and aggregation in model haem compounds which produce non-specific absorptions and cause a slope in the baseline.

2.5.2 EXTENDED MULTIPLICATIVE SCATTER CORRECTION

The physical effects of light scattering pose a major problem in the estimation of chemical properties of particulate systems such as blood, tissue and other biological samples.[47] Extended multiplicative scatter correction (EMSC) allows for the separation of physical light scattering effects, such as those from particle size, from chemical (vibrational) light absorption effects in spectra obtained from powders, turbid solutions or biological samples.[48] EMSC has advantages over multiplicative scatter correction (MSC) for this project, as will be discussed below.

EMSC is similar to MSC since it removes additive and multiplicative effects from spectra.[49] Additive effects are observed as a baseline shift in the spectrum and are associated with absorbance from chemical interferents. Furthermore, the fraction of transmitted light collected by the detector can vary, which can also cause these additive effects observed in the spectrum. This can be explained by varying scattering effects in the sample, which can lead to variations in the angular distribution of light from the sample towards the detector. Multiplicative effects are caused by variation in light scattering in the sample due to the change in optical path length, which is referred to as the ‚diffuse thickness' of the sample.[48-50]

EMSC differs from MSC by compensating for an additional wavelength-dependent spectral effect when observing for variations in light scatter caused by physical effects, which is given by Equation 2.15 below and is the approximate EMSC model:[48-50]

$$A(\bar{\nu}) \approx k(\bar{\nu}) + b + a + d\bar{\nu} + e\bar{\nu}^2 \qquad \textbf{(2.15)}$$

where $A(\bar{\nu})$ is the absorbance at a given wavenumber. The additive effect is represented by a. The multiplicative quantity b represents the sample thickness or optical path length. If b is large, then there is an increased probability that light is absorbed by a molecule in the sample. $k(\bar{\nu})$ is the characteristic absorptivity for a specific sample at a specific wavenumber $(\bar{\nu})$. d and e account for a linear and quadratic wavenumber-dependent effect, respectively.[50] The EMSC corrected spectra can then be calculated according to Equation 2.16 below:

$$A_{corr}(\bar{\nu}) = \left[A'(\bar{\nu}) - a - d\bar{\nu} - e\bar{\nu}^2\right]/b \qquad \text{where } A'(\bar{\nu}) \approx k(\bar{\nu})cb \qquad \textbf{(2.16)}$$

where c is the concentration of the light-absorbing chemical species in the sample.

Mie scattering and dispersion artifacts are the main consequences of physical effects in biological samples. These effects are reduced by the EMSC algorithm. Mie scattering occurs from objects in the sample whose size is approximately the same as the wavelength of the irradiating light (i.e. cellular nuclei). A useful model to describe Mie scattering in RBCs is that of dielectric spheres. Dielectric spheres are known to scatter electromagnetic radiation if the wavelength of the light is similar to the size of

the dielectric sphere.[51] The effect Mie scattering has on the spectrum is the appearance of a wavelength dependent high order polynomial „rippling' wave. Therefore, the EMSC approximates a quadratic curve to the spectrum to reduce the appearance of this effect.

In addition, dispersion artifacts, such as edge effects from the sample (i.e. RBCs), result in the distortion of line shapes due to the superposition of absorptive and dispersive line shapes.[52] This occurs when the wave-front of photons partly hits the sample at the same time as partly hitting an area with no sample. The effect of dispersion artifacts is commonly observed as a negative contribution to the amide I band in spectra taken in the mid-IR region. Due to the negative contribution of the dispersive line shape, the maxima of the absorption spectra can shift and the amide I/II intensity ratio appears to distort.[52] EMSC can reduce dispersion artifacts, but cannot completely remove the effect from the spectrum.

2.5.3 SPECTRAL DERIVATIVES

Biospectroscopists frequently employ derivative techniques to highlight features in the raw spectra, namely contours and shoulders on narrower bands, which are typically difficult to observe. Improved visual separation of intrinsically overlapping bands and greater sensitivity is achieved by the sharpening of fine structural features in the raw spectra. A disadvantage to employing derivitisation to spectra is the rapid degradation of S/N ratio as the order of derivative increases.

Second order derivative is commonly applied to raw spectra because it expresses the rate of change of the gradient. The second derivative spectra calculated in this dissertation used the Savitsky-Golay[53] algorithm with a smoothing second derivative function. Although using second derivatives reduces spectral resolution and precludes

the consideration of spectral intensities in analysis, it was used throughout this dissertation to allow for easier visualisation of spectral change and to minimise the effects of baseline variation in the spectral database. In the second derivative spectra, Raman intensities and FTIR absorbances become minima and therefore negative peaks, whereas in the raw spectra, Raman intensities and FTIR absorbances are positive peaks.

2.5.4 SPECTRAL SUBTRACTION TECHNIQUES

Spectral subtraction can be used to discern spectral contributions resulting from a particular treatment of the sample. In this dissertation, malarial infected RBCs were inoculated with chloroquine (CQ) to observe for structural changes in the formation of malaria pigment (haemozoin). Raw Raman spectra of infected RBCs inoculated with and without CQ were baseline corrected, normalised and then subtracted from each other. The resulting spectrum is a difference between the specific functional groups that undergo a change in their molecular environment.

The advantage of applying a spectral subtraction is that functional groups which do not undergo biochemical change are subtracted from the resulting spectrum. A second derivative technique can also be applied to the difference spectrum to further highlight spectral features by improving the S/N ratio. In addition, smoothing can to some extent reduce the spectral noise, but can compromise the signal.

2.5.5 PRINCIPAL COMPONENTS ANALYSIS

Principal Components Analysis (PCA) constitutes the most fundamental technique used in multivariate data analysis and involves the decomposition of data into a noise and structural component.[54] The dimensionality of the data set is reduced by

plotting the objects (sample spectra) as scores onto principal components (PC's) with each consecutive component orthogonally positioned with respect to the previous PC. Each PC gives rise to a percentage of variance in the data set, with the explained variance decreasing as the PC increases. Hence, PC1 would give rise to the most variance in the data set followed by PC2 as given by:

$$\text{Explained variance} = PC1 > PC2 > PC3 > PC4 > PC5 > PC6 \ldots$$

Individual spectra are represented as a point or a score on a two-dimensional scores plot. The individual variance contribution of the spectrum for each point contributes to the position of each point (spectrum) on a given PC.[55] A plot of these scores (scores plot) shows the location of the sample spectrum along each model component orthogonally positioned to each other in three-dimensional space and plots the data points as positive or negative scores along these axes.

A plot of the scores along each PC (scores plot) allows differences and similarities to be easily recognised. The loadings in a loadings plot represent the variables (wavenumber values) responsible for the most variability in the dataset and can be used in combination with the scores plot to identify the group to which they belong.

In this study, PCA is applied to investigate the spectra of parasites at different stages of the intra-erythrocytic life cycle and to distinguish between chloroquine treated and untreated trophozoite infected erythrocytes. To minimise baseline effects and physical effects, either second derivatives were calculated or the Extended Multiplicative Scatter Correction (EMSC) was applied to the data.[49] If a variable has a

large positive or negative loading, then those variables are the most important for the component concerned. The positive and negative loadings are representative of the positive and negative scores respectively. However, if a PCA decomposition was performed on second derivative spectra, then the positive and negative scores are correlated with the negative and positive loadings respectively.

2.5.6 UNSUPERVISED HIERARCHICAL CLUSTER ANALYSIS

Unsupervised hierarchical cluster analysis (UHCA) is an unsupervised technique used to classify areas of a cluster image based on the grouping of similar spectra within the image.[56] Spectra are clustered into colour coded groups to form an image. UHCA allow the extraction of the mean spectrum which is most representative of the cluster.

Cluster analysis refers to methods used to assign objects (spectra) into groups (clusters) so that objects from the same cluster are more similar to each other than objects from different clusters. Hierarchical cluster analysis is a general approach to cluster analysis, in which spectra are grouped together with other spectra that are similar. Often similarity is assessed according to a distance measure. The calculation of distance measures between spectra and clusters, once spectra begin to group into clusters, is a key component of the analysis.

UHCA can be achieved by first calculating a distance matrix between all spectra. This matrix contains the complete set of inter-spectral distances (measures of dissimilarity). The dimension of the distance matrix is $n \times n$, where n is the number of spectra. For obtaining the distance measures, D-values were calculated and Ward's algorithm was used for sorting the data into clusters. This combination of D-values and Ward's algorithm generally give the best imaging results.[57]

D-values are defined as follows:

$$d_{jk} = (1 - r_{jk}) \times 1000 \quad \textbf{(2.17)}$$

where, r_{jk} is the Pearson's correlation coefficient:

$$r_{jk} = \frac{\left(\sum_{i=1}^{n} y_{ji} \cdot y_{ki}\right) - n \cdot \bar{y}_j \cdot \bar{y}_k}{\sqrt{\left(\sum_{i=1}^{n} y_{ji}^2 - n \cdot \bar{y}_j^2\right) \cdot \left(\sum_{i=1}^{n} y_{ki}^2 - n \cdot \bar{y}_k^2\right)}} \quad \textbf{(2.18)}$$

where, n is the total number of absorbance values in the spectra and y_{ji} and y_{ki} are the i-th absorbance values of the j-th and k-th spectra, respectively.

If the Pearson's correlation coefficient (PCC) is zero, then spectra are completely uncorrelated. Alternatively, if the PCC equals one then spectra are perfectly correlated.

In Ward's algorithm,[58] if two spectra are similar then they are merged into a cluster. The merging of spectra causes the dimensions of the distance matrix to reduce to $(n - 1) \times (n - 1)$. Therefore, the distances of the new formed cluster to all remaining spectra are recalculated and the next two most similar spectra are merged. The process is repeated until all spectra are merged into one cluster. While the clustering process is completely unsupervised, the number of classes that will appear in the cluster image is at the discretion of the researcher.

2.5.7 ARTIFICIAL NEURAL NETWORK

Artificial neural network (ANN) analysis was performed using the NeuroDeveloper® 2.5b 2004 SynthonSoftware©. ANNs are modelled on the biological neural network of the human brain. Within the framework of multivariate classification,

ANNs are generally defined as non-parametric non-linear regression estimators,[59] where non-parametric methods are not based on the *a priori* assumption of a specific model dataset. ANNs were appropriately used in this project to discriminate between the different intra-erythrocytic stages of the malarial parasite as discussed in paper **I**.

Neural networks have several advantages over other data analysis methods such as linear discriminant analysis (LDA) and soft independent modelling by class analogy (SIMCA). First, ANNs are intuitive and can learn from new data; second, the networks can classify non-linear relationships among the input variables of the dataset; third, the networks can correctly classify new data that only generally resembles the original training dataset. Finally, ANNs are computationally very fast because many independent training operations can be executed concurrently due to their highly parallel network structure.

A drawback to the flexibility of the ANN model is their tendency to over-fit calibration data, which may result in a lack of generalisation.[60] Generalisation refers to the capability of a model to produce a valid estimate of the correct output when a new input is presented to the ANN.[60] To guard against overtraining, a validation dataset was used and monitored. Training was stopped when the validation dataset error was minimised. Another drawback of ANNs is their black-box aspect. The black-box aspect of ANNs refers to the difficulty of examining the model's internal structure to identify which spectral features are the most statistically significant for making the classifications. This was overcome by calculating ANN models at different spectral windows and observing for the best specificity and sensitivity measurements.

2.7 REFERENCES

(1) Mantsch, H. H.; Jackson, M. *J. Mol. Struct.* **1995**, *347*, 187-206.

(2) Dorn, A.; Vippagunta, S. R.; Matile, H.; Jacquet, C.; Vennerstrom, J. L.; Ridley, R. G. *Biochem. Pharmacol.* **1998**, *55*, 727-736.

(3) Skoog, D. A.; Holler, E. J.; Nieman, T. A. *Principles of Instrumental Analysis 5th Edition*; Saunders College Publishing: USA, 1992.

(4) Campbell, I. D.; Dwek, R. A. *Biological Spectroscopy*; The Benjamin/Cummings Publishing Company Inc.: California, 1984.

(5) Spiro, T. G.; Strekas, T. *J. Am. Chem. Soc.* **1974**, *96*, 338-345.

(6) Spiro, T. G.; Strekas, T. *Proc. Nat. Acad. Sci. USA.* **1972**, *69*, 2622-2626.

(7) Kramers, H. A.; Heisenberg, W. *Z. Phys.* **1925**, *31*, 681-707.

(8) Dirac, P. A. M. *Proc. Roy. Soc. (London)* **1927**, *114*, 710-728.

(9) Hizhnyakov, V.; Tehver, I. *Phys. Stat. Sol.* **1967**, *21*, 755-768.

(10) Heller, E. J.; Sundberg, R. L.; Tannor, D. *J. Phys. Chem.* **1982**, *86*, 1822-1833.

(11) Tonks, D. L.; Page, J. B. *Chem. Phys. Lett.* **1979**, *66*, 449-453.

(12) Blazej, D. C.; Peticolas, W. L. *J. Chem. Phys.* **1980**, *72*, 3134-3142.

(13) Myers, A. B.; Mathies, R. A. In *Biological Applications of Raman Spectroscopy Volume 2*; Spiro, T. G., Ed.; John Wiley & Sons: New York, 1987; Vol. 2, pp 1-58.

(14) McHale, J. L. *Molecular spectroscopy*; Prentice Hall: Upper Saddle River, 1999.

(15) Tang, J. J.; Albrecht, A. C. *Raman spectrosc.* **1970**, *2*, 33-68.

(16) Spiro, T. G.; Li, X-Y. In *Biological Applications of Raman Spectroscopy*; Spiro, T. G., Ed.; Wiley: New York, 1988; Vol. 3.

(17) Spaulding, L. D.; Chang, C. C.; Yu, N.-T.; Felton, R. H. *J. Phys. Chem. Soc.* **1975**, *97*, 2517-2525.

(18) Kumble, R.; Rush, T. S.; Blackwood, M. E. J.; Kozlowski, P. M.; Spiro, T. G. *J. Phys. Chem. B.* **1998**, *102*, 7280-7286.

(19) Asher, S. A. *Methods in Enzymology* **1981**, *76*, 371-413.

(20) Yarkony, D. R. *J. Phys. Chem.* **1996**, *100*, 18612-18628.

(21) Jahn, H.; Teller, E. *Proc. R. Soc. A.* **1937**, *161*, 220-235.

(22) Spiro, T. G., Strekas, T. *Proc. Nat. Acad. Sci. USA.* **1972**, *69*, 2622-2626.

(23) Gouterman, M. *In the porphyrins*; Academic Press: New York, 1979.

(24) Shelnutt, J. A.; Cheung, L. D.; Chang, R. C. C.; Yu, N. T.; Felton, R. H. *J. Chem. Phys.* **1977**, *66*, 3387-3398.

(25) Burke, J. M.; Kincaid, J. R.; Spiro, T. G. *J. Am. Chem. Soc.* **1978**, *100*, 6077-6083.

(26) Hoard, J. L. *Porphyrins and metalloporphyrins*; American Elsevier: New York, 1975.

(27) Sheidt, W. R.; Gouterman, M. *In Iron Porphyrins Part one*; Addison-Wesley Publishing Company: London, 1983.

(28) Abe, M.; Kitagawa, T.; Kyogoku, K. *J. Chem. Phys.* **1978**, *69*, 4526-4534.

(29) Wood, B. R.; Langford, S. J.; Cooke, B. M.; Lim, J.; Glenister, F. K.; Duriska, M.; Unthank, J. K.; McNaughton, D. *J. Am. Chem. Soc.* **2004**, *126*, 9233-9239.

(30) Frenkel, J. *Phys. Rev.* **1931**, *37*, 17-44.

(31) Frenkel, J. *Phys. Rev.* **1931**, *37*, 1276-1293.

(32) Wannier, G. H. *Phys. Rev.* **1937**, *52*, 191-197.

(33) Akins, D. L.; Özcelik, S.; Zhu, H-R.; Guo, C. *J. Phys. Chem.* **1997**, *101*, 3251-3259.

(34) Knox, R. S. *Theory of Excitons*; Academic Press: New York, 1963.

(35) Kasha, M. *Radiat. Res.* **1963**, *20*, 55-71.

(36) Hollas, M. J. *Modern Spectroscopy*, 3 ed.; John Wiley & Sons: Chichester, 1996.

(37) Akins, D. L. *J. Phys. Chem.* **1986**, *90*, 1530-1534.

(38) Webster, G. T.; McNaughton, D.; Wood, B. R. *J. Phys. Chem. B* **2009**, accepted.

(39) Wood, B. R.; Langford, S. J.; Cooke, B. M.; Glenister, F. K.; Lim, J.; McNaughton, D. *FEBS Lett.* **2003**, *554*, 247-252.

(40) Chen, D.-M.; Zhang, Y.-H.; He, T.-J.; Liu, F.-C. *Spectrochim. Acta.* **2002**, *58*, 2291-2297.

(41) Bhuiyan, A. A.; Seth, J.; Yoshida, N.; Osuka, A.; Bocian, D. F. *J. Phys. Chem. B*. **2000**, *104*, 10757-10764.

(42) Kim, Y. H.; Jeong, D. H.; Kim, D.; Jeoung, S. C.; Cho, H. S.; Kim, S. K.; Aratani, N.; Osuka, A. *J. Am. Chem. Soc.* **2001**, *123*, 76-86.

(43) Zerner, M.; Gouterman, M.; Kobayashi, H. *Theor. Chim. Acta.* **1996**, *6*, 363-399.

(44) Gunzler, H.; Gremlich, H.-U. *IR Spectroscopy, An Introduction*; Wiley-VCH Verlag: Weinham, Germany, 2002.

(45) Kubota, H.; Kaneko, F.; Kawaguchi, T.; Kawasaki, M. *Vib. Spec.* **2003**, *31*, 11-17.

(46) Carr, G. L. *Rev. Sci. Instrum.* **2001**, *72*, 1613-1619.

(47) Thennadil, S. N.; Martens, H.; Kohler, A. *App. Spectrosc.* **2006**, *60*, 315-321.

(48) Martens, H.; Nielsen, J. P.; Engelsen, S. B. *Anal. Chem.* **2003**, *75*, 394-404.

(49) Martens, H.; Starks, E. *J. Pharm. Biomed. Anal.* **1991**, *9*, 625-635.

(50) Kohler, A.; Kirschner, C.; Oust, A.; Martens, H. *App. Spectrosc.* **2005**, *59*, 707-716.

(51) Mohlenhoff, B.; Romeo, M.; Diem, M.; Wood, B. R. *Biophys. J.* **2005**, *88*, 3635-3640.

(52) Romeo, M.; Diem, M. *J. Vib. Spec.* **2005**, *38*, 129-132.

(53) Savitzky, A.; Golay, M. J. E. *Anal. Chem.* **1964**, *36*, 1627-1639.

(54) Esbensen, K. H. *Multivariate Data Analysis In Practice: An Introduction to Multivariate Data analysis and Experimental Design*, 5 ed.; CAMO ASA: Norway, 2001.

(55) Solomonov, I.; Osipova, M.; Feldman, Y.; Baehtz, C.; Kjaer, K.; Robinson, I. K.; Webster, G. T.; McNaughton, D.; Wood, B. R.; Weissbuch, I.; Leiserowitz, L. *J. Am. Chem. Soc.* **2007**, *129*, 2615-2627.

(56) Wood, B. R.; McNaughton, D. *Spectrochemical Analyses Using Multichannel Infrared Detectors*; Blackwell: Cambridge, MA, 2005.

(57) Lasch, P.; Haensch, W.; Naumann, D.; Diem, M. *Biochimica et Biophysica Acta* **2004**, *1688*, 176-186.

(58) Ward, J. H. *J. Am. Stat. Assoc.* **1963**, *58*, 236-244.

(59) Geman, S.; Bienenstock. E.; Doursat, R. *Neural Comput.* **1992**, *4*, 1-58.

(60) Despagne, F.; Massart, D. L. *Analyst* **1998**, *123*, 157R-178R.

Chapter 3

FTIR Spectroscopic Analysis of Malaria Infected Erythrocytes

CHAPTER SUMMARY

This component of the study is mainly concerned with discriminating the different intra-erythrocytic lifecycle stages of the *Plasmodium falciparum* parasite in single erythrocytes based on the specific lipid signature within each lifecycle stage. This was accomplished using FTIR spectroscopy in conjunction with multivariate analysis techniques. In addition, FTIR spectroscopy was able to detect haemozoin biominerals within the later feeding stage (trophozoite) of the parasite. The work builds on previous reports claiming lipids are important catalysts for haemozoin (Hz) formation.[1-5] Given that lipids play this catalytic role, it was expected that differences in the lipid signature as haemozoin accumulates would allow for the detection of the different intra-erythrocytic lifecycle stages as the parasite matures.

During the intra-erythrocytic stage, the *Plasmodium falciparum* parasite has a six-fold increase in its phospholipid content in order to acquire the source of lipids it needs to generate membranes necessary for growth and division.[6,7] The lack of lipid biosynthetic activity of the host erythrocyte and the limited potential for phospholipid remodelling[8,9] force the parasite to undertake some short chain fatty acid biosynthesis as well as mevalonate-independent isoprenoid biosynthesis in its apicoplast.[10-12] However, the bulk of the polar head group and fatty acid building blocks appear to be taken from the host.[9,13] Taken together, these intermediates allow the parasite to remodel and extensively synthesise phospholipids and generate membranes that are enriched in phosphatidylcholine and phosphotidylethanolamine, and that are low in cholesterol and sphingomyelin when compared with the host membrane.[13] A decrease in the levels of polyunsaturated phospholipids in the host cell membrane suggests that it also undergoes some remodelling.[13]

A spectroscopic method for the detection of lipid signatures in infected erythrocytes would seem an ideal approach to confirm the expectation that differing lipid signatures reflect differing stages of early intra-erythrocytic development of the parasite. The first paper (**I**) in this chapter shows the potential of FTIR spectroscopy to effectively determine the developmental stages of the *Plasmodium falciparum* parasite based on the specific lipid structure observed from each individual stage in single red blood cells (RBCs).

It was found (**I**) that the C-H stretching region (3100-2800 cm^{-1}) within the mid-IR spectral window is useful in differentiating, by visual inspection in combination with Principal Components Analysis (PCA), the stages of the intra-erythrocytic lifecycle of the malarial parasite, including the ring and schizont stage. Bands at 2922 cm^{-1}, 2852 cm^{-1} and 1738 cm^{-1}, assigned to the $\nu_{asym}(CH_2$ acyl chain lipids), $\nu_{sym}(CH_2$ acyl chain lipids) and the ester carbonyl band respectively, increase as the parasite matures from its early ring stage, to the trophozoite, and finally to the schizont stage.

Additionally, IR bands from haemozoin are quite easily observed in spectra taken from cells in the trophozoite stage, particularly following a spectral subtraction with an uninfected RBC. The haemozoin bands observed in the IR difference spectrum include the 1712 cm^{-1}, 1664 cm^{-1} and 1209 cm^{-1} bands. Furthermore, this analysis reveals an observable increase in the IR absorbance of lipid bands in infected RBCs when compared to uninfected RBCs. Although synchrotron FTIR spectroscopy can indeed detect haemozoin within a single erythrocyte, the absorbance of proteins and lipids makes it difficult to observe direct evidence for the mode of attachment of quinoline drugs on the haemozoin biomineral within a single RBC.

It was discovered in the second paper (**II**), as part of a larger study, that FTIR-ATR and Raman measurements can be useful in determining the type of quinoline drug

binding that occurs directly on synthetic malaria pigment (β-haematin). The results showed changes in the surface propionic acid groups (1744 cm^{-1}) when the drug was present, which would otherwise be hidden in FTIR spectra by the superposition of the ester carbonyl band of trophozoite infected RBCs. When PCA was applied to the Raman spectra, changes in A_{1g} and B_{1g} modes of β-haematin were apparent, lending support to the model involving a π-π stacked drug binding complex.

REFERENCES

(1) Fitch, C. D.; Cai, G-z.; Chen, Y-F.; Shoemaker, J. D. *Biochimica et Biophysica Acta* **1999**, *1454*, 31-37.

(2) Jackson, K. A.; Klonis, N.; Ferguson, D. J. P.; Adisa, A.; Dogovski, C.; Tilley, L. *Mol. Microbiol.* **2004**, *54*, 109-122.

(3) Oliveira, M. F.; Kycia, S. W.; Gomez, A.; Kosar, A. J.; Bohle, D. S.; Hempelmann, E.; Menezes, D.; Vanier-Santos, M. A.; Oliveira, P. L.; Ferreira, S. T. *FEBS Lett.* **2005**, *579*, 6010-6016.

(4) Egan, T. J.; Chen, J. Y-J.; de Villiers, K. A.; Mabotha, T. E.; Naidoo, K. J.; Ncokazi, K. K.; Langford, S. J.; McNaughton, D.; Pandiancherri, S.; Wood, B. R. *FEBS Lett.* **2006**, *580*, 5105-5110.

(5) Pisciotta, J. M.; Coppens, I.; Tripathi, A. K.; Scholl, P. F.; Shuman, J.; Bajad, S.; Shulaev, V.; Sullivan, D. J. *Biochem. J.* **2007**, *402*, 197-204.

(6) Simoes, A. P.; Roelofsen, B.; Op den Kamp, J. A. *Cell Biol. Int. Rep.* **1992**, *16*, 533-545.

(7) Beaumelle, B. D.; Vial, H. J. *In Vitro Cell Dev. Biol.* **1988**, *24*, 711-718.

(8) Vial, H. J.; Ancelin, M. L. *Subcell. Biochem.* **1992**, *18*, 259-306.

(9) Mitamura, T.; Palacpac, N. M. *Microbes Infect.* **2003**, *5*, 545-552.

(10) Jomaa, H.; Wiesner, J.; Sanderbrand, S.; Altincicek, B.; Weidemeyer, C.; Hintz, M.; Turbachova, I.; Eberl, M.; Zeidler, J.; Lichtenthaler, H. K.; Soldati, D.; Beck, E. *Science* **1999**, *285*, 1573-1576.

(11) Surolia, N.; Surolia, A. *Nat. Med.* **2001**, *7*, 167-173.

(12) Waller, R. F.; Reed, M. B.; Cowman, A. F.; McFadden, G. I. *EMBO J.* **2000**, *19*, 1794-1802.

(13) Vial, H. J.; Eldin, P.; Tielens, A. G.; van Hellemond, J. J. *Mol. Biochem. Parasitol.* **2003**, *126*, 143-154.

Monash University

Declaration for Thesis Chapter (Chapter 3)

Declaration by candidate

In the case of Chapter 3 the nature and extent of my contribution to the work (**Paper I**) was the following:

Nature of contribution	Extent of contribution (%)
Experimental design, interpretation of results, writing of the manuscript	>80%

The following co-authors contributed to the work. Co-authors who are students at Monash University must also indicate the extent of their contribution in percentage terms:

Name	Nature of contribution	Extent of contribution (%) for student co-authors only
Katherine de Villiers	Experimental support at the Australian synchrotron	5
Tim Egan	Drafting of manuscript	-
Samantha Deed	Culturing and fixing of the cells, drafting of manuscript	-
Leann Tilley	Drafting of manuscript	-
Mark Tobin	Australian synchrotron IR beamline technical support, drafting of manuscript	-
Keith Bambery	Artificial Neural Network (ANN) calculation, drafting of manuscript	-
Don McNaughton	Drafting of manuscript, provided supervision	-
Bayden Wood	Drafting of manuscript, provided supervision	-

Candidate's Signature	[redacted]	**Date**
		15/04/09

Declaration by co-authors

The undersigned hereby certify that:

(1) the above declaration correctly reflects the nature and extent of the candidate's contribution to this work, and the nature of the contribution of each of the co-authors.

(2) they meet the criteria for authorship in that they have participated in the conception, execution, or interpretation, of at least that part of the publication in their field of expertise;

(3) they take public responsibility for their part of the publication, except for the responsible author who accepts overall responsibility for the publication;

(4) there are no other authors of the publication according to these criteria;

(5) potential conflicts of interest have been disclosed to (a) granting bodies, (b) the editor or publisher of journals or other publications, and (c) the head of the responsible academic unit; and

(6) the original data are stored at the following location(s) and will be held for at least five years from the date indicated below:

Location(s)	Department of Chemistry, Centre for Biospectroscopy, Monash University, Clayton

Please note that the location(s) must be institutional in nature, and should be indicated here as a department, centre or institute, with specific campus identification where relevant.]

Signature	Date
Department of Chemistry, University of Cape Town, South Africa. [redacted]	24 March 2009
Department of Chemistry and Polymer Science, University of Stellenbosch, South Africa [redacted]	24 March 2009
Department of Biochemistry, La Trobe University Bundoora [redacted]	31/3/09
Dept. Biochemistry La Trobe Uni [redacted]	31/3/09
MARK TOBIN AUSTRALIAN SYNCHROTRON [redacted]	3/4/09
Bayden Wood (Monash University) [redacted]	15/4/09
Keith Bambery (Monash University) is on vacation 30 Bridgwood Rd Sign [redacted]	15/4/09
School of Chem Monash [redacted]	15/4/09

Article

Discriminating the Intraerythrocytic Lifecycle Stages of the Malaria Parasite Using Synchrotron FT-IR Microspectroscopy and an Artificial Neural Network

Grant T. Webster, Katherine A. de Villiers, Timothy J. Egan, Samantha Deed, Leann Tilley, Mark J. Tobin, Keith R. Bambery, Don McNaughton, and Bayden R. Wood

Anal. Chem., **2009**, 81 (7), 2516-2524• DOI: 10.1021/ac802291a • Publication Date (Web): 11 March 2009

Anal. Chem. **2009,** *81,* 2516–2524

Discriminating the Intraerythrocytic Lifecycle Stages of the Malaria Parasite Using Synchrotron FT-IR Microspectroscopy and an Artificial Neural Network

Grant T. Webster,[†] Katherine A. de Villiers,[‡] Timothy J. Egan,[‡] Samantha Deed,[§] Leann Tilley,[§] Mark J. Tobin,[||] Keith R. Bambery,[†] Don McNaughton,[†] and Bayden R. Wood*,[†]

Centre for Biospectroscopy and School of Chemistry, Monash University, Clayton, Victoria 3800, Australia, Department of Chemistry, University of Cape Town, Private Bag, Rondebosch 7701, South Africa, Department of Biochemistry and Centre of Excellence for Coherent X-ray Science, La Trobe University, Melbourne, Victoria 3086, Australia, and Australian Synchrotron, 800 Blackburn Road, Clayton, Victoria 3168, Australia

Synchrotron Fourier transform infrared (FT-IR) spectra of fixed single erythrocytes infected with *Plasmodium falciparum* at different stages of the intraerythrocytic cycle are presented for the first time. Bands assigned to the hemozoin moiety at 1712, 1664, and 1209 cm^{-1} are observed in FT-IR difference spectra between uninfected erythrocytes and infected trophozoites. These bands are also found to be important contributors in separating the trophozoite spectra from the uninfected cell spectra in principal components analysis. All stages of the intraerythrocytic lifecycle of the malarial parasite, including the ring and schizont stage, can be differentiated by visual inspection of the C−H stretching region (3100−2800 cm^{-1}) and by using principal components analysis. Bands at 2922, 2852, and 1738 cm^{-1} assigned to the $\nu_{asym}(CH_2$ acyl chain lipids), $\nu_{sym}(CH_2$ acyl chain lipids), and the ester carbonyl band, respectively, increase as the parasite matures from its early ring stage to the trophozoite and finally to the schizont stage. Training of an artificial neural network showed that excellent automated spectroscopic discrimination between *P. falciparum*-infected cells and the control cells is possible. FT-IR difference spectra indicate a change in the production of unsaturated fatty acids as the parasite matures. The ring stage spectrum shows bands associated with cis unsaturated fatty acids. The schizont stage spectrum displays no evidence of cis bands and suggests an increase in saturated fatty acids. These results demonstrate that different phases of the *P. falciparum* intraerthyrocytic life cycle are characterized by different lipid compositions giving rise to distinct spectral profiles in the C−H stretching region. This insight paves the way for an automated infrared-based technology capable of diagnosing malaria at all intraerythrocytic stages of the parasite's life cycle.

Malaria is an infectious disease caused by unicellular parasites of the genus *Plasmodium*, afflicting over 500 million people, and leading to over one million deaths per year almost all of which are caused by *Plasmodium falciparum*.[1,2] This makes malaria one of the most deadly diseases in the world and therefore a reason for global alarm.[2] The infection begins via the bite of the female *Anopheles* mosquito carrying the unicellular parasite *P. falciparum*. The intraerythrocytic stage of the parasitic lifecycle includes development from an early ring stage to the trophozoite phase, where large amounts of malaria pigment (hemozoin) are produced, and finally to a schizont stage where the parasite replicates. During the trophozoite phase the parasite digests large quantities of hemoglobin releasing toxic free ferrous protoporphyrin IX (Fe(II)PPIX) and denatured globin.[3,4] The Fe(II)PPIX is oxidized to Fe(III)PPIX and aggregates into an insoluble biomineral known as hemozoin (malaria pigment), which is spectroscopically identical to its synthetic analogue β-hematin.[5,6] Hemozoin (Hz) is composed of an array of dimers linked together by reciprocal iron−carboxylate bonds to one of the propionate side chains of adjacent FePPIX groups.[7] Under physiological conditions this pigment remains insoluble and undegraded.[8]

* To whom correspondence should be addressed. E-mail: bayden.wood@sci.monash.edu.au.

[†] Monash University.

[‡] University of Cape Town.

[§] La Trobe University.

[||] Australian Synchrotron.

(1) Greenwood, B.; Mutabingwa, T. *Nature* **2002**, *415*, 670–672.

(2) Sachs, J.; Malaney, P. *Nature* **2002**, *415*, 680–685.

(3) Schmitt, T. H.; Frezzatti, W. A., Jr.; Schreier, S. *Arch. Biochem. Biophys.* **1993**, *307*, 96–103.

(4) Sugioka, Y.; Suzuki, M. *Biochim. Biophys. Acta* **1991**, *1074*, 19–24.

(5) Slater, A. F. G.; Swiggard, W. J.; Orton, B. R.; Flitter, W. D.; Goldberg, D. E.; Cerami, A.; Henderson, G. B. *Proc. Natl. Acad. Sci. U.S.A.* **1991**, *88*, 325–329.

(6) Bohle, D. S.; Conklin, B. J.; Cox, D.; Madsen, S. K.; Paulson, S.; Stephens, P. W.; Yee, G. T. *Am. Chem. Soc. Symp. Ser.* **1994**, *572*, 497–515.

(7) Pagola, S.; Stephens, P. W.; Bohle, D. S.; Kosar, A. D.; Madsen, S. K. *Nature* **2000**, *404*, 307–310.

(8) Deegan, T.; Maegraith, B. G. *Ann. Trop. Med. Parasitol.* **1956**, *50*, 194–211.

10.1021/ac802291a CCC: $40.75
Published on Web 03/11/2009

The importance of lipids as catalysts for Hz formation is well documented.[9−13] The rate of formation of β-hematin under physiological conditions is found to increase in the presence of mono-oleoylglycerol (MOG).[9] Jackson et al.[10] identified neutral lipid bodies composed of di- and triacylglycerols within the digestive vacuole (DV) of the parasite, which may represent storage compartments for lipid intermediates during phospholipid digestion. Hz formation in *Schistosoma mansoni* and *Rhodnius prolixus* occurs in lipid droplets and on the perimicrovillar membranes, respectively.[11] Egan et al.[12] have shown that the Hz analogue, β-hematin, under physiological conditions spontaneously forms at a lipid/water interface. In addition, Pisciotta et al.[13] investigating the crystallization of FePPIX in *P. falciparum* have recently reported TEM (transmission electron microscopy) images of Hz formation in neutral lipid nanospheres at early (ring) and late (trophozoite) stages of the parasitic lifecycle within the DV. Given the importance of lipids in Hz formation, a spectroscopic method for the detection of lipid signatures in infected erythrocytes would seem an ideal approach to distinguish parasites at the early stages of intraerythrocytic development.

Several diagnostic techniques have been employed for malaria detection, these include fluorescence microscopy,[14−18] polymerase chain reaction (PCR)-based assays,[18−20] serological (dipstick) antigen detection,[18,21−23] flow cytometry[18,24] and laser desorption mass spectrometry.[25] Hitherto, the potential of vibrational spectroscopic techniques as malaria diagnostics have not been exploited, which is surprising given the important role the technique has played in understanding the molecular and electronic structure of β-hematin and Hz.[4,6,26,27] In an early study by Slater et al.[5] Fourier transform infrared (FT-IR) spectroscopy was used to identify vibrational modes specifically associated with the propionate groups that link the heme groups together in the heme dimeric array.[5] Initial resonance Raman studies by Ong et al.[28,29] demonstrated the potential of Raman spectroscopy to detect Hz in fixed cells. With the use of resonance Raman spectroscopy, Wood et al.[30] observed dramatic band enhancement of specific vibrational modes of Hz using near-IR excitation wavelengths. This enhancement could be used to identify and image Hz within the DV of single infected functional erythrocytes.[31] More recently the technique has been applied to investigate the interaction of chloroquine-based antimalarial drugs with Hz and β-hematin.[32,33]

Although several resonance Raman studies have been applied to detect and monitor the formation of Hz in erythrocytes, hitherto the diagnostic potential of FT-IR spectroscopy has not been investigated. FT-IR has the advantage of being more sensitive to the lipid moieties than Raman spectroscopy thereby potentially enabling detection of parasites prior to Hz formation. In addition, the lipid bands are very weak when shorter excitation wavelength lasers are applied, and at high Raman excitation laser power it can photodegrade the cell. Furthermore, the time taken to perform a Raman map and produce spectra showing an acceptable signal-to-noise ratio (S/N) is approximately 10−30 min with a conventional Raman microscope as opposed to 1 min with a synchrotron FT-IR microscope. Moreover, to record a map of thousands of cells using a Raman microscope would take many hours compared to 1−3 min when using a conventional FT-IR imaging microscope with a focal plane array (FPA) detector.

Here, after preliminary experiments using FPA IR imaging to confirm the ability of IR analysis to observe Hz directly in infected red blood cells, we combine synchrotron FT-IR microspectroscopy with principal components analysis (PCA) to differentiate between the intraerythrocytic stages of the parasitic lifecycle based on the molecular signatures of Hz and specific lipid markers. To demonstrate the diagnostic utility of FT-IR spectroscopy we employed an artificial neural network (ANN) to unambiguously differentiate the different stages of the parasite. The results show a clear correlation between lipid signature and the stage of the intraerythrocytic development and demonstrate the diagnostic potential of combining FT-IR spectroscopy with neural networks as an independent modality to unequivocally identify parasites at different stages of the erythrocytic life cycle.

EXPERIMENTAL SECTION

Cell Culture. *P. falciparum* (D10 strain) was maintained in continuous culture using human erythrocytes from three different individuals obtained from the Red Cross Blood Bank, Melbourne.[34] Parasitized erythrocytes were cultured in complete

(9) Fitch, C. D.; Cai, G.-z.; Chen, Y.-F.; Shoemaker, J. D. *Biochim. Biophys. Acta* **1999**, *1454*, 31–37.
(10) Jackson, K. A.; Klonis, N.; Ferguson, D. J. P.; Adisa, A.; Dogovski, C.; Tilley, L. *Mol. Microbiol.* **2004**, *54*, 109–122.
(11) Oliveira, M. F.; Kycia, S. W.; Gomez, A.; Kosar, A. J.; Bohle, D. S.; Hempelmann, E.; Menezes, D.; Vanier-Santos, M. A.; Oliveira, P. L.; Ferreira, S. T. *FEBS Lett.* **2005**, *579*, 6010–6016.
(12) Egan, T. J.; Chen, J. Y.-J.; de Villiers, K. A.; Mabotha, T. E.; Naidoo, K. J.; Ncokazi, K. K.; Langford, S. J.; McNaughton, D.; Pandiancherri, S.; Wood, B. R. *FEBS Lett.* **2006**, *580*, 5105–5110.
(13) Pisciotta, J. M.; Coppens, I.; Tripathi, A. K.; Scholl, P. F.; Shuman, J.; Bajad, S.; Shulaev, V.; Sullivan, D. J., Jr. *Biochem. J.* **2007**, *402*, 197–204.
(14) Richards, D. F.; Hunter, D. T.; Janis, B. *Am. J. Clin. Pathol.* **1969**, *51*, 280–283.
(15) Sodeman, T. M. *Am. J. Trop. Med. Hyg.* **1970**, *19*, 40–42.
(16) Shute, G. T.; Sodeman, T. M. *Bull. W.H.O.* **1973**, *48*, 591–596.
(17) Makler, M. T.; Ries, L. K.; Ries, J.; Horton, R. J.; Hinrichs, D. J. *Am. J. Trop. Med. Hyg.* **1991**, *44*, 11–16.
(18) Hanscheid, T. *Clin. Lab. Haematol.* **1999**, *21*, 235–245.
(19) Humar, A.; Ohrt, C.; Harrington, M. A.; Pillai, D.; Kain, K. C. *Am. J. Trop. Med. Hyg.* **1997**, *56*, 44–48.
(20) Humar, A.; Harrington, M. A.; Kain, K. C. *Trans. R. Soc. Trop. Med. Hyg.* **1997**, *91*, 406–409.
(21) Makler, M. T.; Palmer, C. J.; Ager, A. L. *Ann. Trop. Med. Parasitol.* **1998**, *92*, 419–433.
(22) Shiff, C. J.; Minjas, J. N.; Premji, Z. *Parasitol. Today* **1994**, *10*, 494–495.
(23) Garcia, M.; Kirimoama, S.; Marlborough, D.; Leafasia, J.; Rieckmann, K. H. *Lancet* **1996**, *347*, 1549.
(24) van Vianen, P. H.; van Engen, A.; Thaithong, S.; van der Keur, M.; Tanke, H. J.; van der Kaay, H. J.; Mons, B.; Janse, C. J. *Cytometry* **1996**, *14*, 276–280.
(25) Demirev, P. A.; Feldman, A. B.; Kongkasuriyachai, D.; Scholl, P.; Sullivan, D. J., Jr.; Kumar, N. *Anal. Chem.* **2002**, *74*, 3262–3266.
(26) Brémard, C.; Girerd, P.; Kowalewski, P.; Merlin, J. C.; Moreau, S. *Appl. Spectrosc.* **1993**, *47*, 1837–1842.
(27) Wood, B. R.; McNaughton, D. *Expert Rev. Proteomics* **2006**, *3*, 525–544.
(28) Ong, C. W.; Shen, Z. X.; Ang, K. K. H.; Kara, U. A. K.; Tang, J. *Appl. Spectrosc.* **2002**, *56*, 1126–1131.
(29) Ong, C. W.; Shen, Z. X.; Ang, K. K. H.; Kara, U. A. K.; Tang, S. H. *Appl. Spectrosc.* **1999**, *53*, 1097–1101.
(30) Wood, B. R.; Langford, S. J.; Cooke, B. M.; Lim, J.; Glenister, F. K.; Duriska, M.; Unthank, J. K.; McNaughton, D. *J. Am. Chem. Soc.* **2004**, *126*, 9233–9239.
(31) Wood, B. R.; Tait, B.; McNaughton, D. *Appl. Spectrosc.* **2000**, *54*, 353–359.
(32) Cîntă-Pînzaru, S.; Peica, N.; Küstner, B.; Schlücker, S.; Schmitt, M.; Frosch, T.; Faber, J. H.; Bringmann, G.; Popp, J. *J. Raman Spectrosc.* **2006**, *37*, 326–334.
(33) Frosch, T.; Kustner, B.; Schlücker, S.; Szeghalmi, A.; Schmitt, M.; Kiefer, W.; Popp, J. *J. Raman Spectrosc.* **2004**, *35*, 819–821.
(34) Trager, W.; Jensen, J. B. *Science* **1976**, *193*, 673–675.

culture medium (CCM) consisting of RPMI 1640 (GIBCO-BRL), 25 mM hydroxypiperazine-*N*′-2-ethane sulfonic acid (HEPES, Sigma pH 7.4), 2 g/L sodium bicarbonate (AnalaR), and 4 mM Glutamax (Invitrogen). This was supplemented with 0.16% glucose (AnalR), 0.21 mM hypoxanthine (Sigma), 22 μg/mL gentamicin (Sigma), 4% human serum, and 0.25% Albumax I (GIBCO-BRL). The cultures were incubated at 37 °C in a humidified atmosphere of 5% CO_2, 1% O_2, and 90% N_2. Infected red blood cells (RBCs) and uninfected RBCs (controls) were fixed in solution using 2% paraformaldehyde, 0.0075% glutaraldehyde, and 0.1 M cacodylate buffer for 1 h before being washed twice with Milli-Q water and placed on individual 12 mm diameter × 0.5 mm thick CaF_2 IR grade polished windows. Excess water was removed, and the windows were allowed to dry. The experiment was repeated three times.

FT-IR Spectroscopy. FT-IR synchrotron measurements were performed on the FT-IR beamline at the Australian Synchrotron operating at 3 GeV and a maximum current of 200 mA. Spectra were collected with a Bruker Hyperion 2000 IR confocal microscope (Bruker Optics GmbH., Ettlingen, Germany) equipped with a liquid-nitrogen-cooled mercury−cadmium−telluride (MCT) detector with a 36× IR objective. The Hyperion 2000 microscope is coupled to a Bruker Vertex 80v spectrometer. Data collection was carried out using Bruker's proprietary OPUS version 6.5 software, with an additional 3D package (Bruker Optics GmbH., Ettlingen, Germany). The Hyperion microscope and sample was purged with dry nitrogen gas to minimize water vapor contributions in the spectra. For FT-IR mapping and line scans the rectangular aperture was set at 4×4 μm^2. A total of 128 sample scans per spectrum were collected from 30 individual cells for each erythrocytic stage in transmission mode by scanning the computer-controlled microscope stage to preselected points using the video-assisted software. Interferograms were collected double-sided at a resolution of 6 cm^{-1} and Fourier transformed using a Blackman−Harris three-term apodization function with a zero-filling factor of 4.

FT-IR FPA measurements were performed on the Varian Stingray FT-IR microscope system (600 UMA) equipped with a liquid-nitrogen-cooled MCT 64×64 pixel FPA detector with a 15× IR objective. The microscope is coupled to a Varian 7000 spectrometer. The microscope and FT-IR spectrometer were continually purged with nitrogen. Interferograms (128 coadded) were collected in transmission mode double-sided at a resolution of 6 cm^{-1} and Fourier transformed using a Blackman−Harris four-term apodization function with a zero-filling factor of 4.

Attenuated total reflectance (ATR) FT-IR spectra of synthetic hemozoin (β-hematin) were recorded at a resolution of 6 cm^{-1} using a Golden Gate diamond ATR (SPECAC, P/N10500 series) coupled to a Bruker IFS-55 FT-IR spectrometer (Bruker Optics GmbH., Ettlingen, Germany) using OPUS 6.0 spectroscopic software with an extended ATR correction algorithm and equipped with a liquid-nitrogen-cooled MCT detector where 50 scans were averaged.

Data Analysis. Each image from the FPA IR data contained approximately 1000 spectra of a large population of RBCs. Spectra with insufficient S/N or artifacts such as baseline effects and strong Mie scattering were removed from the data set, and the remaining spectra for each lifecycle stage were averaged to produce high S/N ratio spectra with no baseline correction applied. Standard deviation spectra were also calculated and presented.

Initial spectral manipulations on the synchrotron data were carried out under OPUS. Each sample data set contained 30 spectra, which were averaged independently to produce the mean spectra presented. Second-derivative FT-IR spectra were calculated using the Savitzky−Golay algorithm with 13 smoothing points. Although using second derivatives reduces spectral resolution and precludes the use of spectral intensities in analysis we used it here to allow for easier visualization of spectral change and to minimize the effects of baseline variation in the spectral database. N.B. in the second derivate spectra the absorbance maxima become minima and in the discussion below intensities are thus +ve for absorbance spectra and −ve for second-derivative spectra. Difference spectra were calculated directly from vector-normalized raw spectra in absorbance mode and then converted to second derivatives. The converted spectra enable easier visualization of bands within a broad background of multicomponent absorption bands and minimized the effects of Mie scattering.

Principal Components Analysis. In this study, PCA was applied to investigate the spectra of parasites at different stages of the intraerythrocytic life cycle. PCA reduces the dimensionality of a data set by decomposing the data set into a signal and noise part. The objects (spectra) are plotted onto principal components (PCs). Each consecutive PC is orthogonal with respect to the previous and each accounts for a decreasing proportion of the variance. The scores and loadings plots are used to analyze the data when a PCA model is decomposed. A plot of the scores allows similarities and differences in the data to be visualized. Each point in the scores plot represents a single spectrum on a two-dimensional axis. The individual variance calculated for each spectrum contributes to the position of each score on a given PC.[35] The loadings plot is then used in combination with the scores plot to identify the variables (wavenumber values) that contribute to the variability in the data set. PCA was performed on second-derivative spectra after an extended multiplicative scatter correction (EMSC) was applied to the data.[36] PCA was applied to data sets from a control and three test samples: rings, trophozoites, and schizonts. A spectral window between 1800 and 1000 cm^{-1} was used to examine Hz bands and compare the control and the trophozoite groups. Spectral windows of 3100−2800 cm^{-1} were also used to examine lipid bands and compare the control group to each of the three life cycle stages of the parasite. PCA was also performed on all data sets at once (control, rings, trophozoites, and schizonts) using this spectral range. All data were mean-centered, and a full cross validation PCA was performed using the Unscrambler (V9.0 CAMO, Norway) software package.

Artificial Neural Network Classification. ANN analysis was performed using the NeuroDeveloper 2.5b 2004 SynthonSoftware. All the networks were trained to solve a four-class classification problem to test for identification of three classes of infection: ring, trophozoite, and schizonts versus controls from three patients. The available spectra (data set) were split into three subsets: a

(35) Solomonov, I.; Osipova, M.; Feldman, Y.; Baehtz, C.; Kjaer, K.; Robinson, I. K.; Webster, G. T.; McNaughton, D.; Wood, B. R.; Weissbuch, I.; Leiserowitz, L. *J. Am. Chem. Soc.* **2007**, *129*, 2615–2627.
(36) Martens, H.; Starks, E. *J. Pharm. Biomed. Anal.* **1991**, *9*, 625–635.

training set (54%), a validation set (13%), and a test set (33%). Network layout was optimized by testing varying numbers of neurons in the hidden layer for the lowest training and validation data set errors. The number of available sample spectra was limited, and hence, it was necessary (to ensure good theoretical generalization)[37,38] to compress the input spectra with a covariance-based feature selection algorithm. The ANN analysis was performed on second-derivative spectra derived from the raw spectra and processed using a Savitzky−Golay algorithm with 13 smoothing points and then vector-normalized.

ANN analysis was performed on different spectral windows to investigate which bands within the spectra contained the most important information for distinguishing infected cells from uninfected cells. The spectral windows used were (1) 3100−2800 and 1800−1000 cm^{-1}, (2) 3100−2800 cm^{-1}, and (3) 1800−1000 cm^{-1}. In this manner, it was possible to explore the effect on ANN prediction accuracy by leaving out spectral regions associated with the least variability between classes. For each optimized network, the prediction accuracy was determined from classifications performed on the test set. Classification accuracy of an ANN's performance was calculated as the number of correctly classified spectra divided by the total number of test spectra expressed as a percentage. Sensitivity and specificity binary classification measures were calculated where an ANN classification of infected cells (regardless of parasite stage) was taken as a positive test result.

Materials and Synthesis. β-Hematin was prepared as described by Egan et al.[39] by dissolving hemin (Fluka, Biochemika) in 3 mL of 0.1 M NaOH and stirring. To the solution was added 0.3 mL of 0.1 M HCl and 1.74 mL of 12.9 M acetate (pH 5). The reaction was complete after 30 min at 60 °C after which the mixture was cooled for 10 min on ice and then filtered.[39] The resultant solid was dried for 24 h at 37 °C.

RESULTS AND DISCUSSION

Red blood cells make ideal subjects for FT-IR synchrotron spectroscopy because they are anucleated and the microscope aperture (4×4 μm^2) is less than the diameter of the cell ($\sim 8 \times 8$ μm^2); hence, Mie scattering from cell nuclei and dispersion from edge effects that is normally associated with eukaryotic cells is minimized. A synchrotron FT-IR vector-normalized mean spectrum of RBCs (control) and a typical spectrum of a single erythrocyte infected with the *P. falciparum* parasite (trophozoite-infected) are displayed in Figure 1. The most prominent features observed in the spectra are strong broad bands at 1656 and 1542 cm^{-1} assigned to the C=O stretching vibration of proteins coupled to NH_2 in-plane bending vibrations (amide I), with contributions from C=O stretching modes of DNA nucleotides.[31,40−44] The 1542 cm^{-1} band is also from cell

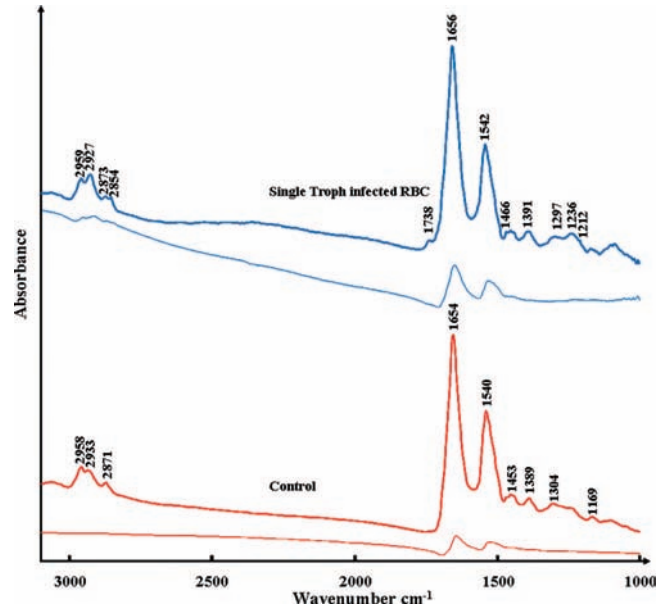

Figure 1. Synchrotron FT-IR vector-normalized spectra of averaged RBCs (control) and a single RBC infected with the *P. falciparum* parasite (trophozoite stage). Standard deviation spectra are shown below each spectrum.

proteins typically from N−H bending coupled to a C−N stretching mode (amide II) and also nucleic acid conformational markers ~1530−1330 cm^{-1} as previously described.[31,45,46] The ester carbonyl band at ~1738 cm^{-1} from lipid moieties is more pronounced in the trophozoite-infected cell. Features attributable to Hz are not immediately obvious in the raw spectra of trophozoite-infected cells; consequently a difference spectrum between the control and the trophozoite spectrum was calculated and is shown in second-derivative form in Figure 2a. Bands are assigned by correlating the minima peaks in the second-derivative difference spectrum to the minima peaks in the second-derivative β-hematin spectrum (Figure 2b). Bands at 1713, 1664, and 1209 cm^{-1} correlate with Hz bands due to the H-bonded carboxylate group, the C=O, and the C−O stretching vibration of the propionate linkage, respectively.[5,30] However, the C=O band from the Hz propionate band is partly obscured by an amide I feature due to protein differences in the two samples and thus appears as a shoulder feature of the amide I mode, while the C−O stretching vibration at 1209 cm^{-1} is very weak in the difference spectrum (Figure 2a). Given that Hz deposits are of the order of 1 μm compared with the 4 μm aperture, it is not surprising that these bands appear weak in the difference spectrum. However, these bands prove that Hz can be detected at the single-cell level. The single-cell difference spectrum below 1000 cm^{-1} is noisy because the 4×4 μm^2 aperture results in diffraction limited energy throughput.[47] The sensitivity is further reduced because of the transmission efficiency of the CaF_2 windows, which decreases dramatically below 1000 cm^{-1}. Here lies the intrinsic value of using the brightness of synchrotron light to analyze RBCs. The synchrotron light source is at least 100 times

(37) Despagne, F.; Massart, D. L. *Analyst* **1998**, *123*, 157R–178R.
(38) Hush, D. R.; Horne, B. G. *IEEE Signal Process. Mag.* **1993**, *1*, 8–39.
(39) Egan, T. J.; Ross, D. C.; Adams, P. A. *FEBS Lett.* **1994**, *352*, 54–57.
(40) Parker, F. S. *Application of Infrared Spectroscopy in Biochemistry, Biology and Medicine*; Plenum: New York, 1971.
(41) Miyazawa, T.; Shimanouchi, T.; Mizushima, S. *J. Chem. Phys.* **1956**, *24*, 408–418.
(42) Miyazawa, T.; Shimanouchi, T.; Mizushima, S. *J. Chem. Phys.* **1958**, *29*, 611–616.
(43) Susi, H., Ed. *Structure and Stability of Biological Macromolecules*; Marcel Dekker: New York, 1969.
(44) Surewicz, W. K.; Mantsch, H. H. *Biochim. Biophys. Acta* **1988**, *952*, 115–130.
(45) Benedetti, E.; Bramanti, E.; Papineschi, F.; Rossi, I.; Benedetti, E. *Appl. Spectrosc.* **1997**, *51*, 792–797.
(46) Susi, H.; Ard, J. S. *Spectrochim. Acta* **1971**, *27A*, 1549–1562.
(47) Carr, G. L. *Rev. Sci. Instrum.* **2001**, *72*, 1613–1619.

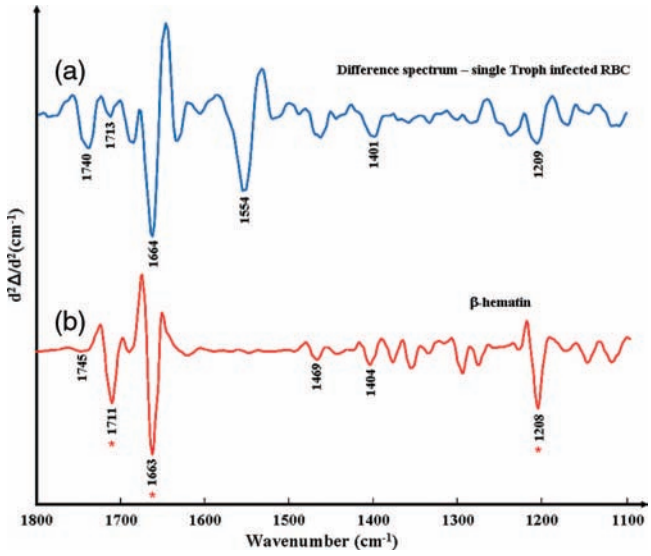

Figure 2. (a) Synchrotron FT-IR difference spectrum (trophozoite RBC − control RBC) shown as a second-derivative spectrum. (b) ATR/FT-IR second-derivative spectrum of β-hematin. (Asterisks indicates the hemozoin marker bands).

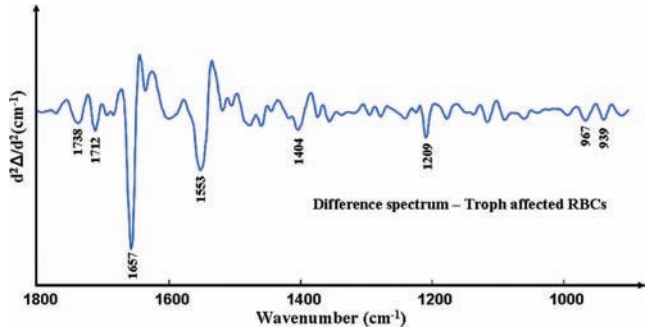

Figure 3. Focal plane array-FT-IR difference spectrum calculated from the average second-derivative spectra of trophozoite stage RBC minus average second-derivative spectra of control RBC.

brighter than a conventional globar source, and this, in combination with the confocal nature of the FT-IR microscope, makes it possible to record spectra with a small 4×4 μm^2 aperture.

The carbonyl band associated with the propionate linkage is observed at 1664 cm^{-1} in the difference spectrum (Figure 2a), which is slightly shifted from its expected literature value of 1662 cm^{-1}.[5,30] The apparent shift is the result of this band being superimposed on the amide I mode. The carbonyl band appears as a shoulder feature on the amide I band in the unprocessed spectrum with the center of this band obscured by the amide I mode. On calculating the difference spectrum the shoulder feature manifests as a band slightly blue-shifted compared to the literature value for isolated Hz. To further investigate these changes an FPA-FT-IR difference spectrum was calculated by subtracting the average trophozoite-affected cells from the average noninfected control (Figure 3). Although it is possible to record spectra of a cluster of cells using a conventional FPA-FT-IR microscope in rapid time and obtain a difference spectrum from uninfected and infected RBCs, it is not possible to resolve spectroscopic detail at the single-cell level with this approach. Bands observed at 1712 and 1209 cm^{-1} are assigned to the H-bonded carboxylate group and C−O stretching vibrations of the propionate linkage from the Hz crystal, respectively.[5,30] A strong feature where the C=O stretching vibrational band of the propionate linkage of Hz is expected supports this assignment, although this region is also affected by protein spectral changes as described below. The FPA enables thousands of FT-IR spectra to be collected simultaneously from a large sample area, and thus the S/N is improved upon averaging. The resulting difference spectrum clearly delineates the major Hz bands, including the 1209 cm^{-1} band, thus confirming the presence of Hz. The absence of the 1662 cm^{-1} band from Hz is due to the superposition of the amide I band from infected cells. Upon spectral subtraction with the control, a band appears at 1657 cm^{-1}, which is slightly shifted from the uninfected control which appears at 1654 cm^{-1} possibly indicative of denatured hemoglobin. The FPA has the advantage of rapid measurement time and ready accessibility without having to resort to a synchrotron source. However, it is not possible to obtain spectra of individual infected cells with the FPA because of the inherent limitations of a globar source and numerical aperture of the Cassegrain objective; thus, a spatial resolution closer to 12−15 μm is achieved rather than the 5.5 μm that might be expected from the pixel size. With the improvement of globar sources and microscope optics it may be possible to achieve single-cell spatial resolution using an FPA in the near future.

PCA analysis was applied to synchrotron FT-IR second-derivative spectra from control and *P. falciparum*-infected cells to assess spectral covariance across a subpopulation of cells. Figure 4A shows a clear separation in the scores plot of controls (0) and trophozoite (T)-infected cells along PC1, while Figure 4B shows the loadings plot for PC1. The PCA loadings plot (Figure 4B) displays strong negative loadings associated with vibrational modes of Hz located at 1712 and 1211 cm^{-1}. The ester carbonyl band from lipid moieties is also a strong negative loading at 1740 cm^{-1}. Strong positive loadings from the vibrational modes of amide I (1650 cm^{-1}) and amide II (1537 cm^{-1}) of proteins from hemoglobin are also strong contributors to the separation along PC1 in the scores plot (Figure 4A). The strong positive and negative loadings for both amide I and amide II are characteristic of different protein types and concentrations between the controls and infected cells. The explained variance for PC1 is 51% followed by 10% for PC2. The loadings plot is similar in appearance to the difference spectrum (Figure 3) calculated by subtracting the average control spectrum from the average trophozoite-infected RBC spectrum. Figure 5 depicts synchrotron FT-IR average baseline-corrected raw spectra from 30 single RBCs infected at various stages of the *P. falciparum* parasite's life cycle including the early ring stage, trophozoite, and schizont stages and for comparison the spectrum of uninfected (control) cells. The spectra, which are vector-normalized between the 3100 and 1000 cm^{-1} spectral range, show distinct and reproducible changes between the different stages. These include an increase in the bands at 2930, 2852, and 1741 cm^{-1} as the parasite matures. These bands are assigned to $\nu_{asym}(CH_2$ acyl chain lipids), $\nu_{sym}(CH_2$ acyl chain lipids), and ester carbonyl stretching vibrations, respectively. This is correlated with an increase in the ester carbonyl band at ~1741 cm^{-1} indicating the changes observed in the C−H stretching region are indeed from lipids. It has previously been hypothesized that as the

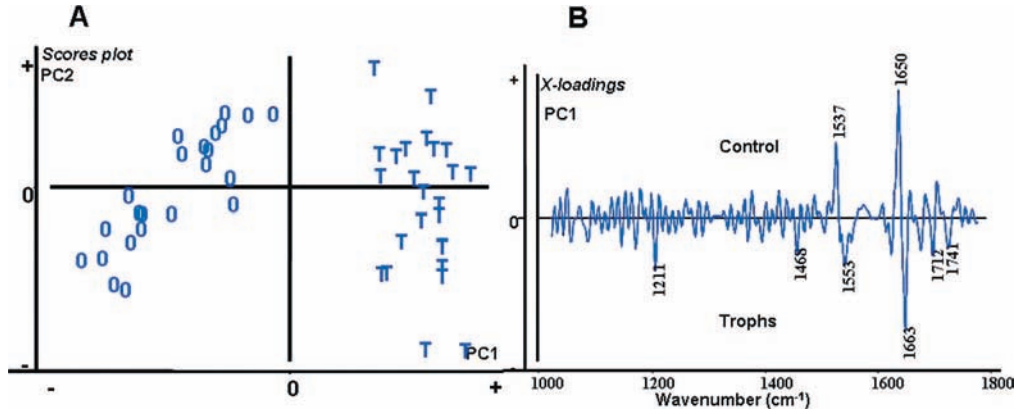

Figure 4. (A) PCA scores plot along PC1 and PC2 of control (0) and trophozoite affected RBC (T) data sets. (B) PCA loadings plot along PC1 of control group and trophozoite-affected cells taken from the PCA scores plot (Figure 3) after a second-derivative function was applied.

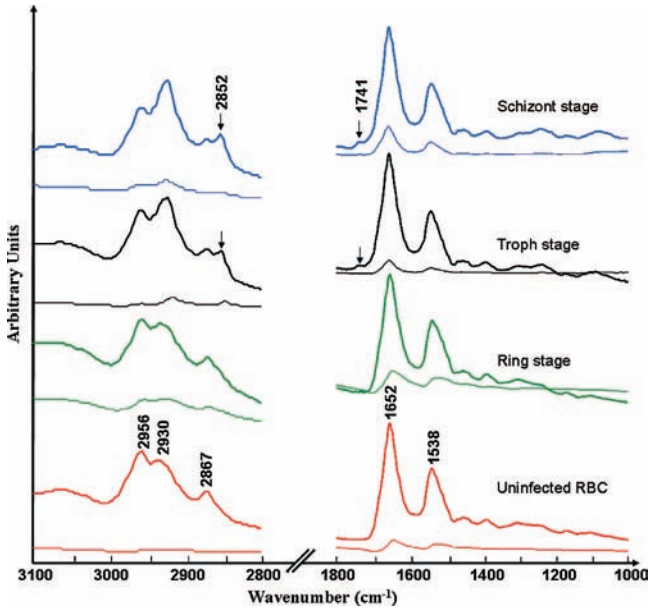

Figure 5. FT-IR averaged normalized spectra of the C−H stretching region and fingerprint region from the Australian Synchrotron of RBCs (control) and the three stages of the parasitic lifecycle (ring, trophozoite, and schizont) within a fixed RBC. Standard deviation spectra are shown below each spectrum for both spectral regions.

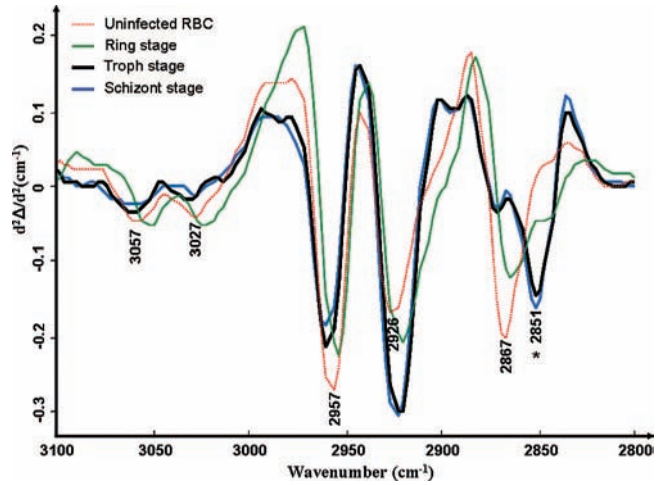

Figure 6. Average second-derivative spectra for infected RBCs (ring, trophozoite, and schizont stage parasites) and uninfected RBCs (control) of the C−H stretching region. (The asterisk indicates the appearance of a lipid band.)

parasite matures and digests hemoglobin, the heme biomineral formed in its DV is engulfed in a lipid nanosphere.[13] As the heme crystal grows within the lipid nanosphere[13] longer chain fatty acids are thought to surround the growing crystal. Figure 6 shows the second-derivative spectra of the C−H stretching region from lipids in the DV of infected RBCs at different stages of the *P. falciparum* parasite intraerythrocytic cycle. The features in this spectral range for the control spectrum include weak bands at 3057 and 3027 cm^{-1}. These bands are assigned to aromatic C−H stretching vibrations of monosubstituted benzenes from amino acid side chains present in hemoglobin.[48,49] In addition, the bands at 2957, 2926, and 2867 cm^{-1} are from $\nu_{asym}(CH_3)$, $\nu_{asym}(CH_2)$, and $\nu_{sym}(CH_3)$ vibrational modes of amino acid side chains, respectively.[31] There is an apparent change in the ratio (or peak position) between the 2867 and 2851 cm^{-1} band in the spectrum (Figure 6) of the ring stage parasites compared to the later stages. From a purely spectroscopic viewpoint, it is tempting to ascribe this change in peak position to be from an increase in concentration of branching in the aliphatic fatty acid side chain and a change in the lipid environment. However, the differences in peak position in the second-derivative spectra are more likely due to the change in slope of the spectral curve; hence, the peak intensities vary based on bandwidth of the raw spectra rather than concentration. Pisciotta et al.[13] have previously demonstrated a lipid association with Hz formation through the use of TEM as part of a broader study to investigate the crystallization of heme in infected erythrocytes. The images at the early stage of the parasite's lifecycle show small heme crystals surrounded by neutral lipid spheres inside the DV compared to a thinner rim of lipids that surrounded a much larger heme crystal at the later trophozoite stage.[13] Fitch et al.[9] showed that unsaturated monoacylglycerols incubated with hematin are the most effective promoters of FePPIX polymerization, whereas saturated lipids are incapable of promoting β-hematin crystal growth in vitro.

(48) Ramaswamy, S.; Rajaram, R. K.; Ramakrishnan, V. *J. Raman Spectrosc.* **2002**, *33*, 689–698.
(49) Cao, X.; Fischer, G. *J. Mol. Struct.* **2000**, *519*, 153–163.

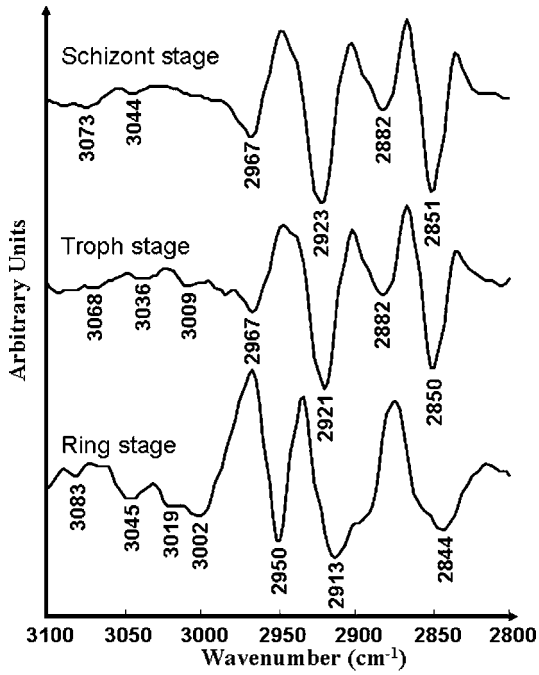

Figure 7. Difference spectrum of the average second-derivative spectra for infected RBCs (ring, trophozoite, and schizont stage parasites) minus average second-derivative spectra of uninfected RBCs (control).

Counter to this finding, electrospray ionization tandem mass spectrometry (ESI-MS/MS) identified the saturated lipids monostearic glycerol (MSG) and monopalmitic glycerol (MPG) present in the parasite's DV, which when combined associate with Hz at a ratio of approximately 2:1.[13] In addition, Jackson et al.[10] present lipid analysis data that indicate di- and triacylglycerols make up these neutral lipid spheres. They hypothesized that these spheres are storage compartments for lipid intermediates during phospholipid digestion in the parasite's DV.[10] Figure 7 shows the difference spectrum for each stage of the parasite's lifecycle calculated within the C−H spectral range (3100−2800 cm^{-1}) from the average spectra presented in Figure 6. The features in the difference spectra (Figure 7) show a number of bands associated with a change in the type of unsaturated fatty acids and the formation of saturated fatty acid chains within the DV of the maturing parasite. The ring stage spectrum shows bands at 3002 and 3019 cm^{-1} associated with cis unsaturated fatty acids. There are also bands at 3036 and 3068 cm^{-1}. From a purely spectroscopic viewpoint it is tempting to assign these bands to trans fatty acids based on lipid model compounds;[50−53] however, to date there is no evidence for trans fatty acids in *P. falciparum*. Ferreri et al.[54] have recently shown that radical chemistry can lead to the formation of trans fatty acids; however, this is not likely the case here. These difference band features are more likely to be due to changes in the aromatic C−H stretching vibrations of the amino acid side chains through digestion of Hb by the parasite. The difference spectrum of the schizont stage shows no evidence of bands associated with a cis conformation of unsaturated lipids and therefore suggests an increase in saturated fatty acids. The methyl and methylene C−H band shifts and an increase in its intensity suggests that the lipid environment surrounding the Hz crystal changes significantly. These changes could be accounted for by a change in the length of fatty acid side chains present in the lipid as the parasite matures.

Figure 8a shows a scores plot based on a PCA performed on all intraerythrocytic stages and the control collectively from decomposing the C−H (3100−2800 cm^{-1}) stretching region. The scores plot shows a separation mainly along PC1 between the three different stages with the schizonts (S) separating furthest away from the control group, followed by the trophozoites (T) and then the rings (R), which in turn cluster very close to the controls with some degree of separation along PC2. The explained variance for PC1 is 68% and 6% for PC2. The loadings plot in Figure 8b displays strong negative loadings, which indicate the variance along PC1 in the infected cells is due to a change in lipid concentration or composition. These changes are evident in the 2921 and 2851 cm^{-1} bands associated with the asymmetric and symmetric methylene C−H stretches from acyl chain lipids. Figure 8c shows strong positive loadings along PC2 at 2962, 2931, 2874, and 2856 cm^{-1}, which are associated with bands from the lipid environment surrounding the Hz crystal. However, these bands have little significance in the separation of infected cells due to the low explained variance of PC2.

Table 1 shows sensitivity and specificity measures for the detection of parasite infection obtained from three ANNs trained on the three different spectral windows. The C−H and fingerprint regions selected together gave the highest sensitivity and specificity. Table 2 shows classification accuracy of all infected stages compared to control. The combined C−H and fingerprint regions produced the highest accuracy with 100% accuracy being achieved for all three infected stages. The ANN was able to classify rings from controls, whereas PCA was unable to clearly separate the two groups on the scores plot observed in Figure 8a. Presumably, the ANN models out performed the PCA because unlike PCA, ANNs are able to exploit nonlinear relations within the data set.

An early study by Slater et al.[5] presented the first FT-IR spectrum of Hz using a conventional FT-IR spectrometer. After sonication of *P. falciparum*-infected RBCs and purification of the resultant Hz pellet the FT-IR spectrum of the Hz was found to be spectroscopically identical to its synthetic analogue β-hematin. Furthermore Wood et al.[55] have previously spectroscopically detected Hz in live parasites using near-IR resonance Raman spectroscopy and compared this with the Raman spectrum of β-hematin. Although this last study showed the presence of Hz in infected erythrocytes using Raman spectroscopy, no study has yet shown the presence of Hz in infected RBCs using FT-IR spectroscopy. We have demonstrated that synchrotron FT-IR spectroscopy in combination with multivariate methods can detect the presence of Hz in single infected RBCs. The technique can also be used to differentiate between the three stages of the parasitic lifecycle based on fatty acid composition within the DV

(50) Shukla, N.; Svedberg, E. B.; Ell, J. *Colloids Surf., A* **2007**, *301*, 113–116.
(51) Sinclair, R. G.; Mckay, A. F.; Myers, G. S.; Jones, R. N. *J. Am. Chem. Soc.* **1952**, *74*, 2578–2585.
(52) Lee, D. H.; Condrate, R.; Lacourse, W. C. *J. Mater. Sci.* **2000**, *35*, 4961–4970.
(53) Vogel-Weill, C.; Gruger, A. *Spectrochim. Acta., Part A* **1996**, *52*, 1737–1755.
(54) Ferreri, C.; Panagiotaki, M.; Chatgilialoglu, C. *Mol. Biotechnol.* **2007**, *37*, 19–25.
(55) Wood, B. R.; Langford, S. J.; Cooke, B. M.; Glenister, F. K.; Lim, J.; McNaughton, D. *FEBS Lett.* **2003**, *554*, 247–252.

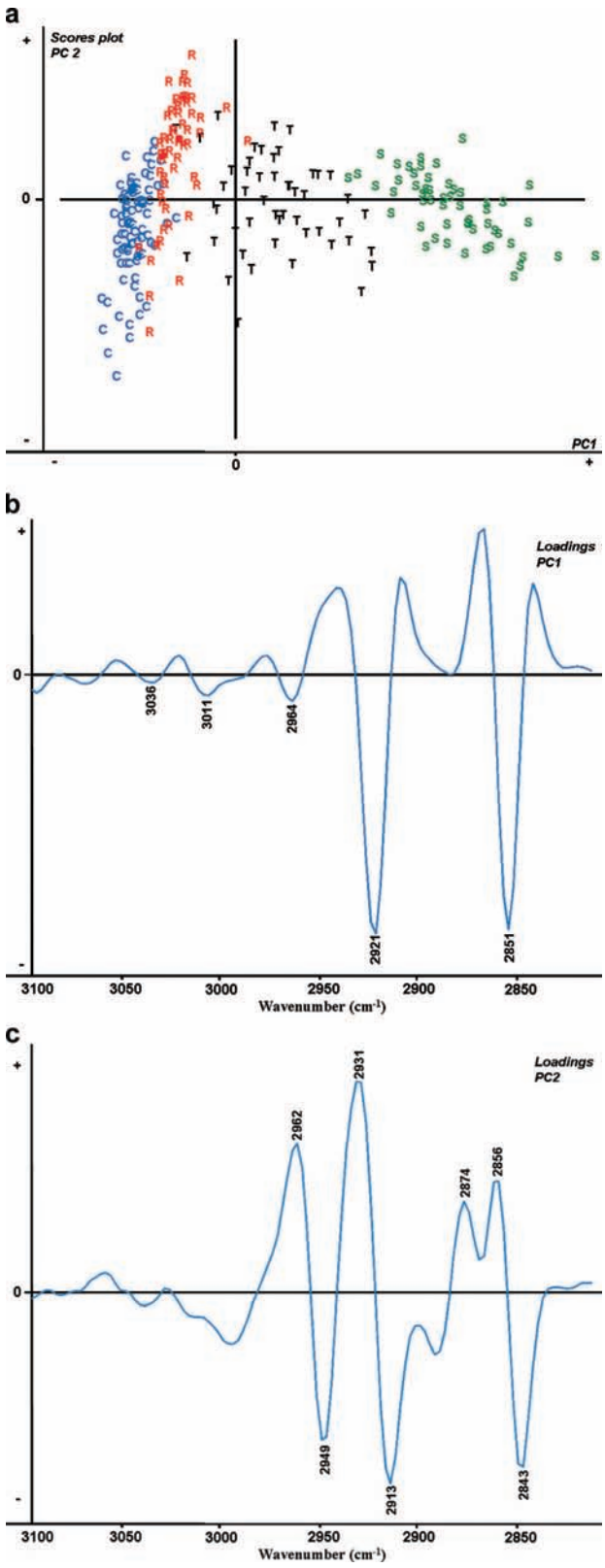

Figure 8. (a) PCA scores plot of the C−H stretching region along PC1 and PC2 of control (0) and all three stages of infection (ring (R), trophozoite (T), and schizont (S)) with RBCs. (b) PCA loadings plot of the C−H stretching region along PC1 of control (0) and all three stages of infection (ring, trophozoite, and schizont) within RBCs after a second-derivative function was applied. (c) PCA loadings plot of the C−H stretching region along PC2 of control (0) and all three stages of infection (ring, trophozoite, and schizont) within RBCs after a second-derivative function was applied.

Table 1. Artificial Neural Network (ANN) Sensitivities and Specificities of Infected and Uninfected RBCs for the Three Spectral Ranges Trialed

spectral range (cm^{-1})	3100−2800, 1800−1000	3100−2800	1800−1000
sensitivity (%)	100	93	99
specificity (%)	92	88	91

Table 2. Artificial Neural Network (ANN) Accuracies for Correctly Classifying Control, Rings, Trophozoites, and Schizonts for the Three Spectral Ranges Trialed

spectral range (cm^{-1})	3100−2800, 1800−1000	3100−2800	1800−1000
control	92	88	91
rings	100	79	96
trophozoites	100	96	100
schizonts	100	92	100

of infected erythrocytes. This provides a fundamental insight into the biochemistry of lipid within the maturing parasite. It shows that besides the morphological differences observed between the intraerythrocytic life cycle stages of the parasite there are specific changes in lipid composition that give rise to a very specific lipid signature in the 3100−2800 cm^{-1} region of the mid-IR spectrum.

Bright-field microscopy has been the standard for malaria diagnosis since the discovery of the disease in 1880. The technique has a number of advantages, the main one being the ability to quantify and identify the parasites at different stages of the parasite's life cycle. With this information it is possible to work out a treatment regime specific for the patient. However, microscopy also has several disadvantages, the major one being that it is subjective and requires experienced personnel to make the diagnosis. Rapid diagnostic tests (RDTs) also known as "dipsticks", provide an alternative to microscopy. RDTs make use of a capture antibody and conjugated detection antibody to detect malarial antigen in blood samples. The advantages of this approach include the rapid turnaround time and the simplicity of use, which allow clinicians to make on-the-spot diagnoses. However, quantification of infected parasites with RDTs is not possible at this time, which is important as knowledge of the parasite number often determines the therapeutic approach. Although the sensitivity is good (40 parasites/μL of blood), the cost of dipsticks has limited their use in the developing world where these tests are needed. Laser desorption mass spectrometry (LD-MS) is able to detect Hz to a sensitivity of 100−1000 parasites/μL of blood, roughly similar to routine microscopy. However, the technique relies on the presence of Hz, and therefore early ring stages of the parasite would elude detection with this approach. Raman microscopy also shows potential as a diagnostic for malaria. However, like LD-MS it currently relies on the detection of Hz in the cells, and consequently at present the technique has only been shown to detect later stages of the parasites life cycle.

Finding inexpensive, sensitive, and rapid methods for malaria diagnosis, which require minimal training for the technician, would have a major impact on malaria management. In this context FT-IR spectroscopy may offer several advantages compared to these other techniques in the foreseeable future. These include (1) the ability to detect all stages of the parasite's life cycle including the early ring stage prior to Hz formation, (2) unambiguous nonsub-

jective diagnosis based on neural network spectral pattern recognition, (3) although the instrumentation is currently expensive the actual cost per test is very cheap especially if one uses inexpensive IR substrates such as Kevley slides, and (4) the technique has a sensitivity of 1 parasite/μL of blood on a thin film when using a synchrotron source.

Of course a synchrotron source is not suited for a clinical environment, but with the continued development of confocal micro-FT-IR imaging spectrometers with powerful globar sources, improved sensitivity FPA detectors, and new advances in computational algorithms for diagnosis, one can envisage FT-IR spectroscopy becoming a new weapon in the fight against malaria. These results lay the foundation for the future development of an IR-based technology that would be rapid, nonsubjective, and may one day not be dependent on the brightness of a synchrotron source to obtain the required spatial resolution for high-performance single-cell spectroscopy.

ACKNOWLEDGMENT

This work is supported by an Australian Research Council Discovery Grant. Dr. Bayden Wood was supported by an Australian Synchrotron Research Fellow Grant and a Monash Synchrotron Research Fellowship. We thank the IR beamline scientist Dr. Ljiljana Puskar from the Australian Synchrotron for FT-IR beamtime and experimental support. Katherine de Villiers was supported by an Equity Development Program scholarship of the Department of Chemistry, University of Cape Town. Support (Timothy Egan and Katherine de Villiers) also came from the National Research Foundation under Grant No. 2061833 and the Medical Research Council of South Africa.

Received for review October 31, 2008. Accepted February 9, 2009.

AC802291A

Monash University

Monash Research Graduate School

Declaration for Thesis Chapter 3

Declaration by candidate

In the case of Chapter 3 the nature and extent of my contribution to the work (**Paper II**) was the following:

Nature of contribution	Extent of contribution (%)
Experimental design, interpretation of results, proof reading the manuscript	10%

The following co-authors contributed to the work. Co-authors who are students at Monash University must also indicate the extent of their contribution in percentage terms:

Name	Nature of contribution	Extent of contribution (%) for student co-authors only
Inna Solomonov	Interpretation of results, experimental design, drafting of manuscript	-
Maria Osipova	Interpretation of results, drafting of manuscript	-
Yishay Feldman	Interpretation of results, drafting of manuscript	-
Carsten Baehtz	Synchrotron experimental support	-
Kristian Kjaer	Drafting of manuscript	-
Ian Robinson	Experimental support, interpretation of results, drafting of manuscript	-
Don McNaughton	Drafting of manuscript, provided supervision and leadership	-
Bayden Wood	Drafting of manuscript, provided supervision and leadership	-
Isabelle Weissbuch	Interpretation of results, drafting of manuscript	-
Leslie Leiserowitz	Interpretation of results, provided leadership, drafting of manuscript	-

Candidate's Signature	[redacted]	Date
		15/04/09

Declaration by co-authors

The undersigned hereby certify that:

(1) the above declaration correctly reflects the nature and extent of the candidate's contribution to this work, and the nature of the contribution of each of the co-authors.

(2) they meet the criteria for authorship in that they have participated in the conception, execution, or interpretation, of at least that part of the publication in their field of expertise;

(3) they take public responsibility for their part of the publication, except for the responsible author who accepts overall responsibility for the publication;

(4) there are no other authors of the publication according to these criteria;

(5) potential conflicts of interest have been disclosed to (a) granting bodies, (b) the editor or publisher of journals or other publications, and (c) the head of the responsible academic unit; and

(6) the original data are stored at the following location(s) and will be held for at least five years from the date indicated below:

Location(s)	
	Department of Chemistry, Centre for Biospectroscopy, Monash University, Clayton
	Department of Materials and Interfaces, The Weizmann Institute of Science.
	Chemical Research Support, The Weizmann Institute of Science.
	Hasylab at DESY.
	Niels Bohr Institute, University of Copenhagen.
	Department of Physics and London Centre for Nanotechnology, University College.

Please note that the location(s) must be institutional in nature, and should be indicated here as a department, centre or institute, with specific campus identification where relevant.]

Signature	Date
Dr B. R. Wood (Monash Uni)	15/4/09
[redacted]	15/4/09
	15/4/09
	15/4/09
	15/4/09
	15/4/09
	15/4/09
	15/4/09

On behalf of all co-authors Dr Bayden Wood will sign due to the unavailability of co-authors at this point in time.

[redacted]	15/4/09
[redacted]	15/4/09
[redacted]	15/4/09

J|A|C|S
ARTICLES
Published on Web 02/10/2007

Crystal Nucleation, Growth, and Morphology of the Synthetic Malaria Pigment β-Hematin and the Effect Thereon by Quinoline Additives: The Malaria Pigment as a Target of Various Antimalarial Drugs

Inna Solomonov,[†] Maria Osipova,[†] Yishay Feldman,[‡] Carsten Baehtz,[§] Kristian Kjaer,[||] Ian K. Robinson,[⊥] Grant T. Webster,[#] Don McNaughton,[#] Bayden R. Wood,[#] Isabelle Weissbuch,*[,†] and Leslie Leiserowitz*[,†]

Contribution from the Department of Materials and Interfaces, The Weizmann Institute of Science, 76100-Rehovot, Israel, Chemical Research Support, The Weizmann Institute of Science, 76100-Rehovot, Israel, Hasylab at DESY, Notkestrasse 85, D-22607 Hamburg, Germany, Niels Bohr Institute, University of Copenhagen, Universitetsparken 5, DK-2100 Copenhagen, Denmark, Department of Physics and London Centre for Nanotechnology, University College, Gower Street, London WC1E 6BT, England, and Centre for Biospectroscopy and School of Chemistry, Monash University, 3800 Victoria, Australia

Received October 17, 2006; E-mail: isabelle.weissbuch@weizmann.ac.il; leslie.leiserowitz@weizmann.ac.il

Abstract: The morphology of micrometer-sized β-hematin crystals (synthetic malaria pigment) was determined by TEM images and diffraction, and by grazing incidence synchrotron X-ray diffraction at the air−water interface. The needle-like crystals are bounded by sharp {100} and {010} side faces, and capped by {011} and, to a lesser extent, by {001} end faces, in agreement with hemozoin (malaria pigment) crystals. The β-hematin crystals grown in the presence of 10% chloroquine or quinine took appreciably longer to precipitate and tended to be symmetrically tapered toward both ends of the needle, due to stereoselective additive binding to {001} or {011} ledges. Evidence, but marginal, is presented that additives reduce crystal mosaic domain size along the needle axis, based on X-ray powder diffraction data. Coherent grazing exit X-ray diffraction suggests that the mosaic domains are smaller and less structurally stable than in pure crystals. IR-ATR and Raman spectra indicate molecular based differences due to a modification of surface and bulk propionic acid groups, following additive binding and a molecular rearrangement in the environment of the bulk sites poisoned by occluded quinoline. These results provided incentive to examine computationally whether hemozoin may be a target of antimalarial drugs diethylamino-alkoxyxanthones and artemisinin. A variation in activity of the former as a function of the alkoxy chain length is correlated with computed binding energy to {001} and {011} faces of β-hematin. A model is proposed for artemisinin activity involving hemozoin nucleation inhibition via artemisinin−β-hematin adducts bound to the principal crystal faces. Regarding nucleation of hemozoin inside the digestive vacuole of the malaria parasite, nucleation via the vacuole's membranous surface is proposed, based on a reported hemozoin alignment. As a test, a dibehenoyl-phosphatidylcholine monolayer transferred onto OTS−Si wafer nucleated far more β-hematin crystals, albeit randomly oriented, than a reference OTS−Si.

Introduction

Malaria, a tropical disease caused by protozoan parasites of the genus *Plasmodium*, has been a primary concern to humanity for centuries and is now extended to more than 40% of the world's population. *Plasmodium falciparum*, the most prevalent species across the globe, is often fatal to humans. During its life stages within the red blood cell, the malaria parasite degrades host hemoglobin as a major source of amino acids. During this proteolysis in an acidic digestive vacuole, free heme, ferriprotoporphyrin IX (Figure 1a), which is toxic to the parasite, is released. But the heme is converted into a crystalline compound called malaria pigment or hemozoin that is harmless to the parasite.

This crystalline product is isostructural[1] with the synthetic phase β-hematin, the crystal structure of which has been solved from its synchrotron X-ray diffraction powder pattern by Bohle and co-workers.[2] The crystal structure, which had previously been assumed to be built of polymeric chains,[3] was shown to be centrosymmetric, space group $P\bar{1}$, consisting of propionate-

[†] Department of Materials and Interfaces, The Weizmann Institute of Science.
[‡] Chemical Research Support, The Weizmann Institute of Science.
[§] Hasylab at DESY.
[||] Niels Bohr Institute, University of Copenhagen.
[⊥] Department of Physics and London Centre for Nanotechnology, University College.
[#] Centre for Biospectroscopy and School of Chemistry, Monash University.

(1) Oliveira, M. F.; Kycia, S. W.; Gomez, A.; Kosar, A. J.; Bohle, D. S.; Hempelmann, E.; Menezes, D.; Vannier-Santos, M. A.; Oliveira, P. L.; Ferreira, S. T. *FEBS Lett* **2005**, *579*, 6010.

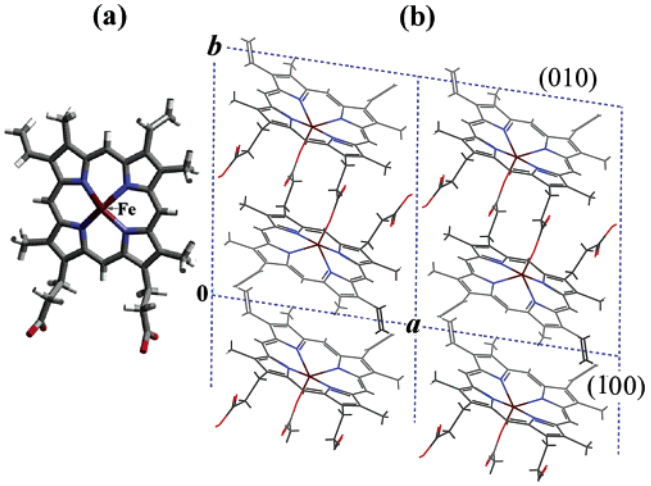

Figure 1. (a) The heme molecular structure. (b) Crystal structure of β-hematin, which consists of molecular heme dimers, viewed along the *c*-axis. The (100) and (010) faces are labeled.

linked (Fe−O−C(═O)CH_2CH_2−) reciprocal head-to-tail cyclic heme dimers interlinked via O−H···O═C hydrogen-bonded cyclic pairs forming chains aligned parallel to the axial direction $a-c$ (Figure 1b). This crystal structure led Bohle et al.[2] to propose, in keeping with previous similar suggestions,[4,5] that antimalarial quinoline-type drugs act by binding to hemozoin crystal faces, which would inhibit their growth and result in a buildup of the toxic heme and thus lead to the death of the parasite. However, no information on the crystal surface binding site was provided, nor details on the habit and {*h*,*k*,*l*} faces of the micrometer-sized hemozoin or β-hematin crystals, in terms of the crystal structure.

By making use of the crystal structure of β-hematin, we have reported its theoretical growth morphology[6] (Figure 2a) which has been shown to be similar in habit and form to that of several reported specimens of hemozoin.[7] A model of binding quinoline drugs to the fast-growing highly corrugated {001} face of hemozoin, shown in Figure 2b for binding of chloroquine, was also determined by theoretical methods,[6] but direct experimental evidence of this binding site was still absent.

The mode of action of quinoline-containing drugs and recently developed resistance to commonly used quinolines by malaria parasites has been recently reviewed by Bray et al.[8] Indeed, it is this resistance, made manifest by reduced drug accumulation in the food vacuole that has motivated the need for a fuller understanding of the mode of action of quinoline drugs and the development of new, effective antimalarial drugs.

Here we describe experiments to glean information on the crystal nucleation process of β-hematin. We use as a basis the fact that the β-hematin molecular dimer is a bolaform amphiphile, the observation that β-hematin crystal formation can be enhanced by the presence of lipids,[9] and the report by Goldberg and co-workers[10] of aligned parallelepiped crystals of hemozoin formed in the digestive vacuole of *Plasmodium falciparum*. It is well-established that crystalline monolayers of amphiphilic molecules induce oriented nucleation of molecular crystals at the amphiphilic−aqueous solution interface by virtue of structural complementarity between the head groups of the monolayer and the layer arrangement within the to-be-nucleated crystal. Thus, we examined the nucleation behavior of β-hematin crystals at an air−water interface and at the interface between a phospholipid monolayer on solid support and a chloroform solution. We present here a characterization of the β-hematin crystal morphology obtained from different solvents in relation to its crystal structure, as well as observed changes in the morphology, time of precipitation, and a possible reduction in domain size of crystals grown in the presence of quinine and chloroquine additives. Experimental evidence in favor of the binding of the quinoline to β-hematin at the surface of the growing crystal is also presented. Various experimental techniques, described in the Supporting Information (SI), were applied to obtain the above information, including grazing incidence X-ray diffraction (GIXD), electron diffraction (ED), transmission electron microscopy (TEM) images, synchrotron X-ray powder diffraction (XRPD), coherent grazing exit synchrotron X-ray scattering, micro-Raman spectroscopy, and IR attenuated total reflectance (ATR) micro-imaging spectroscopy. Micro-Raman and IR-ATR spectroscopies have recently been used to understand the electronic structure of β-hematin and hemozoin in whole red blood cells[11] and are shown to be a useful way of monitoring heme aggregation through specific marker bands in human red blood cells.[12]

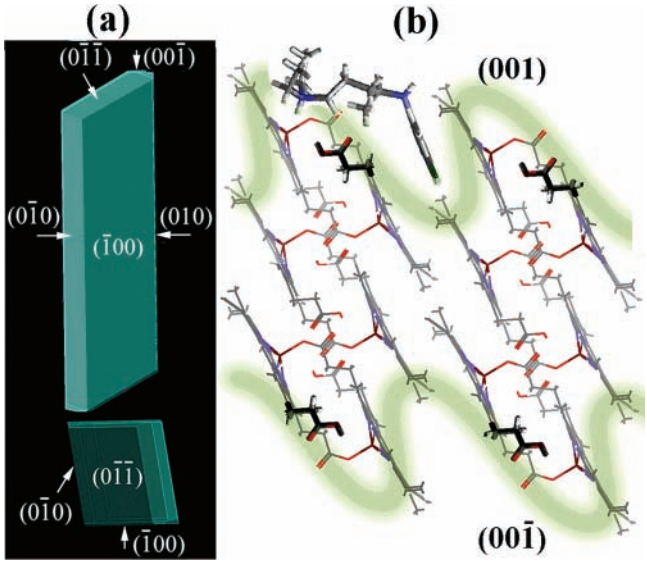

Figure 2. (a) Theoretical growth form of β-hematin viewed: (top) perpendicular to the {100} face, (bottom) along the *c*-axis; (b) corrugated {001} faces of β-hematin, at which adsorption of quinoline drugs has been proposed, as shown for chloroquine bound to the (001) face.[6]

(2) Pagola, S.; Stephens, W. P.; Bohle, D. S.; Kosar, A. D.; Madsen, S. K. *Nature* **2000**, *404*, 307.
(3) Slater, A. F. G.; Swiggart, W. J.; Orton, B. R.; Flitter, W. D.; Goldberg, D. E.; Cerami, A.; Henderson, G. B. *Proc. Natl. Acad. Sci. U.S.A.* **1991**, *88*, 325.
(4) Sullivan, D. J.; Gluzman, I. Y.; Russell, D. G.; Goldberg, D. E. *Natl. Acad. Sci. U.S.A.* **1996**, *93*, 11865.
(5) Sullivan, D. J.; Matile, H.; Ridley, R. G.; Goldberg, D. E. *J. Biol. Chem.* **1998**, *273*, 31103.
(6) Buller, R.; Peterson, M. L.; Almarsson, O.; Leiserowitz, L. *Cryst. Growth Des.* **2002**, *2*, 553−562.
(7) Chen, M. M.; Shi, L.; Sullivan, D. J. *Mol. Biochem. Parasitol.* **2001**, *113*, 1.
(8) Bray, P. G.; Ward, S. A.; O'Neill, P. M. *Drugs, Disease and Post-genomic Biology, Current Topics in Microbiology and Immunology*; Springer-Verlag: Berlin, Heidelberg, 2005; Vol. 295.
(9) Fitch, C. D.; Cai, G. Z.; Shen, Y. F.; Shoemaker, J. D. *Biochim. Biophys. Acta* **1999**, *1454*, 31.
(10) Goldberg, D. E.; Slater, A. F. G.; Cerami, A.; Henderson, G. B. *Proc. Natl. Acad. Sci. U.S.A.* **1990**, *87*, 2931−2935.
(11) Wood, B. R.; Langford, S. J.; Cooke, B. M.; Lim, J.; Glenister, F. K.; Duriska, M.; Unthank, J. K.; McNaughton, D. *J. Am.. Chem. Soc.* **2004**, *126*, 9233−9239.

Chart 1. Generalized Structure of 3,6-Bis-ω-*N*,*N*-diethylamino-alkoxyxanthones, Labeled XN*n*, where *n* is the Number of CH_2 Groups

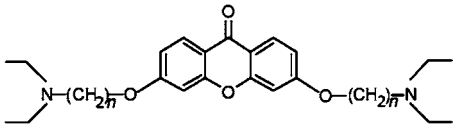

Next we examine by computational means the possibility of hemozoin nucleation/growth inhibition as an important factor in the antimalarial activity of drugs other than quinolines, focusing on diethylamino-alkoxyxanthones and artemisinin. The binding properties of 3,6-bis-ω-diethylamino-alkoxyxanthones (Chart 1) to the surface crystal structure of β-hematin are examined in terms of the antimalarial activity of the drug, which belongs to a novel class of antimalarial compounds with activity against multidrug-resistant *Plasmodium* parasites, reported by Riscoe and co-workers.[13,14]

These compounds, labeled XN*n*, where *n* is the number of CH_2 groups per chain ranging from 2 to 8 (except $n = 7$), form soluble complexes with heme and prevent the precipitation of heme in aqueous solution under the mildly acidic conditions of the parasitic digestive vacuole at pH = 5.2. A strong correlation was found between the heme affinity (K_a) measured in aqueous solution, the alkoxy chain length, and antimalarial potency,[13] shown in Figure S1of the SI. The two most active compounds in the series, $n = 5$ and 6, exhibited low nanomolar 50% inhibitory concentration (IC_{50}) values against strains of chloroquine-susceptible and multidrug-resistant *Plasmodium falciparum* in vitro.

Finally, we consider inhibition of crystal nucleation/growth of hemozoin as a possible mode of action to account for the widely used antimalarial drug, artemisinin, extracted from an ancient Chinese herbal remedy, *Artemisia annu* (sweet wormwood or "qinghao"). Artemisinin and its derivatives (Chart 2a), being highly active against multidrug-resistant strains of malaria parasite, have attracted much attention; the mechanisms of action, resistance, and toxicity have been recently reviewed by Meshnick[15] and by Bray et al.[8] The reactivity of the peroxide function of artemisinin has been considered as the primary factor of the pharmacological activity. A key finding is that artemisinin cannot be cyclically oxidized and reduced; only one free radical can result from one drug molecule, which has a selective toxic effect at very low concentrations. The selective toxicity of artemisinin may arise from alkylation of the heme leading to heme−artemisinin-derived covalent adducts. Heme−artemisinin adducts have been demonstrated in parasite cultures treated with therapeutic concentrations of artemisinin derivatives.[16] Artemisinin forms covalent bonds with heme when incubated in a cell-free solution, and these same artemisinin−heme adducts appear to form in artemisinin-treated parasites. At micromolar concentrations, artemisinin inhibits hemoglobin digestion by malaria parasites and inhibits hemozoin formation, but this has only been demonstrated in cell-free conditions.[17] The structure

Chart 2. (a) Molecular Structure of Artemisinin, and Two Derivatives; (b) alkylation of Iron(II)−Heme by Artemisinin; in these Heme−Artemisinin Adducts the Substitution May Occur at α, β (as shown), γ, or δ Positions, Yielding Products AαH, AβH, AγH, and AδH, Respectively, where A Represents an Artemisinin Moiety Covalently Bound to a Heme H via Sites α, β, γ, δ

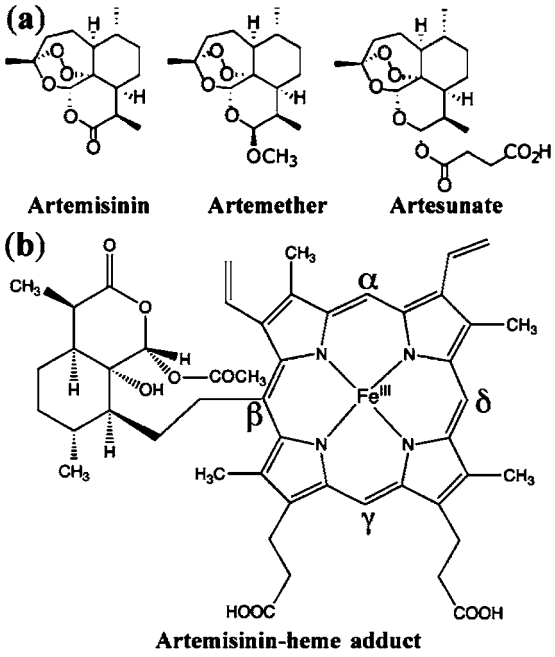

of an artemisinin−porphyrin adduct has been characterized by Meunier and co-workers,[18] following activation of the peroxide function of artemisinin by iron(II)−heme generated in situ from iron(III)−protoporphyrin-IX and glutathione, a biologically relevant reductant. It was found that under mild conditions, such a reaction produced a high yield (85%) of heme derivatives alkylated at α, β, γ, and δ positions by a C4-centered radical derived from artemisinin (Chart 2b), where the regioselectivity at the α, β and δ positions were about the same at 28% on average. The relatively low yield of 13% at the γ-position is presumably due to molecular overcrowding. We shall make use of this structural information to develop a scenario involving hemozoin nucleation inhibition to account for the antimalarial behavior of artemisinin and, as an extension, rationalize the increased antimalarial efficacy when a cocktail of artemisinin and quinoline-type drugs are used in conjunction. We stress, however, that there are various hypotheses on the mechanism of artemisinin-based drug action; besides heme alkylation, a number of other biological targets have been proposed including specific parasite proteins.[8,15]

Results

β-Hematin Crystals at the Air−Water Interface. Little is known on the crystal nucleation of the malaria pigment hemozoin in the digestive vacuole of the malaria parasite. In order to glean some knowledge on the process, albeit indirect, we tried to monitor, by grazing incidence X-ray diffraction (GIXD) using synchrotron radiation, the crystal nucleation of β-hematin (i.e., synthetic hemozoin) in a manner akin to the

(12) Wood, B. R.; Hammer, L.; Davis, L.; McNaughton, D. *J. Biomed. Opt.* **2005**, *10*, 014005/1−01400.5/13.
(13) Kelly, J. X.; Winters, R.; Peyton, D. H.; Hinrichs, D. H.; Riscoe, M. *Antimicrob. Agents Chemother.* **2002**, *46*, 144−150.
(14) Riscoe, M.; Kelly, J. X.; Winter, R. *Curr. Med. Chem.* **2005**, *12*, 2539.
(15) Meshnick, S. H. *Int. J. Parasitol.* **2002**, *32*, 1655−1660.
(16) Hong, Y. L.; Yang, Y. Z.; Meshnick, S. R. *Mol. Biochem. Parasitol.* **1994**, *63*, 121−128.
(17) Pandey, A. V.; Tekwani, B. L.; Singh, R. L.; Chauhan, V. S. *J. Biol. Chem.* **1999**, *274*, 19383.
(18) Robert, A.; Coppel, Y.; Meunier, B. *Chem. Comm.* **2002**, 414−415.

way adopted in following the crystal nucleation of the amphiphile cholesterol from one to three bilayers at the air−water interface.[19] The idea was to take advantage of the fact that the molecular dimeric structure of β-hematin (Figure 1b), the basic building block of the crystal, may be regarded as a bolaform amphiphile and so might form crystalline multilayers at the air−water interface.[20]

When a fresh solution, which contained hemin (chloro(protoporphyrinato)iron(III)) and 2,6-lutidine in chloroform (see experimental details in SI), was spread on water, formation of β-hematin crystals was not detected on examination of the film at the liquid surface by GIXD even after 24 h, nor by FTIR after transfer to solid support. The result remained unchanged when the phospholipid dipalmitoylphosphatidyl-choline or -ethanolamine (DPPC or DPPE), sufficient for about 15% of a full monolayer coverage, was added to the chloroform solution. By contrast, the bulk solutions, yielded β-hematin nanocrystals only after overnight aging, as determined by FTIR and powder X-ray diffraction measurements. For the nanocrystal characterization, samples were prepared by spreading the aged solution on the water surface of a Langmuir trough followed by transferring the insoluble floating material onto a gold-covered silicon wafer. The FTIR spectra obtained were very similar to those of published data,[21] which showed the characteristic strong and narrow bands at 1206 and 1660 cm^{-1}, indicative of the iron-coordinated C−O and C═O stretching vibrations which are absent in hemin. The X-ray powder diffraction pattern matched that of published data.[2] An aged bulk solution, when spread on the water surface, yielded β-hematin crystals floating mainly on their {100} face, according to GIXD and X-ray reflectivity measurements[20,22−24] of the film measured on water (Figure 3) performed on the liquid surface diffractometer at Hasylab. Along the a^*-direction, namely perpendicular to the plane of the {100} face, the domain size of these floating crystals was found to be in the range between 200 and 450 Å, determined from the widths of several {100} Bragg peaks by application of the Scherrer formula.[25] The {100} Bragg reflection of one sample preparation is shown in Figure 3b.

Induced Nucleation of β-Hematin Crystals by a Dibehenoyl-L-α-phosphatidylcholine (DBPC) Monolayer. A well-compressed monolayer of DBPC on the water surface of a Langmuir trough was transferred by the Langmuir−Schaffer technique onto an OTS−Si wafer (see experimental details in SI). The DBPC−OTS−Si wafer was oriented vertically, together with an OTS−Si wafer used as reference, in a vessel containing a chloroform solution of hemin and 2,6-lutidine. The number of β-hematin crystals formed on the DBPC−OTS−Si wafer was much greater than on the OTS−Si wafer, according to visual inspection. An initial measure of the orientation of the β-hematin crystals was determined by a specular X-ray diffraction $\theta/2\theta$ scan (see SI), sensing only crystallographic planes parallel to the plane of a Si wafer, as shown in Figure 4.

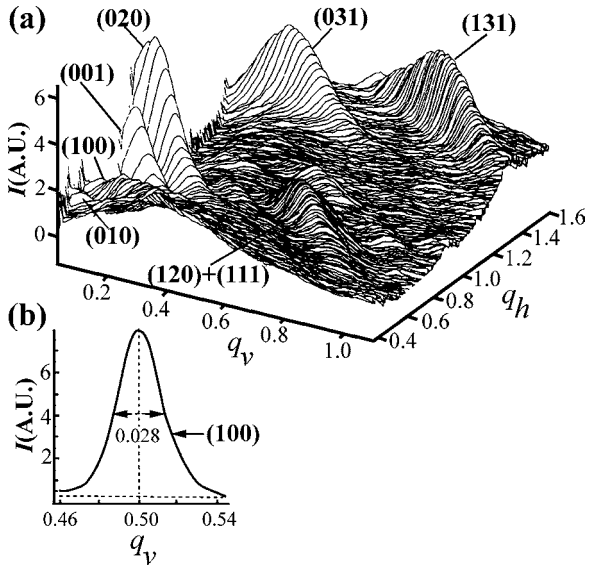

Figure 3. Oriented β-hematin crystallites on the water surface. (a) The GIXD pattern $I(q_h, q_v)$, in which the X-ray scattering vector components q_h and q_v (in $Å^{-1}$) are parallel (i.e., *horizontal*) and perpendicular (i.e., *vertical*) to the water surface respectively. The q_h and q_v values of the various (*h*,*k*,*l*) reflections correspond to β-hematin crystals floating on their *bc* face. This assignment is in agreement with the {100} reflection of β-hematin crystallites obtained from X-ray reflectivity (XR, $q_h \equiv 0$ $Å^{-1}$) measurements depicted in (b). The FWHM of the XR peak (0.028 $Å^{-1}$) corresponds to crystal coherence length L along the direction a^* of 200 Å, applying the Scherrer formula $L = 0.9 \times 2\pi/\text{FWHM}$.[25] Note that the observation of a (100) reflection, albeit very weak, near the horizon ($q_v \approx 0$ $Å^{-1}$) in the GIXD pattern (a) indicates that there is a very small population of crystals floating on their *ac* faces.

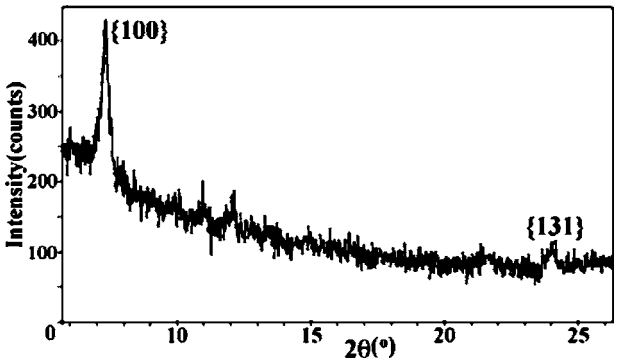

Figure 4. Specular X-ray (wavelength $\lambda = 1.542$ Å) diffraction $\theta/2\theta$ scan probing the orientation of β-hematin crystals nucleated by the exposed polar head groups of a phospholipid DBPC monolayer in contact with an OTS−Si wafer. The {100} and {131} reflections are denoted.

The intense {100} reflection suggests some measure of preferred orientation when comparing the intensities of the {100} and {131} reflections with those of the corresponding reflections in Figure 8c (vide infra), but a pole figure of the {100} reflection showed only a very minor preference for the {100} faces to lie parallel to the surface plane of the DBPC−OTS−Si wafer, the overriding majority of crystals were randomly oriented.

Morphology of Pure β-Hematin Crystals. According to the theoretical growth morphology of β-hematin crystals,[6] in keeping with images of several specimen hemozoin crystals reported by Sullivan and co-workers,[7] the crystals, elongated

(19) Solomonov, I.; Weygand, M. J.; Kjaer, K.; Rapaport, H.; Leiserowitz, L. *Biophys. J.* **2005**, *88*, 1809.
(20) Kuzmenko, I.; Rapaport, H.; Kjaer, K.; Als-Nielsen, J.; Weissbuch, I.; Lahav, M.; Leiserowitz, L. *Chem. Rev.* **2001**, *101*, 1659−1696.
(21) Egan, T. J.; Mavuso, M. W.; Ncokazi, K. K. *Biochemistry* **2000**, *40*, 204−213.
(22) Als-Nielsen, J.; Kjaer, K. In *Proceedings of the Nato Advanced Study Institute, Phase Transitions in Soft Condensed Matter*; Riste, T., Sherrington, D., Eds.; Plenum Press: New York: Geilo, Norway, 1989; Vol. 211, Series B, pp 113−138.
(23) Kjaer, K. *Physica* **1994**, *198*, 100.
(24) Als-Nielsen, J.; Jacquemain, D.; Kjaer, K.; Leveiller, F.; Lahav, M.; Leiserowitz, L. *Phys. Rep.* **1994**, *246*, 251−313.
(25) Guinier, A. *X-ray Diffraction*; Freeman: San Francisco, 1968.

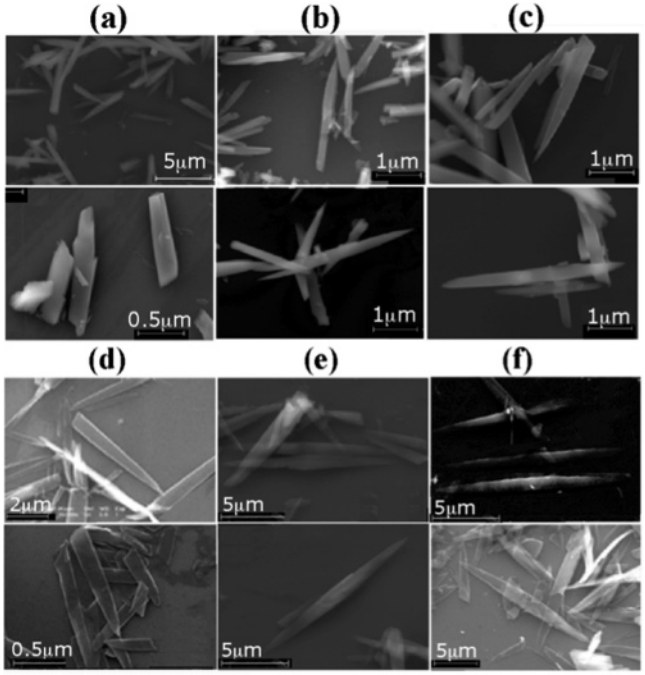

Figure 5. SEM micrographs of β-hematin crystals obtained from: (a−c) MeOH−DMSO and (d−f) $CHCl_3$ solutions. The crystals grown in the absence of the quinolines are shown in (a) and (d); those grown in the presence of 10% quinine and chloroquine are shown in (b, e) and (c, f), respectively.

in the *c*-direction, are delineated by well-developed {100} and {010} side faces and smaller {011} end faces (Figure 2a). In order to experimentally establish this morphology, use was made of TEM images and ED patterns. Here advantage was taken of the small angles between the real (*a*,*b*,*c*) and reciprocal (*a**,*b**,*c**) crystal axes (10°, 8°, 7° respectively) of β-hematin[26] in order to obtain {0*kl*} or {*h*0*l*} diffraction patterns assuming that the crystals would lie on their {100} or {010} faces respectively.

The β-hematin crystals, (grown in MeOH−DMSO[27] or chloroform, see SI), examined by scanning electron microscopy (SEM), appear lath-like in shape, 0.5−10 μm long and 0.05−0.5 μm wide (Figure 5a, d). Several crystals exhibit regular morphologies in keeping with the centrosymmetric $P\bar{1}$ symmetry of the crystal structure. Other crystals tend to be wedge-shaped at one end. We have identified the crystal faces making use of the more regular shaped habit. ED patterns of β-hematin crystals grown in MeOH−DMSO solutions are of the type 0*kl* and *h*0*l* (Figure 6a, b bottom); the corresponding transmission electron microscopy (TEM) images are shown in Figure 6a, b, top. Given the small angles between the real (*a*,*b*,*c*) and corresponding reciprocal (*a**,*b**,*c**) crystal axes (vide supra), the β-hematin crystals displayed in Figure 6a, b lie on their {100} and {010} faces respectively. Of 13 crystals from MeOH−DMSO solution, characterized by TEM micrographs, 11 exposed {010} faces, the remaining two {100} faces. Thus, we may conclude that β-hematin crystals obtained from MeOH−DMSO solutions are tabular needles extended along the *c*-axis, with {010} and {100} side faces, the former being generally more well-developed. A measure of the relative sizes of the exposed {010} and the {100} side faces of a specimen crystal was obtained from a comparison of TEM images of the crystal in its flat position and rotated about its needle axis by 45° (not shown), yielding a width-to-thickness ratio of about 3:1, which is consistent with the observation that most of the crystals observed lay on their {010} face.

The crystals grown in $CHCl_3$ solution expose the {100} face in five of the seven TEM images examined, the remainder the {010} face. The TEM image of a {100} oriented crystal and its corresponding ED pattern are shown in Figure 6c. Thus, the plate and side faces are primarily of the type {100} and {010} respectively for crystals grown in $CHCl_3$ solution.

According to the measurements of several well-formed specimen crystals, four of which are shown in Figure 6a, the edge of the slanted end face makes an angle of 116 ± 4° with the long *c*-axis of the crystal, consistent with an end face of the type {011}, which is the stable end face of the theoretical growth form of β-hematin, and which also appears in several hemozoin specimen crystals.[6] This assignment is consistent with the corresponding ED pattern (Figure 6a, bottom) showing that the diffraction vector *d**(011) is perpendicular to the slanted end face. It is noteworthy that the 0*kl* reciprocal lattice of β-hematin has near *mm* symmetry, the angle between the axes *b** and *c** being 88.8°. Thus, the vectors *d**(011) and *d**(0$\bar{1}$1) are nearly related by mirror symmetry (Figure 6a, bottom) and so it would be difficult to differentiate between slanted faces {011} and {0$\bar{1}$1} by visual inspection only of the TEM image of a specimen crystal. On theoretical grounds, we may preclude formation of the {0$\bar{1}$1} face as commonly occurring, its crystal surface structure being highly corrugated (not shown) and therefore much less stable than the {011} crystal face in accordance with the theoretical crystal growth form computations.[6]

Nucleation and Morphology of β-Hematin Crystals Grown in the Presence of Quinolines. According to our recent study,[6] quinoline-type drugs should inhibit nucleation and growth of hemozoin crystals along the fast-growing *c*-direction as a result of proposed binding onto the {001} faces (Figure 2b), but direct experimental evidence for this model was still missing. In order to provide information on quinoline binding, we examined to what extent the quinoline drugs affected β-hematin crystal nucleation and growth, in terms of time of crystal appearance and change in morphology. Regarding the first question, we found that the presence of 10% quinoline-type additives in chloroform solutions of hemin significantly increased the time for the crystals to appear, indicating a strong inhibition at the nucleation stage. For example, under the experimental conditions used, "pure" β-hematin nanocrystals appeared from chloroform solution after aging for about 12 h (on the basis of 40 experiments). When 10% quinine (Q) or chloroquine (CQ) (mol/mol hemin) was present in the solution, the "drug-affected" crystals appeared with high reproducibility after at least 48 h aging. The time was established from the data of 40 experiments for each additive. Increasing the additive concentration to 20% prevented formation of β-hematin crystals. These data support the comprehensive studies by Egan and co-workers[28] and by

(26) Real and reciprocal unit cell dimensions (Å, Å^{-1}, deg) of β-hematin: a = 12.196 Å, b = 14.684 Å, c = 8.040 Å, α = 90.22, β = 96.80, γ = 97.92, a^* = 0.08338, b^* = 0.06876, c^* = 0.12527, α^* = 88.83° β^* = 83.05°, γ^* = 82.00°. Angles between axes *a* and *a**, *b* and *b**, and *c* and *c**, are 10.5°, 7.9° and 6.8°, respectively.

(27) Bohle, D. S.; Kosar, A. D.; Stephens, W. P. *Acta Crystallogr.* **2002**, *D58*, 1752−1756.

(28) Egan, T. J.; Ross, D. C.; Adams, P. A. *FEBS Lett.* **1994**, *352*, 54−57.

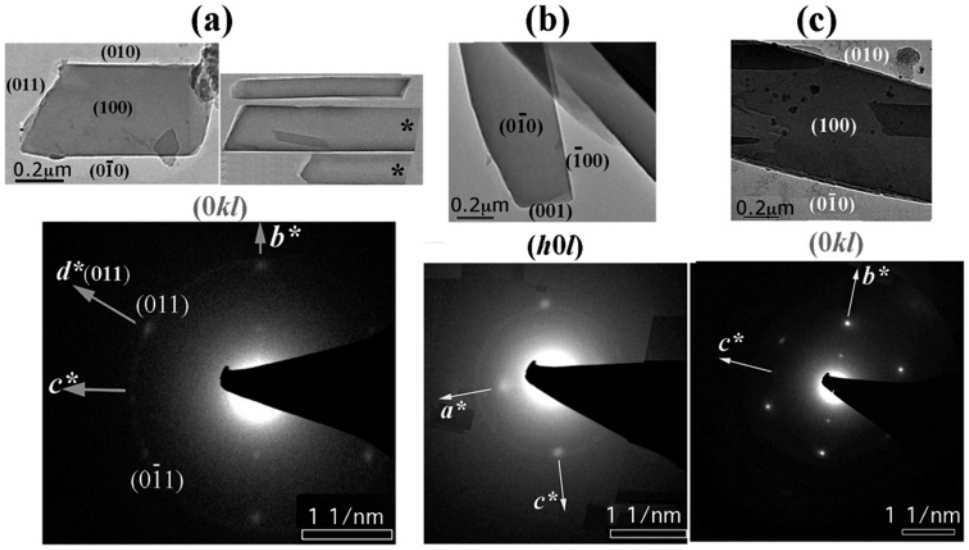

Figure 6. TEM images (top) and corresponding selected-area ED patterns (bottom) of β-hematin crystals obtained from: (a, b) MeOH−DMSO and (c) $CHCl_3$ solutions. The crystal faces are (*h,k,l*) indexed, based on the corresponding ED pattern. The 0*kl* diffraction pattern shown in (a) is from the labeled crystal. The morphologies of three other similarly shaped crystals are shown. The ends of the two crystals denoted by an asterisk were cut off from view in the original TEM image.

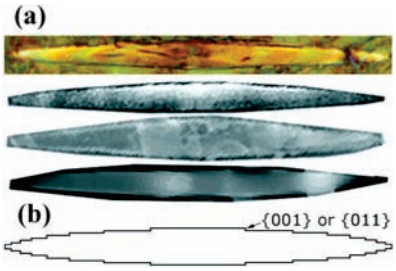

Figure 7. (a) Symmetrically tapered crystals of β-hematin obtained from growth in the presence of the quinoline drugs. The colored crystal was photographed on an optical microscope; the others are from TEM images. (b) Model of stepped face morphology showing {001} and {011} ledges to account for the symmetric tapering.

Chong and Sullivan,[29] which demonstrated that quinoline antimalarials decrease the rate of β-hematin formation.

As for providing evidence that the quinoline-type drugs modify the morphology of the synthetic hemozoin crystals, many of the crystals grown in the presence of CQ and Q were symmetrically tapered at both ends, spine-like in habit (Figure 5b, c, e, f and Figure 7a), primarily those obtained from $CHCl_3$ solution. The average angle between the tapered side faces of four of such spines, shown in Figure 7a is about 11°, in keeping with formation of a stepped-face morphology composed of a series of narrow {001} or {011} facet-type ledges, with an average height/width ratio of *tan*5.5° ≈10, shown schematically in Figure 7b. We propose that such tapering, resulting in growth along the spine axis of thinner and thinner cross-section, reduces the inhibiting effect of the quinoline additive since adsorption occurs primarily on the exposed {011} or {001} ledges.

Detection of the Effect of Quinolines via X-ray Diffraction Methods and Vibrational Micro-Raman and IR-ATR Spectroscopy. In order to glean more direct evidence of crystal growth inhibition at the {001} or {011} faces by stereoselective adsorption thereon of quinoline additives, we applied the concept that the additive, if adsorbed and perhaps occluded via particular crystal faces, should induce a reduction of the crystal mosaic domain size along the corresponding directions. Thus, use was made of synchrotron X-ray powder diffraction (XRPD) and coherent grazing X-ray diffraction[30] (CGXD) in order to detect such an affect, if present.

A quinoline additive, if adsorbed and occluded via a particular {*hkl*} face, should result in a reduction of the crystal coherence length $L\{h,k,l\}$ along the direction perpendicular to that face, as would be made manifest by a broadening of the {*hkl*} Bragg reflection. $L\{h,k,l\}$ may be derived from the FWHM of the Bragg reflection by use of the Scherrer formula.[25] Such a concept had been demonstrated by a comparison of the crystal mosaic domain sizes of pure synthetic and biogenic calcite.[31] Thus, quinoline, if adsorbed and occluded via the {001} or {011} face in sufficient concentration, should reduce the crystalline mosaic domain size along the *c*-direction, resulting in broader {001} or {011} X-ray reflections than those of the pure samples. Thus, synchrotron XRPD measurements[32] (see SI) were performed at Hasylab (Hamburg) on samples of β-hematin grown from MeOH−DMSO and from $CHCl_3$ solutions, in the absence and in the presence of 10% quinoline additive (Q, CQ). Four of these XRPD patterns are shown in Figure 8.

For the analysis of the results, we have assumed that the crystal coherence along the *c*-axis $L\{001\}$ relative to the coherence lengths along the different crystallographic directions $L\{hkl\}$, is a measure of the relative change in $L\{001\}$. In Table 1 the ratios $L\{001\}/L\{hkl\}$, labeled $L_{001/hkl}$, of five well-resolved and sufficiently intense reflections of each powder sample of the "pure" and "affected" crystals are listed, together with the average values of $L_{001/hkl}$. Growth inhibition along the *c*-axis should yield a decrease in the average value of $L_{001/hkl}$, which is not apparent for crystals grown in MeOH−DMSO (Table 1a), although there appears to be a marginally positive effect for crystals grown in $CHCl_3$ (Table 1b). We have no knowledge,

(29) Chong, C. R.; Sullivan, D. J. *Biochem. Pharmacol.* **2003**, *66*, 2201−2212.
(30) Pfeiffer, F.; Zhang, W.; Robinson, I. K. *Appl. Phys. Lett.* **2004**, *84*, 1847.
(31) Berman, A.; Hanson, J.; Leiserowitz, L.; Koetzle, T. F.; Weiner, S.; Addadi, L. *Science* **1993**, *259*, 776−779.
(32) Knapp, M.; Baehtz, C.; Ehrenberg, H.; Fuess, H. *J. Synchrotron Radiat.* **2004**, *11*, 328−334.

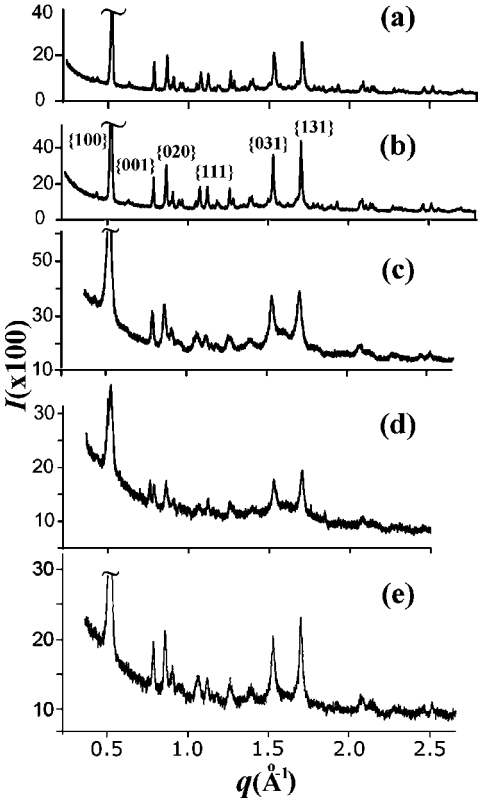

Figure 8. X-ray powder diffraction (XRPD) patterns of β-hematin crystals obtained from (a, b) MeOH−DMSO solution, (c−e) chloroform solution. The XRPD patterns shown in (a, c) correspond to crystals grown in the absence of quinoline additive, those in (b, d, e) to crystals grown in the presence of 10% CQ, Q, and CQ respectively.

Table 1. Crystal Coherence Lengths $L\{hkl\}$ (Å) along Six *hkl* Directions, the Ratios $L\{001\}/L\{hkl\}$, Denoted as $L_{001/hkl}$ and the Average Ratio thereof $\langle L_{001/hkl}\rangle$ along Five *hkl* Directions {100}−{131} Obtained from Different Sets of XRPD Data of β-Hematin, Grown in the Absence of Quinoline Additives (Pure Crystals) and in the Presence of 10% Q and of 10% CQ

pure β-hematin			+10% quinine		+10% chloroquine	
{*hkl*}	$L\{hkl\}$	$L_{001/hkl}$	$L\{hkl\}$	$L_{001/hkl}$	$L\{hkl\}$	$L_{001/hkl}$
Nine Samples of Crystalline Powder obtained from DMSO-MeOH[a]						
{001}	990		1205		1040	
{100}	810	1.22	830	1.45	790	1.31
{020}	550	1.80	670	1.80	610	1.70
{111}	540	1.83	765	1.58	700	1.47
{031}	455	2.18	490	2.46	515	2.02
{131}	500	1.98	505	2.39	510	2.05
		⟨1.80⟩		⟨1.94⟩		⟨1.71⟩
Three Samples of Crystalline Powder Obtained from $CHCl_3$ Solution						
{001}	390		400		470	
{100}	190	2.05	195	2.05	240	1.96
{020}	315	1.24	370	1.08	395	1.19
{111}	245	1.59	415	0.96	295	1.59
{031}	215	1.81	245	1.63	250	1.88
{131}	180	2.17	310	1.29	275	1.71
		⟨1.77⟩		⟨1.40⟩		⟨1.67⟩

[a] Values in each column are the average of three powder samples.

however, of the concentration of quinoline additive stereoselectively adsorbed onto the crystal surface and the fraction thereof eventually occluded into the crystal.

The CGXD experiment produced the diffraction pattern shown in Figure 9 from the crystals grown from MeOH−DMSO solution without additives. The intensity distribution, which is nominally given by the Fourier transform of the shape of the crystal grain, i.e., mosaic domain, that is illuminated, cannot be interpreted simply, but some general conclusions can be drawn. A strain-free perfect crystal should give a locally centrosymmetric diffraction pattern; the lack of symmetry seen here indicates that the crystal is strained. A plate-like shape for the crystal is suggested by the elongation of the diffraction pattern. The crystals grown from MeOH−DMSO in the presence of quinoline additive gave only very weak diffraction signals that disappeared with X-ray exposure. This suggests that the crystal domains grown in the presence of additives were smaller and less structurally stable.

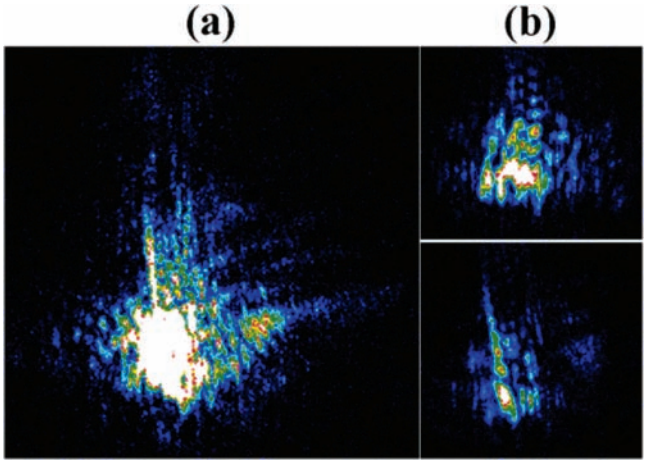

Figure 9. Coherent X-ray diffraction patterns measured for the first peak {100} of the powder diffraction pattern of β-hematin grown without additives: (a) is the center of the rocking curve, whereas in (b) the two smaller panels are offset on either side by a fraction of a degree. The false-color intensity scale is saturated in the center so that the weaker features at the edges of the pattern can be resolved.

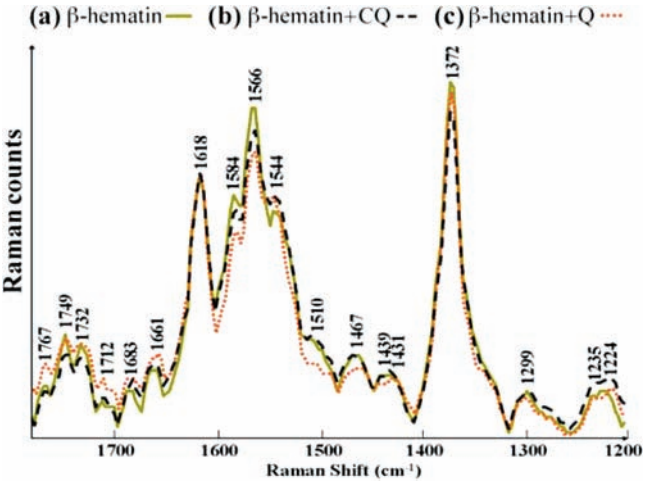

Figure 10. Average micro-Raman spectra in the 1800−1200 cm^{-1} region: (a) pure β-hematin crystals; (b, c) β-hematin grown in the presence of 10% CQ and Q, respectively.

Average micro-Raman spectra[33,34] (see SI) in the 1800−1200 cm^{-1} region of pure β-hematin crystals and β-hematin grown in the presence of 10% quinine and chloroquine (Figure 10) show minor variation, mainly in band widths and relative

(33) Chan, A. K. L.; Kazarian, S. G. *Appl. Spectrosc.* **2003**, *57*, 381−389.
(34) Colley, C. S.; Kazarian, S. G.; Weinberg, P. D.; Lever, M. J. *Biopolymers* **2004**, *74*, 328−335.

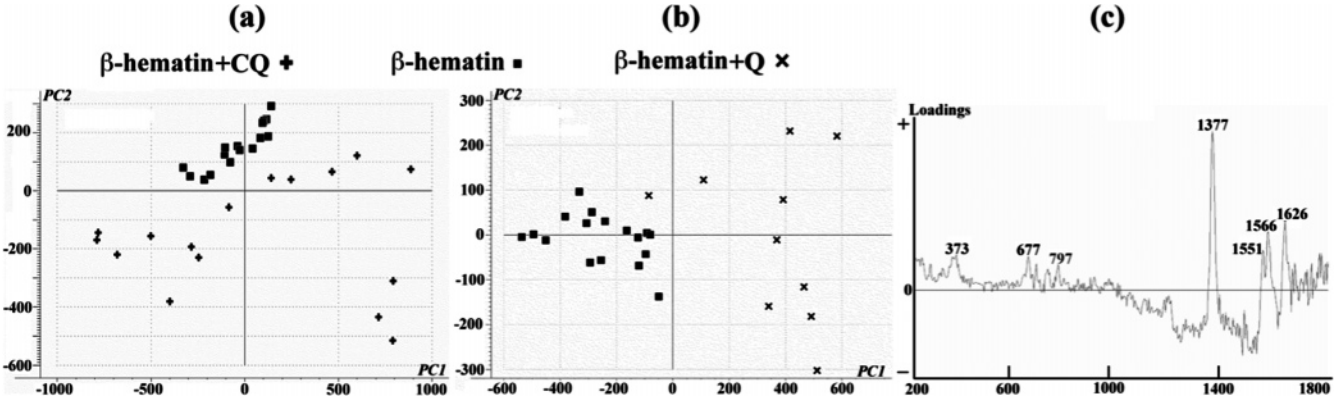

Figure 11. PCA scores plot, PC1 vs PC2 for Raman spectra of (a) pure β-hematin (squares) and β-hematin/chloroquine treated (crosses); (b) pure β-hematin (black squares) and Q-affected β-hematin (crosses); (c) loadings plot for PC1 for (b) with strong positive loadings associated with bands from pure β-hematin and labeled with wavenumber values.

intensity. Band assignments, local symmetry coordinates, symmetry terms, and the spectroscopic notation for β-hematin are based on earlier studies.[11,35]

Bands at 1584 cm^{-1} (assigned to $\nu(C_\alpha C_m)$ of E_u symmetry), 1566 cm^{-1} (assigned to $\nu(C_\beta C_\beta)$ of A_{ig} symmetry also known as ν_2), and 1372 cm^{-1} (assigned to ν(pyrrole half-ring) of A_{1g} symmetry also known as ν_4) appear more intense in the spectra of pure β-hematin crystals compared to those of its drug-affected counterparts. Additionally the band at 1544 cm^{-1} assigned to $\nu(C_\beta C_\beta)$ of B_{1g} (known as ν_{11}) appears less intense in pure β-hematin.

In order to examine variability in the whole dataset of individual spectra principal components analysis (PCA) was used after first preprocessing the data with a multiplicative scatter direction. PCA is a multivariate statistical technique,[36] which breaks the data down into variability within a dataset and allows graphical presentation of the results in the form of scores plots, to determine whether samples group together, and loadings plots, that determine where the variables (in this case spectral wavenumber) that contribute to variance occur. Plots a and b of Figure 11 show PCA scores plots of PC1 vs PC2 for β-hematin grown in the presence of chloroquine (CQ) and quinine (Q), respectively. Each individual score represents a single spectrum plotted as a point in a two-dimensional space, the position of which is dependent on the individual variance contribution of the spectrum to each principal component or basis vector. Overall, pure β-hematin spectra are more tightly clustered than the drug-treated β-hematin spectra in both scores plots, while the quinoline-affected samples have a much larger spectral spread. A distinct separation of the pure β-hematin from that grown in the presence of CQ and Q is observed. For pure β-hematin and CQ-affected β-hematin the separation is mainly along PC2, while for pure β-hematin and Q-affected β-hematin the separation occurs along PC1. Figure 11c depicts the PC1 loadings plot for the β-hematin and Q-affected β-hematin PCA. Bands that have strongly positive or negative loadings are those which are important in explaining the variance and consequently the separation observed in the PC1 vs PC2 scores plot (Figure 11b) between β-hematin and Q-affected β-hematin. The strong positive bands observed in the loadings plot are associated with the pure β-hematin and are mainly of A_{1g} and B_{1g} symmetry and include those at 1626 cm^{-1} (ν_{10}), 1566 cm^{-1} (ν_2), 1551 cm^{-1} (ν_{11}), and 1372 cm^{-1} (ν_4).

The IR-ATR images recorded from β-hematin, CQ-affected β-hematin and Q-affected β-hematin were processed using Cytospec. Each of the three individual images originally contained 4096 spectra in the form of a "spectral hypercube". The spectra were quality tested to remove spectra with low signal/noise and vector normalized, and the second derivative was calculated. Second derivative analysis eliminates the need for baseline correction and sharpens shoulder bands. Band maxima in the raw spectra become minima in the second derivative. The mean second derivative spectrum most representative of the image was determined and extracted using unsupervised hierarchical cluster analysis (UHCA). UHCA is an unsupervised technique used to group similar spectra and is often used for classification in image analysis.[37] Essentially, spectra are clustered by similarity and color coded to form an image. Spectral averages representative of each cluster type can then be extracted. The mean second derivative spectra from the largest cluster (out of a total of four clusters) for each of the conditions are plotted in Figure 12.

The spectra of the CQ-affected β-hematin and Q-affected β-hematin are remarkably similar and distinctly different from pure β-hematin. The band at 1744 cm^{-1} previously attributed to surface propionate groups,[11] but which we now believe to be propionic acid groups, is observed in the spectrum of pure β-hematin but not in the drug-affected samples. There appears to be a shoulder at ~1720 cm^{-1} in the spectra of the drug-affected samples but not in those for pure β-hematin. There are also differences in the bands directly involved in the propionate linkage (to Fe) at ~1660 and 1209 cm^{-1}. A strong shoulder band at ~1670 cm^{-1} can be observed next to the ν(C═O) band at 1657 cm^{-1}, indicating a new carbonyl environment in the drug-affected samples. A close inspection of the C−O band at ~1209 cm^{-1} shows also a slight difference. Distinct differences can also be observed in the 1300−1200 cm^{-1} in drug-affected compared to those of pure β-hematin.

Binding of Diethylamino-alkoxyxanthones (XN*n*) on β-Hematin Crystal Faces and Antimalarial Activity. The relative ability of XN*n* molecules, with $(CH_2)_n$ side chains, $n = 2$ (XN2) and $n = 5$ (XN5), to bind to the crystal surfaces of

(35) Abe, M.; Kitagawa, T.; Kyogoku, K. *J. Chem. Phys.* **1978**, *69*, 4526.
(36) Wood, B. R.; Burden, F. R.; Quinn, M. A.; McNaughton, D. *Biospectroscopy* **1996**, *2*, 145−155.
(37) Wood, B. R.; McNaughton, D. In *Spectrochemical Analyses Using Multichannel Infrared Detectors*; Bhargave, R., Levin, I., Eds.; Blackwell: Cambridge, MA, 2005.

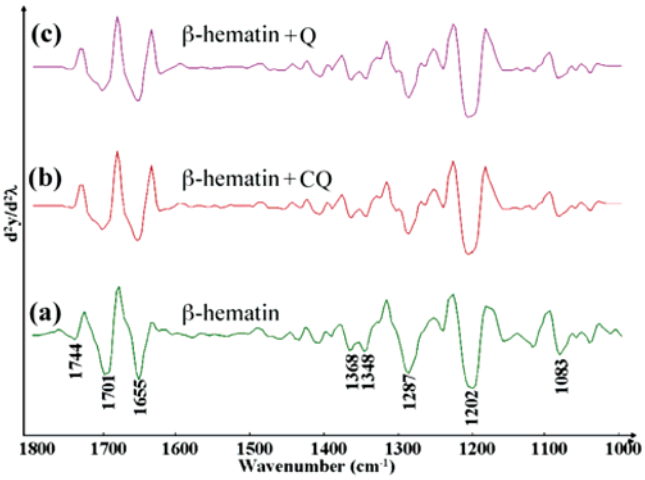

Figure 12. Unsupervised hierarchical cluster analysis (UHCA) cluster average IR spectra (presented as second derivatives) for: (a) β-hematin and (b, c) β-hematin grown in the presence of 10% CQ and Q, respectively. The band at 1744 cm^{-1} in β-hematin, assigned to the carbonyl group of surface propionic acid groups, has disappeared in the drug-treated samples, thus indicating binding through this site.

Table 2. Docking Energies ΔE_b (kcal/mol) of the Diethylamino-hydroxyxanthone Molecules XN2 and XN5 onto the β-Hematin {001} and {011} Crystal Surfaces and the Directions *D* on the Face along Which the Additive Molecules Lie

drug/face	*D*	ΔE_b
	{001}	
XN2	*a*	−25
XN5	*a*	−35
XN5	$2a + b$	−20
	{011}	
XN2	$-b + c$	−5
XN5	*a*	−25

β-hematin was studied by modeling (see SI) the docking of the drug onto the {001} and {011} crystal surfaces. The results are presented in Table 2 and Figure 13.

Artemisinin−Hematin Molecular Dimer Adduct as Inhibitor of Hemozoin Formation. Here we show that the antimalarial drug artemisinin may, in principle, act as a hemozoin growth inhibitor. Meunier and co-workers[18] have demonstrated that artemisinin covalently reacts with the free heme monomer at the three different sites (α, β, δ) on the molecular periphery with about the same regioselectivity of 29%, yielding artemisinin−heme adducts labeled AαH, AβH, and AδH, as depicted in Chart 2b for site β. Reaction at site γ is comparatively low at 13%. We invoke the possibility that each of the four adducts might link to a pure heme monomer in the digestive vacuole of the malaria parasite to form a dimer with a basic skeleton akin to the β-hematin cyclic dimer (Figure 1b), the exact structure thereof depending upon that of the adduct and its relative orientation to the heme monomer prior to dimer formation. Such molecules, if present in the digestive vacuole of the parasite, would act in a manner akin to a classic "tailor-made" additive in solution designed to inhibit crystal nucleation and growth.[38] In principle, four diastereomeric pairs of dimers (labeled AαBH, A$\bar{\alpha}$BH; AβBH, A$\bar{\beta}$BH; AδBH, A$\bar{\delta}$BH; AγBH, A$\bar{\gamma}$BH) may be formed and adsorbed on the six {100}, {010}, and {001} faces of β-hematin.

For the most part, each additive type may be adsorbed at only one of the six faces, as shown somewhat schematically in Figure 14a for binding of the α, $\bar{\alpha}$, β, $\bar{\beta}$, and δ, $\bar{\delta}$ derivatives to the four {100} and {010} crystal side faces. The molecules within each pair are diastereoisomers since artemisinin is chiral and the β-hematin cyclic dimer molecule is centrosymmetric. Using CERIUS^2 software we computed low-energy models of some of the diastereoisomeric dimer structures, which are shown adsorbed onto the different crystal faces in Figure 14b,c.

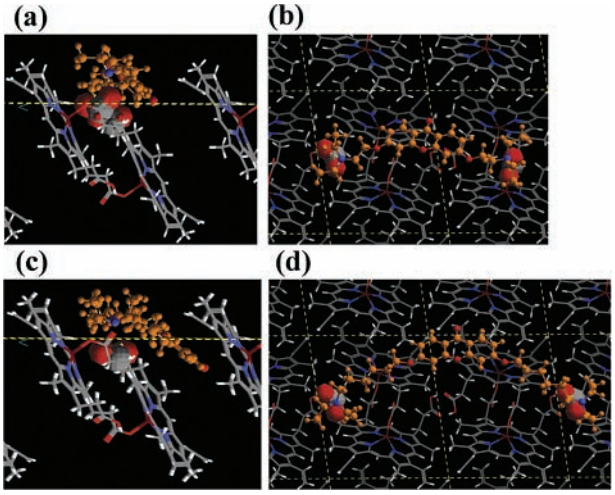

Figure 13. Packing arrangement of β-hematin illustrating the binding to the (001) face of a diethylamino-hydroxyxanthone molecules XN2 shown in (a, b) and XN5 shown in (c, d). Views parallel to the (001) plane (dashed yellow line) are depicted in (a, c) and views perpendicular to the (001) plane are shown in (b, d). The C and H atoms of hydroxyxanthone are colored in orange, the N atoms in blue, and the O atoms in red. The carboxylate O atoms of β-hematin in contact with the NH groups of hydroxyxanthone are large red spheres.

Therefore, on the assumption that the heme−artemisinin reaction products are formed in the digestive vacuole of the parasite in sufficient concentration, an efficient inhibition of growth of hemozoin should occur since the additives may act along all three principal growth directions, *a*, *b*, and *c*. In principle, only a fraction of the additives can be adsorbed onto the small, but fast-growing {001} faces. Therefore, we may expect a stronger inhibition of crystal growth along this direction to occur were quinoline drugs, such as chloroquine or quinine, used in conjunction with artemisinin, given the proposed mechanism of action of artemisinin. Thus, we examined, via the use of a model crystal system of *S*-alanine as described in the SI, whether a combination of tailor-made crystal nucleation retardants, which inhibit crystal growth along different directions, acts more effectively than each alone. The results suggest that simultaneous use of two types of additives, which bind to different crystal faces, has a greater inhibiting effect on nucleation than each of the additives used alone.

Discussion

Nucleation of Hemozoin Crystals. Little is known at the molecular level on the nucleation process of hemozoin in the digestive vacuole of the parasite, including the critical size of the nucleus, and the role played by various molecules in the vacuole to promote the nucleation process. Attempts to glean information on the critical size of β-hematin nuclei by monitoring the early stages of crystallization of β-hematin at the air−water interface using grazing incidence X-ray diffraction were

(38) Weissbuch, I.; Addadi, L.; Lahav, M.; Leiserowitz, L. *Science* **1991**, *253*, 637−645.

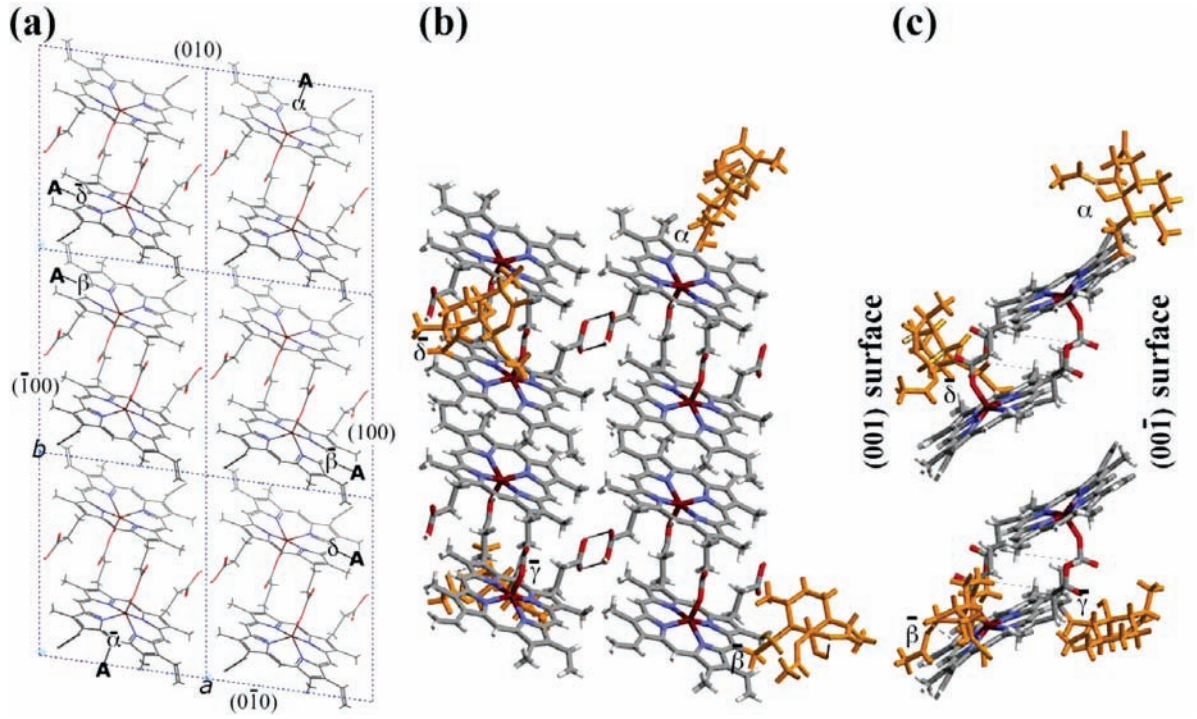

Figure 14. Arrangement of artemisinin−β-hematin dimer adducts on crystal faces of β-hematin. (a) Adsorption of the six adducts AαBH, A$\bar{\alpha}$BH, AβBH, A$\bar{\beta}$BH, AδBH and A$\bar{\delta}$BH, to the four {100} and {010} faces viewed along the *c*-axis, where A represents an artemisinin moiety covalently bound to a heme H, α, β, and δ the three peripheral sites on the heme (see Chart 2b) and BH the molecular dimer. (b, c) Views along the *c* and *a* axes of adsorption of the adducts AαBH, A$\bar{\beta}$BH, AδBH, and A$\bar{\gamma}$BH on the various faces, where the molecular structure of the artemisinin moiety (A) bound to the hematin dimer at the different peripheral sites has been modeled by energy minimization.

not successful. Crystals do not appear to form on the water surface after spreading a fresh chloroform solution containing hemin and lutidine, or with added phospholipids DPPC or DPPE to the spreading solution, even after waiting for 24 h: one possible reason is that the hemin monomer molecules are presumably all oriented with their carboxyl groups in contact with the water surface, so that the β-hematin molecular cyclic dimer (Figure 1b) will not be formed. The solutions, when aged for about 12 h prior to being spread on the water surface, resulted in the appearance of thin oriented β-hematin crystals floating on the water surface primarily on the {100} face according to the GIXD data (Figure 3a). The average domain size of these crystals along the (100) direction was about 300 Å (Figure 3b).

The aligned parallelepiped crystals of hemozoin formed in the digestive vacuole of *Plasmodium falciparum*, displayed in the TEM image (Figure 15), reported by Goldberg and coworkers in their study on the hemoglobin degradation in *Plasmodium falciparum*[10] might yield information on the nucleation process in the digestive vacuole. These authors were struck by the fact that photographs of intact parasites show pigment crystals lined up along a single axis, whereas photographs of isolated vacuoles repeatedly show a disordered array. They suggested that the alignment may merely be an artifact of isolation or fixation or, considering the paramagnetic properties of the iron in hemozoin, that the pH gradient across the vacuolar membrane establishes an electromotive force across the vacuole that causes the pigment crystals to align within the magnetic field so generated. During isolation, the factors needed to maintain a transmembrane pH gradient may be lost, and the crystals would become disordered.

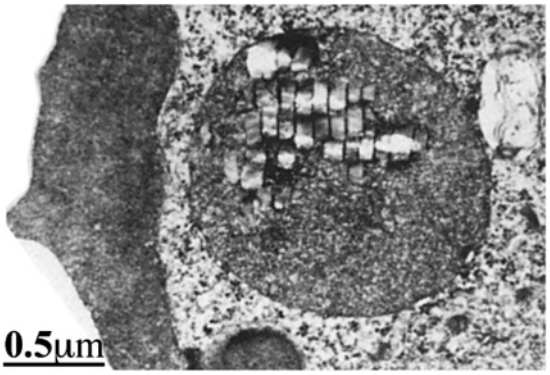

Figure 15. Electron micrograph of the digestive vacuole (dv) of a *Plasmodium falciparum* trophozoite inside an erythrocyte, showing a cluster of hemozoin crystals (bar = 0.5 μm). [Study by Goldberg et al.[10] Reproduced with permission from the author.]

We propose an alternative mechanism involving epitaxial nucleation of the hemozoin crystals via the surface of the vacuole membrane. In this respect we note that β-hematin crystallization can be promoted by lipids[1,9,39] and that neutral lipid nanospheres play a role in living parasite *Plasmodium falciparum* heme crystallization.[40] Furthermore, very recently Egan et al. reported a fast β-hematin formation under physiologically realistic conditions near octanol−water, pentanol−water, and lipid−water interfaces.[41] Given that the crystals of synthetic and biogenic hemozoin tend to grow fastest along the

(39) Bendrat, K.; Berger, B. J.; Cerami, A. *Nature* **1995**, *378*, 138.
(40) Pisciotta, J. M.; Coppens, I.; Tripathi, A. K.; Scholl, P. F.; Shuman, J.; Bajad, S.; Shulaev, V.; Sullivan, D. J. *Biochem. J.* Immediate Publication Published on October 17, 2006.
(41) Egan, T. J.; Chen, J. Y.-J.; deVilliers, K. A.; Mabotha, T. E.; Naidoo, K. J.; Ncokazia, K. K.; Langford, S. J.; McNaughton, D.; Pandiancherri, S.; Wood, B. R. *FEBS Lett* **2006**, *580*, 5105.

c-axis and are delineated by sharp {100} and {010} side faces, the crystals in Figure 15 would appear to be aligned parallel to *c*, so that the nucleation occurs via either the {100} or {010} faces. On the assumption that the nucleation is induced by exposed head groups of membranous lipids, akin to oriented nucleation of various molecular crystals via monolayers of amphiphilic molecules,[42] only a one-dimensional complementarity is required between the lipid head groups capable of forming hydrogen bonds and the propionic acid groups exposed at the {100} face of hemozoin. This model implies that the β-hematin molecular dimer would not be formed within the membrane layer, consistent with the observation (vide supra) that crystals of β-hematin were not obtained at the lipid−water interface when a fresh hemin/phospholipid chloroform solution was spread on the water surface.

The model of induced nucleation of hemozoin is also consistent with the preliminary experiments carried out in $CHCl_3$ solution on induced nucleation of β-hematin at the hydrophilic surface of a monolayer of phospholipid DBPC and hydrophobic surface of OTS; far more crystals were nucleated in the former regime. However, X-ray diffraction measurements indicated that only a very minor proportion of the β-hematin crystals were nucleated via its {100} face at the phospholipid DBPC surface, the majority of crystals were oriented randomly with respect to the {100} face.

Morphology of β-Hematin Crystals Grown in Absence and Presence of Quinolines. Information on the morphology of β-hematin crystals grown in MeOH−DMSO and $CHCl_3$ solutions were obtained from TEM measurements. The crystals were lath-like in habit. Several of these laths were symmetrically shaped, extended along the *c*-direction, and were delineated by {100} and {010} side faces and {011} end faces (Figure 6a), similar to the regular morphologies of β-hematin reported by Bohle et al.[27] Other crystals were asymmetrically tapered toward only one end of the lath (Figure 5a, d), which might be due to an irrational growth process or to the presence of a chiral impurity in the solutions used.

The pure crystals of β-hematin obtained from MeOH−DMSO solutions displayed well-developed {010} faces (Figure 6a), the {100} side face being less so, in keeping with a near rectangular crystal cross-section. The pure crystals obtained from $CHCl_3$ solution were very thin {100} laths, being almost transparent in the SEM micrographs (Figure 5e, f). We might account for this morphology as a result of binding, via an acid−base interaction, of the lutidine molecules to the exposed carboxyl group on the {100} face albeit at an oblique angle (Figure 1b), thus inhibiting growth along the *a*-direction. Here we note that the concentration of lutidine in the $CHCl_3$ solution was about 100 times greater than in the MeOH−DMSO solution.

The regular-shaped pure β-hematin crystals display the same faces {100}, {010}, and {011} as those of the theoretical growth form (Figure 2a), which is also consistent with the morphologies in some hemozoin species.[6] It is noteworthy that the side faces of several specimen crystals of hemozoin from the mammalian *Plasmodium* species, reported by Noland et al.[43] to be bricklike with smooth sides at (near) right angles, clearly correspond to the {100} and {010} side faces between which the dihedral angle is 82°. The possibility that the hemozoin side faces are of the type {110} and $\{1\bar{1}0\}$, the angle between which is 79°, may be ruled out because their crystal surfaces are highly corrugated and thus less stable than the relatively smooth {100} and {010} faces, as may be envisioned from Figure 1b, in agreement with theoretical growth form computations.[6]

Model of Quinoline Binding to the Crystal Faces of β-Hematin. Regarding experimental evidence establishing the direction of the inhibition of growth of hemozoin crystals via the proposed surface binding site of quinoline-type drugs to the {001} face, we had suggested[6] that the darker areas at the {001} end faces terminating the longer sides of several aligned hemozoin crystals, reported by Goldberg and co-workers,[4] correspond to adsorbed or occluded [H^3]chloroquine. However, Egan, in a comprehensive review on hemozoin as a unique crystalline drug target,[44] remarked that the dark areas may merely be regions of increased electron density, although it would be unusual that tabular shaped crystals are thicker at its ends. The doubts raised by Egan, however, imply the need for unambiguous evidence in favor of the crystal surface-binding model. We found that β-hematin crystals grown from MeOH−DMSO and $CHCl_3$ solutions in the presence of quinoline additives display, in a significant amount, crystals tapered at both ends, which are highly symmetric in shape (Figures 5b, c, e, f and 7a). We propose that such tapering is adopted in order to help reduce inhibition of growth along the *c*-axis by adsorption of the quinoline additive on the {001} or {011} faces expressed as ledges in the proposed stepped-face morphology shown in Figure 7b, resulting in a spine formation of thinner and thinner cross-section. It is of relevance that crystals of *R*,*S*-alanine and of ammonium dihydrogen phosphate are also symmetrically tapered when respectively grown in the presence of additive *S*-threonine[45] and particular ionic species[46], a possible explanation being that in this way the inhibiting effect is somewhat ameliorated. In order to provide supporting evidence to the model of quinoline adsorption and crystal growth inhibition, the effect of quinine on *R*,*S*-mandelic acid crystallization was examined (see SI). We found that quinine inhibits the nucleation and growth of *R*,*S*-mandelic acid, explained by acid−base binding of the additive to the crystal faces exposing carboxyl groups.

Analysis of the synchrotron powder X-ray diffraction data of pure and affected β-hematin, grown in the absence and the presence of quinine and chloroquine respectively, suggests, for the crystals grown in chloroform solution, that the additives reduce the crystal mosaic domain size along the *c*-direction (see Table 1). The coherent grazing X-ray diffraction data of pure and affected β-hematin, the latter obtained from MeOH−DMSO solution, appear to be consistent with the above conclusion.

Examination of the Raman spectra in Figure 10 and the infrared spectra in Figure 12 shows no direct evidence of the presence of quinine or chloroquine in any spectra but does show that there are minor, but distinct, changes between quinoline-affected and pure β-hematin crystals. The observed differences in both PCA scores plots (Figure 11a,b) may be explained in terms of the effect of stereoselectively bound quinoline occluded within the bulk of the crystal: the centrosymmetric β-hematin

(42) Weissbuch, I.; Lahav, M.; Leiserowitz, L. *Cryst. Growth Des.* **2003**, *3*, 125−150.
(43) Noland, G. S.; Briones, N.; Sullivan, D. J. *Mol. Biochem. Parasitol.* **2003**, *130*, 91−99.
(44) Egan, T. J. *Targets* **2003**, *2*, 115−124.
(45) Weissbuch, I.; Leiserowitz, L.; Lahav, M. *Adv. Mat.* **1994**, 953−956.
(46) Davey, R. J.; Mullin, J. W. *J. Cryst. Growth* **1974**, 89.

molecular dimers in the vicinity of such poisoned sites, which are asymmetric imparting a local symmetry reduction, undoubtedly adjust their positions to fit into the regular crystal arrangement.

The loadings plots for the Raman data show that both antimalarials have chemically changed the β-hematin and that the changes are commensurate with changes in bands sensitive to lattice perturbation. The enhancement of bands in aggregated heme systems is thought to involve excitonic interactions, where energy in the form of an exciton can migrate throughout the extended porphyrin network due to overlap of π-orbitals[11] This leads to the increase in amplitude of predominately totally symmetric modes such as ν_2 and ν_4 at 1566 and 1377 cm^{-1} but also some B_{1g} modes at 1551 cm^{-1} (ν_{11}) and 1626 cm^{-1} (ν_{10}). The reduction in intensity of these bands in the quinoline-affected samples is attributed to a perturbation in the porphyrin aggregate that impedes exciton migration in the aggregate, resulting in the decrease in amplitude of A_{1g} and B_{1g} modes.

The infrared spectral variations between the three samples show changes in the major involved in the propionate linkages (vide supra). For the cluster map (Figure 12) of the combined data set there is a distinct separation between pure β-hematin and both quinoline-affected β-hematin samples choosing either 2, 3, 4, or 5 clusters, showing that there is great spectral similarity between crystals grown in the presence of the quinoline additives. Apart from changes in bands due to propionate linkages, the small band at 1744 cm^{-1}, observed in the second derivative spectra and attributed to surface propionic acid groups in β-hematin, is essentially absent in the quinoline-affected samples. These changes indicate that the quinoline have indeed modified the crystal surface by binding to the surface acid groups. The Raman data on the other hand indicate the quinoline has perturbed the β-hematin lattice.

All in all, there seems to be little doubt as to the model of quinoline binding to the {001} and {011}, as well as, perhaps, the {100} faces of hemozoin,[6] leading to inhibition of crystal nucleation and growth. During this process a quinoline molecule may also bind to a β-hematin molecular dimer before the latter is adsorbed on a crystal surface, as proposed by Sullivan and Chong,[29] but which has a kinetic disadvantage that the complex must "locate" the appropriate face, (001) or $(00\bar{1})$, onto which to adsorb, depending upon to which of the two carboxyl groups the drug is bound. Naturally if both carboxyl groups of a β-hematin molecular dimer are bound to quinoline, such a complex cannot be stereoselectively adsorbed onto the crystal surface and so will be ineffective as an inhibitor.

Possible Mechanisms of Antimalarial Action of Diethylamino-alkoxyxanthone and Artemisinin-Type Drugs. The antimalarial activity of the diethylamino-alkoxyxanthone drugs had been explained by Riscoe and co-workers[13,14] in terms of the binding constant of the drug to heme in solution (see SI, Figure S1). We propose hemozoin as a primary drug target, involving binding of the drug to the {001}, {011}, and perhaps {100}, crystal faces, leading to inhibition of crystallization. The computed binding energy of the drug to the crystal faces is dependent upon the drug chain length (Table 2). Comparing the antimalarial activity of drugs XN2 and XN5, the latter, with chain lengths appropriate for the two terminal amino groups to bind simultaneously to two carboxyl groups exposed at the {001} or {011} faces and also form favorable van der Waals contacts with the crystal face (Figure 13), is a better antimalarial. This crystal surface binding model also accounts for the reduced antimalarial activity for molecules XN8 (SI, Figure S1) being about 6 Å longer than XN5 and so would bind to the two surface carboxyl groups on the {001} or {011} faces only if the molecular chain would be bent and thus make poorer van der Waals contact with the crystal surface. The efficient antimalarial potency of diamidines, another class of novel drugs embodying proton donor groups (amidine) at either end of the molecule, has been reported some years ago.[47] These authors showed that diamidines inhibit hemozoin formation in vitro with a similar potency to chloroquine. It is likely that these drugs, such as pentamidine ($H_3N_2C-C_6H_4-O-C_5H_{10}-O-C_6H_4-CN_2H_3$) inhibit hemozoin formation as a result of binding of both amidine groups of the molecule to exposed propionic acid groups at the crystal surface. Of relevance to the model proposed for antimalarial action of the diethylamino-alkoxyxanthones is growth inhibition of barium sulfate by an additive with moieties which simultaneously cap onto the crystal surface.[48] Another example, (described in SI), is the crystal nucleation retardation of *S*-alanine by different diamine derivatives, the most effective being an additive with a central chain, the length of which matches the distance between two carboxylate groups exposed at the crystal surface.

Regarding antimalarial action of artemisinin-type drugs, we have described a model involving reaction of four artemisinin−heme-type adducts, (Chart 2b), with a free heme monomer to yield eight derivatives of the cyclic β-hematin dimer, comprising four diasteroisomeric pairs which may bind to the {100}, {010}, and {001} faces of a β-hematin crystal shown in Figure 14. Such molecules, if present in the digestive vacuole of the parasite, would act in a manner akin to that of a classic tailor-made additive in solution designed to inhibit crystal nucleation and growth.[42] According to this model, crystal growth of hemozoin may be inhibited along all three principal crystal directions, *a*, *b*, and *c*, consistent with the report that artemisinin inhibits hemoglobin digestion by malaria parasites and inhibits hemozoin formation,[17] but which has only been demonstrated in cell-free conditions. We stress, in terms of the model presented here, that efficient inhibition of hemozoin formation via artemisinin would seem possible, provided the cyclic β-hematin dimer derivatives are formed in the digestive vacuole of the parasite; the artemisinin−heme-type adducts (Chart 2b) would not be as strongly adsorbed on hemozoin crystal surfaces to act as efficient growth inhibitors.

According to the model only a small fraction of the ensemble of artemisinin−cyclic β-hematin dimer adducts can be adsorbed onto the small, but fast-growing {001} faces. We may therefore rationalize why artemisinin-based combination therapy (ACT) involving artemisinin and quinoline drugs is more effective than each of them applied separately in clinical studies combating malaria.[49−51] The improved efficacy might be explained as

(47) Stead, A. M. W.; Bray, P. G.; Edwards, I. G.; Dekoning, H. P.; Elford, B. C.; Stocks, P. A.; Ward, S. A. *Mol. Pharmacol.* **2001**, 1298.
(48) Coveney, P. V.; Davey, R.; Griffin, J. L. W.; He, Y.; Hamlin, J. D.; Stackhouse, S.; Whiting, A. *J. Am. Chem. Soc.* **2000**, *122*, 11557.
(49) deVries, P. J.; Bich, N. N.; Thien, H. V.; Hung, L. N.; Anh, T. K.; Kager, P. A.; Heisterkamp, S. H. *Antimicrob. Agents Chemother.* **2000**, *44*, 1302−1308.
(50) Gupta, S.; Thapar, M. M.; Mariga, S. T.; Wernsdorfer, W. H.; Bjorkman, A. *Exp. Parasitol.* **2002**, *100*, 28−35.
(51) Olliaro, P. L.; Taylor, T. W. *J. Postgrad. Med.* **2004**, *50*, 40−44.
(52) Wei, K.-T.; Ward, D. L. *Acta Crystallogr.* **1977**, *B33*, 797−800.

follows: quinoline drugs are expected to inhibit growth primarily along the fast-growing needle *c*-axis, and the artemisinin-type drugs have been hypothesized to retard growth along all three principal crystal directions (*a*, *b*, *c*). Thus, a combination of these two types of drugs would be effective inhibitors of overall crystal formation of hemozoin because of a relatively high concentration of drugs available for binding onto the small, yet fast-growing, opposite faces terminating the needle. This hypothesis is in agreement with the experiments on the model crystal system *S*-alanine, suggesting that a combination of tailor-made additives that bind to different crystal surfaces has a greater inhibiting effect on nucleation than each of the additives used alone.

Concluding Remarks

The most dominant crystal faces of β-hematin have been experimentally characterized, in agreement with the shape of some reported hemozoin crystals and the theoretical growth form of β-hematin.[6] An effect of quinine and chloroquine on the growth morphology of β-hematin has been observed and correlated with adsorption of the drugs onto the {001} or {011} crystal faces. This interpretation is in agreement with evidence, although marginal, from synchrotron X-ray diffraction data of powder samples that the quinoline additives reduce the crystal domain size along the *c*-axis and with coherent grazing X-ray diffraction experiments, which suggest that the β-hematin crystals grown in the presence of the additives were smaller and less structurally stable than the pure form. The IR-ATR and Raman spectral results show that β-hematin grown in the presence of the quinoline drugs embodies molecular based differences from pure β-hematin. The results suggest modification of surface and bulk propionic acid linkages and aggregation perturbation within the affected crystal, albeit minor, presumably arising from host molecular rearrangement in the environment of the bulk sites poisoned by occluded quinoline. These proposed changes are consistent with the interpretation of morphological modification, the X-ray diffraction results, and the model computations of surface binding of quinoline antimalarials to the {001} face of β-hematin.[6]

Computational studies carried out on the antimalarial diethylamino-alkoxyxanthanones suggest that the hemozoin crystal is a primary drug target, via stereoselective binding of the two amine groups of the molecule to acid groups exposed at the crystal surface, resulting in inhibition of hemozoin nucleation or growth. A model is proposed for the antimalarial action of artemisinin-type drugs involving efficient inhibition of crystal nucleation of hemozoin by binding onto all principal crystal faces, thus acting akin to classic tailor-made inhibitors of crystal nucleation. This model might also explain the effective antimalarial properties of a combination of artemisinin-type drugs and quinolines, assuming that the latter will inhibit growth along the fast-growing but small faces at the opposite ends of the needle-shaped hemozoin crystal.

A model has been presented of induced epitaxial nucleation of hemozoin via a lipid membrane in the digestive vacuole of a malaria parasite, based on a published electron micrograph of the digestive vacuole of a *Plasmodium falciparum* trophozoite inside a red blood cell, showing a cluster of aligned hemozoin crystals (Figure 15).[10] Studies on oriented nucleation of β-hematin crystals at the interface between lipid monolayers and water, or other liquids, are currently being undertaken.

Acknowledgment. This work was supported in part by the Kimmelmann Center at the Weizmann Institute of Science, the DanSync program of the Danish Natural Science Research Council, the Carlsberg Foundation and the European Community under TMR-Contract ERBFMGECT950059. Thanks are due to HASYLAB for synchrotron beamtime and to Professor Jochen Schneider, Director of HASYLAB. Regarding use of beamtime at the Advanced Photon Source, the UNICAT facility is supported by the Materials Research Laboratory, University of Illinois funded by U.S. DOE award DEFG02-91ER45439, the Oak Ridge National Laboratory, the National Institute of Standards and Technology and UOP LLC. Part of this work is funded by an Australian Research Council Discovery Grant. B.R.W.'s work is supported by an Australian Synchrotron Program Fellowship Grant and a Monash University Synchrotron Fellowship Grant.

Supporting Information Available: Experimental Section; Figure S1 showing the reported[13] effect of carbon chain length on the antimalarial activity (IC_{50}) and heme affinity (K_a) of diethylamino-hydroxyxanthone molecules; section describing inhibition of crystal nucleation of *R,S*-mandelic acid with quinine; section describing a computational study on binding of diethylamino-alkoxyxanthones to β-hematin crystal faces in correlation with antimalarial activity; section describing a model study on inhibition of crystal nucleation of *S*-alanine via additive combinations. This material is available free of charge via the Internet at http://pubs.acs.org.

JA0674183

Crystal Nucleation, Growth and Morphology of the Synthetic Malaria Pigment β-Hematin and the Effect Thereon by Quinoline Additives: The Malaria Pigment as a Target of Various Antimalarial Drugs

Inna Solomonov,[†] *Maria Osipova,*[†] *Yishay Feldman,*[‡] *Carsten Baehtz,*[§] *Kristian Kjaer,*[£] *Ian K. Robinson,*[#] *Grant T. Webster,*[††] *Don McNaughton,*[††] *Bayden R. Wood,*[††] *Isabelle Weissbuch,*[*†] *Leslie Leiserowitz*[*†]

[†]Dept. of Materials and Interfaces, The Weizmann Institute of Science, 76100-Rehovot, Israel;

[‡]Chemical Research Support, The Weizmann Institute of Science, 76100-Rehovot, Israel;

[§]Hasylab at DESY, Notkestr. 85, D-22607 Hamburg, Germany;

[£]Niels Bohr Institute, University of Copenhagen, Universitetsparken 5, DK-2100 Copenhagen, Denmark;

[#]Dept. of Physics and London Centre for Nanotechnology, University College, Gower St, London WC1E 6BT, England;

[††]Centre for Biospectroscopy and School of Chemistry, Monash University, 3800, Victoria, Australia.

Supporting Information

Experimental Section

Preparation of β-hematin crystals. β-Hematin crystals were grown using a standard and reliable way of obtaining β-hematin from a MeOH-DMSO solution containing hemin (Chloro(protoporphyrinato)iron(III) or Ferriprotoporphyrin IX chloride, Sigma) and 2,6-lutidine (2,6-dimethylpyridine) base.[27] In order to adopt the above procedure of crystal formation in the bulk to the

air-water interface, we replaced MeOH-DMSO by chloroform. In the first procedure 0.489g of hemin was dissolved in a minimal amount of dry 2,6-lutidine with stirring. Upon completion of the dissolution a 1:1 (35:35mL) mixture of MeOH and DMSO was added and the flask sealed and protected from moisture and ambient light. Such flasks were allowed to stand undisturbed from a few hours to several months. After an allotted time, the solution was filtered and a black precipitate collected, which was then washed with 50 mL MeOH and with deionized water until decanted water layers were colorless. The solid was dried in a dessicator until made use of.

For the second method of β-hematin preparation, ~3mg of hemin was dissolved in dry 2,6-lutidine (about 0.5mL), sonicated for 5min to form a homogenuous solution, to which chloroform was added to yield a 10 mL solution. After keeping the solution in the dark for 12 hours a black precipitate of β-hematin was formed.

For the induced nucleation of β-hematin crystals by a monolayer of dibehenoyl-*L*-α-phosphatidylcholine (DBPC) transferred on a octadecyltrichlorosilane (OTS)-covered Si wafers, the latter were placed vertically in the chloroform solution. The OTS monolayer on the surface of a Si (111) wafer was prepared according to the following procedure: (i) wafer sonication in acetone for 15 min; (ii) removal of the native SiO_2 layer in 40% NH_4F solution for 1 hour; (iii) sonication in Millipore water for 15 min; (iv) growing a fresh oxide layer in piranha solution (2:1 v of 96% H_2SO_4: 30% H_2O_2) at 90-100 ^oC for 30 min.; (v) sonication in water for 15 min and drying with pure N_2; (vi) immersion in a solution of OTS in bicyclohexyl ($2*10^{-2}$ M) for 24 hours followed by sonication for 15 min. in CCl_4, toluene, ethanol and water and drying with pure N_2. The average thickness of the OTS monolayer was found to be 29±4Å, by ellipsometry. A contact angle of 70º attests to the hydrophobic nature of the OTS-Si wafer. A monolayer of the phospholipid DBPC was compressed 30 mN/m on the water surface of a Langmuir trough and transferred by the Langmuir-Schaffer technique onto the OTS-Si wafer.

X-ray powder diffraction of hematin crystals nucleated by the DBPC monolayer. The measurements were carried out in reflection mode using a TTRAX III (Rigaku) diffractometer equipped

with a rotating anode Cu anode operating at 50 kV and 240 mA. First, specular diffraction (θ/2θ scan) that probes only crystallographic planes parallel to the plane of the Si wafer was made in Bragg-Brentano geometry. Then pole figures of the strong reflections were recorded at fixed Bragg angles using a Multi-purpose Attachment III (Euler cradle) that performed in-plane sample rotation at regularly increasing sample's tilt with respect to incident/diffracted beams plane.

Transmission Electron Microscopy (TEM) Measurements. The crystalline powders of β-hematin were dispersed in water and a drop deposited onto specimen grids (SPI, Cu 300 mesh) coated with carbon (upper) and polymer films. Selected specimen crystals were characterized in a TEM Philips CM120 microscope operated at 120 kV. Care was taken to minimize the time of beam irradiation received by each specimen during its imaging since crystal damage by the electron beam was sometimes observed. Electron diffraction (ED) patterns of single crystals were obtained from various specimens by selected area ED and their *d*-spacings measured with an accuracy of ±0.005 nm, using Gold and asbestos ED patterns as reference standards.

Grazing Incidence X-ray Diffraction (GIXD) Measurements. Chloroform solutions of hemin and 2,6-lutidine were spread at the air-water interface for the GIXD measurements, which were performed on the liquid surface diffractometer at the BW1 undulator beamline at the HASYLAB synchrotron source at DESY, Hamburg. The solutions were spread at room temperature on the water surface in a Langmuir trough. The air surrounding the trough was replaced by helium to reduce X-ray background scattering. The X-ray diffraction measurements were performed upon cooling the water subphase to 5°C. A monochromatic X-ray beam (λ=1.304Å) was adjusted to strike the liquid surface at an incident angle $\alpha_i < 0.85\alpha_c$ where α_c is the critical angle for total external reflection; this maximizes surface sensitivity. The GIXD signals are obtained from thin film crystallites that are randomly oriented about the water surface normal in the form of a 2D “powder”. A detailed description of GIXD applied to films on liquid surfaces has been given elsewhere.[20,22-24]

Synchrotron Powder X-ray Diffraction. The experiments were performed on a powder X-ray

diffractometer[32] at beamline B2 located at a bending magnet of the storage ring DORIS at HASYLAB, Hamburg. For monochromatisation, a water-cooled Si (111) double flat-crystal monochromator is used. A Ge (111) analyzing crystal in front of a scintillation counter allows collection of well-resolved powder diffraction data with a high signal-to-noise ratio. The samples, which -- in order to avoid affecting crystal coherence -- were not milled, were filled in glass capillaries with an outer diameter of 0.9 mm and a wall thickness of 0.01mm. The wavelengths of the synchrotron radiation used were 0.4528, 0.47 and 0.4996Å. The measurements were carried out at room temperature; a step size of 0.003° was chosen and the time for data collection was between 12 and 15h. In general the full width at half maximum (FWHM) of a reference material (LaB_6, 660a NIST standard) is $2\theta \approx 0.007^o$ with the setup, measured with a step size of 0.001°.

Coherent Grazing Exit X-ray Scattering. To examine the morphology of the crystal grains, Coherent X-ray Diffraction (CXD) experiments were undertaken at the 34-ID-C beamline of the Advanced Photon Source, Argonne National Laboratory, USA. The geometry used was similar to the coherent grazing exit scattering geometry for probing the structure of thin films[30], except that the detector was set to the Bragg angle of one of the strong powder reflections. The incident beam was focused to about 1 micron to limit the number of grains illuminated. Searches of the sample position and angle were made until the diffraction from a single grain was centered on the detector. The 2D direct-detection charge-coupled device (CCD) X-ray detector with a 20-micron pixel size was placed 1m from the sample to record the detailed sample of the Bragg reflection.

IR Attenuated Total Reflectance (ATR) spectroscopy. IR-ATR hyperspectral images were collected ($6cm^{-1}$ resolution and 64 co-added scans) on a Varian Stingray imaging spectrometer (Varian inc, US), equipped with a 64 × 64 MCT Focal Plane Array (FPA) detector and a Ge ATR objective. The large refractive index of the Ge objective allows sub diffraction limit spectroscopy, providing a spatial resolution that is almost as good as the Raman microscope[33,34]. The depth penetration of the IR-ATR is wavelength dependent and approximately equal to the wavelength of the radiation (*ca* 5-10 μm for the

wavenumber region of interest) so for infrared images the spectrum associated with each "pixel" is of a number of crystals. The Raman spectra, in contrast, are of individual crystals. The Ge objective was lowered on to β-hematin crystals on a microscope slide until sufficient pressure was applied to obtain adequate S/N. The hyperspectral images thus provided 4096 spectra of β-hematin, and quinine/chloroquine treated β-hematin. Spectral images were analyzed using the Cytospec software (Cytospec inc, NY, USA).

Micro-Raman Imaging Spectroscopy. Raman spectra were acquired on a Renishaw micro-Raman system 2000 (Renishaw pty ltd, Wootton-under-edge, UK) using 830nm excitation and a ×60 water immersible objective. Single crystals in a flat orientation were targeted. Spectra of 17 crystals of β-hematin and 16 crystals of β-hematin, grown in the presence of quinine and chloroquine, were recorded. Principal Components Analysis (PCA) within Unscrambler (Camo, Norway) was used to analyze the dataset. Each spectrum was recorded in 10 seconds with a *ca* 1-2 μm laser spot size and approximately 2-3 mW power on the sample.

Figure S1. Reported effect of carbon chain length on the antimalarial activity (IC_{50}) and heme affinity (K_a) of diethylamino-hydroxyxanthone molecules[13].

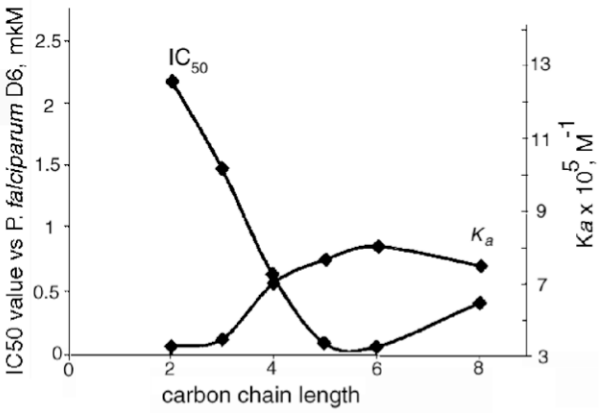

Inhibition of Crystal Nucleation of *R,S*-Mandelic Acid with Quinine. It is noteworthy that quinoline additives may inhibit the nucleation and growth of carboxylic acid crystals. For example, the crystal

precipitation time of *R,S*-mandelic acid increases significantly in the presence of 2.5% quinine and the crystals grow at a much slower rate (Table S1) although they do not change their shape relative to that of the pure form (Figure S2c).

Table S1. Visual inspection and estimate of the percentage of surface covered with crystal bunches of *R,S*-mandelic acid after the solution was poured in Petri dishes, cooled to RT and one single crystal seed inserted into each dish. (Q denotes additive quinine)

Time hrs	4g/10mL H_2O 6 exp.	4g/10mL H_2O 2.5%mol Q 3 exp.	4g/10mL H_2O 1%mol Q 6 exp.	4.5g/10mL H_2O 1.0%mol Q 6 exp.	4.5g/10mL H_2O 0.5%mol Q 6 exp.
0.5	fully crystallized	seed	seed	seed	few bunches
1.0		seed	seed	few bunches	~20%
1.5		seed	few bunches	~20-30%	~40%
2.0		seed+2 crystals	~50%	~50%	70-80%
4.0		few bunches	fully crystallized	70-80%	fully crystallized

This behavior may be understood in terms of the crystal structure of *R,S*-mandelic acid[52]; quinine should be able to inhibit growth of the eight symmetry-related {111} side faces as well as the {010} plate-like faces crystal, from which the carboxyl groups emerge (Figure S2a, b).

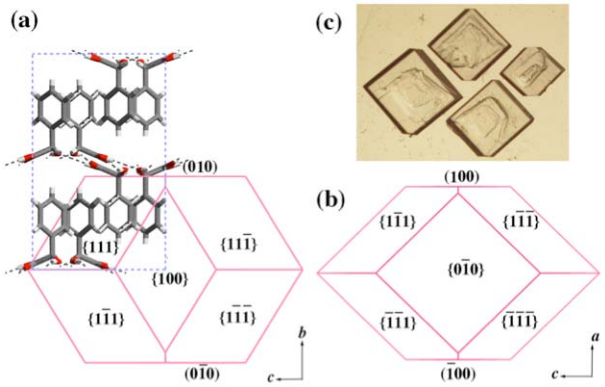

Figure S2. (a) Part of crystalline packing arrangement of *R,S*-mandelic acid. (b) Theoretical growth morphology depicting the various faces. (c) Photographs of {010} plate-like crystals of *R,S*-mandelic acid obtained from solution.

Binding of Diethylamino-alkoxyxanthones on β-Hematin Crystal Faces and Antimalarial Activity. In the Introduction, we alluded to the antimalarial activity of the diethylamino-alkoxyxanthones (Formula 1, main text), labeled XN*n*, *n* = 2-8, as expressed by a strong correlation, shown in SI Figure S1, between the heme affinity (*Ka*) measured in aqueous solution, the chain length and antimalarial potency as measured by the inhibitory concentration IC_{50} values[13]. Here we compare, by computation, the relative ability of XN*n* molecules with $(CH_2)_n$ side chains, *n*=2 (XN2) and *n*=5 (XN5), which have distinctly different IC_{50} values (2.2 *vs* 0.1 μM), to bind to the {011} and {001} crystal surfaces of β-hematin.

The drug has at each opposite end of the molecular chain an amino group that may bind to a surface-exposed β-hematin propionic acid moiety, via an $N\text{-}H^{+\cdots -}OOC$ interaction. The presence of an amine group at each end of the drug should, in principle, produce a stronger binding than a single amine group provided both ends are linked to the crystal surface by $N\text{-}H^{+\cdots -}O_2C$ hydrogen bonds. Such simultaneous binding would constitute more efficient "surface capping"[48] and subsequent crystal growth inhibition, leading to increased antimalarial efficiency of the drug. We confined the computational search of possible surface binding sites to those that would not only allow both amino groups of the drug to participate in hydrogen bonds, but also permit the formation of favorable van der Waals contacts between the crystal surface and the drug along its length. This constraint limited the search. The CERIUS[2] (Accelrys) software package was made use of for modeling the docking of the drug onto the {001} and {011} crystal surfaces and for eventual energy minimization of the system.

The length of molecule XN2 in extended form is ~17Å and thus too long to effectively bind to two carboxyl groups separated by the axial distance *a* = 12.2Å, but too short to bind to two such groups separated by 2*a*. Nevertheless, the molecule can align itself on the {001} face along the *a* axis and form an acid-base $NH^+\ldots{}^-O_2C$ bond at one end and a weaker $NH^+\ldots$ O=C-(Fe) interaction at its opposite end (Figure 13c,d). The computed docking energy is ~ -25 kcal/mol (Table 2).

Although we find a clear-cut correlation between the computed docking energies and the experimental IC_{50} values, other factors obviously may be at play. For example, molecule XN5, being longer than XN2, will induce a greater distortion about its immediate crystalline environment during the deposition of oncoming β-hematin molecular layers and so will be a stronger inhibitor to further growth and thus be a more effective antimalarial. Furthermore, we note that the smooth {100} face may also be a suitable $NH^{+}\cdots^{-}O_2C$ binding substrate for XN additives even though the face exposes carboxyl groups at an oblique angle to the surface, yet which are conformationally flexible (Figure 1b). Once again XN5 has the advantage that it can bind to the {100} face in more ways than XN2.

Model Study of Inhibition of Crystal Nucleation of *S*-alanine via Additive Combinations. We made use of *S*-alanine (*S*-Ala) as the host crystal, which consists of H-bonded chains aligned parallel to the *c*-axis (Figure S3a). The crystals, grown under ambient conditions from aqueous solutions of concentration 25g/100mL, were obtained after about 15-20 min (Figure S3b). *S*-Ala crystals grown in the presence of 1% *S*-phenylalanine (Phe) appeared after two hours as [001] needles (Figure S3e), a change in habit due to binding *S*-Phe to the crystal side faces (Figure S3d). Retardation of growth in the *c*-direction was attempted using three diamines, *o*- and *p*-phenylenediamines (labeled OPD and PPD) and 1,6-diaminohexane (DAH), the idea being that the amino groups would H-bond to the carboxylate groups exposed at the {011} faces of *S*-ala. The presence of 10% of each in the solution did not change the crystal habit, yet did delay precipitation time. The solution containing OPD and PPD yielded crystals within half an hour and two hours respectively, DAH delayed crystallization for 2-4 hours (based on 27 experiments). We propose that DAH is the better retarder of crystal nucleation because of chain flexibility and a molecular length (6.4Å) that matches the distance of 6Å between carboxylate groups on the {011} face (Figure S3f). A cocktail of 1% *S*-Phe and 10% DAH delayed appearance of *S*-Ala crystals from 8-20 hours, indicating that simultaneous use of two types of additives, which bind to different crystal faces, has a greater inhibiting effect on nucleation than each of the additives used alone.

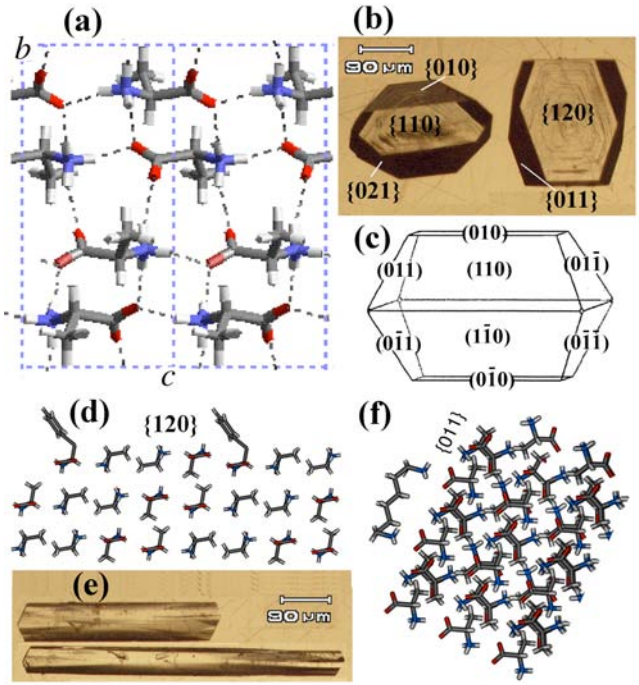

Figure S3. (a) Molecular packing arrangement of crystalline *S*-ala. (b) Photographs of the two different morphologies obtained from aqueous solution. The crystals faces are indexed. (c) Theoretical growth morphology. (d) Edge-on view of a {120} face of *S*-ala crystal, showing additive *S* Phe adsorbed thereon. (e) Morphology of *S*-ala crystals grown in the presence of additive *S* Phe. (f) Edge-on view of a {011} face of *S*-ala crystal, showing additive 1,6-diaminohexane (DAH) adsorbed thereon.

Chapter 4

Raman Spectroscopic Analysis of Malaria Infected Erythrocytes

CHAPTER SUMMARY

Although FTIR spectroscopy can detect lipid changes at different lifecycle stages of the parasite and can detect haemozoin in single erythrocytes, it cannot detect structural changes of haemozoin following quinoline drug treatment of trophozoite infected erythrocytes. This fact directed research towards investigating the applications of resonance Raman spectroscopy, in combination with PCA, to detect structural changes in the haemozoin biomineral within live trophozoite infected parasites in red blood cells after incubation with CQ. This research is discussed in the first manuscript of this chapter (**III**). The second manuscript in this chapter (**IV**) builds upon these findings and describes the use of resonance Raman in combination with partial dark-field microscopy to detect, in thick blood films, small inclusions of haemozoin in infected red blood cells that would otherwise be difficult to see with conventional bright-field microscopy.

While widespread resistance to chloroquine now means that it has lessened clinical utility, its putative target, haemozoin, remains an eminently suitable target for new drugs as its formation is unique to the malaria parasite. In addition, it is not subject to genetic mutation as it is of host origin and is a chemically specific molecule. Manuscript **III** in this chapter demonstrates that chloroquine has a measurable influence on the chemical structure or composition of haemozoin as opposed to the amount of haemozoin generated in the digestive vacuole. A number of bands assigned to A_{1g} and B_{1g} modes characteristic of the haemozoin biomineral are reduced in intensity in the CQ-treated cells. This is a significant finding given that it displays CQ acting directly on haemozoin in live parasites.

Manuscript **II** shows that FTIR-ATR measurements taken of quinoline treated β-haematin demonstrate that quinoline can affect its surface propionic acid groups.

However, there is no evidence in the Raman spectrum of such a drug binding mechanism. Resonance Raman spectroscopy supports a model in which quinoline binds to the face of the crystal within the digestive vacuole of the malaria parasite via a sandwich complex of supramolecular interactions. However, it does not rule out surface propionic acid group binding as a contributing mechanism because these modes are not Raman active at near-IR excitation wavelengths.

The second paper in this chapter (**IV**) reports on a serendipitous discovery of a partial dark-field effect from the experimental setup, which allowed the haemozoin deposits to "light up" and be selectively targeted with the Raman microscope. The presence of haemozoin deposits was confirmed by the 1569 cm^{-1} band in the Raman spectrum, which is a haemozoin marker band. An Unsupervised Hierarchical Cluster Analysis (UHCA) from a Raman image of a thick blood film of infected erythrocytes was performed in the 1700 – 1300 cm^{-1} spectral range. A 5 coloured cluster map shows very small nano-haemozoin inclusions (coloured in red) that appear in some of the trophozoite infected cells and also in other cells, where trophozoite infection was not immediately obvious. In normal bright-field microscopy, it is impossible to observe for these nano-haemozoin inclusions and because they are difficult to see in partial dark-field images it is difficult to confirm these deposits as nano-haemozoin inclusions. However, the relative intensity of the 1569 cm^{-1} band compared to the 1639 cm^{-1} band is strong evidence. This shows the potential of partial dark-field Raman microscopy to observe for early trophozoite stage parasites.

Monash University

Monash Research Graduate School

Declaration for Thesis Chapter 4

Declaration by candidate

In the case of Chapter 4 the nature and extent of my contribution to the work (**Paper III**) was the following:

Nature of contribution	Extent of contribution (%)
Experimental design, interpretation of results, writing of manuscript	- >80%

The following co-authors contributed to the work. Co-authors who are students at Monash University must also indicate the extent of their contribution in percentage terms:

Name	Nature of contribution	Extent of contribution (%) for student co-authors only
Samantha Deed	Culturing of cells, drafting of manuscript	-
Leann Tilley	Drafting of manuscript	-
Don McNaughton	Drafting of manuscript, provided supervision	-
Bayden Wood	Drafting of manuscript, provided supervision	-

Candidate's Signature

Date

15/04/09

Declaration by co-authors

The undersigned hereby certify that:

(1) the above declaration correctly reflects the nature and extent of the candidate's contribution to this work, and the nature of the contribution of each of the co-authors.

(2) they meet the criteria for authorship in that they have participated in the conception, execution, or interpretation, of at least that part of the publication in their field of expertise;

(3) they take public responsibility for their part of the publication, except for the responsible author who accepts overall responsibility for the publication;

(4) there are no other authors of the publication according to these criteria;

(5) potential conflicts of interest have been disclosed to (a) granting bodies, (b) the editor or publisher of journals or other publications, and (c) the head of the responsible academic unit; and

(6) the original data are stored at the following location(s) and will be held for at least five years from the date indicated below:

Location(s)	Department of Chemistry, Centre for Biospectroscopy, Monash University, Clayton

Please note that the location(s) must be institutional in nature, and should be indicated here as a department, centre or institute, with specific campus identification where relevant.]

Signature	Date
Department of Biochemistry, La Trobe University Bundoora [redacted]	31/3/09
Dept. Biochem. La Trobe Uni [redacted]	31/3/09
Bayden R. Wood (Monash Uni) [redacted]	15/4/09
Don Mcnaughton (Monash) [redacted]	15/4/09

FEBS Letters 582 (2008) 1087–1092

Resonance Raman spectroscopy can detect structural changes in haemozoin (malaria pigment) following incubation with chloroquine in infected erythrocytes

Grant T. Webster[a], Leann Tilley[b,c], Samantha Deed[b,c], Don McNaughton[a], Bayden R. Wood[a,*]

[a] *Centre for Biospectroscopy and School of Chemistry, Monash University, Clayton, Vic. 3800, Australia*
[b] *Department of Biochemistry, La Trobe University, Melbourne, Vic. 3086, Australia*
[c] *Centre of Excellence for Coherent X-ray Science, La Trobe University, Melbourne, Vic. 3086, Australia*

Received 15 January 2008; revised 25 February 2008; accepted 25 February 2008

Available online 4 March 2008

Edited by Richard Cogdell

Abstract **Resonance Raman spectroscopy was applied to monitor the effects of chloroquine (CQ) treatment on cultures of *Plasmodium falciparum* trophozoites. A number of bands assigned to A_{1g} and B_{1g} modes characteristic of the haemozoin aggregate are reduced in intensity in the CQ-treated cells, however, no bands from the CQ are observed. The intensity changes are attributed to intermolecular drug binding of the CQ in a sandwich type complex between ferriprotoporphyrin IX (FePPIX) dimer units. It is postulated that the CQ binds via π–π interactions between adjacent and orientated porphyrins thereby disrupting the haemozoin aggregate and reducing excitonic interactions between adjacent haems. The results show the potential of Raman microscopy as a screening tool for FePPIX:drug interactions in live cells.**

Keywords: Malaria; Resonance Raman spectroscopy; Chloroquine; Chemometrics; Haemozoin

1. Introduction

Malaria is still considered to be one of the most deadly diseases in the world, affecting over 500 million people and causing over 1 million deaths per year [1]. The parasite, *Plasmodium falciparum*, invades the body via the bite of the female *Anopheles* mosquito and undergoes the vertebrate host stages of its lifecycle. During the intraerythrocytic stage haemoglobin is degraded inside the digestive vacuole of the parasite into toxic free haem and denatured globin [2,3]. The process of detoxification involves the conversion of iron-protoporphyrin IX (FePPIX) to haemozoin, also known as malaria pigment, which is an insoluble compound located in the food vacuole of the parasite. Haemozoin is spectroscopically identical to its synthetic analogue β-haematin [4,5], which is known to be an array of dimers linked through reciprocal iron-carboxylate bonds to one of the propionate side chains of an adjacent Fe(III)PPIX moiety [6]. Quinoline drugs such as chloroquine, quinine and amodiaquine are thought to inhibit the FePPIX crystallisation by binding to monomeric or dimeric Fe(III)PPIX, resulting in the build up of toxic free FePPIX which can kill the parasite [7–10]. de Villiers et al. [10] propose a model in which the spontaneously formed aqueous Fe(III)PPIX dimer non-covalently interacts with the unligated faces of two five-coordinate H_2O/HO^-Fe(III)PPIX molecules, with the axial H_2O/HO^- ligands pointing outwards. Three models for drug–FePPIX interactions have been proposed. The first involves inhibition of the growth of the haemozoin crystal by chiral specific binding of the drug to the corrugated surface of haemozoin through the vinyl and methyl groups located on the Fe(III)PPIX surface [11]. In the second model drug binding occurs via a sandwich complex to the face of the crystal through π–π interactions [12]. In the third model quinoline drugs are thought to form π–π interactions with haematin μ-oxo dimers ($[Fe(III)PPIX]_2O$) [13]. This is thought to decrease the availability of monomeric haematin (H_2O/OH^-Fe(III)PPIX) for incorporation into haemozoin by shifting the equilibrium towards the μ-oxo dimer [14]. It should be noted however that the existence of a μ-oxo dimer form of haematin under the conditions of the digestive vacuole has been questioned [10].

While several studies have applied spectroscopic methods to investigate Fe(III)PPIX:drug interactions in solution [13,15] and the solid state [16] hitherto no spectroscopic study has investigated the effect of drug treatment on single *P. falciparum*-infected red blood cells. Using polarisation-resolved resonance Raman spectroscopy Frosch et al. [15] observed small wavenumber shifts when CQ was mixed with haematin in solution, which further supports a non-covalent Fe(III)PPIX:drug complex. Frosch et al. [17] recently reported UV resonance Raman spectra of chloroquine under physiological conditions. In this work mode assignment was performed by comparison with Density Functional Theory (DFT) calculations which suggested that the protonation states of chloroquine greatly influence the molecular geometry, vibrational modes and molecular orbitals important for π–π interactions with haemozoin [17]. Near IR Surface Enhanced Raman Spectroscopy (NIR-SERS) measurements [18] of a CQ–FePPIX complex were compared with data for haematin and CQ alone. The CQ–FePPIX complex indicated an interaction between the quinoline ring of the drug and the porphyrin ring [18].

In this work, we combine Raman microscopy using 782 nm excitation, with Principal Components Analysis (PCA) to investigate the effect of CQ treatment on the physical organisation of haemozoin within the digestive vacuole of *P. falciparum* trophozoites. We present evidence that CQ has an effect on the molecular environment of haemozoin within a red blood cell and provide the first spectroscopic evidence of CQ interfering

*Corresponding author. Fax: +61 3 9905 4597.
E-mail address: bayden.wood@sci.monash.edu.au (B.R. Wood).

0014-5793/$34.00
doi:10.1016/j.febslet.2008.02.062

with haemozoin formation, which paves the way to monitor such FePPIX:drug interactions in situ.

2. Experimental

2.1. Cell culture

P. falciparum (a CQ sensitive strain, D10) was maintained in continuous culture using human erythrocytes obtained from the Red Cross Blood Bank, Melbourne [19]. Parasitised erythrocytes were cultured in complete culture medium (CCM) consisting of RPMI 1640 (GIBCO BRL), 25 mM hydroxypiperazine-*N*′-2-ethane sulfonic acid (HEPES, Sigma, pH 7.4), 2 g/l sodium bicarbonate (AnalR) and 4 mM Glutamax (Invitrogen). This was supplemented with 0.16% glucose (AnalR), 0.21 mM hypoxanthine (Sigma), 22 μg/ml gentamycin (Sigma) and 4% human serum and 0.25% Albumax I (GIBCO-BRL). The cultures were kept at 37 °C in a humidified atmosphere of 5% CO_2, 1% O_2 and 90% N_2. Synchronised cultures (~5% parasitemia) of late ring stage parasites were treated for 20 h with 100 nM CQ. This concentration is sufficient to inhibit growth of the parasites by approximately 80% as monitored by uptake of [^{3}H]-hypoxanthine (data not shown). Infected RBCs (10 μl) were suspended in 10 ml of 0.9% saline solution and were placed in an 80 mm diameter glass aluminium sputter coated Petri dish; this was over-coated with poly-L-lysine to adhere the blood cells to the base of the dish. The experiment was repeated three times.

2.2. Raman microscopy

Raman spectra of control and CQ-treated *P. falciparum*-infected erythrocytes were recorded as described previously [20,21]. When the power is kept low and measurements are recorded in growth media in a temperature regulated environment, live infected red blood cells show no visible damage to the membrane or photo-decomposition of the haemoglobin. The Renishaw system 2000 spectrometer used was equipped with a 782 nm diode laser with ~18 mW raw output power and ~3–4 mW power at the sample, a BH2-UMA Olympus optical microscope and a Zeiss water immersion 60× objective. The instrument was calibrated daily using the 520.5 cm^{-1} band of a silicon wafer. Raman spectra were recorded by focusing the laser directly on the haemozoin pigment within the live infected red blood cells. For both the control and the CQ incubated cells spectra were recorded from 30 different cells. Raman spectra were recorded in the spectral range 1800–200 cm^{-1} using a single 10 s exposure at 10% power. All spectra were normalised to the ν_{10} $\nu(C_\alpha C_m)_{asym}$ B_{1g} vibrational mode. Spectra of haematin, haematin μ-oxo dimer and chloroquine were derived by averaging 30 spectra taken at various different positions on several crystals for each compound using a normal 50× objective.

2.3. Data analysis

PCA is a fundamental technique used in multivariate data analysis and involves the decomposition of data into noise and structural components. The dimensionality of the data set is reduced by plotting the objects onto principal components (PC's) with each consecutive component orthogonally positioned with respect to the previous PC. Each PC gives rise to a percentage of variance in the data set, with the explained variance decreasing as the PC increases. A plot of the scores along each PC (scores plot) allows differences and similarities to be easily recognised. Each score represents a single spectrum and is plotted as a point on a two-dimensional axis and the position of each point is dependent on the individual variance contribution of the spectrum to each PC [16]. The loadings plot is used in conjunction with the scores plot to identify the variables that induce the most variability in the data set. In this work, we applied PCA to ascertain biological variability and investigate the uptake of drugs in a population of *P. falciparum* trophozoites. Two different methodologies were used to minimize baseline affects. Firstly, an Extended Multiplicative Scatter Correction (EMSC) was applied to all data to remove physical affects, primarily baseline variation between spectra of each data set. Secondly, a second derivative with a 13 point Savitzky–Golay smoothing function was applied.

2.4. Materials and synthesis

The μ-oxo dimer form of haematin was prepared by dissolving haematin (Sigma–Aldrich) in aqueous base (0.1 M NaOH) and 10% (v/v) pyridine to produce 15.6 mM haematin μ-oxo dimer solution [10,22]. The solution was characterised by its characteristic UV–VIS spectroscopy [10,22]. The 15.6 mM haematin μ-oxo dimer solution was dried onto aluminium sputter coated slide and the characteristic Raman band (ν(Fe–O_{sym})) at 413 cm^{-1} was observed in the Raman spectrum [23–26]. The solution was also dried onto a Golden Gate™ Diamond attenuated total reflectance ATR accessory on a Bruker Equinox FTIR spectrometer and spectra recorded at a resolution of 4 cm^{-1}. The band at ~880 cm^{-1} assigned to the IR ν_{asym} (Fe–O–Fe) absorbance confirms the presence of the μ-oxo dimer (data not shown). Chloroquine diphosphate was purchased from Sigma–Aldrich.

3. Results and discussion

The haemozoin crystal is readily located as a dark pigment granule in brightfield images of live infected red blood cells (Fig. 1, inset). The spectrum from the region of the haemozoin is compared with spectra of haematin and the haematin μ-oxo-dimer in Fig. 1. For comparative purpose the spectra are normalised to the band designated ν_{10}(1623 cm^{-1}). The mode notation is based on that proposed by Abe et al. [27] for the resonance Raman spectra of nickel octa-ethyl porphyrin; where under the D_{4h} symmetry point group the modes are designated ν_1–ν_9 for A_{1g}, ν_{10}–ν_{18} for B_{1g}, ν_{19}–ν_{26} for A_{2g}, ν_{27}–ν_{35} for B_{2g}, and ν_{36}–ν_{55} for E_u modes. The A_{1g} modes are totally symmetric while the B_{1g}, A_{2g}, B_{2g} modes are non-totally symmetric. The E_u modes are IR and Raman active. The symmetry of ferric high spin haems such as haemozoin, haematin and β-hameatin is ideally C_{4v} because the Fe atom is translocated out of the porphyrin plane but the D_{4h} notation is often adopted by convention. The γ symbol is used to designate out-of-plane modes of which there are a number of categories which include (1) out-of-plane wagging modes, (2) tilting, and (3) internal folding of the pyrrole rings. The strong bands in the haemozoin spectrum include the in-plane asymmetric stretch of the porphyrin ring ν_{10}($\nu(C_\alpha C_m)_{asym}$) at 1623 cm^{-1} and the in-plane stretch of the vinyl group ν_{11}($\nu(C_\beta C_\beta)$) at approximately 1552 cm^{-1}. Bands at 1570, 1376, 1238 and 972 $cm^{-1}$are assigned to ν_2($\nu(C_\beta C_\beta)$), ν_4(ν(pyrrole half-ring)$_{sym}$), ν_{42}($\delta(C_mH)$), and ν_{46}(δ(pyrrole deform)$_{asym}$), respectively, and are listed in Table 1. Bands present at 796 and 753 cm^{-1} are assigned to

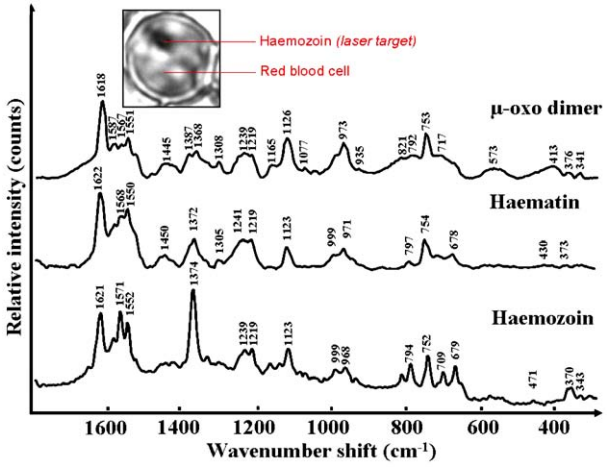

Fig. 1. Resonance Raman spectra of haemozoin in live red blood cells, and of dried samples of haematin and haematin μ-oxo dimer using a 782 nm excitation wavelength. Inset: Brightfield and resonance Raman image of a *P. falciparum*-infected red blood cell. The spot represents the region from which the Raman spectrum was collected.

Table 1
Band assignments for haemozoin, haematin μ-oxo-dimer and haematin

Haemozoin (cm^{-1})	Haematin (cm^{-1})	μ-oxo dimer (cm^{-1})	Assignment	Symmetry term	Vibrational mode
1623	1622	1618	ν_{10}	B_{1g}	$\nu(C_\alpha C_m)_{asym}$
1570	1568	1567	ν_2	A_{1g}	$\nu(C_\beta C_\beta)$
1552	1550	1551	ν_{11}	B_{1g}	$\nu(C_\beta C_\beta)$
–	–	1387	–	–	$\nu_{sym}(COO^-)$
1376	1372	1368	ν_4	A_{1g}	ν(pyrrole half-ring)$_{sym}$
1238	1241	1239	ν_{42}	E_u	$\delta(C_mH)$
972	971	973	ν_{46}	E_u	δ(pyrrole deform)$_{asym}$
796	797	792	ν_6	A_{1g}	ν(pyrrole breathing)
751	754	753	ν_{15}	B_{1g}	ν(pyrrole breathing)
709	–	–	γ_{15}	B_{2u}	ν(pyrrole fold)$_{asym}$
678	678	–	ν_7	A_{1g}	ν(pyrrole deform)$_{sym}$
–	–	413	–	–	$\nu(Fe–O)_{sym}$
343	–	341	ν_8	A_{1g}	ν(Fe–N)

ν = In-plane stretch, γ = out-of-plane stretch, δ = deformation mode, α, β and m refer to carbon positions on the porphyrin.

the full pyrrole ring breathing modes ν_6 and ν_{15} whilst bands at 712, 680 and 343 $cm^{-1}$are assigned to γ_{15} (ν(pyrrole fold)$_{asym}$), ν_7(ν(pyrrole deform)$_{sym}$) and Fe-ligand stretching modes [27]. In some controls and CQ-treated cultures an unassigned band at 472 cm^{-1} was observed, the origin of which is not understood. Most of the bands reported above are also observed in the haematin monomer and μ-oxo dimer but are less intense when compared with the normalisation band ν_{10} (1623 cm^{-1}) and in some cases are slightly shifted. The intensities of the Raman bands of the haematin monomer and μ-oxo dimer relative to ν_{10} are reduced compared to the bands for haemozoin. The differences in spectral intensity may reflect differences in π–π interactions between porphyrins in the crystalline array. We have previously identified atypical resonance Raman enhancement in haematin, haemozoin and β-haematin when exciting with near-IR wavelengths including 780 and 830 nm [28]. Bands assigned to totally symmetric A_{1g} modes were dramatically enhanced relative to ν_{10} (1623 cm^{-1}). These bands normally become enhanced when exciting into the Soret band at ~400 nm from a type A or Frank–Condon mechanism. The enhancement was found to be stronger for haemozoin and β-haematin compared to haematin. It was hypothesised that energy in the form of an exciton can migrate throughout the FePPIX array through the superposition of excited electronic states in the aggregate. Excitonic interactions have been shown to cause unusual Raman enhancement patterns [28] and mechanisms such as Aggregated Enhanced Raman Scattering (AERS) have been put forward to explain such patterns [29–36]. It was reasoned that anti-malarials that bond via π–π interactions to FePPIX could in theory act as molecular spacers and reduce the excitonic effects in the porphyrin array. This in-turn would manifest in the Raman spectrum as a reduction in intensity of vibrational modes sensitive to the electron density of the porphyrin such as ν_4, which is referred to as the "electron density marker band" or the "oxidation state marker band".

To test this hypothesis ring stage infected RBCs were incubated in the presence or absence of 100 nM CQ for 20 h. This caused an 80% decrease in parasite growth as determined by uptake of [^{3}H] hypoxanthine (data not shown). Fig. 2 presents average Raman spectra from the region of the haemozoin crystal in control (n = 30) and CQ-treated (n = 30) samples. The average spectrum from the CQ-treated cells shows a distinct reduction in the intensity of the A_{1g} modes: 1570, 1376, 796, 678 cm^{-1} and the B_{1g} modes: 1552, 751 cm^{-1} when compared

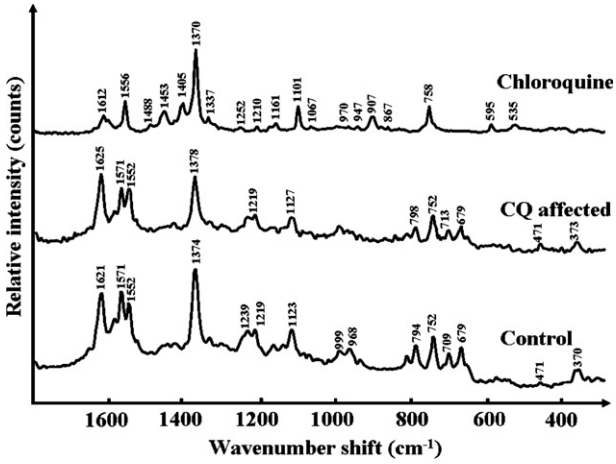

Fig. 2. Micro-Raman spectra, using 782 nm excitation of haemozoin in untreated (control) and CQ-treated infected red blood cells. A spectrum of a dried sample of chloroquine disphosphate (CQ) is shown for comparison.

with the controls. This intensity reduction for some of these modes is more easily seen in the bar graph presented in Fig. 3. There is a consistent but small shift in some of the Raman bands (Table 2) whilst ν_2, which remains at 1552 cm^{-1}, appears to broaden (6.8–7.4 cm^{-1}) in response to the drug treatment. These changes in position, intensity and the shape of the Raman bands following CQ treatment indicate changes in molecular environment of the malaria pigment upon drug interaction. It is interesting to note the sensitivity of the so called "electron density marker band", ν_4 to the drug treatment. The position of this band is thought to be sensitive to oxidation state [37]. In this case the relative intensity of ν_4 may be an indicator of the strength of π–π interactions. The other band that appears sensitive to electron density is the other A_{1g} mode ν_2 at 1552 cm^{-1}. Fig. 4a shows the difference spectrum calculated from the average spectra presented in Fig. 2. The difference spectrum shows a number of derivative like features associated with changes in intensity, position and width of haemozoin bands including the A_{1g} and B_{1g} modes.

PCA was applied to ascertain the spectral variance within the population of cells and detect underlying patterns within the data. In the PC1 versus PC2 scores plot each spectrum is represented as a point plotted on a set of PC orthogonal axes

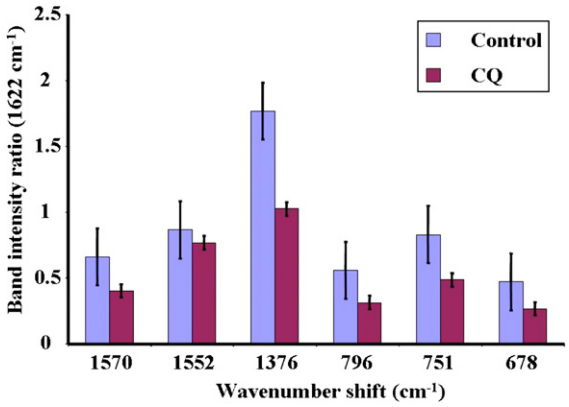

Fig. 3. Plot of intensities (relative to the 1622 cm^{-1} band for A_{1g} and B_{1g} vibrational modes for haemozoin in control and CQ-treated infected red blood cells.

Table 2
Raman band shifts and broadening for haemozoin from control and CQ-treated red blood cell

Control (cm^{-1})	CQ affected (cm^{-1})
1623	1626
1552[a]	1552[a]
1376	1378
796	799
709	712

[a]Band broadening.

that describes the variance in the data set. An initial PCA analysis was performed on second derivative data from control and drug inoculated cells. The PC1 versus PC2 scores plot showed some separation (data not shown) but the first PC explained only 17% of the explained variance. An examination of the loadings plot revealed strong loadings associated with the totally symmetric A_{1g} modes: 1567, 1370, 791, 675 cm^{-1} and B_{1g} modes at 1617 and 744 cm^{-1} (Fig. 4b). The loadings plot correlates well with the difference spectrum calculated using the average spectra. The most extreme variables were selected in Fig. 4b, as indicated by all the variables outside the dashed lines, and the PCA was recalculated to reduce the noise level and increase the explained variance along PC1. The resulting scores plot (Fig. 5) shows a clear separation along PC1 between CQ-treated and control data sets. The explained variance for PC1 is 52% followed by 11% for PC2.

Previous studies [16] have supported the suggestion of π–π stacking of quinoline drugs to malaria pigment. Solomonov et al. [16] found that when quinine and chloroquine were bound to β-haematin, the intensity of the bands attributed to A_{1g} modes appeared less intense compared to the controls and there was a significant degree of separation in PCA scores plots for both data sets. The spectrum of chloroquine, itself, is displayed in Fig. 2 and a vibrational assignment for all significant modes for chloroquine can be found in the work of Frosch et al. [17]. The spectrum for haemozoin in the CQ-treated infected red blood cells (Fig. 2) displays no peaks attributable to chloroquine, probably because the concentration of chloroquine employed (100 nM) is too low to be detected within the sensitivity limits of the Raman instrument. Hence there is no simple direct evidence for drug binding to the surface of the crystal. However, Solomonov et al. [16] show indirect evidence of drug binding to the surface of β-haematin crystals using IR-ATR analysis, where changes in what are hypothesised to be surface propionic acid groups [14] are observed. An equivalent band is not observed in the Raman spectrum because it is not Raman active. Furthermore, there is no evidence of distinct Raman bands from the μ-oxo dimer form of haematin observed in the spectrum, in either control or CQ-treated samples.

The differences observed in the spectra for the CQ-treated cells are subtle changes in the intensity and position of haemozoin bands. The small shifts and intensity differences provide support for a model where the CQ binds between the FePPIX dimer units and is held in place by π–π interactions

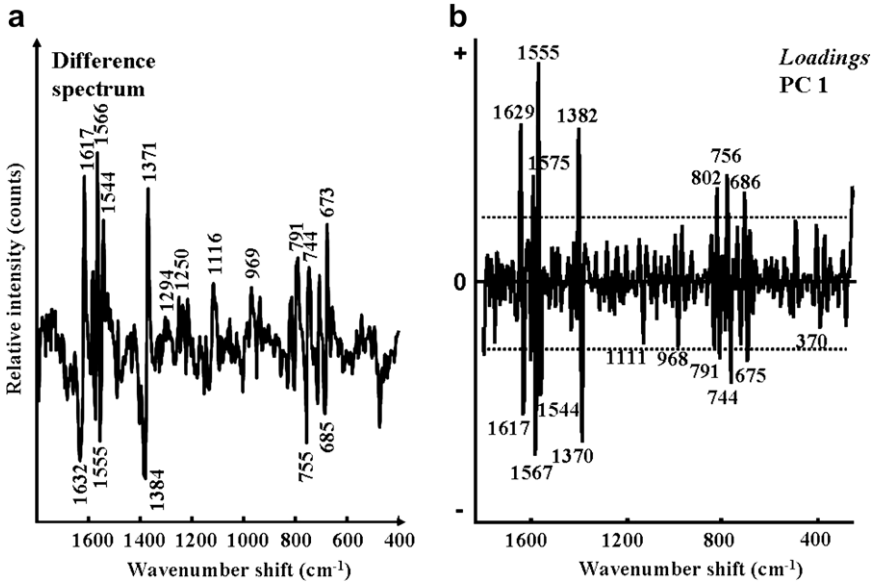

Fig. 4. (a) Difference spectrum of the average spectra for haemozoin in CQ-treated and control infected red blood cell. (b) PCA loadings plot of CQ-treated and control groups taken from the PCA scores plot (Fig. 3) along PC1 after a 2nd derivative function was applied.

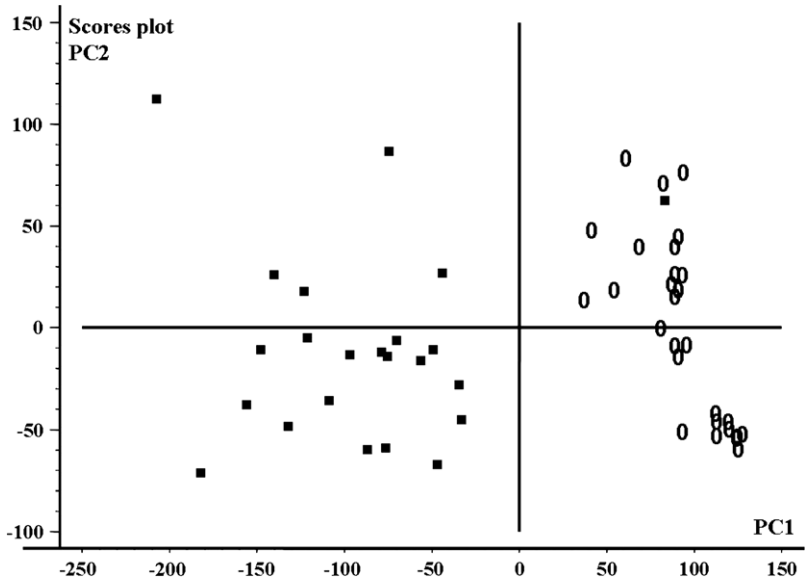

Fig. 5. PCA scores plot of control (0) and CQ-treated (■) infected red blood cell data sets taken from the PCA loadings plot (Fig. 4b) along PC1 of the extreme variables.

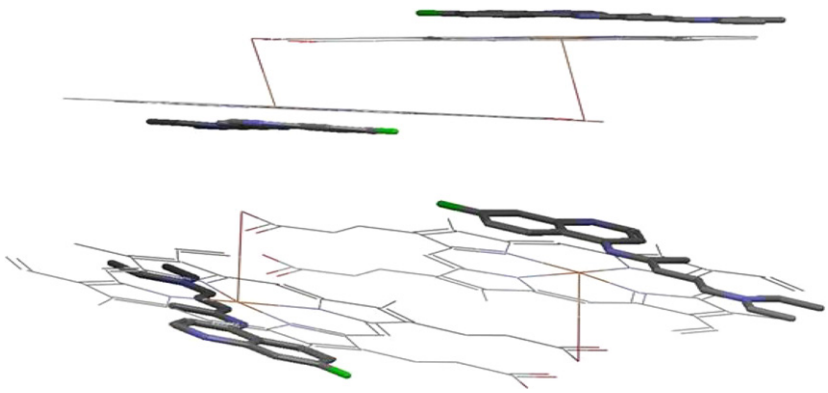

Fig. 6. Model structure of a β-haematin dimer with the antimalarial drug chloroquine binding via π–π interactions of the quinoline rings to the porphyrin rings of the Fe(III)PPIX.

as displayed in Fig. 6. Such a molecular spacer could potentially reduce the probability of intermolecular migration of energy in the form of an exciton throughout the crystal. This model is supported by previous studies which show that CQ, when mixed with haematin in solution, results in only small wavenumber (cm^{-1}) shifts in the spectra [15]. Similar studies on β-haematin (synthetic malaria pigment) coated with antimalarials (CQ and quinine) show a very clear separation in the scores plot along PC1 [16]. The loadings plot for the β-haematin/quinine data set also showed that the A_{1g} and B_{1g} modes including (ν_{10}) 1626 cm^{-1}, (ν_2) 1566 cm^{-1}, (ν_2) 1551 cm^{-1}, (ν_4) 1372 cm^{-1}, (ν_6) 797 cm^{-1} and (ν_7) 677 cm^{-1} are the modes affected, again supporting a non-covalent π–π drug binding orbital overlap mechanism.

Although previous IR-ATR [16] have shown that drug binding may affect the surface propionic acid groups, there is no evidence in the Raman spectrum of such a drug binding mechanism. Resonance Raman spectroscopy supports drug binding via a sandwich complex through π–π orbital overlap to the face of the crystal [12] within the digestive vacuole of the malarial parasite. However, it does not rule out surface propionic acid group binding as a contributing mechanism because these modes are not Raman active at near-IR excitation wavelengths.

Acknowledgements: This work is supported by Discovery and Centre of Excellence grants from the Australian Research Council. Dr. Bayden Wood was supported by an Australian Synchrotron Research Fellow Grant and is currently supported by a Monash Synchrotron Fellowship Grant. We thank Mr. Finlay Shanks (Monash University) for instrument support and maintenance.

References

[1] Sachs, J. and Malaney, P. (2002) The economic and social burden of malaria. Nature 415, 680–685.
[2] Schmitt, T.H., Frezzatti, W.A.J. and Schreier, S. (1993) Haemin-induced lipid membrane disorder and increased permeability: a molecular model for the mechanism of cell lysis. Arch. Biochem. Biophys. 307, 96–103.
[3] Sugioka, Y. and Suzuki, M. (1991) The chemical basis for the ferriprotoporphyrin IX–chloroquine complex induced lipid peroxidation. Biochim. Biophys. Acta 1074, 19–24.

[4] Slater, A.F.G., Swiggard, W.J., Orton, B.R., Flitter, W.D., Goldberg, D.E., Cerami, A. and Henderson, G.B. (1991) An iron-carboxylate bond links the haem units of malaria pigment. Proc. Natl. Acad. Sci. 88, 325–329.
[5] Bohle, D.S., Conklin, B.J., Cox, D., Madsen, S.K., Paulson, S., Stephens, P.W. and Yee, G.T. (1994) Structural and spectroscopic studies of β-haematin (the haem coordination polymer in malaria pigment). Am. Chem. Soc. Symp. Ser. 572, 497–515.
[6] Pagola, S., Stephens, P.W., Bohle, D.S., Kosar, A.D. and Madsen, S.K. (2000) The structure of malaria pigment β-haematin. Nature 404, 307–310.
[7] Ridley, R.G. (2002) Medical need, scientific opportunity and the drive for antimalarial drugs. Nature 415, 686–693.
[8] Egan, T.J., Hunter, R., Kaschula, C.H., Marques, H.M., Misplon, A. and Walden, J. (2000) Structure–function relationships in aminoquinolines: effect of amino and chloro groups on quinoline–haematin complex formation, inhibition of β-haematin formation, and antiplasmodial activity. J. Med. Chem. 43, 283–291.
[9] Egan, T.J. and Marques, H.M. (1999) The role of haem in the activity of chloroquine and related antimalarial drugs. Coord. Chem. Rev. 190–192, 493–517.
[10] de Villiers, K.A., Kaschula, C.H., Egan, T.J. and Marques, H.M. (2007) Speciation and structure of ferriprotoporphyrin IX in aqueous solution: spectroscopic and diffusion measurements demonstrate dimerisation, but not μ-oxo dimer formation. J. Biol. Inorg. Chem. 12, 101–117.
[11] Buller, R., Peterson, M.L., Almarsson, O. and Leiserowitz, L. (2002) Quinoline binding site on malaria pigment crystal: a rational pathway for antimalaria drug design. Cryst. Growth Des. 2, 553–562.
[12] Sullivan, D.J.J., Gluzman, I.Y., Russell, D.G. and Goldberg, D.E. (1996) On the molecular mechanism of chloroquine's antimalarial action. Proc. Natl. Acad. Sci. 93, 11865–11870.
[13] Egan, T.J. (2006) Interactions of quinoline antimalarials with haematin in solution. J. Inorg. Biochem. 100, 916–926.
[14] Dorn, A., Vippagunta, S.R., Matile, H., Jacquet, C., Vennerstrom, J.L. and Ridley, R.G. (1998) An assessment of drug–haematin binding as a mechanism for inhibition of haematin polymerisation by quinoline antimalarials. Biochem. Pharmacol. 55, 727–736.
[15] Frosch, T., Kustner, B., Schlucker, S., Szeghalmi, A., Schmitt, M., Kiefer, W. and Popp, J. (2004) In vitro polarization-resolved resonance Raman studies of the interaction of haematin with the antimalarial drug chloroquine. J. Raman Spectrosc. 35, 819–821.
[16] Solomonov, I., Osipova, M., Feldman, Y., Baehtz, C., Kjaer, K., Robinson, I.K., Webster, G.T., McNaughton, D., Wood, B.R., Weissbuch, I. and Leiserowitz, L. (2007) Crystal nucleation, growth, and morphology of the synthetic malaria pigment β-haematin and the effect thereon by quinoline additives: the malaria pigment as a target of various antimalarial drugs. J. Am. Chem. Soc. 129, 2615–2627.
[17] Frosch, T., Schmitt, M., Gerhard, B., Wolfgang, K. and Popp, J. (2007) Structural analysis of the anti-malaria active agent chloroquine under physiological conditions. J. Phys. Chem. B 111, 1815–1822.
[18] Pinzaru, S.C., Peica, N., Kustner, B., Schlucker, S., Schmitt, M., Frosch, T., Popp, J. and Kiefer, W. (2006) Surface-enhanced Raman spectroscopy employed in antimalarial mechanism of chloroquine drug upon haematin. Romanian J. Biophys. 16, 57–62.
[19] Trager, W. and Jensen, J.B. (1976) Human malaria parasites in continuous culture. Science 193, 673–675.
[20] Wood, B.R., Langford, S.J., Cooke, B.M., Lim, J., Glenister, F.K., Duriska, M., Unthank, J.K. and McNaughton, D. (2004) Resonance Raman spectroscopy reveals new insight into the electronic structure of β-Haematin and malaria pigment. J. Am. Chem. Soc. 126, 9233–9239.
[21] Wood, B.R., Langford, S.J., Cooke, B.M., Glenister, F.K., Lim, J. and McNaughton, D. (2003) Raman imaging of haemozoin within the food vacuole of *Plasmodium falciparum* trophozoites. FEBS Lett. 554, 247–252.
[22] O'Keeffe, D.H., Barlow, C.H., Smythe, G.A., Fuchsman, W.H., Moss, T.H., Lilienthal, H.R. and Caughey, W.S. (1975) Magnetic and spectroscopic probes for FeOFe [iron–oxygen–iron] linkages in haemin systems. Bioinorg. Chem. 5, 125–147.
[23] Kowalewski, P., Merlin, J.C., Bremard, C. and Moreau, S. (1988) Resonance Raman evidence for μ-oxo linkage in ferriporphyrins. J. Mol. Struct. 175, 55–60.
[24] Burke, J.M., Kincaid, J.R. and Spiro, T.G. (1978) Resonance Raman spectra and vibrational modes of iron(III) tetraphenylporphine μ-oxo dimer. Evidence for phenyl interaction and lack of dimer splitting. J. Am. Chem. Soc. 100, 6077–6083.
[25] Chottard, G., Battioni, P., Battioni, J.P., Lange, M. and Mansuy, D. (1981) Resonance Raman spectra of iron tetraphenylporphyrin complexes: characterisation of structure and bonding sensitive bands. Inorg. Chem. 20, 1718–1722.
[26] Plowman, J.E., Loehr, T.M., Schauer, C.K. and Anderson, O.P. (1984) Crystal and molecular structure of the (μ-oxo)bis[aquobis(phenanthroline)iron(III)] complex, a Raman spectroscopic model for the binuclear iron site in haemerythrin and ribonucleotide reductase. Inorg. Chem. 23, 3553–3559.
[27] Abe, M., Kitagawa, T. and Kyogoku, K. (1978) Resonance Raman spectra of octaethylporphyrinatonickel(II) and meso-deuterated and nitrogen-15 substituted derivatives. II. A normal coordinate analysis. J. Chem. Phys. 69, 4526–4534.
[28] Bhuiyan, A.A., Seth, J., Yoshida, N., Osuka, A. and Bocian, D.F. (2000) Resonance Raman characterization of excitonically coupled meso, meso-linked porphyrin arrays. J. Phys. Chem. B 104, 10757–10764.
[29] Akins, D.L. and Macklin, J.W. (1989) Dependence of Raman scattering by aggregated 2,2-cyanine on pH and excitation wavelength. J. Phys. Chem. 93, 5999–6007.
[30] Akins, D.L., Macklin, J.W., Parker, L.A. and Zhu, H.-R. (1990) Raman excitation spectra of aggregate modes of 2,2′-cyanine. Chem. Phys. Lett. 169, 564–568.
[31] Akins, D.L., Macklin, J.W. and Zhu, H.-R. (1991) Fourier transform Raman spectra and the structure of adsorbed 2,2′-cyanine. J. Phys. Chem. 95, 793–798.
[32] Akins, D.L., Zhu, H.-R. and Guo, C. (1994) Absorption and Raman scattering by aggregated meso-tetrakis(*p*-sulfonatophenyl)porphine. J. Phys. Chem. 98, 3612–3618.
[33] Akins, D.L., Zhuang, Y.H., Zhu, H.-R. and Liu, J.Q. (1994) Raman excitation spectra of exciton–phonon modes of aggregated 2,2′-cyanine using an internal Raman standard. J. Phys. Chem. 98, 1068–1072.
[34] Akins, D.L., Ozcelik, S., Zhu, H.-R. and Guo, H. (1996) Fluorescence decay kinetics and structure of aggregated tetrakis(*p*-sulfonatophenyl)porphyrin. J. Phys. Chem. 100, 14390–14396.
[35] Akins, D.L., Zhu, H.-R. and Guo, C. (1996) Aggregation of tetraaryl-substituted porphyrins in homogeneous solution. Phys. Chem. 100, 5420–5425.
[36] Akins, D.L., Ozcelik, S., Zhu, H.-R. and Guo, C. (1997) Aggregation-enhanced Raman scattering of a cyanine dye in homogeneous solution. J. Phys. Chem. 101, 3251–3259.
[37] Spiro, T.G. and Li, X-Y. (1988) (Spiro, T.G., Ed.), Biological Applications of Raman Spectroscopy, vol. 3, Wiley, New York.

Monash University

Monash Research Graduate School

Declaration for Thesis Chapter 4

Declaration by candidate

In the case of Chapter 4 the nature and extent of my contribution to the work (**Paper IV**) was the following:

Nature of contribution	Extent of contribution (%)
Raman band assignments, interpretation of results, proof reading the manuscript	10%

The following co-authors contributed to the work. Co-authors who are students at Monash University must also indicate the extent of their contribution in percentage terms:

Name	Nature of contribution	Extent of contribution (%) for student co-authors only
Bayden Wood	Experimental design, interpretation of results, writing of manuscript	-
A. Hermelink	Drafting of manuscript, Raman measurements	-
Peter Lasch	Cytospec help	-
Keith Bambery	Worked on partial dark field effect	-
Mehdi Asghari-Khiavi	Resonance Raman band assignments, proof reading the manuscript	10
Brian Cooke	Provided cells, drafting of manuscript	-
Samantha Deed	Culturing of cells, drafting of manuscript	-
Dieter Naumann	Leadership, advice on instrumentation	-
Don McNaughton	Drafting of manuscript, provided leadership	-

Candidate's Signature	[redacted]	**Date** 15/04/09

Declaration by co-authors

The undersigned hereby certify that:

(1) the above declaration correctly reflects the nature and extent of the candidate's contribution to this work, and the nature of the contribution of each of the co-authors.

(2) they meet the criteria for authorship in that they have participated in the conception, execution, or interpretation, of at least that part of the publication in their field of expertise;

(3) they take public responsibility for their part of the publication, except for the responsible author who accepts overall responsibility for the publication;

(4) there are no other authors of the publication according to these criteria;

(5) potential conflicts of interest have been disclosed to (a) granting bodies, (b) the editor or publisher of journals or other publications, and (c) the head of the responsible academic unit; and

(6) the original data are stored at the following location(s) and will be held for at least five years from the date indicated below:

Location(s)	Department of Chemistry, Centre for Biospectroscopy, Monash University, Clayton

Please note that the location(s) must be institutional in nature, and should be indicated here as a department, centre or institute, with specific campus identification where relevant.]

On behalf of all co-authors Dr Baden Wood has signed for the co-authors considering due to unavailability at this point in time.

Signature	Date
Baden Wood (Monash University)	15/4/09
[redacted]	15/4/09
	15/4/09
	13/4/09
	15/4/09
	15/4/09
	13/4/09
	13/4/09
t clam, Monash	15/4/09

Resonance Raman microscopy in combination with partial dark-field microscopy lights up a new path in malaria diagnostics†

Bayden R. Wood,[ab] Antje Hermelink,[b] Peter Lasch,[b] Keith R. Bambery,[a] Grant T. Webster,[a] Mehdi Asghari Khiavi,[a] Brian M. Cooke,[c] Samantha Deed,[d] Dieter Naumann[b] and Don McNaughton*[a]

Received 16th December 2008, Accepted 19th March 2009
First published as an Advance Article on the web 31st March 2009
DOI: 10.1039/b822603b

Our goal is to produce a rapid and accurate diagnostic tool for malaria using resonance Raman spectroscopy to detect small inclusions of haemozoin in *Plasmodium falciparum* infected red blood cells. In pursuit of this aim we serendipitously discovered a partial dark-field effect generated by our experimental setup, which helps identify in thick blood films potential parasites that are normally difficult to see with conventional bright-field microscopy. The haemozoin deposits 'light up' and these can be selectively targeted with the Raman microscope to confirm the presence or absence of haemozoin by the strong 1569 cm^{-1} band, which is a marker for haemozoin. With newly developed imaging Raman microscopes incorporating ultra-sensitive rapid readout CCDs it is possible to obtain spectra with a good signal-to-noise ratio in 1 second. Moreover, images from a smear of potentially infected cells can be recorded and analysed with multivariate methods. The reconstructed images show what appear to be sub-micron-inclusions of haemozoin in some cells indicating that the technique has potential to identify low pigmented forms of the parasite including early trophozoite-stage infected cells. Further work is required to unambiguously confirm the presence of such forms through systematic staining but the results are indeed promising and may lead to the development of a new Raman-based malaria diagnostic.

Introduction

Malaria remains one of the most devastating diseases on the planet, afflicting some 500 million people each year and resulting in 1–3 million deaths. Eighty percent of all cases occur in Africa, with children under 5 years of age and pregnant women being the major victims.[1] The female *Anopheles* mosquito can host the unicellular parasite *Plasmodium falciparum* and initiates the infection through a skin bite that releases sporozoites from the mosquito's salivary glands into the bloodstream. These sporozoites are cleared from the bloodstream within 30 minutes and quickly invade liver cells. The liver-stage parasites differentiate and multiply over a 14-day period resulting in the generation of thousands of merozoites. The merozoites burst from the liver cells and invade the erythrocytes. The following 48-hour cycle is known as the intra-erythrocytic stage of the parasite's life cycle during which the parasite undergoes several morphologically distinct developmental stages, including rings, trophozoites and schizonts. The schizonts contain 12–16 merozoites, which upon release invade other red blood cells. For a full description of the life cycle see http://malaria.wellcome.ac.uk/node40036.html. During the trophozoite phase the parasite catabolizes large amounts of haemoglobin, releasing toxic free ferrous protoporphyrin IX (Fe(II)PPIX) and denatured globin.[2,3] The Fe(II)PPIX is oxidized to Fe(III)PPIX and aggregates into an insoluble biomineral known as haemozoin (malaria pigment) which is spectroscopically identical to its synthetic analogue β-haematin.[4,5] Haemozoin is comprised of an array of dimers linked together by reciprocal iron–carboxylate bonds to one of the propionate side chains of adjacent FePPIX groups.[6] Under physiological conditions this pigment remains insoluble and undegraded.[7]

Strategies to diagnose malaria are based on detecting the parasite in the bloodstream. Besides conventional optical microscopy several diagnostic techniques have been developed for malaria detection including serological (dipstick) antigen detection,[8–11] fluorescence microscopy,[11–15] PCR-based assays,[11,16,17] flow cytometry,[11,18] NMR-based metabolic profiling[19] magneto-optic-based technology[20] and laser desorption mass spectrometry (LD-MS).[21,22] Hitherto, the potential of optical-based spectroscopic techniques as malaria diagnostics have not been fully exploited, although resonance Raman spectroscopy is showing potential due to the huge resonant enhancement of haemozoin bands.[23–26] We have been exploring resonance Raman micro-spectroscopy as a possible diagnostic tool for malaria both at the single cell level using a Raman microscope[26,27] and also at the population level using an acoustic levitation device coupled to a Raman microscope.[23] Raman images of trophozoites have also been reported[26–29] but the time required to obtain a map of a single cell makes it impractical for

[a]*Centre for Biospectroscopy, School of Chemistry, Monash University, Clayton, 3800, Victoria, Australia. E-mail: don.mcnaughton@sci.monash.edu.au*
[b]*Robert Koch Institute, Nordufer 10, 15513 Berlin, Germany*
[c]*Department of Microbiology, Monash University, Clayton, 3800, Victoria, Australia*
[d]*Department of Biochemistry and Centre of Excellence for Coherent X-ray Science, La Trobe University, Melbourne, Victoria 3800, Australia*
† This paper is part of an *Analyst* themed issue on Optical Diagnosis. The issue includes work which was presented at SPEC 2008 Shedding Light on Disease: Optical Diagnosis for the New Millennium, which was held in São José dos Campos, São Paulo, Brazil, October 25–29, 2008.

a clinical setting. Using newly developed purpose-built Raman confocal imaging microscopes with fast readout CCDs and fibre optic technology these spectral images can now be recorded in rapid time while still preserving a very good signal-to-noise ratio.

The standard technique for malaria diagnosis is bright-field microscopy. The technique has a number of advantages with the main one being the ability to quantify and identify the parasites at different stages of the parasite's life cycle. However, the technique is subjective and requires experienced personnel to make the diagnosis. Rapid diagnostic tests (RDTs), also known as 'dipsticks', make use of a capture antibody and conjugated detection antibody to detect malarial antigen in blood samples. RDTs have a rapid turnaround time and are simple to use, enabling clinicians to make on-the-spot diagnoses but the technique is not quantitative. Quantitation is important because knowledge of the parasite number often determines the therapeutic approach. The sensitivity (40 parasites/μL of blood) of the RDTs is good; however, the cost is relatively expensive for their target market, which is the developing world. Laser desorption mass spectrometry (LD-MS) has a sensitivity of 100–1000 parasites/μL of blood, similar to routine microscopy. Like Raman microscopy it relies on the presence of haemozoin for detection. More recently, synchrotron FTIR microscopy in combination with a neural network has also shown potential as a diagnostic tool for malaria.[30] Specific lipid signatures along with haemozoin bands enabled the identification of parasites at all stages of the erythrocytic life cycle.[30] Currently the main drawback with this approach is that it requires a synchrotron source to achieve the spatial resolution required for diagnosis at the single cell level.

The Raman micro-spectroscopic technique has a number of advantages compared to other diagnostic approaches. The main one being that haemozoin can be unambiguously identified because of the extremely strong resonance enhancement of characteristic marker bands, especially when using near-IR excitation.[23–26] The Raman technique requires no addition of stains or fluorophores and can also be applied to live cells because water is a very weak Raman scatterer. Moreover, the technique can be automated to detect parasitised cells using multivariate[29] or neural network algorithms to detect the presence or absence of haemozoin. One of the drawbacks of resonance Raman microscopy is the time required to screen a full blood film containing parasites, and any method to assist in the selective targeting of potentially infected cells would greatly improve the diagnostic value of this technology. The detection of malaria parasites using dark-field microscopy has been known for many years[31,32] and more recently attempts have been made to make the technique more routine and sensitive enough to detect ring forms of the parasite.[33,34] It does have other drawbacks in addition to its inability to routinely detect the early forms of malaria including (a) a requirement for a specialized sample mounting which entails using a mounting compound and 2 coverslips and (b) that artifacts from other crystal structures and debris can lead to false positives. The technique also requires a person experienced in diagnosing parasites in dark-field conditions plus dark-field condensers for the microscope.

We have developed a new approach for detecting malaria parasites by combining a partial dark-field effect in a simple mounting arrangement with Raman micro-spectroscopy to unequivocally identify parasites. We prove this concept by recording Raman images of the parasites and correlating these directly with the dark-field images.

Experimental

Cell culture

P. falciparum (D10 line) was maintained in continuous culture using human erythrocytes obtained from the Red Cross Blood Bank, Melbourne.[35] Parasitised erythrocytes were cultured in complete culture medium (CCM) consisting of RPMI 1640 (GIBCO BRL), 25 mM hydroxypiperazine-*N*′-2-ethane sulfonic acid (HEPES, Sigma pH 7.4), 2 g/L sodium bicarbonate (AnalR) and 4 mM Glutamax (Invitrogen). This was supplemented with 0.16% glucose (AnalR), 0.21 mM hypoxanthine (Sigma), 22 μg/mL gentamicin (Sigma) and 4% human serum and 0.25% Albumax I (GIBCO-BRL). The cultures were incubated at 37 °C in a humidified atmosphere of 5% CO_2, 1% O_2 and 94% N_2. Infected erythrocytes and uninfected erythrocytes (controls) were fixed in solution using 2% paraformaldehyde, 0.0075% glutaraldehyde and 0.1 M cacodylate buffer for 1 hour before being washed twice with Milli-Q water and placed on individual 12 mm diameter × 0.5 mm thick CaF_2 IR-grade polished windows. Excess water was removed and the windows were allowed to dry in air.

Chemicals

β-Haematin was prepared by dissolving hemin (Fluka, Biochemika) in 3 mL of 0.1 M NaOH and stirring. To the solution was added 0.3 mL of 0.1 M HCl and 1.74 mL of 12.9 M acetate (pH 5). The reaction was complete after 30 min at 60 °C after which the mixture was cooled for 10 min on ice and then filtered. The resultant solid was dried for 24 hours at 37 °C. Haemoglobin was purchased from Sigma-Aldrich and used without further purification.

Partial dark-field effect

In bright-field microscopy the sample and surrounds are illuminated directly and contrast is provided by the varying absorbance within the sample. The surrounding empty field appears bright and the sample appears darker than the field areas. However, in dark-field microscopy direct illumination rays are stopped from entering the microscope aperture and the sample is only observable if it can scatter the indirect illumination light into the microscope aperture. This results in a dark, close to black, background with bright objects visualised because of the collection of scattered light from these objects. The image contrast is thus provided by the variation of light scattering intensity from various objects within the sample.

In our experiment the CaF_2 window was stuck down onto a Petri dish using a tiny drop of Superglue™ and the Petri dish then filled with water and placed on the stage of the microscope. The partial dark-field illumination was achieved without the use of any dark-field microscope accessories, thus eliminating some of the complications of dark-field microscopy (*i.e.* no occluding disks or stops were fitted to either the illuminator or the objective lens). The microscope was configured for reflected-mode

bright-field observations except with the illuminator intensity and the condenser focus set to provide a relatively poorly illuminated field (by bright-field standards). Consequently, less than optimal contrast was achieved for objects in the image as can be seen in Fig. 1A. The Petri dish was located on the microscope scan table, which is equipped with roughened steel base-plate to avoid movement of the sample while scanning. This base-plate reflected some light back upward through the Petri dish and the sample cells. Because the base-plate has a rough surface much of this light will be directed off the optical axis of the microscope. It is only through scattering interactions with the sample that these rays can be redirected to angles accepted by the microscope aperture. Under these conditions a partial bright-field mixed with partial dark-field illumination occurs. Since the sample is bright-field illuminated the dark-field contribution can only be observed if the sample contains some particularly efficient light scattering particles, as is the case for the malaria pigment.[31,32] The dark-field illumination contribution causes strongly scattering objects to have the appearance of 'bright lights', brighter in fact than the surrounding empty field areas (Fig. 1A).

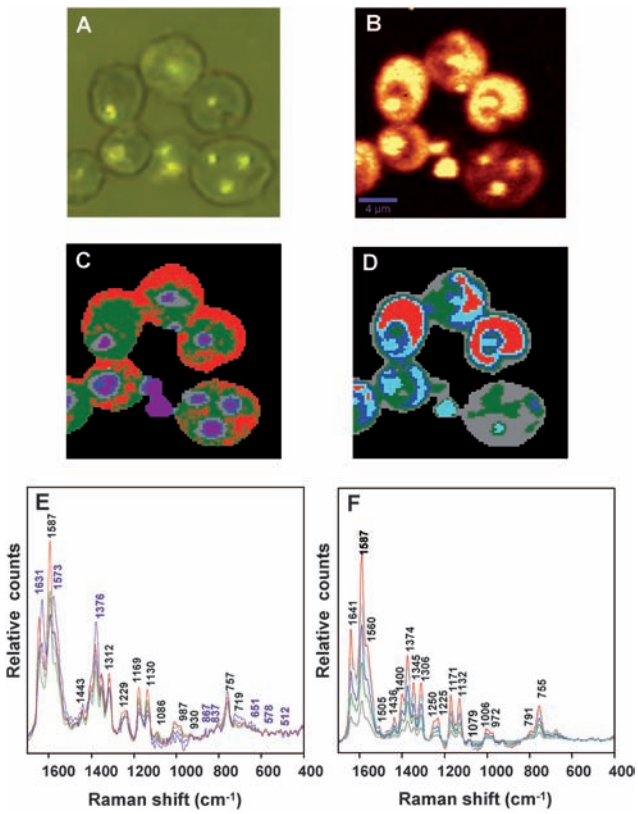

Fig. 1 (A) Visible micrograph showing the partial dark-field effect lighting up haemozoin deposits in several parasite infected cells. The infected erythrocyte towards the bottom right corner is triply infected. (B) Chemical map generated by integrating the region between 1680 and 1620 cm^{-1}. The lighter colour shows regions of stronger counts. (C) Unsupervised Hierarchical Cluster Analysis (UHCA) map generated using the *D*-values distance algorithm for the 1700–1300 cm^{-1} range for 5 clusters. (D) UHCA map generated using the Euclidean distance algorithm for the 1700–1300 cm^{-1} range for 5 clusters. (E) Mean spectra extracted from *D*-values calculation of the UHCA map in (D). The purple labels correspond to bands mainly associated with haemozoin while the black labels are characteristic haemoglobin bands. (F) Mean spectra extracted from Euclidean distance calculation. The spectra have characteristic bands of haemoglobin but not haemozoin.

Resonance Raman mapping

Resonance Raman micro-spectroscopic maps were collected with 531.8 nm excitation (frequency doubled Nd-YAG laser with 36 mW laser power) using a confocal Raman microscope (CRM300), WITec, Inc. (Ulm Germany), at a dwell time of 1 s per pixel. The CRM300 is equipped with an ultra-high throughput spectrometer (UHTS300) and a DV401 CCD camera as the detector. The grating was 600 grooves/mm blazed at 500 nm. A Nikon 60× water immersion objective (N.A. 1.0) was used for all measurements. Raman backscattered radiation was collected through the objective and passed through an edge filter to block Rayleigh scattered and reflected laser light before being focussed into a multi-mode fibre optic. The UHTS 300 is an *f*/4 lens-based spectrometer with a focal length of 300 mm. The Raman signal from the confocal microscope is directed to the spectrometer using a multi-mode optical fibre with a core diameter of 50 μm which acts as the entrance slit (2nd pinhole) of the spectrometer and is finally detected by a back-illuminated deep-depletion, 1024 × 128 pixel charge-coupled device camera operating at −62 °C with a quantum efficiency of more than 90%. With the above combination of laser and this objective, the lateral spatial resolution is about 300 nm, and the depth resolution about twice that value. The spectral resolution for the instrument in this configuration is 4 cm^{-1}. Exact power at the sample is difficult to determine but is approximately 12 mW.

Data processing

All data processing was performed in Cytospec™ (www.cytospec.com) version 1.4.00. After cosmic ray removal the data range was cut so that only the spectral range between 1800 and 400 cm^{-1} was included in subsequent calculations. The spectra were then quality tested to remove spectra from background areas low in counts and then the baseline corrected using a 3rd order polynomial function and 9 baseline points. Unsupervised Hierarchical Cluster Analysis (UHCA) was performed over the 1700–1300 cm^{-1} spectral region using the *D*-values algorithm based on Pearson's correlation coefficient and, for comparison, the Euclidean distance algorithm. The cluster analysis was performed using Ward's algorithm.

In UHCA each spectrum consists of wavenumber and intensity information with *X* and *Y* spatial coordinates. This raw data set is referred to as a spectral 'hypercube'. Each data cube that makes up the hypercube contains a Raman spectrum providing qualitative and quantitative chemical information. To enable a visual inspection of such large data sets, the individual spectra are converted into a two-dimensional false colour representation. This can be accomplished by uni- or multi-variate methods. In univariate analyses, a spectral property for each spectrum (for example, intensity, integrated intensity or intensity ratio at two wavenumber values) is colour coded, and represented as a function of spatial coordinates to yield a two-dimensional false colour map. Different colour hues represent different values of the displayed spectral property.

In multivariate methods, the information of the entire spectrum can be utilized for data analysis. Supervised pattern recognition techniques such as linear discriminant analysis have been employed to investigate skin tumours,[36] while unsupervised hierarchical clustering techniques and also ANN classification algorithms show enormous potential in diagnosing colorectal adenocarcinoma,[37] cirrhotic liver tissue[38] and cervical cancer.[39] Unsupervised hierarchical cluster analysis is a general approach to cluster analysis, in which the object is to group together objects or records that are 'close' to one another. The analysis entails repeated calculation of distance measures between objects, and between clusters once objects begin to be grouped into clusters. The outcome is represented graphically as a dendrogram or alternatively as a false colour map. In this study we employ an unsupervised clustering approach to investigate malaria infected red blood cells. The unsupervised clustering approach is well described in the literature[37–39] and only a brief overview is given below.

In cluster analysis a measure of similarity is established for each class of related spectra and a mean characteristic spectrum can be extracted for each class. The first step in the computation is to derive the distance matrix by calculating the Euclidean distance between every spectrum,

$$d_{jk} = \sqrt{\sum_{i=1}^{n} \left(x_{ji} - x_{ki}\right)^2} \quad (1)$$

where x_j and x_k are spectra being compared and are one-dimensional vectors of intensity values for n equidistant data points. Consequently, every spectrum is referenced to all other spectra with the resulting d_{jk} matrix containing $n \times n$ entries, where n is the total number of spectra within the data set. Alternatively, the distance matrix can be mean-centred through a method based on Pearson's correlation coefficient. This is known as the D-values method,[37]

$$d_{jk} = 1 - \frac{\left(\sum_{i=1}^{n} x_{ji} \cdot x_{ki}\right) - \bar{x}_j \cdot \bar{x}_k}{\sqrt{\left(\sum_{i=1}^{n} {x_{ji}}^2 - n \cdot \bar{x}_j^2\right) \cdot \left(\sum_{i=1}^{n} {x_{ki}}^2 - n \cdot \bar{x}_k^2\right)}} \quad (2)$$

where, $\bar{x}_j$ and $\bar{x}_k$ are the average mean values for each vector. The 'overlap' or similarity between a spectrum and reference ranges from 0 for no fit and up to 1.0 for a perfect fit. Step 2 involves using Ward's algorithm for merging all spectra into clusters, or classes of spectra, such that similar spectra appear in the same cluster. The process of merging spectra into new clusters is repeated until all spectra have been combined into a few clusters. Ward's algorithm is often employed because it minimizes the heterogeneity of the clusters. In the final step all spectra in a cluster are assigned the same colour. In the false colour maps the assigned colour for each spectral cluster is displayed at the coordinates at which each spectrum belonging to the cluster was collected. The mean spectrum of a cluster represents all spectra in a cluster and can be used for the interpretation of the chemical or biochemical differences between clusters.

In this project we compare two different algorithms that are part of the Cytospec software suite, namely the D-values algorithm and the Euclidean distance algorithm. The essential difference between the algorithms is that in the D-values algorithm the distances between the spectra are divided through by the residuals of the standard deviation, while in the Euclidean algorithm this does not occur. The net effect is that in the former the spectral distances are intrinsically normalized whereas in the latter case they are not. Thus the Euclidean algorithm gives a more quantitative result based on absolute Raman counts whereas the D-values calculation gives an indication of more subtle spectral differences associated with changes in band shape.

Results and discussion

Thin film

Fig. 1A shows the partial dark-field effect in a thin film of malaria parasite infected red blood cells in the late trophozoite stage. The haemozoin crystals appear as 'bright lights'; however, one cannot be certain that all the 'bright lights' are indeed haemozoin crystals. To confirm the presence of haemozoin it is possible to selectively target the individual bright spots with the Raman microscope or alternatively record Raman maps of the total area. By using the latter approach a spatial correlation between the visible photomicrograph and a Raman image of haemozoin deposits can be achieved. Fig. 1B depicts a chemical map recorded of 5 cells generated by integrating the 1680–1620 cm^{-1} region of the spectra and thus showing regions of high haemoglobin and haemozoin density. The high spatial resolution enables the clear resolution of a triply infected cell (lower right corner) showing 3 haemozoin deposits within the one cell. UHCA was performed in the 1700–1300 cm^{-1} region using both the D-values and the Euclidean distance algorithms and 5 cluster maps are presented in Fig. 1C and Fig. 1D respectively. The two

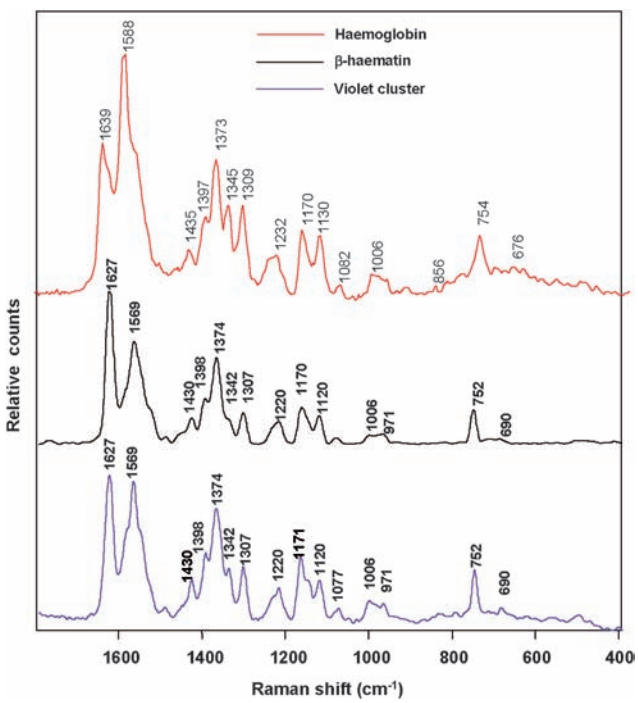

Fig. 2 Resonance Raman spectra of haemoglobin, β-haematin and the mean spectrum extracted spectrum from the violet cluster presented in Fig. 1E. All spectra were recorded using 531.8 nm excitation.

processes yield distinctly different cluster maps. In the calculation of *D*-values the haemozoin deposits are clearly resolved and correlate well with the partial dark-field visible image. The mean-extracted spectra (Fig. 1E) show the violet cluster to be predominantly of haemozoin, while the mid-blue and grey clusters are a mixture of haemozoin and haemoglobin. The green and red clusters are entirely composed of haemoglobin as evinced by the strong 1639 and 1588 cm^{-1} bands, assigned to ν_{10} and ν_2 porphyrin core vibrations, respectively. The red cluster is correlated to a higher density of haemoglobin compared to the green cluster as evinced by the intensity of ν_{10} and ν_2 bands compared to the red spectrum. The spectra of β-haematin (a spectroscopically synthetic analogue of haemozoin), haemoglobin and the mean-extracted spectrum of the violet cluster, which is predominantly haemozoin, are compared in Fig. 2. The spectrum of the violet cluster closely matches that of β-haematin, especially in terms of band position and relative intensity for the majority of the bands. The spectrum of crystallized haemoglobin is quite different, especially in the 1700–1600 cm^{-1} region where the 1639 and 1588 cm^{-1} bands clearly distinguish it from the β-haematin and the violet cluster spectra. Band assignments and symmetry terms are based on previous isotopic substitution studies and density functional calculations and are presented in Table 1.[40,41] The cluster map based on the Euclidean distance calculation (Fig. 1D) correlates well with the chemical map shown in Fig. 1B and is essentially based on differences in haemoglobin density within the cell. Unlike the *D*-values cluster map (Fig. 1C) the haemozoin inclusions are not obvious. It should be noted that because this is a confocal map the resulting cluster map represents the density of haemoglobin approximately half way into the cell and not the haemoglobin density throughout the whole cell. The mean-extracted spectra for the Euclidean cluster map (Fig. 1F) confirm that the variation observed in this cluster map is predominantly from differences in haemoglobin density.

Thick film

Fig. 3A shows a thick film of infected erythrocytes using the Raman microscope in optical mode. The dark spots are mainly haemozoin crystals, which are distributed in large numbers throughout the sample while Fig. 3B shows the partial dark-field effect. Fig. 3C shows a Raman chemical map of approximately

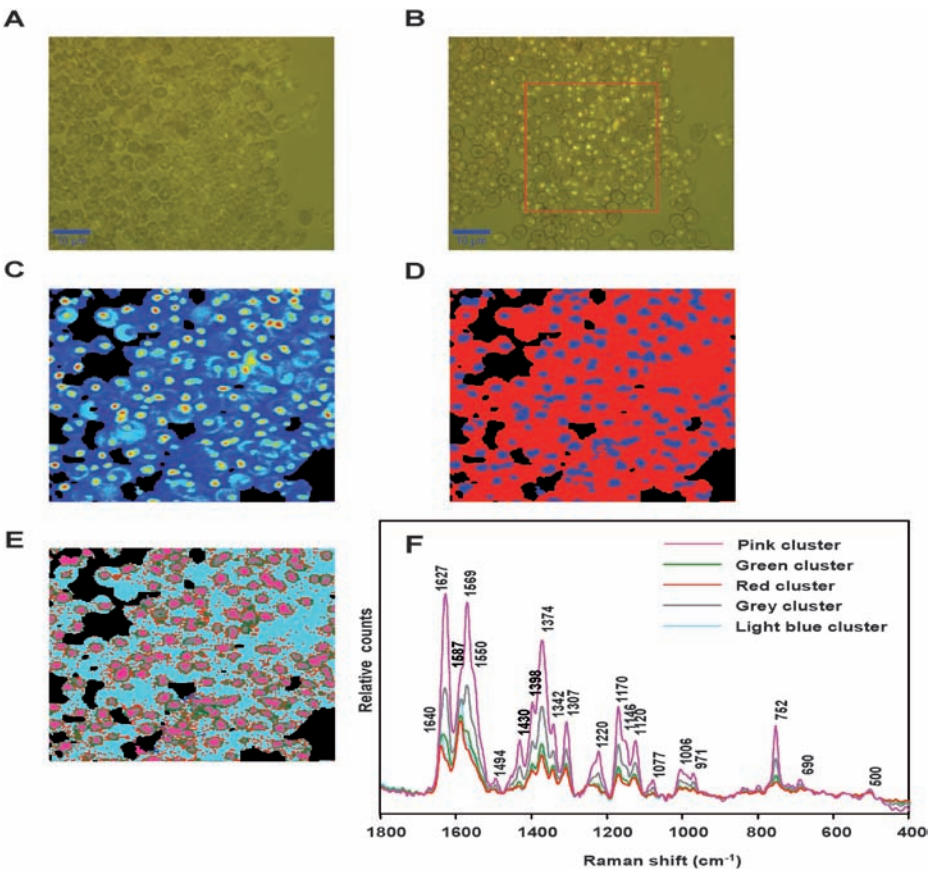

Fig. 3 (A) Visible micrograph of a thick film of malaria infected cells. (B) Visible micrograph showing partial dark-field effect with trophozoites 'lit up'. (C) Chemical map of approximately the area bounded by the red square in (B), calculated by integrating the area between 1680 and 1620 cm^{-1}. The lighter colours show the haemozoin deposits in the trophozoites. (D) UHCA performed using the *D*-values algorithm and in the 1700–1300 cm^{-1} range showing 2 clusters. The blue cluster shows the haemozoin deposits while the red is associated with haemoglobin. (E) Same as (D) except that 5 clusters are presented. The pink cluster correlates to the haemozoin deposits within late-stage trophozoites. The green and grey clusters are a mixture of haemoglobin and haemozoin. The light blue cluster correlates well with haemoglobin within the cell while the red-sub-micron sized dots (300 nm) appear to be inclusions of haemozoin observed in both trophozoite infected cells and possibly other stages of the *P. falciparum* life cycle. (F) Mean spectra extracted from the cluster map presented in (E).

Table 1 Band assignments, symmetry terms and local coordinates for resonance Raman of haemoglobin and β-haematin. The names in each column refer to the following: Hb = haemoglobin, β-Hm = β-haematin, ν = in-plane stretch, γ = out-of-plane vibration, δ = deformation mode, pyr = pyrrole, prop = propionate, vw = very weak. Labelling and notation scheme is based on the work of ref. 40

Hb	β-Hm	Assignment	Symmetry	Local coordinates
1639	1627	ν_{10}	B_{1g}	$\nu(C_\alpha C_m)_{as}$
1588	1569	ν_2	A_{1g}	$\nu(C_\beta C_\beta)$
1435	1430			$\delta(=C_bH_2)_{sym}$
1398	1398	ν_{29}	B_{2g}	ν(pyr quarter-ring)
1373	1374	ν_4	A_{1g}	ν(pyr half-ring)$_{sym}$
1345	1342	ν_{41}	E_u	ν(pyr half-ring)$_{sym}$
1309	1307	ν_{21}	A_{2g}	$\delta(C_mH)$
1232	—	ν_{13}	B_{1g}	$\delta(C_mH)$
—	1220			prop $\delta(CH_2)$ twisting
1170	1170	ν_{30}	B_{2g}	ν(pyr half-ring)$_{as}$
1130	1120	$\nu_6 + \nu_8$	A_{1g}	$\nu(C_\alpha–C_\beta)_{sym} + \nu$(Fe–N)
1130	1120	ν_{22}	A_{2g}	ν(pyr half-ring)$_{as}$
1082	1082			$\delta(=C_bH_2)_{as}$
1006	1006			$\gamma(C_aH=)$
971	971			ν(Cc–Cd)
754	752	ν_{15}	B_{1g}	ν(pyr breathing)
697 vw	690	γ_{15}	B_{2u}	δ(pyr fold)$_{sym}$
676	676	ν_7	A_{1g}	δ(pyr def)$_{sym}$

the area outlined by the red square in Fig. 3B, produced by integrating the 1680–1620 cm^{-1} region of the Raman spectra. The intensity distribution (bright = high; dark = low) of this region correlates very well with the bright spots in the partial dark-field visible image. However, the information in this map simply shows baseline corrected counts and it is therefore not definitive proof of haemozoin crystals. To gain more insight into the chemistry of the cell population UHCA was performed in the 1700–1300 cm^{-1} region using the *D*-values and Ward's algorithm. Fig. 3D shows a 2-cluster map while Fig. 3E shows a 5-cluster map. The 2-cluster map clearly shows the haemozoin crystal deposits (blue) in the digestive vacuole of the trophozoites, which can be readily correlated with the bright spots in the partial dark-field image. Precise correlations here are difficult because the optical paths for the partial dark-field microscopy and the Raman microscopy are different. The correlation is achieved by overlaying the two figures. The red cluster is associated predominantly with haemoglobin. More interesting is the 5-cluster map which also shows the large haemozoin deposits (now pink) along with an outer cluster around the haemozoin deposit (grey) and very small sub-micron sized spots (red) that appear in some of the trophozoite infected cells but more importantly also in other cells that are not obviously infected with late-stage trophozoites. The mean-extracted spectra are presented in Fig. 3F and show similar profiles to those in Fig. 1E. However, careful inspection of the 1700–1500 cm^{-1} region expanded in Fig. 4 shows that the spectrum correlating to the red nano-dots observed in the cluster map is in fact of haemozoin mixed with haemoglobin as evinced by the intensity of the band at 1569 cm^{-1}, characteristic of haemozoin compared to the 1639 cm^{-1} band associated with oxygenated haemoglobin. In the red spectrum the 1569 cm^{-1} has a similar intensity to the 1639 cm^{-1} band but in the light blue spectrum, which is almost entirely haemoglobin, the 1639 cm^{-1} band is more intense than the 1569 cm^{-1} shoulder feature. The red dots thus appear from the Raman spectra to be sub-micron-haemozoin inclusions. It is difficult to observe these inclusions in the partial-dark-field image and impossible to observe them in the bright-field image, hence it is not possible to unequivocally confirm these deposits as sub-micron-haemozoin inclusions but the relative intensity of the 1569 cm^{-1} compared to the 1639 cm^{-1} is strong evidence. If this is indeed the case then it should be possible to identify low-pigmented forms of the parasite including the early trophozoite stage using this Raman signature.

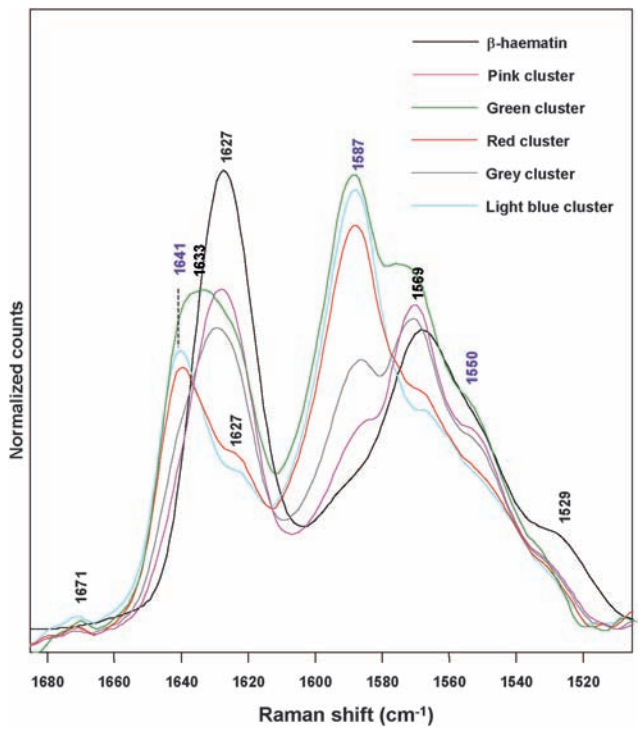

Fig. 4 Expanded region of spectra presented in Fig. 3F showing the region between 1600 and 1500 cm^{-1}. Note the differences in the red and light blue spectra. The strong shoulder on the red spectrum centred at 1569 cm^{-1} indicates that the sub-micron-dots observed in Fig. 3E are from inclusions of haemozoin.

Conclusion

The combination of using a partial-dark-field effect to determine targets for Raman spectroscopy followed by rapid confocal Raman imaging paves the way for a new diagnostic tool for malaria. The extremely high spatial resolution (300 nm) and the ability to record good quality spectra in 1 second suggest that this approach may be suitable for clinical laboratories. The partial dark-field effect helps identify potential parasites in thick films that may be overlaid by other cells and thus obscured using conventional bright-field microscopy. The technique shows potential to detect low-pigmented phases of the parasite's life cycle including early trophozoites; however, these results remain to be verified through conventional staining approaches and/or fluorescence microscopy which is the subject of future studies. The combination of Raman and dark-field microscopy could have potential as a diagnostic in remote locations with the emergence of more portable spectrometers and microscopes. The experience required to operate a purpose-built Raman dark-field

microscope would be no more difficult than a conventional microscope with the main advantage being that the operator is not required to make the diagnosis.

Acknowledgements

We thank Professor Leann Tilley (La Trobe University) for advice on the biology and biochemistry of malaria parasites and supplying parasites for this study. Dr Wood was funded by an Alexander von Humboldt Fellowship. B. M. C. is supported by the National Health and Medical Research Council of Australia. The work and B. R. W. are also supported through an Australian Research Council Discovery Grant.

References

1 R. W. Snow, C. A. Guerra, A. M. Noor, H. Y. Myint and S. I. Hay, *Nature*, 2005, **434**, 214–217.
2 T. H. Schmitt, W. A. Jr Frezzatti and S. Schreier, *Arch. Biochem. Biophys.*, 1993, **307**, 96–103.
3 Y. Sugioka and M. Suzuki, *Biochim. Biophys. Acta*, 1991, **1074**, 19–24.
4 A. F. G. Slater, W. J. Swiggard, B. R. Orton, W. D. Flitter, D. E. Goldberg, A. Cerami and G. B. Henderson, *Proc. Natl. Acad. Sci. U. S. A.*, 1991, **88**, 325–329.
5 D. S. Bohle, B. J. Conklin, D. Cox, S. K. Madsen, S. Paulson, P. W. Stephens and G. T. Yee, *ACS Symp. Ser.*, 1994, **572**, 497–515.
6 S. Pagola, P. W. Stephens, D. S. Bohle, A. D. Kosar and S. K. Madsen, *Nature*, 2000, **404**, 307–310.
7 T. Deegan and B. G. Maegraith, *Ann. Trop. Med. Parasitol.*, 1956, **50**, 194–211.
8 M. T. Makler, C. J. Palmer and A. L. Ager, *Ann. Trop. Med. Parasitol.*, 1998, **92**, 419–433.
9 C. J. Shiff, J. N. Minjas and Z. Premji, *Parasitol. Today*, 1994, **10**, 494–495.
10 M. Garcia, S. Kirimoama, D. Marlborough, J. Leafasia and K. H. Rieckmann, *Lancet*, 1996, **347**, 1549.
11 T. Hanscheid, *Clin. Lab. Haematol.*, 1999, **21**, 235–245.
12 D. F. Richards, D. T. Hunter and B. Janis, *Am. J. Clin. Pathol.*, 1969, **51**, 280–283.
13 T. M. Sodeman, *Am. J. Trop. Med. Hyg.*, 1970, **19**, 40–42.
14 G. T. Shute and T. M. Sodeman, *Bull. W. H. O.*, 1973, **48**, 591–596.
15 M. T. Makler, L. K. Ries, J. Ries, R. J. Horton and D. J. Hinrichs, *Am. J. Trop. Med. Hyg.*, 1991, **44**, 11–16.
16 A. Humar, C. Ohrt, M. A. Harrington, D. Pillai and K. C. Kain, *Am. J. Trop. Med. Hyg.*, 1997, **56**, 44–48.
17 A. Humar, M. A. Harrington and K. C. Kain, *Trans. R. Soc. Trop. Med. Hyg.*, 1997, **91**, 406–409.
18 P. H. van Vianen, A. van Engen, S. Thaithong, M. van der Keur, H. J. Tanke, H. J. van der Kaay, B. Mons and C. J. Janse, *Cytometry*, 1996, **14**, 276–280.
19 K. Cottingham, *J. Proteome Res.*, 2008, **7**, 3369.
20 D. M. Newman, J. Heptinstall, R. J. Matelon, L. Savage, M. L. Wears, J. Beddow, M. Cox, H. D. F. H. Schallig and P. F. Mens, *Biophys. J.*, 2008, **95**, 994–1000.
21 R. Petkewich, *Anal. Chem.*, 2002, **74**, 409A.
22 P. A. Demirev, A. B. Feldman, D. Kongkasuriyachai, P. Scholl, D. Sullivan Jr and N. Kumar, *Anal. Chem.*, 2002, **74**, 3262–3266.
23 L. Puskar, R. Tuckermann, T. Frosch, J. Popp, V. Ly, D. McNaughton and B. R. Wood, *Lab Chip*, 2007, **7**, 1125–1131.
24 G. T. Webster, L. Tilley, S. Deed, D. McNaughton and B. R. Wood, *FEBS Lett.*, 2008, **582**, 1087–1092.
25 B. R. Wood, S. Langford, B. M. Cooke, J. Lim, F. K. Glenister, M. Duriska, J. Unthank and D. McNaughton, *J. Am. Chem. Soc.*, 2004, **126**, 9233–9239.
26 B. R. Wood, S. J. Langford, B. M. Cooke, J. Lim, F. K. Glenister and D. McNaughton, *FEBS Lett.*, 2003, **554**, 247–252.
27 B. R. Wood and D. McNaughton, *Expert Rev. Proteomics Res.*, 2006, **3**, 525–544.
28 T. Frosch, S. Koncarevic, L. Zedler, M. Schmitt, K. Schenzel, K. Becker and J. Popp, *J. Phys. Chem. B*, 2007, **111**, 11047–11056.
29 A. Bonifacio, S. Finaurini, C. Krafft, S. Parapini, D. Taramelli and V. Sergo, *Anal. Bioanal. Chem.*, 2008, **392**, 1277–1282.
30 G. T. Webster, K. A. de Villiers, T. J. Egan, S. Deed, L. Tilley, M. J. Tobin, K. R. Bambery, D. McNaughton and B. R. Wood, *Anal. Chem.*, 2009, DOI: 10.1021/ac802291a.
31 A. Wolter, *Dermatol. Z.*, 1932, **63**, 69–72.
32 H. Packer, *J. Natl. Malaria Soc.*, 1945, **4**, 331–340.
33 G. Jamjoom, *J. Clin. Microbiol.*, 1983, **17**, 717–721.
34 G. Jamjoom, *R. Soc. Trop. Med. Hyg.*, 1991, **85**, 38–3934.
35 W. Trager and J. B. Jensen, *Science*, 1976, **193**, 673–675.
36 J. R. Mansfield, L. M. McIntosh, A. N. Crowson, H. H. Mantsch and M. Jackson, *Appl. Spectrosc.*, 1999, **53**, 1323–1330.
37 P. Lasch and D. Naumann, *Cell. Mol. Biol.*, 1998, **44**, 189–202.
38 L. Chiriboga, H. Yee and M. Diem, *Appl. Spectrosc.*, 2000, **54**, 1–8.
39 B. R. Wood, K. R. Bambery, C. J. Evans, M. A. Quinn and D. McNaughton, *BMC Medical Imaging*, 2006, **6**, 12.
40 M. Abe, T. Kitagawa and K. Kyogoku, *J. Chem. Phys.*, 1978, **69**, 4526–4534.
41 S. Hu, K. M. Smith and T. G. Spiro, *J. Am. Chem. Soc.*, 1996, **118**, 12638–12646.

Chapter 5

Raman Spectroscopic Analysis of Supramolecular Interactions in Haem Aggregates

CHAPTER SUMMARY

The results of the previous study (**III**) indicate that a number of bands assigned to A_{1g} and B_{1g} modes characteristic of the haemozoin aggregate are reduced in intensity in chloroquine-treated cells. The intensity changes are attributed to intermolecular drug binding of chloroquine (CQ) in a sandwich type complex between Fe(III)PPIX dimer units. It is postulated that CQ binds via π-π interactions between adjacent and oriented porphyrins, thus disrupting the haemozoin aggregate and reducing excitonic interactions between adjacent haems.

Although the results of that study are promising, further work was required to monitor antimalarial drug interactions with Fe(III)PPIX in solution. This chapter of the dissertation is mainly concerned with two topics: first, determining the effectiveness of potential antimalarial compounds that are thought to exert their antimalarial activity by binding to Fe(III)PPIX, consequently inhibiting the growth of haemozoin; and second, a proposition that supramolecular interactions are responsible for excitonic effects observed in haem aggregates.

The first manuscript in this chapter (**V**) is separated into two parts, which discusses aggregated enhanced Raman scattering (AERS) in Fe(III)PPIX solutions and the effect of (a) concentration and (b) CQ on excitonic interactions. The concentration study allows the researcher to understand the mechanism that accounts for the Raman photophysical behaviour of haems at high concentrations. This provides an indirect method to monitor antimalarial drug interactions. The results show that as the concentration of Fe(III)PPIX increases there is an increased probability of supramolecular interactions between Fe(III)PPIX units. In addition, UV-Visible spectra showed that as the concentration of Fe(III)PPIX increased in solution the Soret band

was slightly blue-shifted and the Q band significantly broadened, which supports the excitonic hypothesis. The chloroquine drug study used excitonic Raman enhancement of the ν_4 totally symmetric A_{1g} mode to investigate CQ non-covalently binding to the unligated faces of Fe(III)PPIX-OH/H_2O monomers, π-π dimers and μ-oxo dimers, which form in highly concentrated solutions approaching those of the digestive vacuole of the *Plasmodium falciparum* parasite. Non-covalent CQ drug binding can cap the faces of the haemozoin dimer sub-unit and reduce the amount of haemozoin formed.

The second manuscript (**VI**) builds on these results in the solid phase and suggests that supramolecular interactions, such as hydrogen bonding interactions, are responsible for the NIR Raman excitonic enhancement of ν_4 observed in malaria pigment and other related haem aggregates.

Monash University

Monash Research Graduate School

Declaration for Thesis Chapter 5

Declaration by candidate

In the case of Chapter 5 the nature and extent of my contribution to the work (**Paper V**) was the following:

Nature of contribution	Extent of contribution (%)
Experimental design, Interpretation of results, writing of manuscript	>80%

The following co-authors contributed to the work. Co-authors who are students at Monash University must also indicate the extent of their contribution in percentage terms:

Name	Nature of contribution	Extent of contribution (%) for student co-authors only
Don McNaughton	Drafting of manuscript, provided supervision	-
Bayden Wood	Drafting of manuscript, provided supervision	-

Candidate's Signature	[redacted]	**Date** 15/04/09

Declaration by co-authors

The undersigned hereby certify that:

(1) the above declaration correctly reflects the nature and extent of the candidate's contribution to this work, and the nature of the contribution of each of the co-authors.

(2) they meet the criteria for authorship in that they have participated in the conception, execution, or interpretation, of at least that part of the publication in their field of expertise;

(3) they take public responsibility for their part of the publication, except for the responsible author who accepts overall responsibility for the publication;

(4) there are no other authors of the publication according to these criteria;

(5) potential conflicts of interest have been disclosed to (a) granting bodies, (b) the editor or publisher of journals or other publications, and (c) the head of the responsible academic unit; and

(6) the original data are stored at the following location(s) and will be held for at least five years from the date indicated below:

Location(s)	Department of Chemistry, Centre for Biospectroscopy, Monash University, Clayton

Please note that the location(s) must be institutional in nature, and should be indicated here as a department, centre or institute, with specific campus identification where relevant.]

Signature	Date
Bayden Wood (MONASH UNIVERSITY) [redacted]	15/4/09
[redacted]	15/4/09

ohio2/yjp-yjp/yjp-yjp/yjp99907/yjp7313d07z | xppws | 23:ver.3 | 4/4/09 | 18:34 | Msc: jp-2008-11028a | TEID: mac00 | BATID: jp5d125

Aggregated Enhanced Raman Scattering in Fe(III)PPIX Solutions: The Effects of Concentration and Chloroquine on Excitonic Interactions

Grant T. Webster, Don McNaughton, and Bayden R. Wood*

Centre for Biospectroscopy and School of Chemistry, Monash University, Clayton, Victoria 3800, Australia

Received: December 14, 2008; Revised Manuscript Received: March 20, 2009

Resonance Raman spectra of hematin and hemin solutions are reported for 413 and 514 nm wavelengths. Enhancement of A_{1g} modes (1569 and 1370 cm^{-1}) and B_{1g} modes (1124 and 755 cm^{-1}) as a function of increased concentration are observed when irradiating with 514 nm laser excitation but not 413 nm. This can be rationalized by considering an excitonic coupling mechanism. As the concentration of hematin increases there is an increased probability of supramolecular interactions between iron(III) protoporphyrin IX (Fe(III)PPIX) units occurring. The Fe(III)PPIX concentration reaches a saturation point in solution and excitonic coupling reaches a maximum causing the enhancement profile to plateau when applying 514 nm excitation. In contrast, when using 413 nm excitation there were no changes in band intensity with increased concentration showing that excitonic coupling through supramolecular interactions for aggregated solutions is wavelength dependent. Electronic absorption spectra show that as the concentration of Fe(III)PPIX increases in solution the Soret band is slightly blue shifted and the Q-band significantly broadens supporting the excitonic hypothesis. Understanding the mechanism that accounts for the Raman photophysical behavior of hemes at high concentrations provided an indirect method to monitor antimalarial drug interactions. A second aim was to investigate chloroquine binding to Fe(III)PPIX-OH/H_2O monomers, $\pi-\pi$ dimers and μ-oxo dimers formed in highly concentrated solutions approaching those of the digestive vacuole of the *P. falciparum* malaria parasite using excitonic Raman enhancement. It was hypothesized that the Raman excitonic enhancement mechanism could be impeded in heme aggregated solutions by the addition of chloroquine. This would result in a reduction in heme bands associated with the A_{1g} modes including ν_4. Resonance Raman spectra recorded using 514 nm excitation show that chloroquine (CQ) acts as a molecular spacer and binds noncovalently through dispersion interactions giving rise to $\pi-\pi$ interactions, between μ-oxo dimer units of Fe(III)PPIX as evinced by the decrease in intensity of ν_4 in the Raman spectrum as a function of increasing CQ mole ratio. In comparison, electronic spectra show that CQ can bind to the unligated face of Fe(III)PPIX-OH/H_2O monomers, potentially reducing the formation of $\pi-\pi$ dimers. This study has important implications in determining the effectiveness of potential antimalarial compounds that are thought to exert their effectiveness by binding through supramolecular interactions to the unligated faces of Fe(III)PPIX-OH/H_2O monomers and μ-oxo dimers.

Introduction

Resonance Raman spectroscopy is a powerful tool to study porphyrin moieties including hemes and other metallo-porphyrins.[1] The intrinsic symmetry and chromophoric structure of iron-protoporphyrin IX (Fe(PPIX)) molecules such as hemin (Fe(PPIX-Cl)) and hematin (Fe(PPIX-OH)) results in strong Raman scattering upon excitation at many wavelengths. Resonance or preresonance with the Soret and Q bands that are observed in the UV−visible spectrum of metallo-porphyrins results in enhancement of totally symmetric (A_{1g}) and nontotally symmetric (B_{1g}, B_{2g}, and A_{2g}) modes, respectively. Two important resonance Raman scattering terms determined by Tang and Albrecht[2] provide insight into the relationship between vibrational Raman intensities and excited-state structure. Type A depends on the product of the Franck−Condon integrals between the intermediate level and the initial and final vibrational states, with totally symmetric modes having nonzero values.[1] This results in enhancement of A_{1g} modes when using excitation wavelengths in the vicinity of the Soret band near 400 nm. For type B scattering, vibrational overlap depends on the displacement of the normal coordinate and how this perturbs the excited-state structure and can be nonzero for nontotally symmetric (B_{1g}, B_{2g}, and A_{2g}) modes when exciting with a laser in the Q-band region (500−600 nm). In this case, vibronic mixing usually via a low frequency nontotally symmetric mode can enhance the intensity by coupling to a nearby strong allowed transition.[1] Both Raman scattering mechanisms act as excellent models to explain the resonance Raman spectra in the case of dilute solutions; however, the above model does not hold for aggregated solids. Akins[3] observed unusual scattering in small aggregates of covalently linked porphyrin arrays and cyanine dyes absorbed onto surfaces. Akins[3] described this phenomenon as aggregated enhanced Raman scattering (AERS), whereby an increase in the number of aggregated chromophores produces near-resonance of both the A and B terms in the polarizability tensor.[3] The electronic states are split into a broadband of states with different geometries, energies, and oscillator strengths through excitonic coupling and the extent of this coupling will affect the intensity of the Raman signal for a particular wavelength.[4] Previous studies by Kasha[5] defined molecular excitons as the resonance interaction between the excited states of loosely bound molecular aggregates. Under certain conditions,

* To whom correspondence should be addressed.

10.1021/jp811028a CCC: $40.75

ohio2/yjp-yjp/yjp-yjp/yjp99907/yjp7313d07z | xppws | 23:ver.3 | 4/4/09 | 18:34 | Msc: jp-2008-11028a | TEID: mac00 | BATID: jp5d125

he described it as either locally excited states of the excited molecular aggregate that produce a collective excitation, or a superposition of these collective excited states which describes the excitation in terms of a traveling-wave packet of excitation energy known as the exciton.[5] Previous studies show that covalently meso-meso-linked Cu(II)[6,7] and Zn(II)[8] porphyrin arrays display strong excitonic interactions and distinct splitting of the Soret band resulting in atypical Raman scattering patterns. Aratani et al.[9] reported the UV−visible absorption spectra of various ZnP-H_2P hybrid diporphyrin aggregates with a blue shift in the Soret band and broadening in the Q-bands supporting a face-to-face multiporphyrinic system. de Villiers and co-workers[10] propose a model in which the spontaneously formed aqueous Fe(III)PPIX dimer noncovalently interacts with the unligated faces of two five-coordinate H_2O/HO^-Fe(III)PPIX molecules with the axial H_2O/HO^- ligands pointing outward. Understanding the photophysical behavior of hemes at high concentrations may have important implications in developing antimalarial drugs that are designed to inhibit the formation of hemozoin, a byproduct formed from the catabolism of hemoglobin by the malaria parasite *Plasmodium falciparum.*

Malaria is still a widespread tropical disease that affects 500 million people causing over 1 million deaths per year.[11] During the intraerythrocytic stage of the *Plasmodium sp.* lifecycle, hemoglobin is degraded into toxic-free heme (Fe(PPIX)) and denatured globin.[12,13] Detoxification then involves the conversion of Fe(III)PPIX to hemozoin, also known as malaria pigment, within the parasites digestive vacuole.[10,14−16] Quinoline antimalarial drugs such as chloroquine are believed to exert their action by targeting Fe(III)PPIX in the form of hematin, its μ-oxo dimer ([Fe(III)PPIX]$_2$O) or the biomineralized hemozoin ([Fe(III)PPIX]$_2$) pellet within the digestive vacuole of the malaria parasite.[17] Cohen et al.[18] first reported complex formation between chloroquine (CQ) and Fe(III)PPIX in the 1960s. Chou and co-workers[19] later discovered that Fe(III)PPIX is a molecular drug target for chloroquine (CQ) and other quinoline drugs and that interactions between these drugs and Fe(III)PPIX results in antimalarial activity. Using polarization-resolved resonance Raman spectroscopy Frosch et al.[20] observed small wavenumber shifts, which supports a noncovalent Fe(III)PPIX/drug complex, when CQ was mixed with hematin in solution. Measurements of a CQ-Fe(III)PPIX complex were compared with data from hematin and CQ using Near IR Surface Enhanced Raman Spectroscopy (NIR-SERS).[21] The CQ-Fe(III)PPIX complex showed $\pi-\pi$ interaction between the porphyrin ring and the quinoline ring of the drug.[21] Red shifts in the Soret band were previously observed[22] in the UV−visible absorbance spectra upon CQ-porphyrin π stacking of these complexes. The Q bands decrease in intensity, while a significant blue shift in the charge-transfer band is observed upon Fe(III)PPIX-quinoline complexation.[15] The affect of Fe(III)PPIX-quinoline interactions on antimalarial activity and inhibition of hemozoin and/or β-hematin has been previously addressed[23−26] and therefore will not be discussed in detail here. The above studies indicate $\pi-\pi$ orbital overlap is involved in the intermolecular interaction between chloroquine and Fe(III)PPIX porphyrin. In this study we provide support for the notion that the interaction between CQ and Fe(III)PPIX-OH/H_2O monomers and μ-oxo dimers is initiated through supramolecular interactions (particularly dispersion interactions), with resultant $\pi-\pi$ interactions.

In this work, we combine resonance Raman spectroscopy using 413 and 514 nm excitation and UV−visible measurements to investigate the enhancement profile of Fe(III)PPIX solutions as a function of concentration and explore the structural changes occurring upon CQ-Fe(III)PPIX interaction in solution. We present evidence for AERS in Fe(III)PPIX solutions based on an intensity increase observed for A_{1g} modes as a function of concentration and demonstrate that this phenomenon is excitation wavelength dependent. We also hypothesize that CQ acts as a molecular spacer and binds to the unligated faces of μ-oxo dimer Fe(III)PPIX units through $\pi-\pi$ interactions and other supramolecular interactions leading to a reduction in excitonic interactions, which manifests in the spectra as a decrease in intensity of the A_{1g} totally symmetric modes as a function of increasing CQ concentration. Electronic spectra provide further evidence that CQ binds to the unligated faces of Fe(III)PPIX-OH/H_2O monomer units, which potentially reduce formation of $\pi-\pi$ dimers as evinced by a red shift in the Soret band as a function of increasing the CQ mole ratio.

Experimental Section

Resonance Raman Spectroscopy. Raman spectra of aqueous hemin and hematin solutions were recorded using a Renishaw inVia Raman Microscope spectrometer (Renishaw Pty Ltd., Wooton-under-edge, UK) with ×20 objective. The instrument was calibrated daily using the 520.5 cm^{-1} band of a silicon wafer. The excitation source was a krypton−argon laser with ca. 50 mW raw output power and ca. 0.5−1 mW power at the sample for 413 nm excitation and ca. 300 mW raw output power and ca. 8−10 mW power at the sample for 514 nm excitation. The solutions were continuously pumped through a glass tube (flow-through-cell (FTC)) using a peristaltic pump, and under these experimental conditions there was no evidence of photodecomposition or sample damage. For hemin, hematin, and hematin/CQ μ-oxo dimer solutions, 30 spectra were recorded in the range 1800−200 cm^{-1} using a single 10 s exposure. All Raman spectra were normalized to the ν_{10} $\nu(C_\alpha C_m)_{asym}$ B_{1g} vibrational mode at ca. 1625 cm^{-1}. Spectra of hematin, hemin, μ-oxo dimer, $\pi-\pi$ Fe(III)PPIX-OH dimer/CQ, and Fe(III)PPIX/CQ μ-oxo dimer solutions were derived by averaging 30 spectra taken at different positions within the solution using the Bruker OPUS software and the experiments were repeated three times. Standard deviation spectra were calculated using the Bruker OPUS software.

UV−visible Spectroscopy. UV−visible absorbance spectra were recorded for hemin and hematin solutions at various concentrations (1.25, 2.5, 5, 7.5, and 10 μM) using a CARY 100 Bio UV−visible spectrometer. Sample solutions were prepared by dissolving the compounds in 0.1 M NaOH to make a 4 mL 0.01 M Fe(III)PPIX stock solution. In order to maintain absorbance below 0.7 a 2 mm cuvette was used to obtain the absorbance of the Soret band while a 1 cm cuvette was used to acquire the absorbance of the Q bands. Nine millimolar stock solutions of hematin μ-oxo dimer (control) and hematin μ-oxo dimer/CQ mole ratio mixtures (1:1, 1:2, and 1:5) were diluted 100-fold in aqueous 0.1 M NaOH/10% pyridine solution and absorbance spectra were taken using a 2 mm cuvette. The above dilution of the 9 mM stock solution of control and hematin μ-oxo dimer/CQ mole ratio mixtures was repeated with distilled water and absorbance spectra were recorded using a 2 mm cuvette.

Data Analysis. Initial spectral manipulations on the Raman spectra were carried out under OPUS. Each sample data set contained 30 Raman spectra, which were averaged independently to produce the mean spectra presented. All second derivative spectra were calculated using the Savitsky−Golay algorithm with 13 smoothing points. N.B. In the second derivative spectra the Raman intensities become minima and

ohio2/yjp-yjp/yjp-yjp/yjp99907/yjp7313d07z | xppws | 23:ver.3 | 4/4/09 | 18:34 | Msc: jp-2008-11028a | TEID: mac00 | BATID: jp5d125

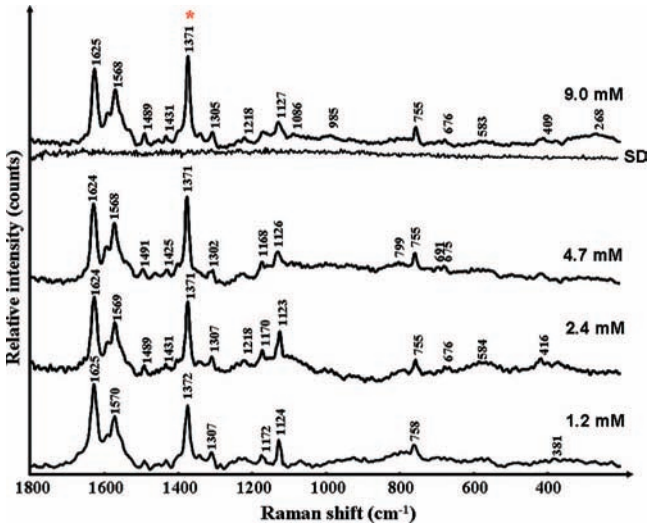

Figure 1. Raman spectra of hematin solution concentrations using 514 nm excitation laser. The spectra were normalized to the ν_{10} band positioned at ca. 1625 cm^{-1}. The asterisk indicates band enhancement. The standard deviation spectrum calculated for the 9 mM concentration is representative for all concentrations shown.

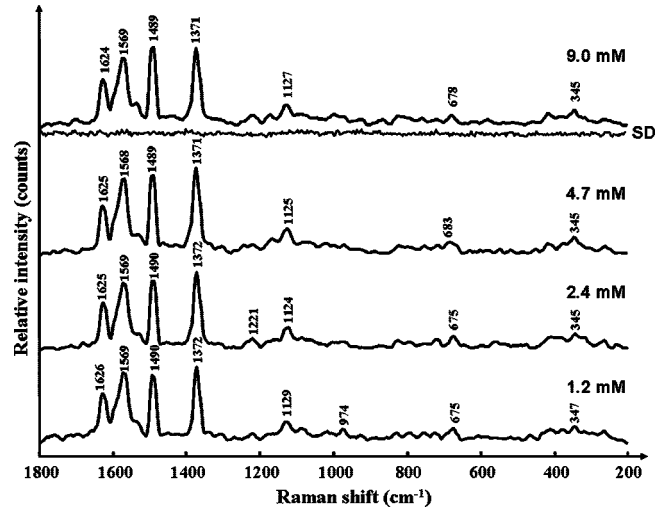

Figure 2. Raman spectra of hematin solution concentrations using 413 nm excitation. The spectra were normalized to the ν_{10} band positioned at ca. 1625 cm^{-1}. The standard deviation spectrum calculated for the 9 mM concentration is representative for all concentrations shown.

in the discussion below intensities are thus +ve for Raman intensity and −ve for second derivative spectra.

Materials and Synthesis. Stock solutions (0.1 M) of hemin (Fluka) and hematin (Sigma-Aldrich) were prepared by dissolving the solid compounds separately in aqueous base (0.1 M NaOH). Ten milliliters of 0.1 M NaOH solution was added to a vial which was used independently as the reaction vessel for both compounds. Volume increments of stock solution (250 μL) were titrated into the reaction vessel for each sample run and were magnetically stirred. The cumulative volume of the reaction vessel for both hemin and hematin solutions was 12.5 mL each and the final concentration range for both was 1.15−20 mM. The solution was continually pumped into the FTC and recycled back into the reaction vessel using a peristaltic pump. Nine millimolar stock solutions of Fe(III)PPIX μ-oxo dimer solutions from hematin and hemin were prepared separately by dissolving the solid compounds in 10% aqueous organic base (0.1 M NaOH/10% pyridine). Chloroquine diphosphate purchased from Sigma-Aldrich was dissolved in 0.1 M NaOH/10% pyridine to make up the mole ratio mixtures.

Results and Discussion

Heme Concentration Study. Raman spectra of hematin solutions at a range of concentrations using 514 nm excitation are presented in Figure 1. For comparative purposes the spectra are normalized to the ν_{10} band at 1625 cm^{-1}. Following convention the mode notation is based on studies by Abe et al.[27] for the resonance Raman spectra of nickel octa-ethyl porphyrin and all mode notations in the present study refer to the idealized D_{4h} symmetry point group, although ferric high spin hemes such as hematin, hemin, and oxy-hemoglobin have the Fe atom translocated out of the porphyrin plane and so strictly have C_{4v} symmetry. Totally symmetric (A_{1g}) modes and nontotally symmetric (B_{1g}, A_{2g} and B_{2g}) modes are designated $\nu_1-\nu_9$ for A_{1g}, $\nu_{10}-\nu_{18}$ for B_{1g}, $\nu_{19}-\nu_{26}$ for A_{2g}, $\nu_{27}-\nu_{35}$ for B_{2g}, and ν_{36}-ν_{55} for E_u.[4,27,28] The strong bands in Fe(III)PPIX-OH spectra include the in-plane asymmetric stretch of the porphyrin ring $\nu_{10}(\nu(C_\alpha C_m)_{asym})$ at 1625 cm^{-1}. Bands at 1568, 1371, 1127, and 755 cm^{-1} are assigned to $\nu_2(\nu(C_\beta C_\beta))$, $\nu_4(\nu(\text{pyrrole half-ring})_{sym})$, $\nu_{13}(\delta(C_mH))$ and ν_{15}(pyrrole breathing), respectively. When the excitation wavelength is near the absorbance maximum of the Soret band the spectra show enhancement of totally symmetric (A_{1g}) modes. This is typical when the Franck−Condon or type A scattering mechanism dominates. The totally symmetric ν_4 vibrational mode (electron density marker band) of hematin relative to ν_{10} increases as a function of concentration. This may be explained by invoking an excitonic coupling mechanism. In the same manner as in the experiments of Akins[29] when the concentration of hematin increases there is an increased chance of aggregation. Energy in the form of an exciton would then be delocalized throughout the Fe(III)PPIX supramolecular ensemble. In order for excitonic interactions to occur an electronic transition is required. A *z*-polarized charge transfer (CT) band is observed at ca. 550 nm for ferric high spin systems in the vicinity of the 514 nm excitation wavelength.[4] Increasing the aggregation increases the probability and strength of supramolecular interactions between intermolecular units through $\pi-\pi$, $\pi-$HC− and other supramolecular interactions such as O−HC− for hematin and Cl−HC− for hemin. For comparison Raman spectra of hematin solution concentrations using 413 nm excitation are presented in Figure 2. Although enhancement of the A_{1g} band ν_3 ($C_\alpha C_m)_{sym}$ mode) at 1490 cm^{-1} is observed, there is no enhancement of ν_4 relative to ν_{10} as a function of concentration. This wavelength dependent enhancement behavior in solution is most likely due to the fact that at 413 nm the excitation is not in resonance with the *z*-polarized CT band, which based on an earlier study,[4] appears necessary for excitonic enhancement in some heme systems. Raman spectra from both hemin and hematin solutions show that this AERS enhancement is independent of near-resonance and resonance Raman enhancement. Raman spectra of these Fe(III)PPIX-OH $\pi-\pi$ dimer aggregates were compared to Fe(III)PPIX μ-oxo dimers in solution in the same concentration range (data not shown). However, Fe(III)PPIX μ-oxo-dimer spectra did not show a wavelength dependent enhancement of the totally symmetric ν_4 mode relative to ν_{10} as a function of concentration. Fe(III)PPIX μ-oxo-dimers have two unligated faces resulting in fewer sites for intermolecular interactions and probably reducing dispersion forces and consequently the binding affinity between adjacent μ-oxo-dimer units. The consequence of this would lead to little or no enhancement of ν_4.

ohio2/yjp-yjp/yjp-yjp/yjp99907/yjp7313d07z | xppws | 23:ver.3 | 4/4/09 | 18:34 | Msc: jp-2008-11028a | TEID: mac00 | BATID: jp5d125

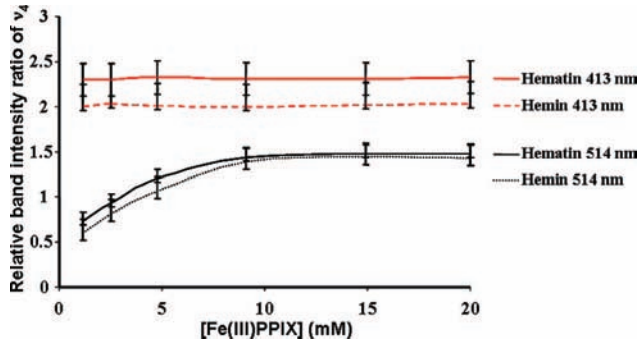

Figure 3. Plot of Fe(III)PPIX concentration vs band intensity of ν_4 relative to ν_{10}.

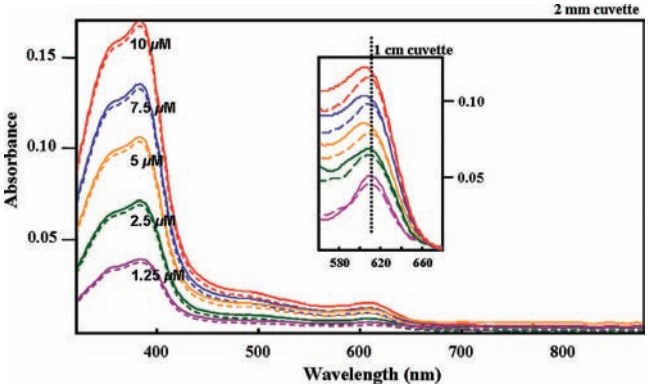

Figure 4. UV−visible absorbance spectra of hematin (——) and hemin (-----) solutions at varying concentrations.

A previous study[30] has shown that a nonlinear increase in fluorescence intensity is correlated with increased porphyrin IX concentration in aqueous solution and hence indicates a plateau in the aggregation of monomer units. Figure 3 shows a plot of concentration versus the Raman band intensity ratio of ν_4 relative to ν_{10} for Fe(III)PPIX-OH and Fe(III)PPIX-Cl. For 514 nm excitation as the concentration of Fe(III)PPIX-OH/Cl increases, the relative intensity of ν_4 increases and then plateaus whereas for 413 nm excitation the relative intensity of ν_4 is independent of concentration. The degree of AERS enhancement and thus the excitonic coupling is wavelength dependent. Previous UV−visible studies[9] have found that for ZnP-H_2P meso-meso-linked diporphyrins with a face-to-face geometry an extremely broad and featureless Q-band results and the Soret band is blue shifted while head-to-tail meso-meso-linked hybrid diporphyrins are characterized by splitting of the blue-shifted Soret band and orthogonal meso-meso-linked diporphyrin J-aggregates display a split red-shifted Soret band. In contrast, band splitting in the Q-band region occurs for meso-meso linked dimers where the strength of exciton coupling is mainly determined by the center-to-center distance between the porphyrin monomers.[9] Figure 4 shows how the UV−visible absorption spectra for hematin (——) and hemin (------) vary with increasing concentration. Electronic transitions from the ground state (S_0) to the two lowest singlet excited states S_1 and S_2 result in the UV−visible Q-band (550−650 nm) and Soret band (380−450 nm) respectively.[6] As the concentration of Fe(III)PPIX-OH/Cl increases in solution the Soret band is slightly blue shifted (ca. 2−3 nm) and the Q-band broadens, showing that the spectral changes observed are of the same type as for the face-to-face packing arrangement of meso-meso-linked diporphyrins described by Aratani.[9] We propose that supramolecular interactions, which include $\pi-\pi$ orbital overlap and other intermolecular concerted interactions, increase the probability of excitonic interactions

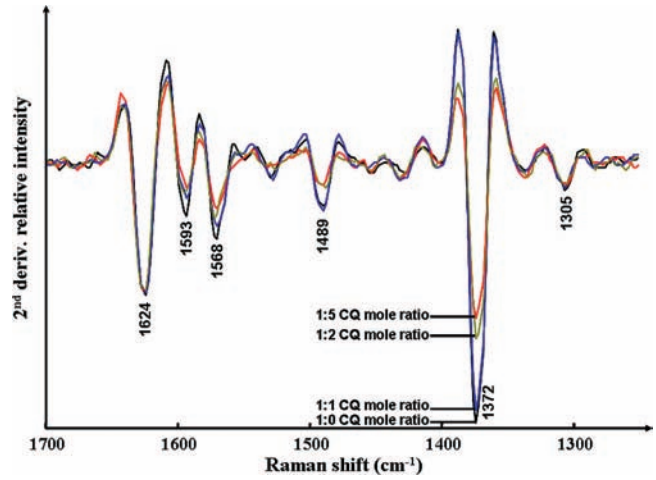

Figure 5. Raman second derivative spectra (514 nm excitation) of hematin and hemin at varying mole ratios of CQ in solution. The spectra were normalized to the ν_{10} band positioned at ca. 1624 cm^{-1} prior to the second derivative calculation.

as the concentration of Fe(III)PPIX-OH/Cl increases. This hypothesis is supported by the increase in Raman band intensity of ν_4 for 514 nm excitation observed in Figure 3. Once the concentration of Fe(III)PPIX-OH/Cl has reached a point where the face-to-face alignment of porphyrins is at a maximum throughout the system (9 mM), the relative band intensity of ν_4 is quenched. This maximizes excitonic coupling throughout the extended Fe(III)PPIX array through the superposition of excited electronic states.[28] We propose that supramolecular interactions and intermolecular concerted interactions give rise to $\pi-\pi$ orbital overlap and increase the probability of excitonic interactions as the concentration of Fe(III)PPIX-OH/Cl increases. We hypothesize that a molecular spacer like chloroquine that binds cofacially to hematin and its related dimers will impede excitonic interactions thus reducing the intensity of the A_{1g} modes. The following study tests that hypothesis.

Chloroquine Drug Study. Previous studies[10] have shown that Fe(III)PPIX in the presence of an organic base in alkaline aqueous solution (0.1 M NaOH/10% pyridine) induces the formation of the μ-oxo dimer species. Spectra of μ-oxo dimer Fe(III)PPIX-CQ mixture in aqueous solution (0.1 M NaOH/10% v/v pyridine) using 514 nm excitation are presented in Figure 5. For comparative purposes, the spectra in Figure 5 are normalized to the band at ν_{10}(1624 cm^{-1}). The strong bands in μ-oxo dimer Fe(III)PPIX-CQ spectra include the in-plane asymmetric stretch of the porphyrin ring $\nu_{10}(\nu(C_\alpha C_m)_{asym})$ at 1624 cm^{-1}. Bands at 1593, 1568, 1489, 1372, and 1305 cm^{-1} are assigned to $\nu(C_\alpha C_m)_{asym}$, $\nu_2(\nu(C_\beta C_\beta))$, $\nu_3(\nu(C_\alpha C_m)_{sym})$, $\nu_4(\nu(\text{pyrrole half-ring})_{sym})$, and $\delta(C_mH)$, respectively. The intensity of the totally symmetric ν_4 vibrational mode relative to ν_{10} decreases as a function of CQ mole ratio because the ν_4 vibrational mode is sensitive to electron density of the porphyrin. Raman spectra of Fe(III)PPIX-CQ solutions using 413 nm excitation are compared in Figure 6. There is a significant decrease in the A_{1g} band positioned at 1491 cm^{-1} as a function of increased mole ratio of CQ in solution with only a slight decrease in the intensity of ν_4. The decrease in the intensity of the $\nu(C_\alpha C_m)_{asym}$ mode positioned at 1491 cm^{-1} at increased mole ratios of CQ suggests that the drug is indeed affecting the molecular environment of Fe(III)PPIX. Quinoline antimalarial drugs such as chloroquine are believed to exert their action by targeting Fe(III)PPIX in the form of hematin, its μ-oxo dimer ([Fe(III)PPIX]$_2$O) or the biomineralized hemozoin ([Fe(III)P-

ohio2/yjp-yjp/yjp-yjp/yjp99907/yjp7313d07z | xppws | 23:ver.3 | 4/4/09 | 18:34 | Msc: jp-2008-11028a | TEID: mac00 | BATID: jp5d125

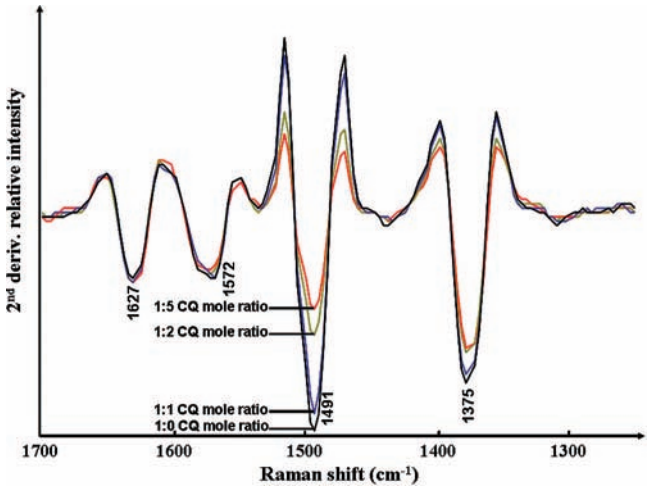

Figure 6. Raman second derivative spectra (413 nm excitation) of hematin and hemin at varying mole ratios of CQ in solution. The spectra were normalized to the ν_{10} band positioned at ca. 1624 cm^{-1} prior to the second derivative calculation.

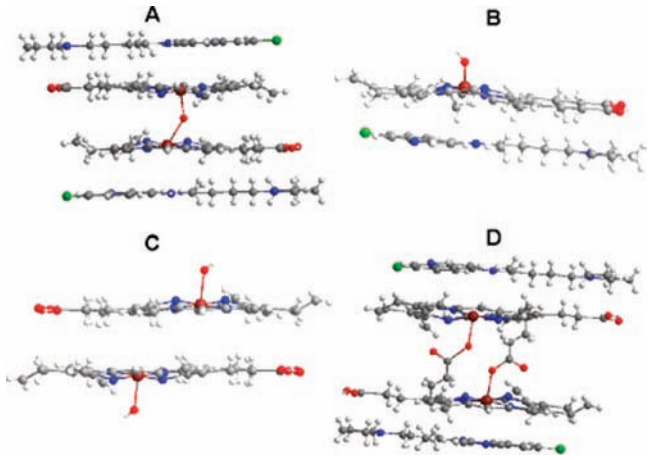

Figure 7. Model structures of the five coordinate Fe(III)PPIX μ-oxo dimer (a), Fe(III)PPIX-OH monomer (b), Fe(III)PPIX-OH $\pi-\pi$ dimer (c), and hemozoin dimer unit (d). CQ noncovalently binds through $\pi-\pi$ interactions and other dispersion forces to the unligated faces of panels a, b, and d but not panel c.

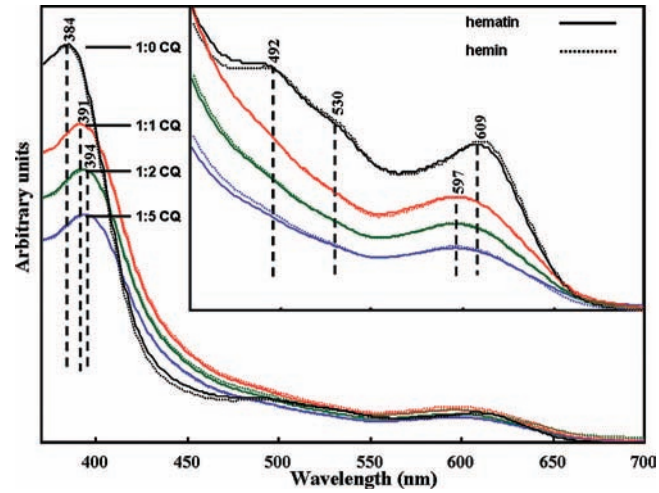

Figure 8. UV−visible absorbance spectra of hematin (——) and hemin (-----) solutions at varying mole ratios of CQ.

PIX]$_2$) pellet within the digestive vacuole of the malaria parasite.[17] Under these experimental conditions (0.1 M NaOH/10% pyridine) Fe(III)PPIX-OH dimerizes and exists predominantly in the form of its μ-oxo-dimer.[10,31] Here, CQ is acting as a molecular spacer between Fe(III)PPIX μ-oxo dimer units and associates to the unligated faces of the μ-oxo dimer via a $\pi-\pi$ mechanism as shown in Figure 7a. This in turn reduces excitonic interactions and also demontrates how a Raman supramolecular photophysical phenomenon can be used as method to monitor heme/drug interactions. Previous studies by Webster et al.[28] using resonance Raman spectroscopy to analyze hemozoin/CQ interactions within live malaria infected parasites show a significant reduction of ν_4 that indicate CQ binds via $\pi-\pi$ interactions between adjacent and orientated porphyrins, thereby disrupting the hemozoin aggregate. The current study supports these earlier findings and moreover indicates that CQ binds to the unligated faces of Fe(III)PPIX-OH/H_2O $\pi-\pi$ dimers, Fe(III)PPIX-OH/H_2O monomer and the μ-oxo dimer via a $\pi-\pi$ mechanism as shown in Figure 7a−d. In the parasite the effect would be to cap the growth of the hemozoin dimer, thus increasing the amount of free heme in the digestive vacuole, which would ultimately kill the parasite. However, it is likely that the hemozoin dimer does not form directly from the μ-oxo dimer unit, but rather from a monomeric intermediate. This is because the large magnitude of the dimerization constant of Fe(III)PPIX in an aqueous environment would involve a large activation energy.[10] In contrast to the μ-oxo dimer model, the $\pi-\pi$ dimer proposed by de Villiers et al.[10] (Figure 7c) would not need to dissociate in order to form the hemozoin dimer. All that is required is for each of the propionate side chains to adopt a conformation where they are in close proximity to their reciprocal Fe(III) center. This is followed by displacement of the axial (−OH/H_2O) ligands from the opposite face once the Fe(III)-propionate linkage is formed. However, it is likely that before $\pi-\pi$ dimers form, CQ can associate to the unligated face of monomers, which reduces the formation of $\pi-\pi$ dimers in the digestive vacuole. It is also possible that CQ can associate to the unligated faces of the hemozoin dimer directly through supramolecular interactions after there is a lateral shift in the $\pi-\pi$ dimer to form a hemozoin dimer unit with the axial ligands displaced as shown in Figure 7d. All three CQ drug binding models (Figure 7a,b,d) bind CQ noncovalently through dispersion interactions to the unligated faces of Fe(III)PPIX, which can be directly responsible for capping the unligated faces of the hemozoin dimer and preventing formation of a propionate linkage to the Fe(III) center of adjacent hemozoin dimer units. In comparison, Solomonov et al.[32] as part of a larger study also showed ν_4 to appear more intense in Raman spectra of pure β-hematin crystals compared to those of its drug-affected counterparts. The effects of CQ mole ratio on $\pi-\pi$ Fe(III)PPIX-OH dimer aggregates were compared to those of μ-oxo dimer Fe(III)PPIX-OH species and the Raman spectra were examined (data not shown). The Raman spectra showed no effect of CQ on $\pi-\pi$ Fe(III)PPIX-OH dimer aggregates as there was no decrease in intensity of the totally symmetric ν_4 vibrational mode relative to ν_{10} as a function of CQ mole ratio. This is probably due to Fe(III)PPIX-OH forming higher order aggregates at 9 mM concentration and so the ligated faces of the $\pi-\pi$ Fe(III)PPIX (−OH/H_2O) dimer will be sterically hindered, reducing the available sites for CQ attachment. However, the UV−visible absorbance spectra (Figure 8) supports monomer-Fe(III)PPIX-OH/Cl/CQ complexation. The spectra are identical to aggregation of Fe(III)PPIX monomers in 40% aqueous DMSO reported by Egan et al.[15] after dilution (1:100) of the complexes in distilled water and suggests the equilibrium is pushed from μ-oxo dimer formation to Fe(III)PPIX-OH/Cl monomer aggregates due to the dilution of pyridine in the

ohio2/yjp-yjp/yjp-yjp/yjp99907/yjp7313d07z | xppws | 23:ver.3 | 4/4/09 | 18:34 | Msc: jp-2008-11028a | TEID: mac00 | BATID: jp5d125

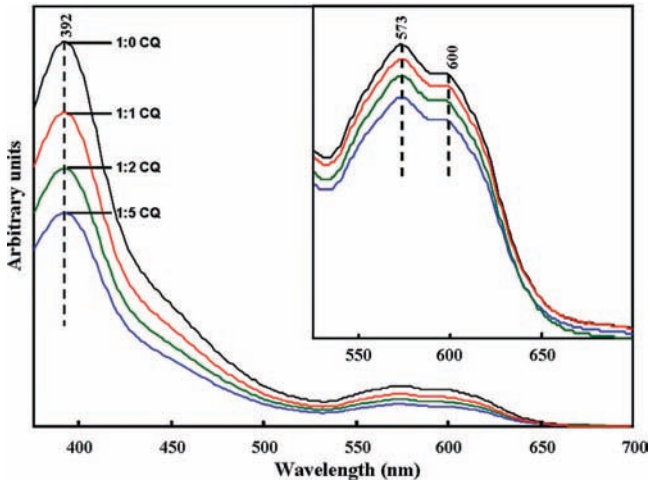

Figure 9. UV−visible absorbance spectra of hematin μ-oxo dimer solutions at varying mole ratios of CQ.

system. The Soret band red shifts upon CQ-Fe(III)PPIX monomer stacking from 384 nm with no CQ to 394 nm at higher mole ratios of CQ. The Q bands at 492 and 530 nm reduce significantly and a shift from 609 to 597 nm in the CT band is observed when CQ is introduced. These changes reflect noncovalent binding of CQ on Fe(III)PPIX.[33] The effects of CQ on Fe(III)PPIX-OH aggregation can easily be seen in the UV−visible spectra and not in the Raman spectra because the concentration of Fe(III)PPIX-OH is diluted 100-fold. Thus, at lower concentration there is a higher probability prior to the formation of possible $\pi-\pi$ dimers that CQ associates to the unligated face of aggregated Fe(III)PPIX-OH monomer units giving rise to a red shift of the Soret band in the UV−visible spectrum. Previous studies[10,17] have supported the suggestion of $\pi-\pi$ stacking of quinoline drugs to Fe(III)PPIX. de Villiers et al.[10] also reported UV−visible spectra that show a noncovalent dimer being the dominant species at CQ concentrations above 10^{-5} M. Egan and co-workers[17] show UV−visible spectroscopic evidence of Fe(III)PPIX binding to CQ through $\pi-\pi$ stacked complexes in solution and invoke an exciton model. Because of the Fe(III)PPIX-quinoline complex being much smaller than the wavelength of light, the oscillating electric field of a photon will simultaneously interact with electrons from both molecules of the complex.[17] Since, the transition dipole moments are positioned within the planes of these molecules this can cause the transition dipoles of both molecules in the complex to overlap which induces excitonic coupling and consequent band splitting. The Soret band of Fe(III)PPIX is the net absorbance envelope of closely spaced bands consisting of $\pi \rightarrow \pi^*$ electronic transitions. Therefore, upon quinoline $\pi-\pi$ stacking the symmetry of the complex reduces and further splits the bands. This accounts for the strong hypochromic effects observed in the UV−visible spectra.[17] UV−visible absorbance spectra of μ-oxo dimer Fe(III)PPIX/CQ complex solutions are compared (Figure 9). The Soret band has shifted from 384 nm in the monomer to 392 nm in the μ-oxo dimer. This is evidence that aggregation is occurring, which splits the electronic energy levels into a broadband of states with different energies through excitonic coupling.[4,7] Upon increasing the amount of CQ relative to Fe(III)PPIX μ-oxo dimer, there is no change in the Soret band.

Conclusion

An early study by Wood et al.[4] presented resonance Raman band enhancement profiles of β-hematin and hemin at various laser excitation wavelengths in the solid phase. Excitation into the Soret band produces a type A scattering pattern and enhancement of several totally symmetric A_{1g} modes. Excitation in the Q-band region showed a decrease in enhancement of the A_{1g} modes. Although this last study showed the enhancement profile of Fe(III)PPIX in the solid phase using resonance Raman spectroscopy, no study has shown AERS enhancement of Fe(III)PPIX in solution using resonance Raman spectroscopy. For the iron(III) protoporphyrin IX (Fe(III)PPIX) compounds hemin and hematin we have observed within the millimolar concentration range an increase in Raman intensity of the ν_4 totally symmetric A_{1g} mode (ca. 1370 cm^{-1}) relative to ν_{10} with increasing concentrations in aqueous solutions. This increase is seen to be wavelength dependent. From a band intensity analysis of different concentration solutions we conclude that AERS occurs in Fe(III)PPIX solutions. This study provides new insight into the nature of excitonic coupling which initially occurs due to supramolecular interactions resulting in the $\pi-\pi$ stacking of Fe(III)PPIX units in solutions. This may have important implications in understanding energy transfer processes in heme systems.

To test the excitonic hypothesis we introduced chloroquine, which based on UV−visible spectroscopy is known to bind cofacially via $\pi-\pi$ interactions to Fe(III)PPIX. The results indicate CQ acts as a molecular spacer binding to the unligated faces of μ-oxo dimer through $\pi-\pi$ interactions and other dispersion forces. The CQ thus reduces the probability of heme excitonic interactions throughout the supramolecular network explaining the decrease in ν_4 as a function of increased CQ concentration. The same CQ drug binding mechanism to the unligated face of Fe(III)PPIX-OH monomers manifests in the electronic spectra as a red shift in the Soret band at increasing CQ mole ratios. This also reduces the formation of Fe(III)PPIX-OH/H_2O $\pi-\pi$ aggregates in the system. This study has important implications in understanding the photophysical behavior of hemes in concentrated solutions. Moreover, the study shows that resonance Raman spectroscopy can be used to indirectly monitor drug:heme interactions by studying the intensity of excitonically sensitive bands such as ν_4.

Acknowledgment. This work is supported by an Australian Research Council Discovery grant. We thank Mr Finlay Shanks (Monash University) for instrument support and maintenance.

References and Notes

(1) Spiro, T. G.; Li, X-Y. *Resonance Raman spectroscopy of metalloporphyrins*; Wiley: New York, 1988; Vol. 3.
(2) Tang, J. J.; Albrecht, A. C. *J. Raman Spectrosc.* **1970**, *2*, 33.
(3) Akins, D. L. *J. Phys. Chem.* **1986**, *90*, 1530.
(4) Wood, B. R.; Langford, S. J; Cooke, B. M; Lim, J; Glenister, F. K; Duriska, M; Unthank, J. K; McNaughton, D. *J. Am. Chem. Soc.* **2004**, *126*, 9233.
(5) Kasha, M. *Radiat. Res.* **1963**, *20*, 55.
(6) Chen, D.-M.; Zhang, Y.-H.; He, T.-J.; Liu, F.-C. *Spectrochim. Acta* **2002**, *58*, 2291.
(7) Bhuiyan, A. A.; Seth, J.; Yoshida, N.; Osuka, A.; Bocian, D. F. *J. Phys. Chem. B* **2000**, *104*, 10757.
(8) Kim, Y. H.; Jeong, D. H.; Kim, D.; Jeoung, S. C.; Cho, H. S.; Kim, S. K.; Aratani, N.; Osuka, A. *J. Am. Chem. Soc.* **2001**, *123*, 76.
(9) Aratani, N.; Osuka, A.; Cho, H-S.; Kim, D. *J. Photochem. Photobiol., C* **2002**, *3*, 25.
(10) de Villiers, K. A.; Kaschula, C. H.; Egan, T. J.; Marques, H. M. *J. Biol. Inorg. Chem.* **2007**, *12*, 101.
(11) Sachs, J.; Malaney, P. *Nature (London)* **2002**, *415*, 680.
(12) Schmitt, T. H.; Frezzatti, Wilson, A., Jr; Schreier, S. *Arch. Biochem. Biophys.* **1993**, *307*, 96.
(13) Sugioka, Y.; Suzuki, M. *Biochim. Biophys. Acta* **1991**, *1074*, 19.
(14) Ridley, R. G. *Nature (London)* **2002**, *415*, 686.
(15) Egan, T. J.; Hunter, R; Kaschula, C. H; Marques, H. M; Misplon, A; Walden, J. *J. Med. Chem.* **2000**, *43*, 283.

(16) Egan, T. J.; Marques, H. M. *Coord. Chem. Rev.* **1999**, *190*−*192*, 493.
(17) Egan, T. J. *J. Inorg. Biochem.* **2006**, *100*, 916.
(18) Cohen, S. N.; Phifer, K. O; Yielding, K. L. *Nature (London)* **1964**, *202*, 805.
(19) Chou, A. C.; Chevli, R; Fitch, C. D. *Biochem.* **1980**, *19*, 1543.
(20) Frosch, T.; Kustner, B.; Schlucker, S.; Szeghalmi, A.; Schmitt, M; Kiefer, W.; Popp, J. *J. Raman Spectrosc.* **2004**, *35*, 819.
(21) Pinzaru, S. C.; Peica, N.; Kustner, B.; Schlucker, S.; Schmitt, M.; Frosch, T.; Popp, J.; Kiefer, W. *Rom. J. Biophys.* **2006**, *16*, 57.
(22) Schneider, H.; Wang, M. *J. Org. Chem.* **1994**, *59*, 7464.
(23) Ziegler, J.; Linck, R; Wright, D. W. *Curr. Med. Chem.* **2001**, *8*, 171.
(24) Sullivan, D. J. *Int. J. Parasitol.* **2002**, *32*, 1645.
(25) Egan, T. J. *Targets* **2003**, *2*, 115.
(26) Egan, T. J. *Drug Des. Rev. Online* **2004**, *1*, 93.
(27) Abe, M.; Kitagawa, T; Kyogoku, K. *J. Chem. Phys.* **1978**, *69*, 4526.
(28) Webster, G. T.; Tilley, L; Deed, S; McNaughton, D; Wood, B. R. *FEBS Lett.* **2008**, *582*, 1087.
(29) Akins, D. L.; Macklin, J. W; Zhu, H-R. *J. Phys. Chem.* **1991**, *95*, 793.
(30) Margalit, R.; Rotenberg, M. *Biochem. J.* **1984**, *219*, 445.
(31) O'Keeffe, D. H.; Barlow, C. H.; Smythe, G. A.; Fuchsman, W. H.; Moss, T. H.; Lilienthal, H. R.; Caughey, W. S. *Bioinorg. Chem.* **1975**, *5*, 125.
(32) Solomonov, I.; Osipova, M.; Feldman, Y.; Baehtz, C.; Kjaer, K.; Robinson, I. K.; Webster, G. T.; McNaughton, D.; Wood, B. R.; Weissbuch, I.; Leiserowitz, L. *J. Am. Chem. Soc.* **2007**, *129*, 2615.
(33) Egan, T. J.; Mavuso, W. W; Ross, D. C; Marques, H. M. *J. Inorg. Biochem.* **1997**, *68*, 137.

JP811028A

Monash University

Monash Research Graduate School

Declaration for Thesis Chapter 5

Declaration by candidate

In the case of Chapter 5 the nature and extent of my contribution to the work (**Paper VI**) was the following:

Nature of contribution	Extent of contribution (%)
Experimental design, Interpretation of results, drafting of manuscript	25%

The following co-authors contributed to the work. Co-authors who are students at Monash University must also indicate the extent of their contribution in percentage terms:

Name	Nature of contribution	Extent of contribution (%) for student co-authors only
Puntharod Ratchadaporn	Experimental design, interpretation of results, drafting of manuscript	60
Mehdi Asghari-Khiavi	Resonance Raman and UV-Visible band assignments, drafting of the manuscript	5
Keith Bambery	ATR measurements and proof reading	-
Feryal Safinejad	Quantum calculation of UV-visible bands	-
Kenneth Haller	Supervision, leadership and drafting manuscript	-
Bayden Wood	Supervision, leadership and drafting manuscript	-

Candidate's Signature [redacted]

Date 15/04/09

drafting

manuscript

Date

Candidate's Signature

Declaration by co-authors

The undersigned hereby certify that:

(1) the above declaration correctly reflects the nature and extent of the candidate's contribution to this work, and the nature of the contribution of each of the co-authors.

(2) they meet the criteria for authorship in that they have participated in the conception, execution, or interpretation, of at least that part of the publication in their field of expertise;

(3) they take public responsibility for their part of the publication, except for the responsible author who accepts overall responsibility for the publication;

(4) there are no other authors of the publication according to these criteria;

(5) potential conflicts of interest have been disclosed to (a) granting bodies, (b) the editor or publisher of journals or other publications, and (c) the head of the responsible academic unit; and

(6) the original data are stored at the following location(s) and will be held for at least five years from the date indicated below:

Location(s)

Department of Chemistry, Centre for Biospectroscopy, Monash University, Clayton

School of Chemistry, Institute of Science, Suranaree University of Technology, Nakhon Ratchasima

Please note that the location(s) must be institutional in nature, and should be indicated here as a department, centre or institute, with specific campus identification where relevant.]

LOCATION		Signature / Date	
SUT	Ratchadaporn Puntharod	[redacted]	7 April 2009
MONASH	Grant Webster		
MONASH	Mehdi Asghari-Khiavi	[redacted]	15/4/09
MONASH	Keith Bambery		15/4/09
MONASH	Feryal Safinejad	[redacted]	15/4/09
SUT	Kenneth J. Haller	[redacted]	7 April 2009
MONASH	Bayden Wood	[redacted]	15/4/2009

B. R. Wood signing on their behalf due to absence at this point in time.

Supramolecular Interactions Play an Integral Role in the Near-Infrared Raman "Excitonic" Enhancement Observed in Malaria Pigment and Other Related Heme Aggregates

Journal:	*Journal of the American Chemical Society*
Manuscript ID:	draft
Manuscript Type:	Article
Date Submitted by the Author:	
Complete List of Authors:	Punthrod, Ratchadaporn; Suranaree University of Technology, School of Chemistry Webster, Grant; Monash University, Centre for Biospectroscopy and School of Chemistry Asghari-Khiavi, Mehdi; Monash University Bambery, Keith; Monash University, Centre for Biospectroscopy and School of Chemistry Safinejad, Feryal; Monash University, school of chemistry Haller, Kenneth; Suranaree University of Technology, School of Chemistry Wood, Bayden; Monash University, Centre for Biospectroscopy and School of Chemistry

Supramolecular Interactions Play an Integral Role in the Near-Infrared Raman "Excitonic" Enhancement Observed in Malaria Pigment and Other Related Heme Aggregates

Ratchadaporn Puntharod[1,2], Grant T. Webster[2], Mehdi Asghari-Khiavi[2], Keith R. Bambery[2], Feryal Safinejad[2], Kenneth J. Haller[1,] and Bayden R. Wood[2,*]*

1. SCHOOL OF CHEMISTRY, INSTITUTE OF SCIENCE, SURANAREE UNIVERSITY OF TECHNOLOGY, I

30000, THAILAND

2. CENTRE FOR BIOSPECTROSCOPY AND SCHOOL OF CHEMISTRY, MONASH UNIVERSITY, VICTOR

EMAIL_BAYDEN.WOOD@SCI.MONASH.[redacted]

*CORRESPONDING AUTHORS: DR. BAYDEN R. WOOD, CENTRE FOR BIOSPECTROSCOPY AND SCH P.O. BOX 23, MONASH UNIVERSITY, VICTORIA 3800, AUSTRALIA. TEL.: +61 3 9905 5721. FAX: +61 4597. EMAIL: BAYDEN.WOOD@SCI.MONASH.EDU.AU. DR. KENNETH J. HALLER, SCHOOL OF CHEM UNIVERSITY OF TECHNOLOGY, NAKHON RATCHASIMA 30000, THAILAND. TEL.: 66+81-547-5377. I 224-185. EMAI[redacted]

Abstract: TO GAIN MORE UNDERSTANDING INTO THE MECHANISM THAT ENABLES THE DRAMA ENHANCEMENT OF TOTALLY SYMMETRIC MODES OBSERVED IN HEMOZOIN (MALARIA PIGME HEME SUPRAMOLECULAR AGGREGATES WHEN APPLYING NEAR-INFRARED EXCITATION WA PORPHYRINS FE(TPP)CL, [FE(TPP)]$_2$O, FE(OEP)CL, AND [FE(OEP)]$_2$O WERE ANALYZED IN THE SOLID STA USING RESONANCE RAMAN SPECTROSCOPY. THE CRITICAL FINDING WAS THAT FROM THE INVESTIGATED ONLY [FE(OEP)]$_2$O DID NOT SHOW THE ENHANCEMENT OF THE TOTALLY SYMMETRIC MODE ν_4 WHEN EXCITING THE MOLECULES WITH 782 AND 830 NM LASER LINES. THROUGH A DETAILED CO CRYSTALLOGRAPHIC STRUCTURES IT IS PROPOSED THAT INTERMOLECULAR NONCOVALENT I ROLE IN ENABLING EXCITONIC INTERACTIONS TO OCCUR IN THESE HEME SUPRAMOLECUL DERIVATIVES INVESTIGATED HAVE SIMILAR STEREOCHEMISTRY WITH A FIVE-COORDINATE HI CRYSTALLOGRAPHIC DATA INDICATE NO SIGNIFICANT DIFFERENCES IN PORPHYRIN GEOMETR DERIVATIVES STUDIED. HOWEVER, [FE(OEP)]$_2$O CONTAINS LESS (WEAKER) INTERMOLECULAR INTERA COMPARISON TO THE OTHER SPECIES. THE RESULTS INDICATE THAT THE STRONG INTERACTION OF ν_4 IS MEDIATED BY C H···X HYDROGEN BONDING INTERACTIONS WHERE X IS AN ELECTRON DONATING ENTITY. THIS IS TIME THAT HYDROGEN BONDS HAVE BEEN IMPLICATED IN CAUSING RR ENHANCEMENT VIA TH MECHANISM. SUCH INFORMATION MAY HAVE IMPORTANT IMPLICATIONS IN THE DESIGN A ANTIMALARIAL DRUGS THAT SPECIFICALLY INTERFERE WITH HEMOZOIN FORMATION. MOREO IMPORTANT ROLE NONCOVALENT INTERACTIONS PLAY IN ENERGY TRANSFER IN HEME SUPRA PAVE THE WAY FORWARD TO THE DEVELOPMENT OF NANO-WIRE HEME BASED ASSEMBLIES A PHOTON TRANSFER DEVICES.

KEYWORDS: IRON(III) PORPHYRIN, RESONANCE RAMAN SPECTROSCOPY, HEMOZOIN, MALARIA EXCITONIC ENHANCEMENT, , SUPRAMOLECULAR INTERACTION

Introduction*

HEMOZOIN (MALARIA PIGMENT) IS A VIRTUALLY INSOLUBLE BYPRODUCT PRODUCED FRO HEMOGLOBIN BY THE MALARIA PARASITE *Plasmodium falciparum* AND OTHER SPECIES.[1,2] THE COMPOUND IS SPECTROSCOPICALLY IDENTICAL TO SYNTHETIC β-HEMATIN, WHICH WAS FOUND TO BE A HEME DIMER LINKED VIA CARBOXYLATE GROUPS WITH THE DIMERS IN TURN LINKED TOGETHER INTO A SUPRAMOLE ARRAY.[4] THE INTEREST IN HEMOZOIN STEMS FROM THE FACT THAT QUINOLINE BASED ANTIMAL BIND TO HEMOZOIN, THEREFORE PREVENTING ITS FORMATION OR CAPPING CRYSTAL GROWT BUILD UP OF TOXIC FREE HEME, WHICH CAN KILL THE PARASITE.[5-8] CONSEQUENTLY, KNOWLEDGE ON THE ELECT VIBRONIC, AND MOLECULAR STRUCTURE OF HEMOZOIN COULD LEAD TO THE DEVELOPMENT O TARGET AND BLOCK HEMOZOIN FORMATION. IN PURSUIT OF NEW APPROACHES TO EXAM INTERACTIONS AND GAIN MORE INSIGHT INTO THE STRUCTURE OF THIS IMPORTANT COMPOUN NEAR-INFRARED (IR) RESONANCE RAMAN (RR) SPECTROSCOPY.[5,9-11]

RR SPECTROSCOPY HAS LONG BEEN USED TO PROVIDE STRUCTURAL INFORMATION ON INCLUDING METALLOPORPHYRINS AND IN PARTICULAR IRON PORPHYRINS THAT SERVE AS PR PROTEINS.[12] ISOTOPIC SUBSTITUTION STUDIES AND THEORETICAL CALCULATIONS HAVE LED TO T BANDS IN THE RR SPECTRA OF METALLOPORPHYRINS AND IN PARTICULAR HEMES.[13,14] EARLY RR STUDIES REPORTED THA SPECIFIC VIBRATIONAL MODES ARE SENSITIVE TO BOTH THE OXIDATION STATE AND COORI CENTRAL METAL ION.[15,16] ONE BAND DESIGNATED AS ν_4, ASSIGNED TO THE TOTALLY SYMMETRIC PYRROLE BREATHING MODE,[13] APPEARED PARTICULARLY SENSITIVE TO OXIDATION STATE, SHIFTING FROM ~1375 CM^{-1} IN FERRIC HEMES TO ~1355 CM^{-1} IN FERROUS HEMES AS A RESULT OF INCREASED BACK-DONATION OF E FROM FE (D_{xz}, D_{yz}) TO PORPHYRIN π^* MOLECULAR ORBITALS.[15,16] THIS BAND WAS FOUND GENERALLY ENHANC RR SPECTRA OF HEMOGLOBIN SOLUTIONS WHEN USING EXCITATION WAVELENGTHS IN RESO BAND AT ~400 NM AND DIMINISHED WHEN EXCITING IN THE VICINITY OF THE Q (0,0) AND Q (0,1)

* IUPAC NAMES: TPP = 5,10,15,20-TETRAPHENYLPORPHYRIN; OEP = 2,3,7,8,12,13,17,1 OCTAETHYLPORPHYRIN; PPIX = 3,8,13,17-TETRAMETHYL-7,12-DIVINYLPORPHYRIN-2,18 DIPROPION

AND 575 NM, RESPECTIVELY.[17,18] THE ENHANCEMENT CAN BE EXPLAINED THROUGH THE TYPICAL A-TERM AND B-TERM CLASSICAL SCATTERING MECHANISMS BASED ON THE SUM-OVER-STATES APPROACH TO LIGHT DISPERSION AND HEISENBERG AND DIRAC[19,20] FROM SECOND-ORDER TIME DEPENDENT PERTURBATION THEORY.

IN TYPE A SCATTERING OR FRANCK-CONDON SCATTERING ONLY TOTALLY SYMMETRIC MODES ARE ENHANCED. THESE ARE INEFFECTIVE IN MIXING THE ELECTRONIC STATES. THE INTENSITY OF A PARTICULAR MODE IS DEPENDENT ON THE SQUARE OF THE TRANSITION DIPOLE MOMENT AND MORE IMPORTANTLY ON THE WAVEFUNCTION INTEGRALS BETWEEN THE INITIAL, INTERMEDIATE, AND FINAL VIBRATIONAL STATES (EQUATION 1). THE ENHANCEMENT OF TOTALLY SYMMETRIC MODES IS COMMONLY SEEN WHEN EXCITING IN TO THE SORET BAND REGION WHERE THERE IS LITTLE ELECTRONIC CONFIGURATION INTERACTION OCCURRING.[21] B SCATTERING TYPE INVOLVES A VIBRONIC COUPLING MECHANISM DUE TO STRONG ELECTRONIC CONFIGURATION INTERACTION BETWEEN NEIGHBORING ELECTRONIC STATES. NON-SYMMETRIC MODES CAN BECOME ENHANCED. THE INTENSITY OF A BAND IS DEPENDENT ON THE SQUARE OF THE NORMAL COORDINATE WITH RESPECT TO THE TRANSITION DIPOLE BUT MORE IMPORTANTLY ON HOW THE NORMAL COORDINATE, USUALLY A LOW FREQUENCY NON-TOTALLY SYMMETRIC MODE, CAN COUPLE THE STATES TO GIVE RISE TO THE GREATEST WAVEFUNCTION OVERLAP BETWEEN THE INITIAL, INTERMEDIATE, AND FINAL SUMMED OVER ALL THE VIBRATIONAL STATES (EQUATION 2).[22] THIS EXPLAINS THE ENHANCEMENT OF THE TOTALLY SYMMETRIC MODES OBSERVED WHEN EXCITING HEMES WITH EXCITATION WAVELENGTHS AT 600 NM.

$$A = (\mu_e)^2 \frac{1}{\hbar} \sum_{v} \frac{\langle j|v\rangle\langle v|i\rangle}{\Delta\nu_v + i\Gamma_v}, \qquad (1)$$

$$B = \mu_e \left(\frac{\partial \mu_e}{\partial Q}\right) \frac{1}{\hbar} \sum_{v} \frac{\langle j|Q|v\rangle\langle v|i\rangle + \langle j|v\rangle\langle v|Q|i\rangle}{\Delta\nu_v + i\Gamma_v} \qquad (2)$$

WHERE $|i\rangle$ AND $|j\rangle$ ARE THE INITIAL AND FINAL VIBRATIONAL WAVE FUNCTIONS OF THE GROUND

REPRESENTS THE NORMAL COORDINATE OPERATOR, $|v\rangle$ REPRESENTS THE INTERMEDIATE VIBRATIONAL WAVE F

THE RESONANT EXCITED STATE, Δ_v IS THE DIFFERENCE BETWEEN THE FREQUENCY OF LASER EXCITATI

AND THE FREQUENCY OF THE VIBRATION IN THE EXCITED STATE, Γ_v IS THE HALF-WIDTH OF THE VIBRATIONAL

FUNCTION FOR THE EXCITED STATE AND REPRESENTS THE LIFETIME OF THE EXCITED STATE, $\hbar$ IS PLANK

CONSTANT).[12]

RECENT RR STUDIES OF HEMOZOIN DEMONSTRATED THAT THE COMPOUND PRODUCED DRAM

THE TOTALLY SYMMETRIC MODE (ν_4) WHEN IRRADIATED WITH NEAR-IR EXCITATION WAVELENGTHS (782

WELL AWAY FORM THE SORET AND Q BANDS.[10,11] IT WAS POSTULATED THAT THE ENHANCEMENT WAS ATT

EXCITONIC INTERACTIONS OCCURRING THROUGHOUT THE SUPRAMOLECULAR HEMOZOIN.[10] TO FURTHER

THIS EXCITONIC ENHANCEMENT WE INVESTIGATED A NUMBER OF STRUCTURALLY RELATED H

RR SPECTROSCOPY AND CORRELATED THESE RESULTS WITH X-RAY CRYSTALLOGRAPHIC STRUC

RR SPECTRA OF MODEL HEME COMPLEXES INCLUDING IRON TETRAPHENYLPORPHYRIN

OCTAETHYLPORPHYRIN FE(OEP) DERIVATIVES IN BOTH MONOMERIC AND DIMERIC FORMS HA

STUDIED.[21] FURTHERMORE, THE CRYSTAL STRUCTURES OF FE(TPP)CL,[22,23] [FE(TPP)]$_2$O,[24,25] FE(OEP)CL,[26] AND

[FE(OEP)]$_2$O[27] HAVE BEEN ANALYZED FOR SUPRAMOLECULAR INTERACTIONS. THE STEREOCHEM

[FE(TPP)]$_2$O, [FE(OEP)]$_2$O, AND [FE(PPIX)]$_2$(β-HEMATIN) ARE SIMILAR, EACH CONSISTING OF A HI

FIVE-COORDINATE FE(III) DISPLACED ABOVE THE MEAN PLANE OF THE PORPHYRIN TOWARDS T

O ATOM. CONSEQUENTLY, THESE STRUCTURES SERVE AS EXCELLENT MODEL COMPLEXES TO S

OF HEMOZOIN AND PROVIDE EXCELLENT MODELS TO INVESTIGATE THE RAMAN "EXCIT

MECHANISM PREVIOUSLY REPORTED FOR MALARIA PIGMENT AND β-HEMATIN.[10,11] SYNTHETIC ANALOGU

EXCITATION WAVELENGTHS.

IN THIS STUDY WE COMPARE EXCITATION PROFILES FOR RAMAN BANDS OF CRYSTALLINE M

AND FE(OEP)CL AND OF THE CORRESPONDING DIMERIC [FE(TPP)]$_2$O AND [FE(OEP)]$_2$O. ONLY ONE OF THE FOUR

COMPOUNDS INVESTIGATED NAMELY [FE(OEP)]$_2$O DOES NOT SHOW THE ENHANCEMENT OF THE TOTALLY S

MODES AT NEAR-IR EXCITATION. BASED ON X-RAY CRYSTALLOGRAPHIC RESULTS IT IS H
ENHANCEMENT COULD BE IN PART ATTRIBUTED TO NONCOVALENT SUPRAMOLECULAR INTE
LIGANDS AND THE PERIPHERAL SUBSTITUTION GROUPS ARE DIFFERENT FOR MONOMERS AND
FE(OEP), THEIR INTERMOLECULAR INTERACTIONS ARE ALSO DIFFERENT WHICH IN TURN
INTERACTIONS THROUGHOUT THE AGGREGATES. TO DATE, THERE HAS BEEN NO REPORT ON TH
BANDS OF THESE COMPOUNDS AT NEAR-IR EXCITATION.

THIS STUDY PROVIDES NEW INSIGHT INTO THE MECHANISM OF RAMAN EXCITONIC ENHANC
NEAR-IR EXCITATION WAVELENGTHS IN HEME COMPOUNDS THUS PROVIDING ADDITIONA
SUPRAMOLECULAR STRUCTURE OF MALARIA PIGMENT. THE COMBINATION OF RR SPECT
CRYSTALLOGRAPHY INDICATES A CORRELATION BETWEEN THE PRESENCE OF INTER-HEME
C–H···X HYDROGEN BONDING (WHERE X (E.G. X = CL OR O) IS AN ELECTRON DONATING ENTITY) AND THE ENH
ν_4 IN HEME COMPLEXES AT NEAR-IR EXCITATION. CONSEQUENTLY, THE ENHANCEMENT OF ν_4 AT NEAR-IR EXCITATION
CAN BE USED AS AN INDICATOR OF INTERMOLECULAR INTERACTIONS IN HEME COMPLEXES E
SUCH INFORMATION COULD BE USED TO MONITOR THE EFFECTS OF ANTI-MALARIAL DRUG
HEMOZOIN FORMATION IN *Plasmodium falciparum* INFECTED ERYTHROCYTES. MOREOVER, THE RESULTS UN
THE IMPORTANCE OF NONCOVALENT INTERACTIONS IN EXCITONIC ENERGY TRANSFER PROCE
WHICH COULD HAVE ENORMOUS IMPLICATIONS IN THE DEVELOPMENT OF HEME BASED NEA
DEVICES.

Experimental

Compounds. FE(TPP)CL AND FE(OEP)CL WERE PURCHASED FROM SIGMA ALDRICH AND [FE(TPP)]$_2$O AND [FE(OEP)]$_2$O WERE PREPARED BASED ON THE METHOD OF CHENG *et al*[27]

Electronic Absorbance Spectra. ELECTRONIC ABSORPTION SPECTRA OF SAMPLES IN THE SOLID
RECORDED USING A J&M MSP400 VISIBLE SPECTROMETER EQUIPPED WITH A LEICA DM4000M MICR

AND AN ×40 QUARTZ VISIBLE OBJECTIVE WITH A 27 μM APERTURE SIZE IN THE SPECTRAL RANGE 940–1 AS 20 ACCUMULATIONS USING A 1.2 SEC INTEGRATION TIME PER ACCUMULATION.

FTIR Spectroscopy. FTIR SPECTRA OF SAMPLES WERE RECORDED WITH A VARIAN 600-UM MICROSCOPE EQUIPPED WITH AN HGCDTE DETECTOR AND COUPLED TO A VARIAN 7000 FTI SPECTRA WERE RECORDED IN REFLECTION MODE OVER KEVLEY REFLECTIVE SLIDE SUBSTRATES (6 RESOLUTION, 128 CO-ADDED SCANS, APODIZED USING A BLACKMAN HARRIS 4 TERM FUNCTION FACTOR OF 2).

Resonance Raman Spectroscopy. RR SPECTRA OF PRODUCTS WERE RECORDED ON A RENISHA 2000 SPECTROMETER USING A 413 NM (OR 514 NM) EXCITATION LINE (SPECTRA-PHYSICS KR SYSTEM), A 633 NM EXCITATION LINE GENERATED BY COHERENT 31-MW HELIUM-NEON LASER, OR A 782 NM (OR 830 NM) EXCITATION LINE GENERATED BY DIODE LASERS (RENISHAW RM2000) IN A BACK SCATTE LASER POWER ON THE SAMPLE WAS APPROXIMATELY 39, 130, 160, 300, AND 600 μW FOR THE EXCITATION WAVELENGTHS 413, 514, 633, 782, AND 830 NM, RESPECTIVELY. THE SYSTEM WAS EQUIPPED WITH OPTICAL MICROSCOPE AND A ZEISS ×60 WATER IMMERSION OBJECTIVE TO ENABLE SPECTRAL A PREVENT THE THERMAL DEGRADATION OF THE SOLID SAMPLES. ALL SPECTRA PRESENTED H NORMALIZED AFTER INTERACTIVE BASELINE-CORRECTION USING THE CONCAVE RUBBER BAN SOFTWARE.

Crystallographic Calculations. SUPRAMOLECULAR INTERACTION CONTACT DISTANCES AND CALCULATED WITH *ORTEP-III*[28] AND ARE REPORTED WITH THE CONVENTIONAL D···A NOTATION OR WITH D–H···(A–A') NOTATION WHERE THE ACCEPTOR POSITION IS THE MIDPOINT OF THE RELEVANT AROMATIC SYSTEM. COORDINATES FOR [FE(TPP)CL][23], [FE(TPP)CL]$_2$[25], FE(OEP)CL[26], TRICLINIC [FE(OEP)CL]$_2$[27] AND MONOCLINIC [FE(OEP)CL]$_2$[27] WERE OBTAINED FROM THE CAMBRIDGE STRUCTURAL DATABASE[29] REFCODES: KANYUT, PPORFE01, TOYRUU, YIKJOR, AND YIKJOR01, RESPECTIVELY.

Results

FTIR Spectroscopy. OXO-BRIDGED DIMERS OF TRANSITION METALS INCLUDING FE(III) PORPHYR CHARACTERIZED BY ATR/FTIR SPECTROSCOPY OF MICROCRYSTALLINE SAMPLES. THE IR ABSO REGION 800-900 CM^{-1} HAS BEEN USED AS EVIDENCE OF THE μ-OXO-BRIDGED DIMER FOR SEVERAL TRANSITIO COMPLEXES.[30] THE FTIR SPECTRA OF DIMERS PRESENTED IN FIGURES 1 AND 2 EXHIBIT THE ASYMME VIBRATION OF THE Fe-O-Fe AT 877 AND 876 CM^{-1} FOR $[FE(TPP)]_2O$[31] AND $[FE(OEP)]_2O$[21(F)], RESPECTIVELY WHICH CONFIRM THE FORMATION OF THE μ-OXO-DIMER COMPLEXES.

Solid State Resonance Raman Spectroscopy. FIGURES 3 AND 4 COMPARE THE SOLID STATE RR SPEC MONOMERS AND DIMERS OF FE(TPP) AND FE(OEP) AT DIFFERENT EXCITATION WAVELENGTHS V S2 (SUPPORTING INFORMATION) GIVE A COMPLETE LISTING OF THE OBSERVED BANDS AI ENHANCEMENT AT EACH EXCITATION WAVELENGTH. IT SHOULD BE NOTED THAT ALL SPECT NORMALIZED TO FACILITATE THE COMPARISON. THE VIBRATIONAL MODE NOTATION IS BASED *et al.*[13] FOR NI(OEP) WITH SOME AMENDMENTS TO THE ASSIGNMENTS MADE BY HESS *et al.*[32] IN THEIR STUDIES ON NI(TPP). ALTHOUGH THE AXIAL LIGANDS LOWER THE ACTUAL SYMMETRY, THE SELECTION RULES ARE FOLLOWED CLOSELY ENOUGH TO MAINTAIN THE ASSIGNMENT SCHEME AND ARE AD

WHEN EXCITING INTO THE SORET BAND USING A 413 NM LASER, ALL HEME DERIVATIVES I DRAMATIC ENHANCEMENT OF THE TOTALLY SYMMETRIC MODES AS EXPECTED WHEN THE TERM RR SCATTERING MECHANISM IS THE DOMINANT TERM. RELATIVE ENHANCEMENT OF INCLUDING ν_4 AND ν_8 (IN TPPS), AND ν_6 (IN $[FE(OEP)]_2O$) ARE ALSO OBSERVED.

WHEN EXCITING AT 514 NM, IN TPPS, TOTALLY SYMMETRIC MODES MONOMER), AND (IN MONOMER) AGAIN DOMINATE THE SPECTRA ALTHOUGH IS ALSO ENHANCED. HOWEVER, IN OEPS NON-TOTALLY SYMMETRIC MODES ν_{10}, ν_{11}, ν_{19}, ν_{21}, AND ν_{29} DOMINATE THE SPECTRA AND THE IS ALSO ENHANCED.

WHEN EXCITING WITH A 633 NM LASER LINE ALL TYPES OF MODES ARE OBSERVED IN TPPS IN (ν_2, ν_4, ν_1, ν_8), DEPOLARIZED (ν_{11}, ν_{30}), AND INVERSE POLARIZED MODES (ν_{19}, ν_{20}). HOWEVER, IN OEPS, THE SPECTRA ARE DOMINATED BY B_{1G} (ν_{10}, ν_{11}, ν_{13}, ν_{15}) AND A_{2g} (ν_{19}, ν_{21}) MODES.

FINALLY, WHEN USING NEAR-IR EXCITATION WAVELENGTHS (782 AND 830 NM), THE SPECTRA DOMINATED BY TOTALLY SYMMETRIC MODES (ν_2, ν_4, ν_1, ν_8), AS HOWEVER, IN THE SPECTRA OF FE(OEP)CL BOTH B_{1G} (ν_{11}, ν_{13}) AND A_{2g} (ν_2, ν_4) MODES ARE DRAMATICALLY ENHANCED WHILE THE SPECTRA OF [FE(OEP)]$_2$ ARE DOMINATED BY B_{1G} MODES (ν_{10}, ν_{11}, AND ν_{13} AND THE A_{1G} MODE ν_4 HAS VIRTUALLY DISAPPEARED. NOTABLY, THE PATTERN OF THE BANDS IN THE SPECTRUM OF [FE(OEP)]$_2$ RESEMBLES THE FT-RAMAN SPECTRA (AT 1064 NM EXCITATION) OF HEME DERIVATIVES INDICATING A LACK OF ANY TYPE OF RR ENHANCEMENT.[23,24]

THE BAND AT ~366 CM^{-1} OBSERVED IN THE SPECTRA OF [FE(OEP)]$_2$ IS ASSIGNED TO THE FE−O−FE SYMMETRIC STRETCH, WHILST THE BAND AT ~390 CM^{-1} IS ASSIGNED TO AN IN-PLANE DEFORMATION MODE THAT INCLUDES CONTRIBUTIONS FROM THE FE−N STRETCHING VIBRATION.[21(D)] THE RELATIVE INTENSITY OF THESE BANDS RADICALLY CHANGES DEPENDING ON THE EXCITATION WAVELENGTH APPLIED. AT 413, 782, AND 830 NM THE BAND AT ~390 CM^{-1} IS MUCH GREATER THAN THE BAND AT 366 CM^{-1} AND THE OPPOSITE IS OBSERVED WHEN EXCITING AT 514 AND 633 NM WHERE THE 366 CM^{-1} BAND IS MUCH MORE INTENSE THAN THE 390 CM^{-1} BAND. MOREOVER, THE AXIAL LIGAND VIBRATIONS (ν_{FE-CO}) AND ν_{SYM} (FE–O–FE) ARE ENHANCED AT 633 NM AND NEAR-IR EXCITATION EXCEPT FOR [FE(OEP)]$_2$ IN WHICH THE ν_{SYM} (FE–O–FE) BAND IS VIRTUALLY ABSENT AT ALL EXCITATION WAVELENGTHS STUDIED.

PHENYL INTERNAL MODES OF THE TPP DERIVATIVES ARE OBSERVED ENHANCED FOR ALL WAVELENGTHS. THE ENHANCEMENT OF THESE MODES IS EXPLAINED THROUGH KINEMATIC MIXING OF THE PHENYL MODES WITH PORPHYRIN SKELETAL MODES.[35] BASED ON ISOTOPIC SUBSTITUTION AND POLARIZATION STUDIES BY WORKERS[21(D)] ASSIGNED BANDS APPEARING AT 1599, 1030, AND 886 CM^{-1} IN [FE(TPP)]$_2$ TO SOLUTIONS TO THE PHENYL MODES. THESE BANDS ARE ALSO OBSERVED IN THE SOLID PHASE SPECTRA, ALBEIT SMALL WHEN USING VISIBLE EXCITATION WAVELENGTHS. INTERESTINGLY, THESE BANDS BECOME MUCH SOLID PHASE WHEN USING NEAR-IR EXCITATION WAVELENGTHS. THE FACT THAT THESE MODES

TOTALLY SYMMETRIC A_{1g} PORPHYRIN MODES, WHICH ARE ALSO ENHANCED WHEN USING NEAR-I
WAVELENGTHS, INDICATES THERE IS ANOTHER MECHANISM AT WORK CONTRIBUTING TO THEIR

Solid State UV-visible Spectroscopy. THE UV–VISIBLE ABSORPTION SPECTRA OF TPP AND C
DERIVATIVES ARE DEPICTED IN FIGURE 5. THE "NORMAL" ABSORPTION SPECTRUM OF METALL
SHARP INTENSE SORET BAND AT APPROXIMATELY 400 NM ALONG WITH TWO SMALLER BANDS
(500–600 NM). HOWEVER, DIFFERENT TYPES OF ABSORPTION SPECTRA ARE USUALLY OBSERVE
CHARACTERISTICS OF THE CENTRAL METAL ION AND THE SUBSTITUENT GROUPS. THE PERTU
SPECTRUM IS PARTLY CAUSED BY INTRAMOLECULAR CHARGE TRANSFER FROM THE π PORPHYR
ORBITALS,[36] WHICH IS USUALLY CONNECTED WITH AN UNSYMMETRICAL AXIAL COORDINATION OF
NONPLANAR COORDINATION OF THE METAL ION TO THE PORPHYRIN. THE HIGH-SPIN FIVE COOR
GENERALLY DISPLAY SEVERAL OVERLAPPING BANDS IN THE VISIBLE REGION. ASSIGNMENT OF
HAS BEEN CONTROVERSIAL.[17,21(D),37] HOWEVER, THE MAJOR ELECTRONIC BANDS OBSERVED IN THESE CO
STILL FROM $\pi \rightarrow \pi^*$ TRANSITIONS OCCURRING AT APPROXIMATELY 400 NM (SORET) AND BETWEEN
(*Q* BANDS). OTHER TRANSITIONS INCLUDE VARIOUS CHARGE-TRANSFER TRANSITIONS FROM
BETWEEN IRON AND AXIAL LIGAND.

AS SHOWN IN FIGURE 5, THE SPECTRAL PROFILES HAVE REMARKABLE DIFFERENCES BETW
DIMERS ALTHOUGH RR ENHANCEMENT PATTERNS ARE VERY SIMILAR (EXCEPT AT NEAR-IR
ANOTHER FACTOR THAT INFLUENCES THE ABSORPTION SPECTRUM OF METALLOPORPHYRIN
INTERACTIONS AND EXCITONIC EFFECTS IN AGGREGATES. MOST OF THE PREVIOUS STUDIES F
AGGREGATION ON ABSORPTION SPECTRA OF PORPHYRINS ARE FOCUSED ON SORET AND Q BA
EXCITON INTERACTION DEPENDS ON THE SQUARE OF THE TRANSITION MOMENT, GENERALI
(INCLUDING SPLITTING OF BANDS) IN THE VISIBLE REGION ARE SUBSTANTIALLY LESS THAN
HOWEVER, THE DISCOVERY OF "EXCITONIC" ENHANCEMENT OF A_{1g} MODES AT NEAR-IR EXCITATION[28] IN OUR LA
INDICATES THAT EXCITONIC TRANSITION BANDS (ALBEIT WEAK) IN NEAR-IR REGION CAN HAV
THE PATTERN OF RR SPECTRA. SINCE THERE IS NO VIBRONIC COUPLING IN THIS REGION, THE RE

A_{1G} MODES VIA RESONANCE WITH A SMALL EXCITONIC TRANSITION CAN MAKE TOTALLY SYMM
THE SPECTRUM. AN INSPECTION OF THE NEAR-IR REGION OF THE UV–VISIBLE SPECTRA PRESENTED IN FIGURE 5 SH
THERE IS POSSIBLY A VERY BROAD WEAK ABSORPTION BAND BETWEEN 700–900 NM AND ANOTHER BETWEEN 700–
NM.

Figure 5. UV-VISIBLE ABSORBANCE SPECTRA OF CRYSTALLINE HEME DERIVATIVES.

RECENTLY PAULAT AND LANGHOFF[37] HAVE ASSIGNED IN DETAIL THE MAGNETIC CIRCULAR DICHROISM (
UV–VISIBLE BANDS OF FE(TPP)CL USING TD-DFT. HOWEVER, THE NATURE OF TWO WEAK BA
(MCD, BROAD) AND 738 NM (UV–VISIBLE) REMAINED UNCLEAR. USING A HIGHER BASIS SET (TZVP) WE
THE CALCULATIONS AND COULD ASSIGN THE BROAD BAND AT 875 NM (IN OUR SPECTRUM OF F
D_π TRANSITION (TABLE S3, SUPPORTING INFORMATION). SIMILAR CALCULATIONS ON FE(OEP)CL ARE
UNDER WAY. WE BELIEVE THERE SHOULD BE SIMILAR ELECTRONIC TRANSITIONS IN THE NEA
SPECTRA OF [FE(TPP)]$_2$O AND FE(OEP)CL, WHICH SHOW THE RR ENHANCEMENT OF THE A_{1G} MODES AT NEAR-IR
EXCITATION. THERE IS A SIMILAR BROAD BAND (AT 867 NM) IN THE ABSORPTION SPECTRUM
PRONOUNCED β-HEMATIN AND HAS ALREADY BEEN EVOKED TO EXPLAIN RR ENHANCEMENT OF THE A_{1G} MODES IN
NEAR-IR EXCITED SPECTRA OF THESE COMPOUNDS.[10]

Solution Resonance Raman Spectroscopy. IT IS IMPORTANT TO NOTE THAT WE WERE UNABLE T
SOLUTION PHASE RR SPECTRA OF FE(OEP)CL AND FE(TPP)CL ALONG WITH THE μ-OXO DIMERS EVEN
USING NEAR-IR EXCITATION WAVELENGTHS EVEN AT HIGH CONCENTRATIONS (>10 MM) AND
POWER (20 MW). THE SOLUTION PHASE SPECTRA AT THESE EXCITATION WAVELENGTHS SHOW
BASELINE WITH NO EVIDENCE OF ANY BANDS. HOWEVER, A NUMBER OF STUDIES HAVE REPORT
SPECTRA OF FE(TPP) AND FE(OEP) MONOMERS AND μ-OXO DIMERS USING VISIBLE EXCITATION WAVELENG[21]
A VERY RECENT STUDY WE INVESTIGATED THE RR SPECTRA OF HEMATIN AND HEMIN AT DIF
USING 413 AND 514 NM EXCITATION. AS THE CONCENTRATION OF HEMATIN/HEMIN INCREASES T
PROBABILITY OF SUPRAMOLECULAR INTERACTIONS BETWEEN IRON(III) FE(PPIX) UNITS OCCU

FE(PPIX) CONCENTRATION REACHES A SATURATION POINT IN SOLUTION AND EXCITONIC
MAXIMUM CAUSING THE ENHANCEMENT PROFILE TO PLATEAU WHEN APPLYING 514 NM EXC
WHEN USING 413 NM EXCITATION THERE WERE NO CHANGES IN BAND INTENSITY WITH INCR
SHOWING THAT EXCITONIC COUPLING THROUGH SUPRAMOLECULAR INTERACTIONS FOR
WAVELENGTH DEPENDENT.[29]

X-ray Crystallography. (a) General Comments. *ORTEP-III*[28] ILLUSTRATIONS OF MONOMERIC A
DIMERIC [FE(TPP)] AND [FE(OEP)] MOLECULES, AS THEY EXIST IN CRYSTAL STRUCTURES, ARE
S1–S5 (SUPPORTING INFORMATION). IN THE PREVIOUS STUDIES, THE STRUCTURAL PARAMET
PRIMARILY THE CONFORMATIONAL CHARACTERISTICS OF THE IRON ATOM AND PORPHYRIN
LENGTHS OF THE FE–N AND FE–X AXIAL LIGAND AS WELL AS THE DISPLACEMENT OF IRON ATOM OUT OF THE
FROM THE X-RAY CRYSTALLOGRAPHIC RESULTS, THESE FEATURES ARE SIMILAR, ALL SHOWIN
PYRAMIDAL GEOMETRY IN THE HIGH-SPIN FERRIC STATE. TABLE 1 SUMMARIZES THE AVERAGE, MAXIMUM, MINIMUM, AND
FE(III) DISPLACEMENTS FROM THE PORPHYRIN PLANE, AND SHORTEST PORPHYRIN-PORPHYRIN C

HOWEVER, THE FACT THAT [FE(OEP)] DOES NOT EXHIBIT THE ENHANCEMENT OF ELECTRON DENS
BAND ν_4 AT NEAR-IR EXCITATION WAVELENGTHS REVEALS THAT THERE SHOULD BE ADDITION
INFLUENCE THE RR ENHANCEMENT MECHANISMS. TO FURTHER INVESTIGATE THE MECHANISM
TOTALLY SYMMETRIC MODES A DETAILED ANALYSIS OF THE CRYSTAL STRUCTURES IS REQUIR
SUPRAMOLECULAR CHEMISTRY OF TPP AND OEP DERIVATIVES AS A POSSIBLE FACTOR TO EXP
OF TOTALLY SYMMETRIC MODES (PARTICULARLY AT NEAR-IR EXCITATION WAVELENGTHS). SI
THE PERIPHERAL SUBSTITUENT GROUPS ARE DIFFERENT IN MONOMERS AND DIMERS OF FE(TP
INTERMOLECULAR INTERACTIONS MAY ALSO BE DIFFERENT WHICH IN TURN COULD AFFECT
THROUGHOUT THE AGGREGATES. IN THE FOLLOWING, THE VARIOUS INTRA- AND INTER-MO
CONSIDERED AND SUPPORT THE HYPOTHESIS THAT SUPRAMOLECULAR INTERACTIONS ARE ON
ENHANCEMENT OF ν_{10} MODES IN TPPS AND OEP MONOMER AND THE DRAMATIC REDUCTION OF THE S
THE OEP DIMER. THE NUMBER OF NONCOVALENT INTERMOLECULAR INTERACTIONS FOR THE H
STUDY ARE ALSO INCLUDED IN TABLE 1.

(b) Distance between Porphyrin Planes. IN THE CASE OF DIMERIC *β*-HEMATIN, THE CLOSEST INTERMOLECULAR DISTANCE BETWEEN PORPHYRIN PLANES IS 3.4 Å (*Diamond*[40] CALCULATION; FIGURE S6). THE AVERAGE MEAN PLANE SEPARATIONS BETWEEN TWO PORPHYRIN RINGS FOR THE FE(TPP) AND AND DIMERS ARE ALL GREATER THAN 4 Å (TABLE 1), INDICATING MINIMAL *π*–*π* INTERACTIONS BETWEEN THE TW CHROMOPHORES IN THESE SPECIES. HOWEVER, IN THE CASE OF THE TRICLINIC FE(OEP) DIM CONSTRAINTS OF THE NEARLY ECLIPSED PORPHYRIN CORES WITH A Fe–O–Fe ANGLE OF 172° LEADS TO PORPHYRIN-PORPHYRIN CONTACT DISTANCES BETWEEN THE NONPARALLEL CORES AS SHORT A

(c) Delocalized π System and Steric Interaction. THE APPEARANCE OF ENHANCEMENT OF RAMAN B ASSIGNABLE TO INTERNAL MODES OF THE PHENYL RINGS, IN RESONANCE WITH THE *π*–*π** TRANSITION, PORPH DEMONSTRATES AN INTERACTION BETWEEN THE PHENYL AND PORPHYRIN *π* SYSTEMS PREVIOUSLY ATTRIBUTED INTRAMOLECULAR DELOCALIZATION BETWEEN THE PORPHYRIN AND PHENYL *π* SYSTEMS.[41] HOWEVER, SINCE THE PHENYL RINGS ARE TILTED WITH RESPECT TO THE PORPHYRIN RING (BY ANGLES FROM 53 TO 83°), AND BARRIER TO ROTATION, REFLECTING THE STERIC HINDRANCE BETWEEN THE *ortho* HYDROGEN ATOMS OF THE PHENY GROUPS AND THE ADJACENT PYRROLE RINGS,[24,42] OVERLAP BETWEEN THE PHENYL AND PORPHYRIN *π* SYSTEMS IN THE GROUND STATE HAS BEEN QUESTIONED.[41,43] IT IS ALSO SIGNIFICANT THAT THE ENHANCEMENT OBSERVED H *solid state* EFFECT. NMR EVIDENCE FOR PHENYL RING ROTATION IN SOLUTION FROM FIVE-COORDIN *para*-SUBSTITUTED PHENYL ANALOGUES FINDS AN ACTIVATION BARRIER OF ROUGHLY 16 KCAL MOL^{-1} FOR CHLORO IRON(III) ANALOGUES, A ALSO FACILITATION OF THE AVERAGING OF NONEQUIVALENT *ortho*-PHENYL PROTONS BY ADDITION OF CHLORI ION,[42] SUGGESTING A DISSOCIATION MECHANISM IS ALSO OPERATING TO AVERAGE THE NO *ortho* HYDROGEN ATOMS. FURTHERMORE, ROTATION OF THE PHENYL RINGS IN THE SOLID STATE DESTROY THE CRYSTAL LATTICE, AS OCCURS WITH AS LITTLE AS 35° ROTATION OF AXIAL PYRI OF [FE(OEP)(3-CLPY)$_2$]$^+$ TO ACHIEVE AN $S = {}^3/_2$ (QUANTUM-ADMIXED INTERMEDIATE-SPIN STATE)[44]-TO-$S = {}^1/_2$ (LOW SPIN STATE)[45] TRANSITION, WHERE THE TRANSITION IS ACCOMPANIED BY FRAGMENTATION OF THE

IN ANY CASE, THE FACT THAT THE ALIPHATIC SUBSTITUENTS ON FE(OEP)CL DO NOT ALLO EXTENDED DELOCALIZATION AND YET FE(OEP)CL EXHIBITS ENHANCEMENT OF ν_{1G} MODES AT NEAR-IR EXCITATION

INDICATES THERE SHOULD BE OTHER FACTORS THAT ACCOUNT FOR THE ENHANCEMENT OF THE A_{1g} MODES, THE LACK OF ENHANCEMENT IN THE SOLUTION PHASE RR SPECTRA EVEN AT HIGH CONCENTR DERIVATIVES INVESTIGATED HERE WHEN USING NEAR-IR EXCITATION WAVELENGTHS SUGGES IS NOT DUE TO AN INTRAMOLECULAR MECHANISM. THIS PROVIDES SUPPORTING EVIDEN ENHANCEMENT OBSERVED WHEN APPLYING NEAR-IR EXCITATION IS A SOLID STATE PHE INTERMOLECULAR INTERACTIONS.

(d) Hydrogen Bonding. β-HEMATIN SHOWS THE ENHANCEMENT OF A_{1g} MODES AT NEAR-IR EXCITATION WAVELENGTHS.[19] THE INTERPRETATION OF THE HIGH-RESOLUTION POWDER DIFFRACTION DATA OF β-HEMATIN IND CONTAINS CENTROSYMMETRIC DIMERS WITH RECIPROCAL PROPIONATE LINKAGES, AND THA TOGETHER BY STRONG HYDROGEN BONDS.[4] THESE EXHIBIT HYDROGEN BOND INTERACTIONS INCLUDING C SYSTEM OF PHENYL AND/OR PORPHYRIN RINGS (DIMER OR MONOMER) AS SHOWN IN FIGURES 6 AND 7. BO OEP DERIVATIVES ALSO SHOW HYDROGEN BOND INTERACTIONS BETWEEN THE PROPIONIC ACID SIDE CHAINS AND PORPHYRIN METHYLENE AND METHYL GROUPS (FIGURE 8) AND NUMEROUS INTERACTIONS IN THE MONO (FIGURE 9). THE TOTAL NUMBER OF INTERMOLECULAR INTERACTIONS (INCLUDED IN TABLE FE(OEP) MONOMER AND BOTH THE FE(TPP) MONOMER AND DIMER IS MUCH LARGER THAN F DIMER.

Discussion

DETAILED INVESTIGATION OF THE ABOVE RESULTS REVEALS THAT THERE ARE A FEW DEVIA PROFILES EXPECTED FOR THE INTERMOLECULAR HEME COMPOUNDS BASED ON THE CONVENTION RESONANCE RAMAN ENHANCEMENT MECHANISMS.

1- EXCITING SOLID PHASE TPP DERIVATIVES WITH 514 NM IN THE Q BAND REGION IS SIMILAR SPECTRA REPORTED BY BURKE AND CO-WORKERS[21(D),21(E)] FOR [FE(TPP)]$_2$O WHICH IN TURN SHOWS A SIMILAR EXCITATION PROFILE TO THOSE REPORTED BY BOCIAN *et al.*[46] FOR [FE(TPP)]Cl. THE SPECTRA SHOW ENHANCEMENT O NON-TOTALLY SYMMETRIC MODES INCLUDING A_{2g} AND B_{1g} AS WELL AS A_{1g} MODES IN A LESSER EXTENT. THIS WAS INTERPRETED

IN TERMS OF STRONG VIBRONIC COUPLING BETWEEN THE Q AND B (SORET) STATES, SUPERI
AMOUNT OF JAHN-TELLER ACTIVITY[46] EXCITING WITH LASER WAVELENGTHS IN THE Q BAND REGION ALS
THE ENHANCEMENT OF TOTALLY SYMMETRIC[18] MODES INCLUDING BANDS AT 1362 AND 1590 CM^{-1}. SHELNUTT AND
CO-WORKERS[46] OBSERVED SIMILAR ENHANCEMENT PROFILES FOR CR(TPP)CL AND INTERPRETED T
MODE" BEHAVIOR. IN CASE OF [FE(TPP)]$_2$O THE BAND AT ~1362 CM^{-1} HELPS THE 390 AND 363 CM^{-1} MODES BY
VIRTUE OF ITS LARGE ORIGIN SHIFT IN THE Q STATE PRODUCING A PRODUCTIVE VIBRONIC INTERACTION INVOLVING
SCATTERING INTO THE 390 AND 363 CM^{-1} MODES VIA AN INTERMEDIATE STATE WITH ONE QUANTUM OF
THE 1359 CM^{-1} MODE.[21(D),46] THROUGH THIS MECHANISM BOTH A AND B TERM SCATTERING CAN RESULT
THEORIZED BY WARSHEL AND DAUBER.[47]

2- IN GENERAL THE FE−O−FE, FE−N AND FE−CL STRETCHING MODES ARE ENHANCED AT 633 N
EXCITATION FOR TPPS AND OEP MONOMER BUT NOT AT 413 NM. THE INTENSITY OF THESE
EXPECTED TO ARISE FROM RESONANCE WITH A CHARGE TRANSFER TRANSITION.[21(C),31] HOWEVER,
THIS SEEMS TOO LOW AN ENERGY FOR A CHARGE-TRANSFER FROM OXIDE OR HALIDE TO HIG
DEPENDENT DENSITY FUNCTIONAL THEORY (TD-DFT) CALCULATIONS DO NOT SHOW ANY C
CHLORIDE TO FE ION IN FE(TPP)CL AT NEAR-IR REGION (TABLE S3, SUPPORTING INFORMA
ARGUMENT IS THE EFFECT OF ANGLE ON THE INTENSITY OF THESE MODES. X-RAY CRYSTAL
PREDICT A POTENTIAL MINIMUM AT AN ANGLE SMALLER THAN 150º BUT STERIC INTERACTION
TWO PORPHYRIN RINGS CAN INCREASE THE FE−O−FE ANGLE.[43] IN [FE(TPP)]$_2$O THE OBSERVED FE−O−FE ANGLE IS 174.5º[24]
AN INCREASE OF ANGLE COULD PROMOTE THE OVERLAP OF IRON D ORBITALS AND OXYGEN
DECREASES THE ENERGY OF THE FE(III) CHARGE TRANSFER TRANSITION.[21(C)] HOWEVER, THE LACK OF RR
ENHANCEMENT OF ν_{SYM}(FE–O–FE) IN [FE(OEP)]$_2$O (WITH FE–O–FE ANGLE SIMILAR TO THAT OF TPP DIME
RULES OUT THE GENERALITY OF THIS ARGUMENT. MOREOVER, A CORRELATION BETWEEN MO
IRON ATOMS HAS BEEN EVOKED AS THE MECHANISM TO EXPLAIN THE COUPLING BETWEEN TH
AND THE A_{1g} BREATHING MODE.[21(D)] MOTION OF THE IRON ATOM INTO THE PLANE OF THE PYRROLE NITR
MADE EASIER IF THE NITROGEN ATOMS SIMULTANEOUSLY MOVE OUTWARD. THIS PROVID

COUPLING THE FE–O–FE STRETCH WITH THE ν_4 PYRROLE-BREATHING MODE. OUR RESULTS CORROBO ARGUMENT. FOLLOWING THE LACK OF ENHANCEMENT OF ν_4 AT 633 AND NEAR-IR EXCITED RR SPECTRA O [FE(OEP)]$_2$O, THE INTENSITY OF ν_{SYM}(FE–O–FE) IS NEAR ZERO WHILE THE DRAMATICALLY ENHANCED ν_4 BREATHING MODE IN TPPS AND OEP MONOMER HELP THE AXIAL LIGAND STRETCHING MODES TO BE ENHANC

3- A STRIKING OBSERVATION, FIRST OBSERVED IN OUR LAB FOR HEMOZOIN AND β-HEMATIN[10], IS THE DRAMATIC ENHANCEMENT OF THE TOTALLY SYMMETRIC RR MODES AT NEAR-IR EXCITATION OF ALL HEME EXCEPT FOR [FE(OEP)]$_2$O. IT WAS NOTED THAT WHEN EXCITING WITH 782 AND 830 NM LINES A NUMBE SYMMETRIC MODES INCLUDING ν_4 (1374 CM^{-1}), ν_2 (1572 CM^{-1}), AND ν_7 (678 CM^{-1}) DRAMATICALLY ENHANCE RELATIVE TO ν_{10} (1625 CM^{-1}). SUCH ENHANCEMENT CAN ONLY OCCUR UNDER A-TERM MECHANISM. IT WAS SUGGESTED THAT THE DRAMATIC A-TYPE ENHANCEMENT OBSERVED AT NEAR-IR EXCITATION WAVELENG FROM ANY OF THE MAJOR OPTICAL ELECTRONIC TRANSITIONS WAS THE RESULT OF EXCITON THROUGHOUT THE HEME AGGREGATE. A SMALL BROAD ELECTRONIC TRANSITION OBSERVED ACIDIFICATION OF FE(PPIX)CL (HEMIN) TO β-HEMATIN, WAS IMPLICATED IN THE MECHANISM OF ENHANCE

SIMILAR ENHANCEMENT OF THESE MODES WAS ALSO OBSERVED FOR THE MONOMERIC PR FE(PPIX)OH (HEMATIN) BUT NOT AS MUCH AS THAT OBSERVED IN THE DIMER COMPLEX INTERACTION BETWEEN PORPHYRINS IN MONOMERIC FORMS. BASED ON SYMMETRY ARGUM SPECTROSCOPIC MONITORING OF THE ACIDIFICATION OF HEMIN TO β-HEMATIN WHICH SHOWS A RED SHIFTING OF SORET, Q, AND A BAND AT ~867 NM, IT WAS HYPOTHESIZED THAT AN EXCITONIC MECHANISM IS OBSERVED ENHANCEMENT.[10] IN THIS SCENARIO, THE SYMMETRIC ELECTRONIC COMPONENT OF THE N COUPLES THE EXCITED STATES OF CHARGE TRANSFER TRANSITIONS RESULTING IN A SUPERPO THE CONTRIBUTIONS TO THE FRANCK–CONDON INTEGRALS.

TO THE BEST OF OUR KNOWLEDGE, THERE HAS BEEN NO OTHER REPORT IN THE LI ENHANCEMENT OF A_{1G} MODES AT NEAR-IR EXCITED RR SPECTRA OF FE(OEP) AND FE(TPP) PORP HOWEVER, UNUSUAL RESONANCE RAMAN ENHANCEMENT HAS BEEN OBSERVED FOR PORPHYR EXCITING IN THE VISIBLE REGION. RR SPECTRA OF THE *meso,meso*-LINKED ARRAYS RECORDED IN THE B-ST

EXCITATION RANGE EXHIBIT A COMPLEX AND UNUSUAL SCATTERING PATTERN. BRUHWILER *et al.*[48] NOTED SEVERAL SIMILAR FEATURES ABOUT THE SPECTRA (1) THE OBSERVATION OF ONLY A1g MODES (A1g FOR D4h) IN THE RR SPECTRUM, (2) THE ENHANCEMENT OF ANOMALOUSLY POLARIZED *B*-STATE EXCITATION, AND (3) THE LARGE DIFFERENTIAL ENHANCEMENT OF SYMMETRIC VERSUS VIBRATIONS WITH EXCITATION ACROSS THE *B*-STATE ABSORPTIONS. BRUHWILER *et al.*[48] SURMISED THAT THESE SCATTERING CHARACTERISTICS WERE DUE TO THE EFFECTS OF SYMMETRY LOWERING VIBRONIC COUPLING. THE ASYMMETRY INHERENT TO THE *meso,meso*-LINKED ARRAYS CONTRIBUTES TO SYMMETRY LOWERING IN BOTH THE EXCITED ELECTRONIC STATES. STRONG UNIAXIAL EXCITONIC INTERACTIONS MAKE AN ADDITIONAL SYMMETRY LOWERING IN THE EXCITED STATE(S) PROMOTING NON-TOTALLY SYMMETRIC SCATTERING MECHANISMS IN THE *B*-STATE(S) OF THE ARRAYS. COLLECTIVELY, THESE STUDIES OF THE *meso,meso*-LINKED ARRAYS PROVIDE INSIGHT INTO THE TYPE OF RR SCATTERING THAT MIGHT BE ANTICIPATED FOR OTHER EXHIBIT STRONG EXCITONIC INTERACTIONS AMONG THE CONSTITUENT CHROMOPHORES. THE SCATTERING PATTERNS OBSERVED BY BRUHWILER *et al.*[48] DO NOT EXPLAIN THE ENHANCEMENT OBSERVED EXCITING FE(OEP)CL, FE(TPP)CL AND [FE(TPP)]2O WITH NEAR-IR EXCITATION WAVELENGTHS BECAUSE MODES ARE MUCH MORE ENHANCED IN THE NEAR-IR COMPARED TO THE EXTREMELY STRONG SCATTERING BY THE A1g MODES IMPLICATES A TRUE ENHANCEMENT MECHANISM AT WORK WITH LITTLE OR NO VIBRONIC COUPLING.

AKINS *et al.*[49,50] REPORTED THAT IN HIGHLY CONJUGATED SYSTEMS SUCH AS CYANINE DYES AND OTHER ENHANCEMENT EFFECTS CAN ALSO BE SIGNIFICANT. ONE SUCH IMPORTANT MECHANISM IS ENHANCED RAMAN SCATTERING (AERS) WHERE BANDS CAN BECOME ENHANCED THROUGH EXCITON COUPLING BETWEEN NEIGHBORING CHROMOPHORES.[49,50] IN THIS CASE ENERGY IN THE FORM OF AN EXCITON IS TRANSFERRED VIA COVALENT LINKAGES BETWEEN CHROMOPHORES OR DIRECTLY THROUGH π-π ORBITALS, RESULTING IN THE ENHANCEMENT OF PARTICULAR VIBRATIONAL MODES. THE ENHANCED MODES CAN BE EXPLAINED IN TERMS OF AN INCREASE-SIZE EFFECT AND NEAR-RESONANCE POLARIZABILITY.[51] EXCITONIC COUPLING ESSENTIALLY SPLIT THE ELECTRONIC STATES INTO A BROAD

WITH DIFFERENT GEOMETRIES, ENERGIES, AND OSCILLATOR STRENGTHS. THE RAMAN INTEN
WAVELENGTH WILL THEN REFLECT THE EXTENT OF THE EXCITONIC COUPLING. TA AND
TYPE *B* MODES CAN BECOME ENHANCED IN THESE HIGHLY CONJUGATE SYSTEMS.

TO PROVIDE MORE INSIGHT INTO THE ENHANCEMENT MECHANISM, WE UTILIZED ADDITIONA
AND CRYSTALLOGRAPHIC TOOLS TO FIND POSSIBLE FACTORS INVOLVED IN THE ENHANCEMEN
THE SIMILAR MODEL COMPOUNDS WITH DIFFERENT ENHANCEMENT BEHAVIOR. IN ORDER FOR E
OCCUR THERE MUST BE AN ELECTRONIC TRANSITION. UV-VISIBLE MEASUREMENTS SHOW POSS
ABSORPTION BAND BETWEEN 800 AND 900 NM FOR FE(OEP)CL AND ANOTHER BETWEEN 700 FOR THE
FE(TPP)CL AND $[FE(TPP)]_2O$ BUT NO SUCH BAND IS OBSERVED FOR $[FE(OEP)]_2O$. THEORETICAL CALCULATION
HAVE ASSIGNED A TRANSITION AT 875 NM TO A $a_{2u}(\pi) \rightarrow e_g(\pi^*)$ TRANSITION IN FE(TPP)CL WHICH IS NOT OBVIOUS IN
UV-VISIBLE SPECTRUM INDICATING OTHER TRANSITIONS MAY BE IN THIS REGION BUT LOW T
CIRCULAR DICHROISM MEASUREMENTS ARE REQUIRED TO VALIDATE THESE FINDINGS.

BY FAR THE MOST COMPELLING DIFFERENCE BETWEEN THE HEME COMPOUNDS THAT SHOW
OF A_{1G} MODES WHEN IRRADIATING WITH NEAR-IR EXCITATION WAVELENGTHS IS THE $[FE(OEP)]_2O$
THE NUMBER OF INTERMOLECULAR INTERACTIONS ARE REDUCED BY THE
THAT THE ENHANCEMENT OF SOME A_{1G} MODES IN HEMATIN RESULTS FROM EXCITONIC COUPLING
EXTENDED HEME AGGREGATE THROUGH STRONG INTERMOLECULAR INTERACTIONS. SIMIL
CONCERTED WEAKER INTERMOLECULAR INTERACTIONS BETWEEN THE RESPECTIVE PORPHYRIN
FACTOR IN EXPLAINING THE ENHANCEMENT OF TOTALLY SYMMETRIC A_{1G} MODES WHEN EXCITING WITH NEAR-IR
EXCITATION WAVELENGTHS. FEWER INTERMOLECULAR HYDROGEN BOND INTERACTIONS
FE(OEP) DIMER MAY DECREASE THE PROBABILITY OF EXCITONIC INTERACTIONS IN THE FE(OEP
SUPPORTING THIS ARGUMENT IS THE INDICATION OF INTERMOLECULAR CONTACT, AS BETWEE
PORPHYRIN CORES OF THE $[FE(OEP)]_2O$ DIMER, MAY NOT BE A SUFFICIENT CONDITION TO ENABLE ENHAN

Conclusions

RR SPECTRA OF HEME DERIVATIVES FE(TPP)CL, [FE(TPP)]$_2$O, AND FE(OEP)CL REVEAL A DRAMATIC ENHANCEMENT OF TOTALLY SYMMETRIC MODES (PARTICULARLY A_{1g}) AT NEAR-IR EXCITATION WAVELENGTHS; HOWEVER, [FE(OEP)]$_2$O DOES NOT EXHIBIT THIS FEATURE. THE ENHANCEMENT OF ν_4 MODES IN HEME PORPHYRINS AT NEAR-IR EXCITATION COULD BE INTERPRETED IN TERMS OF THE PRESENCE OF HYDROGEN BONDING WHERE X IS A π SYSTEM OR AN ELECTRON DONOR ATOM. CONSEQUENTLY, THE ENHANCEMENT OF ν_4 MODES IN NEAR-IR EXCITATION CAN BE USED AS AN INDICATOR OF THE SUPRAMOLECULAR INTERACTIONS MOREOVER THE RELATIVE INTENSITY OF ν_4 MAY BE AN INDICATOR OF THE STRENGTH OF CONCERTED SUPRAMOLECULAR INTERACTIONS IN HEME SYSTEMS. THIS IS THE FIRST TIME THAT HYDROGEN BONDS HAVE BEEN SHOWN TO INDUCE RR ENHANCEMENT VIA THE EXCITONIC COUPLING MECHANISM. THIS STUDY HAS POTENTIAL IMPACT ON THE DEVELOPMENT OF ANTIMALARIAL DRUGS THAT ARE DESIGNED TO DISRUPT HYDROGEN BONDING. THE DISCOVERY OF THE IMPORTANCE OF HYDROGEN BONDING INTERACTIONS TO TRANSFER ENERGY IN THE NEAR-IR MAY HAVE IMPORTANT IMPLICATIONS IN THE DEVELOPMENT OF HEME-BASED NANO-WIRES.

Acknowledgment. R. PUNTHAROD ACKNOWLEDGES FINANCIAL SUPPORT FROM THE OFFICE OF THE HIGHER EDUCATION, THAILAND. THE AUTHORS THANK THE SUPPORT OF MONASH E-RESEARCH AND ITS-RESEARCH SUPPORT SERVICES FOR THE USE OF THE MONASH SUN GRID CLUSTER. WE WOULD LIKE TO THANK DR. EVAN ROBERTSON (MONASH UNIVERSITY) FOR ASSISTANCE IN CALCULATIONS AND MR. PETER INSTRUMENT MAINTENANCE. THIS WORK IS SUPPORTED BY AN AUSTRALIAN RESEARCH COUNCIL GRANT.

Supporting Information Available: TABLE S1 AND S2. OBSERVED RAMAN BANDS (ω_1), ASSIGNMENTS, LOCAL COORDINATES, SYMMETRY MODES AND RELATIVE ENHANCEMENT FACTORS FOR FE(TPP)CL, [FE(TPP)]$_2$O, FE(OEP)CL AND [FE(OEP)]$_2$O AT 413, 514, 633, 782 AND 830 NM. TABLE S3. ASSIGNMENT OF THE UV-VISIBLE ABSORPTION SPECTRA OF FE(TPP)(CL) S9. THE *ORTEP* CALCULATED INTERACTIONS OF FE(TPP)CL, [FE(TPP)]$_2$O, FE(OEP)CL, TRICLINIC AND MONOCLINIC [FE(OEP)]$_2$O, AND HEMATIN. FIGURE S1–S5 *ORTEP* DIAGRAMS SHOWING MOLECULAR STRUCTURE OF FE(TPP)(CL), [FE(TPP)]$_2$O, FE(OEP)CL, TRICLINIC

AND MONOCLINIC [FE(OEP)]2. FIGURE S6. β-HEMATIN MOLECULES IN THE CRYSTAL STRUCTURE SH

CLOSEST PORPHYRIN PLANE TO PORPHYRIN PLANE CONTACT DISTANCE. FIGURE S7. CONTOU

MOLECULAR ORBITALS OF FE(TPP)CL.

FIGURE CAPTIONS

FIGURE 1. FTIR SPECTRA OF FE(TPP)CL AND [FE(TPP)]$_2$O.

FIGURE 2. FTIR SPECTRA OF FE(OEP)CL AND [FE(OEP)]$_2$O.

FIGURE 3. RR SPECTRA OF FE(TPP)CL AND [FE(TPP)]$_2$O. SOLID LINES CORRESPOND TO THE OXO DIMER COMPLEXES AND THE DASHED LINES CORRESPOND TO THE CHLORO MONOMERS.

FIGURE 4. RR SPECTRA OF FE(OEP)CL AND [FE(OEP)]$_2$O. SOLID LINES CORRESPOND TO THE OXO AGGREGATES AND THE DASHED LINES CORRESPOND TO THE MONOMERS.

FIGURE 5. UV-VISIBLE ABSORBANCE SPECTRA OF HEME DERIVATIVE SOLID CRYSTALS.

FIGURE 6. *Diamond* DIAGRAM OF FE(TPP)CL SHOWING (A) THE C–H···π_{PHENYL} (B) C–H···$\pi_{PYRROLE}$ AND (C) C–H···CL HYDROGEN BOND INTERACTIONS.

FIGURE 7. *Diamond* DIAGRAM OF [FE(TPP)]$_2$O SHOWING (A) THE C–H···π_{PHENYL} AND (B) C–H···$\pi_{PYRROLE}$ HYDROGEN BOND INTERACTIONS.

FIGURE 8. *Diamond* DIAGRAM OF [FE(OEP)]$_2$O SHOWING C–H···$\pi_{PYRROLE}$ HYDROGEN BOND INTERACTIONS.

FIGURE 9. *Diamond* DIAGRAM OF FE(OEP)CL SHOWING C–H···($\pi_{PYRROLE}$) AND (B) C–H···CL HYDROGEN BOND INTERACTION.

TABLE

Table 1. MOLECULAR PARAMETERS INCLUDING INTERMOLECULAR DISTANCE AND INTERACTION IN THIS STUDY.

HEME DERIVATIVES	O.S. OF FE	SPIN STATE OF FE	C.N. OF FE	AXIAL LIGAND	D[FE-N] (Å)	DISPLACEMENT OF FE (Å)	INTERMOLECULAR DISTANCE BETWEEN PORPHYRIN RING	TYPE OF INTERACTION (**)	ENHANCEMENT OF ν_4 BAND (ν_0–CN, ~1375 CM^{-1}) AT NEAR-IR EXCITATION LASER
FE(TPP)CL MONOMER[23] *P2₁/n*, Z = 4	3+	HIGH SPIN	5	CL	2.070(9)	0.57	4.5 (BY *Diamond*[40])	C–H···CL (3) C–H···$\pi_{PYRROLE}$ (10) C–H···π_{PHENYL} (1)	✓
[FE(TPP)]$_2$O DIMER[24] *C2ca*, Z = 4	3+	HIGH SPIN	5	O *μ*-OXO	2.087(3)	0.54	~ 5.20	C–H···$\pi_{PYRROLE}$ (18) C–H···π_{PHENYL} (6)	✓
FE(OEP)CL MONOMER[26] *P2₁/c*, Z = 4	3+	HIGH SPIN	5	CL	0.271(2)	0.49	4.02	C–H···CL (4) C–H···$\pi_{PYRROLE}$ (11)	✓
[FE(OEP)]$_2$O DIMER[27] *P–1*, Z = 4 *P2₁/c*, Z = 4	3+	HIGH SPIN	5	O *μ*-OXO	2.077(3) FOR TRICLINIC 2.080(5) FOR MONOCLINIC	0.50 FOR TRICLINIC 0.54 FOR MONOCLINIC	4.5 FOR TRICLINIC 4.6 FOR MONOCLINIC	C–H···$\pi_{PYRROLE}$ (6)	✗
β-HEMATIN DIMER[4] *P–1*, Z = 2	3+	HIGH SPIN	5	O	2.061	0.47	3.4 (BY *Diamond*[40])	C–H···O (17) (**) O–H···O (2) C–H···$\pi_{PYRROLE}$ (24)	✓

(*) THE NUMBERS IN PARENTHESES REFER TO THE NUMBER OF CALCULATED INTERACTIONS E Å AND D[D···A] ≤ 4.0 Å (EXCEPT A = N; D[H···A] ≤ 3.2 Å). (**) THE CALCULATED INTERACTIONS OF ARE ONLY CALCULATED IF D[D···A] DUE TO HYDROGEN ATOMS WERE NOT INCLUDED IN THE ORIGINA TABLES S49 (SUPPORTING INFORMATION) FOR FULL LISTINGS OF THE CALCULATED H-BOND PAR

REFERENCES

(1) RIDLEY, R. G. *Nature* **2002**, *415*, 686–693.

(2) BROWN, W. H. *J. Exp. Med.* **1911**, *13*, 290–299.

(3) OLIVEIRA, M. F.; SILVA, J. R.; DANSA-PETRETSKI, M.; DE SOUZA, W.; LINS, U.; BRAGA S.; MASUDA, H.; OLIVEIRA, P. L. *Nature* **1999**, *400*, 517–518.

(4) PAGOLA, S.; STEPHENS, P. W.; BOHLE, D. S.; KOSAR, A. D.; MADSEN, S. K. *Nature* **2000**, *404*, 307–310.

(5) SOLOMONOV, I.; FELDMAN, I.; BAEHTZ, C.; KJAER, K.; ROBINSON, I. K.; WEBSTER, MCNAUGHTON, D.; WOOD, B. R.; WEISSBUCH, I.; LEISEROWITZ, L. *J. Am. Chem. Soc.* **2006**, *129*, 2615–2627.

(6) BOHLE, D. S.; CONKLIN, B. J.; COX, D.; MADSEN, S. K.; PAULSON, S.; STEPHENS, P. W.; G. T. *Am. Chem. Soc. Symp. Ser.* **1994**, *572*, 497–515.

(7) FRANCIS, S.; SULLIVAN, D. J.; GOLDBERG, D. *Annu. Rev. Microbiol.* **1997**, *51*, 97–123.

(8) TILLEY, L.; LORIA, P.; FOLEY, M.; INGRAM, V. In *Antimalarial Chemotherapy*; ROSENTHAL, P. J., ED.; HUMANA PRESS: TOTOWA, N. J., 2001; pp. 87–

(9) WEBSTER, G. T.; TILLEY, L.; DEED, S.; MCNAUGHTON, D.; WOOD, B. R. *FEBS Lett.* **2008**, *582*, 1087–1092.

(10) WOOD, B. R.; LANGFORD, S.; COOKE, B. M.; LIM, J.; GLENISTER, F. K.; DURISKA, UNTHANK, J.; MCNAUGHTON, D. *J. Am. Chem. Soc.* **2004**, *126*, 9233–9239.

(11) WOOD, B. R.; LANGFORD, S. J.; COOKE, B. M.; LIM, J.; GLENISTER, F. K.; MCNAUGHTO *FEBS Lett.* **2003**, *554*, 247–252.

(12) SPIRO, T. G. *Biological Applications of Raman Spectroscopy*; WILEY: NEW YORK, 1988; VOL. 3.

(13) ABE, M.; KITAGAWA, T.; KYOGOKU, K. *J. Chem. Phys.* **1978**, *69*, 4526–4534.

(14) HU, S.; SMITH, K. M.; SPIRO, T. G. *J. Am. Chem. Soc.* **1996**, *118*, 12638–12646.

(15) SPIRO, T. G.; STREKAS, T. C. *J. Am. Chem. Soc.* **1974**, *96*, 338–345.

(16) YAMAMOTO, T.; PALMER, G. *J. Biol. Chem.* **1973**, *248*, 5211–5213.

(17) STREKAS, T. C.; PACKER, A. J.; SPIRO, T. G. *J. Raman Spectrosc.* **1973**, *1*, 197–206.

(18) STREKAS, T. C.; SPIRO, T. G. *J. Raman Spectrosc.* **1973**, *1*, 387–392.

(19) KRAMERS, H. A.; HEISENBERG, W. *Z. Phys.* **1925**, *31*, 681–707.

(20) DIRAC, P. A. M. *Proc. Roy. Soc. (London)* **1927**, *114*, 710–728.

(21) (A) SPAULDING, L. D.; CHANG, C. C.; YU, N.-T.; FELTON, R. H. *J. Am. Chem. Soc.* **1975**, *97*, 2517–2525. (B) ADAR, F.; SRIVASTAVA, P. *Proc. Nat. Acad. Sci. USA* **1975**, *72*, 4419–4424. (C) KITAGAWA, T.; ABE, M.; KYOGOKU, Y. *J. Phys. Chem.* **1976**, *80*, 1181–1186. (D) BURKE, J. M.; KINCAID, J. R.; SPIRO, T. G. *J. Am. Chem. Soc.* **1978**, *100*, 6077–6083. (E) BURKE, J. M.; KINCAID, J. R.; PETERS, S.; GAGNE, R. R.; COLLMAN, J. P.; SPIRO, T. G. *J. Am. Chem. Soc.* **1978**, *100*, 6083–6088. (F) HOFMANN, J. A.; BOCIAN, D. F. *J. Phys. Chem.* **1984**, *88*, 1472–1479. (G) KOWALEWSKI, P.; MERLIN, J. C.; BREMARD, C.; MOREAU, J. *J. Mol. Struct.* **1988**, *175*, 55–60. (H) FIDLER, V.; OGURA, T.; SATO, S.; AOYAGI, K.; KITAGAW T. *Bull. Chem. Soc. Jpn.* **1991**, *64*, 2315–2322. (I) BRÉMARD, C.; KOWALEWSKI, P. MERLIN, J. C.; MOREA

S. *J. Raman Spectrosc.* **1992**, *23*, 325–333. (J) SHANTHA, P. K.; THANGA, H. H.; VERMA, A. *J. Raman Spectrosc.* **1998**, *29*, 997–1001.

(22) HOARD, J. L.; COHEN, G. H.; GLICK, M. D. *J. Am. Chem. Soc.* **1967**, *89*, 1992–1996.

(23) SCHEIDT, W. R.; FINNEGAN, M. G. *Acta Cryst. C* **1989**, *45*, 1214–1216.

(24) HOFFMAN, A. B.; COLLINS, D. M.; DAY, V. W.; FLEISCHER, E. B.; SRIVASTAVA, T. S.; HO L. *J. Am. Chem. Soc.* **1972**, *94*, 3620–3626.

(25) SWEPSTON, P. N.; IBERS, J. A. *Acta Cryst. B* **1985**, *41*, 671–673.

(26) SENGE, M. O. *Acta Cryst. E* **2005**, *61*, 399–400.

(27) CHENG, B.; HOBBS, J. D.; DEBRUNNER, P. G.; ERLEBACHER, J.; SHELNUTT, J. A.; SCHEI *Inorg. Chem.* **1995**, *34*, 102–110.

(28) BURNETT, M. N.; JOHNSON, C. K. *ORTEP-III: Oak Ridge Thermal Ellipsoid Plot Program for Crystal Structure Illustrations*, REPORT ORNL-6895, OAK RIDGE NATIONAL LABORATORY, OAK RIDG **1996**.

(29) CAMBRIDGE STRUCTURAL DATABASE VERSION 5.27 UPDATES AUGUST 2006.

(30) SADASIVAN, N.; EBERSPAECHER, H. I.; FUCHSMAN, W. H.; CASEY, W. S. *Biochem.* **1969**, *8*, 534–541.

(31) FLEISCHER, E. B.; SRIVASTAVA, T. S. *J. Am. Chem. Soc.* **1969**, *91*, 2403–2405.

(32) RUSH, T. S. I.; KOZLOWSKI, P. M.; PIFFAT, C. A.; KUMBLE, R.; ZGIERSKI, M. Z.; SPIRO, T *J. Phys. Chem. B.* **2000**, *104*, 5020–5034.

(33) OZAKI, Y.; MIZUNO, A.; SATO, H.; KAWAGUCHI, K.; MUROISHI, S. *Appl. Spectrosc.* **1992**, *46*, 533–535.

(34) WOOD, B. R.; TAIT, B.; MCNAUGHTON, D. *Biochim. Biophys. Acta* **2004**, *1539*, 58–70.

(35) KINCAID J. R. *The Porphyrin Handbook*, VOL. 7; KADISH K. M.; SMITH K. M.; GUILLARD R. (EDS); ACADEMIC PRESS, **1999**, PP 225–

(36) ZERNER, M.; GOUTERMAN, M.; KOBAYASHI, H. *Theoret. Chim. Acta* **1966**, *6*, 363–399.

(37) PAULAT, F.; LEHNERT, N. *Inorg. Chem.* **2008**, *47*, 4963–4976.

(38) SELENSKY, R.; HOLTEN, D.; WINDSOR, M. W; PAINE, J. B.; *Chemical Physics* **1981**, *60*, 33–46.

(39) WEBSTER, G. T.; MCNAUGHTON, D.; WOOD, B. R. *J. Phys. Chem. B.* **2009**, ACCEPTED PENDING REVISION.

(40) CRYSTAL IMPACT. *DIAMOND*. VERSION 3.1. CRYSTAL IMPACT GBR, BONN, GERMANY, **2006**.

(41) FUCHSMAN, W. H.; SMITH, Q. R.; STEIN, M. M. *J. Am. Chem. Soc.* **1977**, *99*, 4190–4192.

(42) EATON, S. S.; EATON, G. R. *J. Am. Chem. Soc.* **1975**, *97*, 3660–3666.

(43) TSUBAKI, M.; SRIVASTAVA, R. B.; NAI-TENG, Y. *Biochem.* **1982**, *21*, 1130–1140.

(44) SCHEIDT, W. R.; GEIGER, D. K.; HAYES, R. G.; LANG, G. *J. Am. Chem. Soc.* **1983**, *105*, 2625–2632.

(45) SCHEIDT, W. R.; GEIGER, D. K.; HALLER, K. J. *J. Am. Chem. Soc.* **1982**, *104*, 495–499.

(46) SHELNUTT, J. A.; CHEUNG, L. D.; CHANG, R. C. C.; YU, N.; FELTON, R. H. *J. Phys. Chem.* **1977**, *66*, 3387–3398.

(47) WARSHEL, A.; DAUBER, P. *J. Phys. Chem.* **1977**, *66*, 5477–5488.

(48) BHUIYAN, A. A.; SETH, J.; YOSHIDA, N.; OSUKA, A.; BOCIAN, D. F. *J. Phys. Chem. B.* **2000**, *104*, 10757−10764.

(49) AKINS, D. L. *J. Phys.Chem.* **1986**, *90*, 1530−1534.

(50) AKINS, D. L.; ZHU, H. -R; GUO, C. *J. Phys.Chem.* **1996**, *100*, 5420−5425.

(51) AKINS, D. L.; ZELIK, S.; ZHU, H. -R.; GUO, C. *J. Phys.Chem.* **1997**, *101*, 3251−3259.

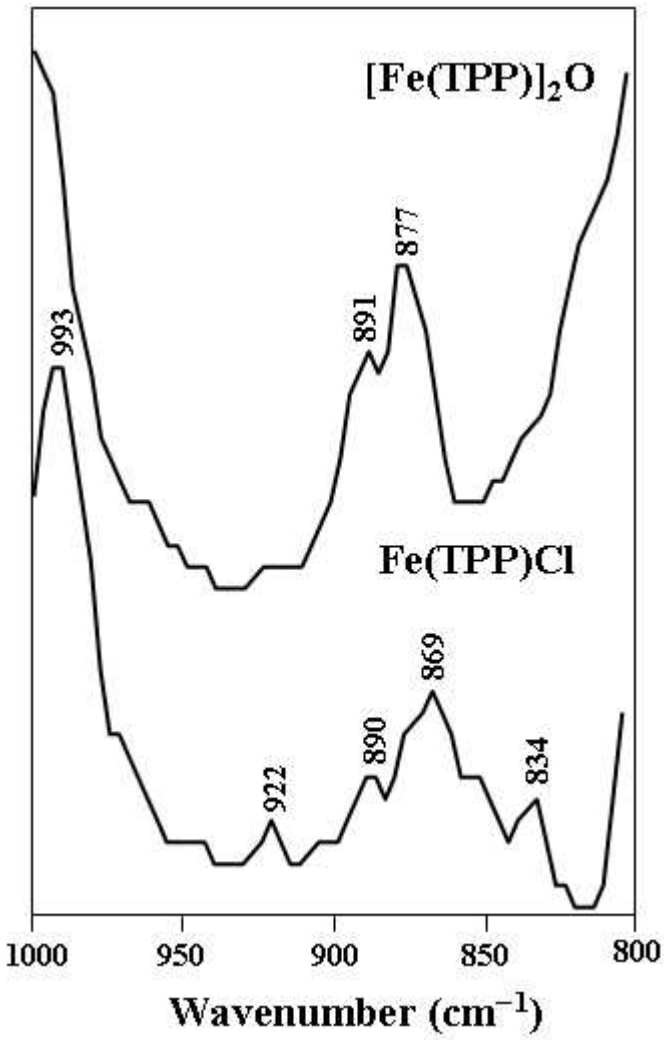

Figure 1
90x138mm (96 x 96 DPI)

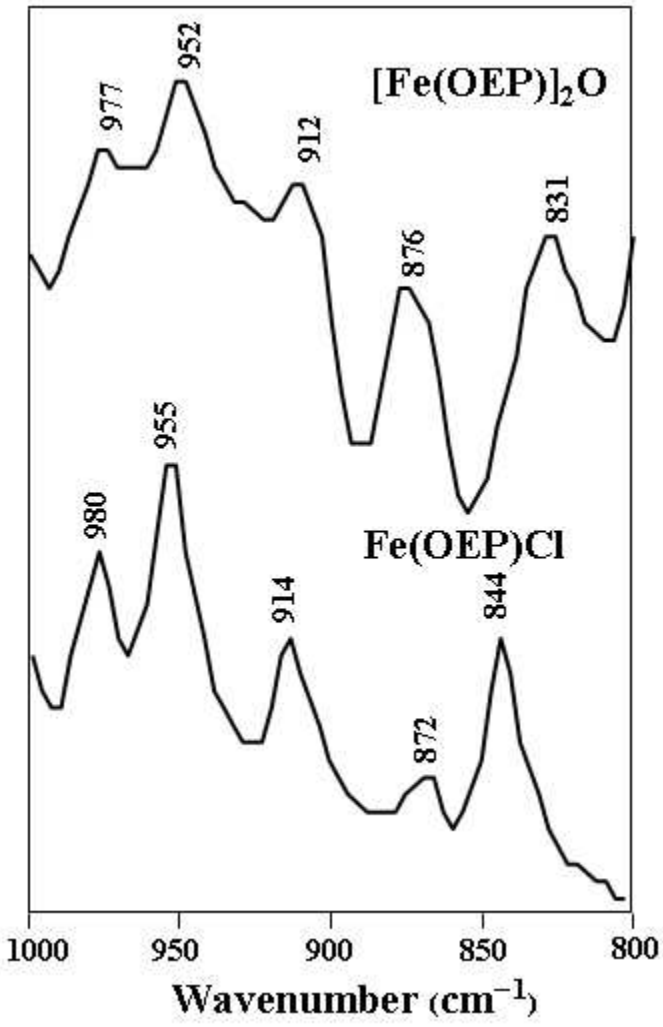

Figure 2
89x135mm (96 x 96 DPI)

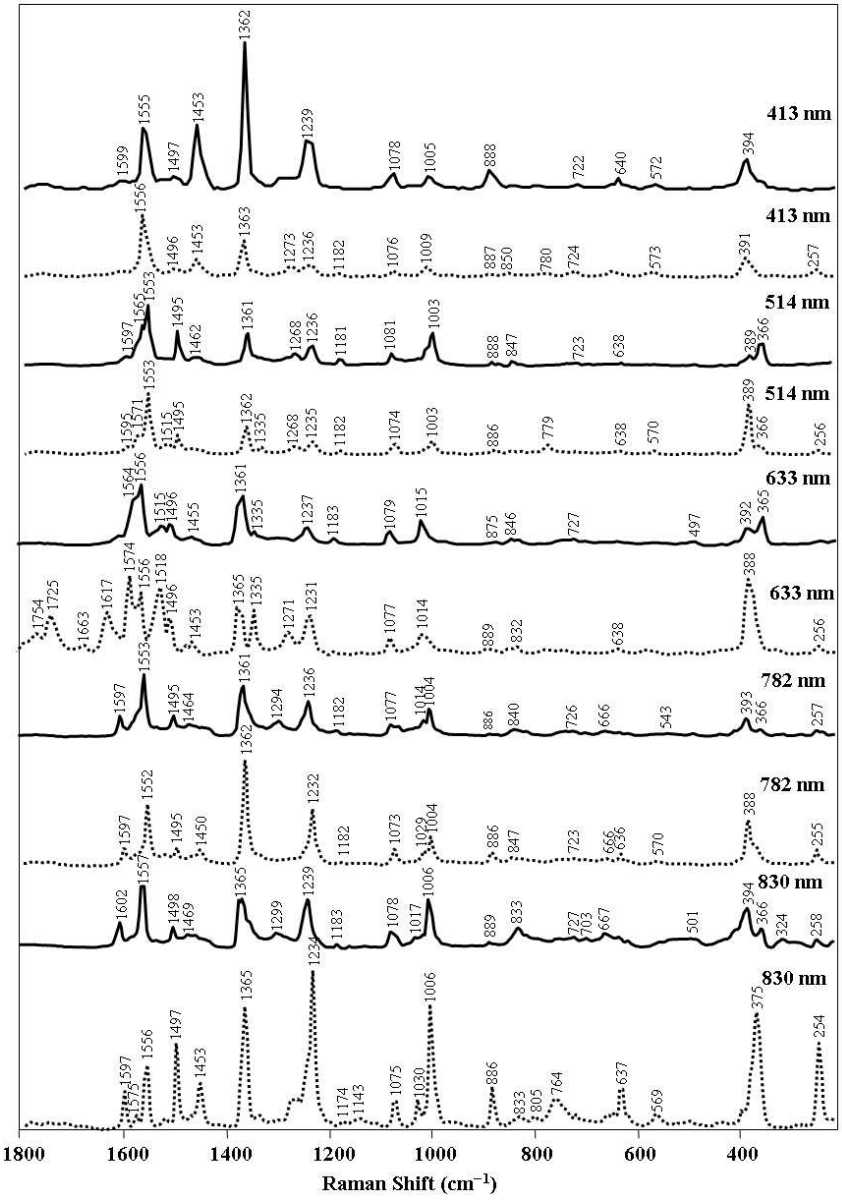

Figure 3
227x323mm (96 x 96 DPI)

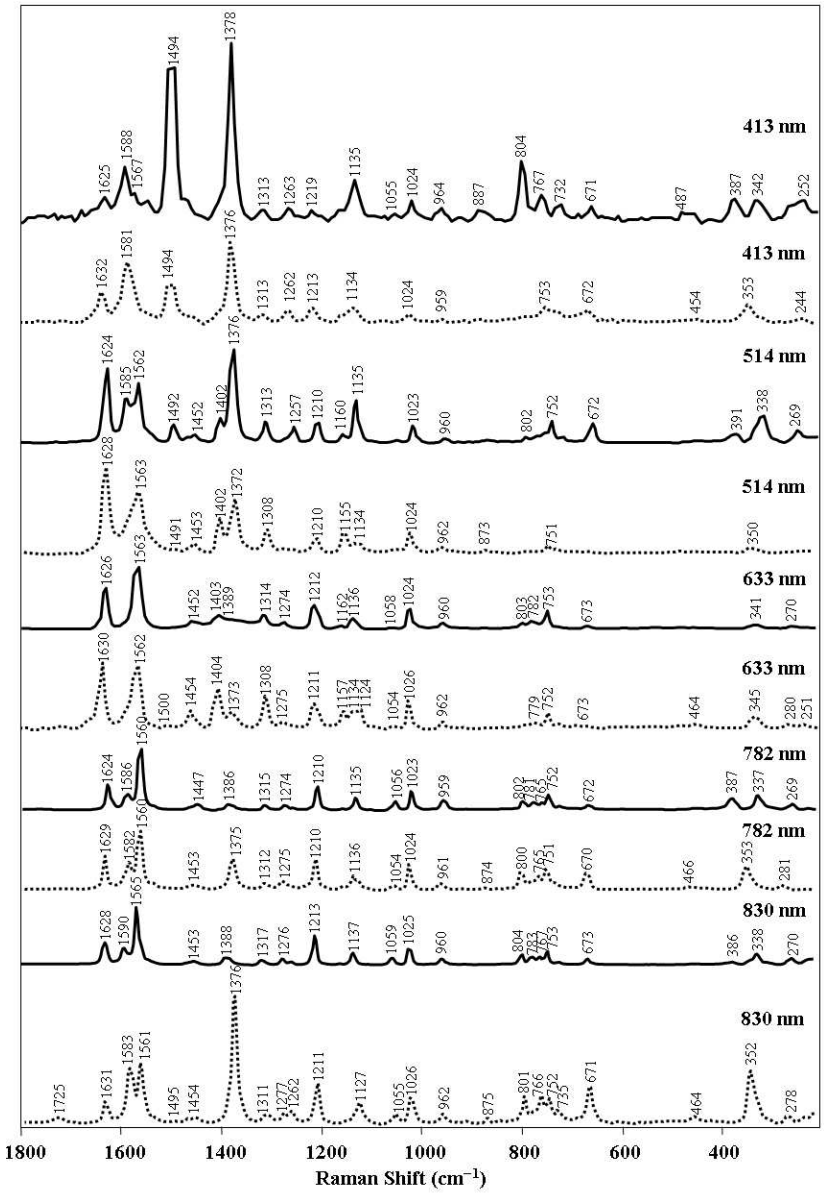

Figure 4
226x330mm (96 x 96 DPI)

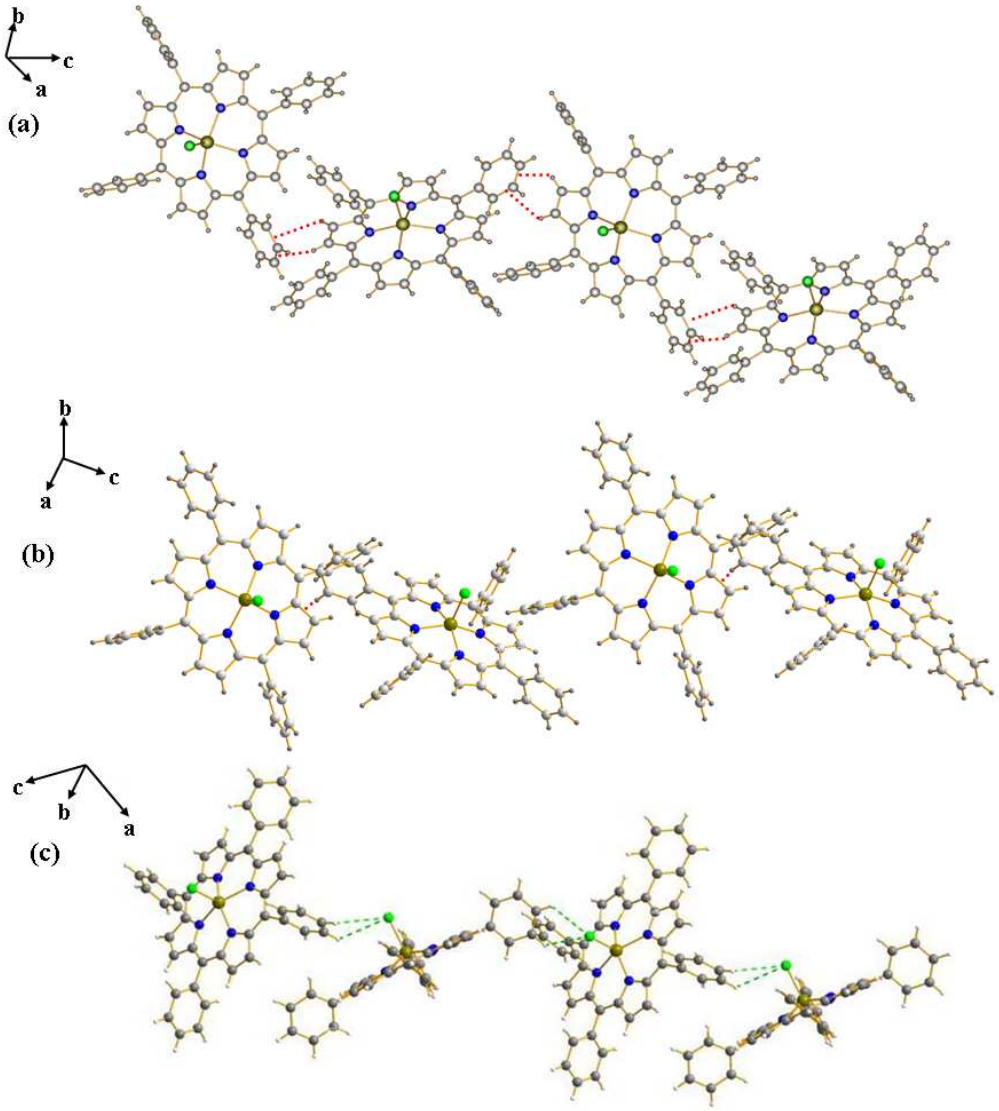

Figure 6
231x258mm (96 x 96 DPI)

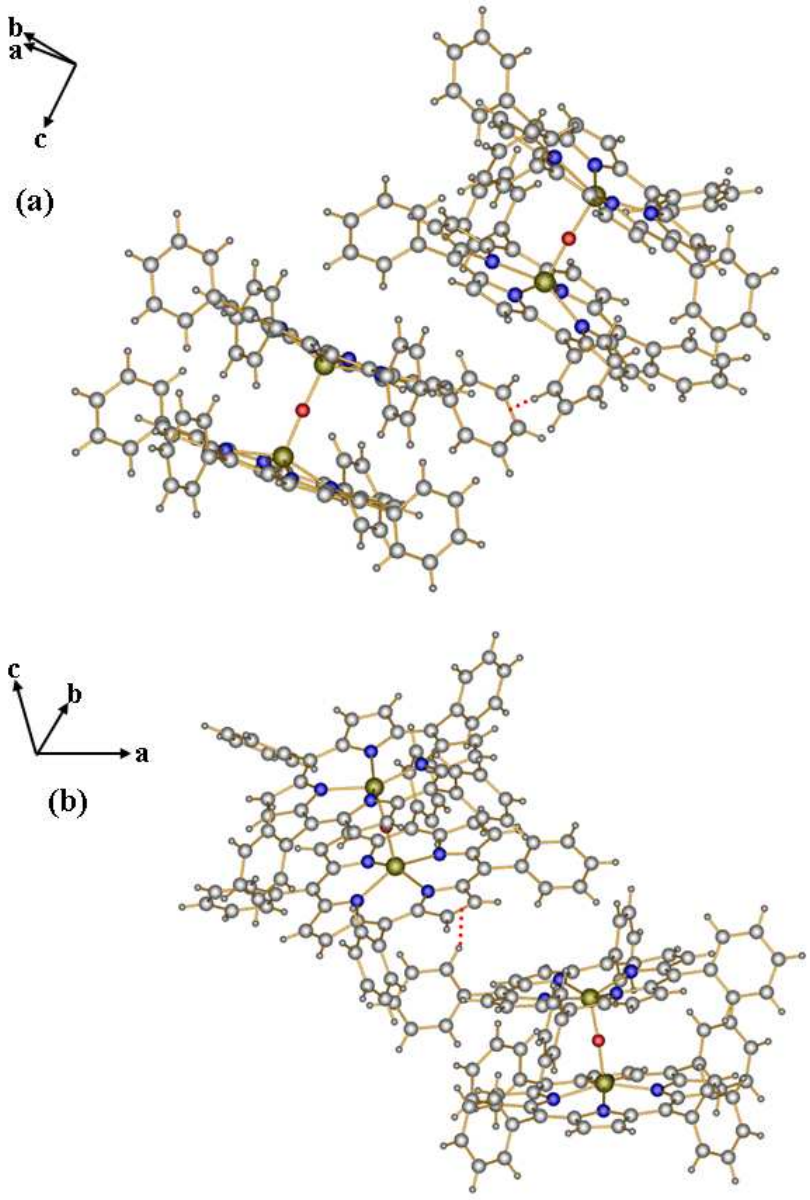

Figure 7
153x226mm (96 x 96 DPI)

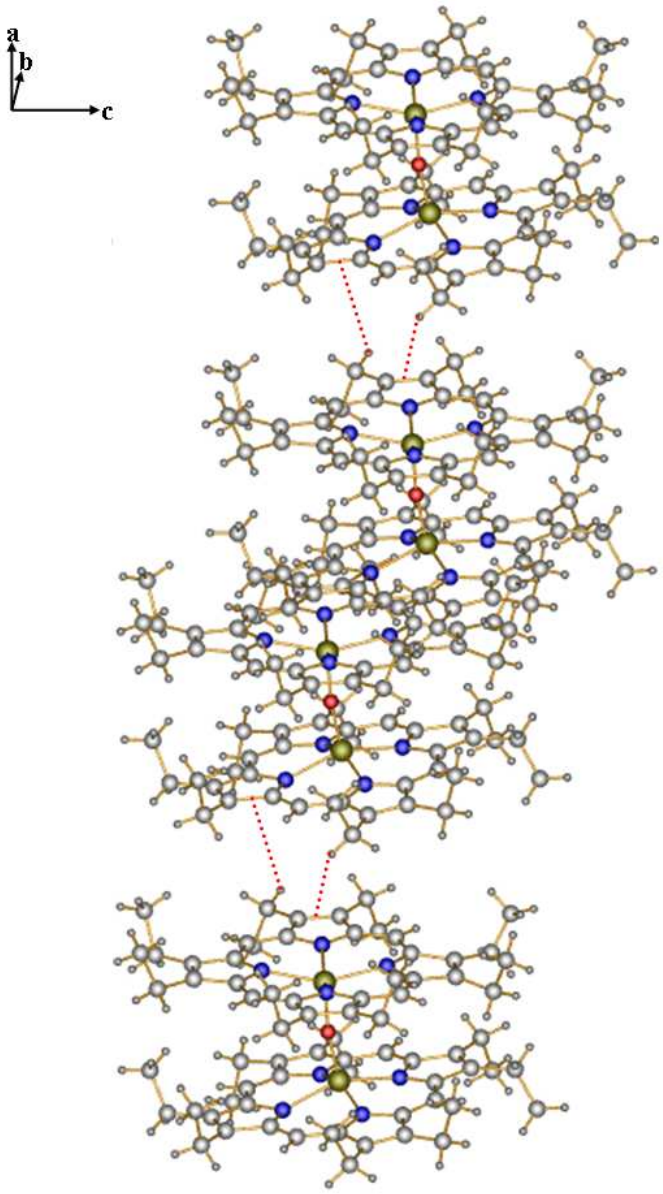

Figure 8
136x244mm (96 x 96 DPI)

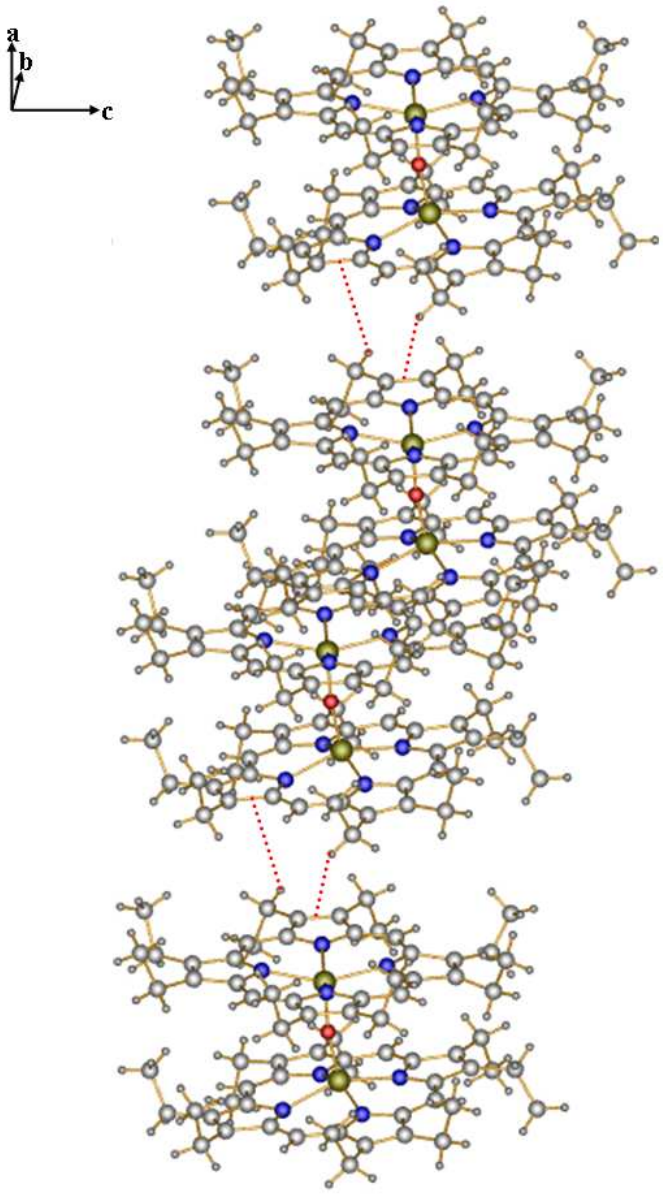

Figure 8
136x244mm (96 x 96 DPI)

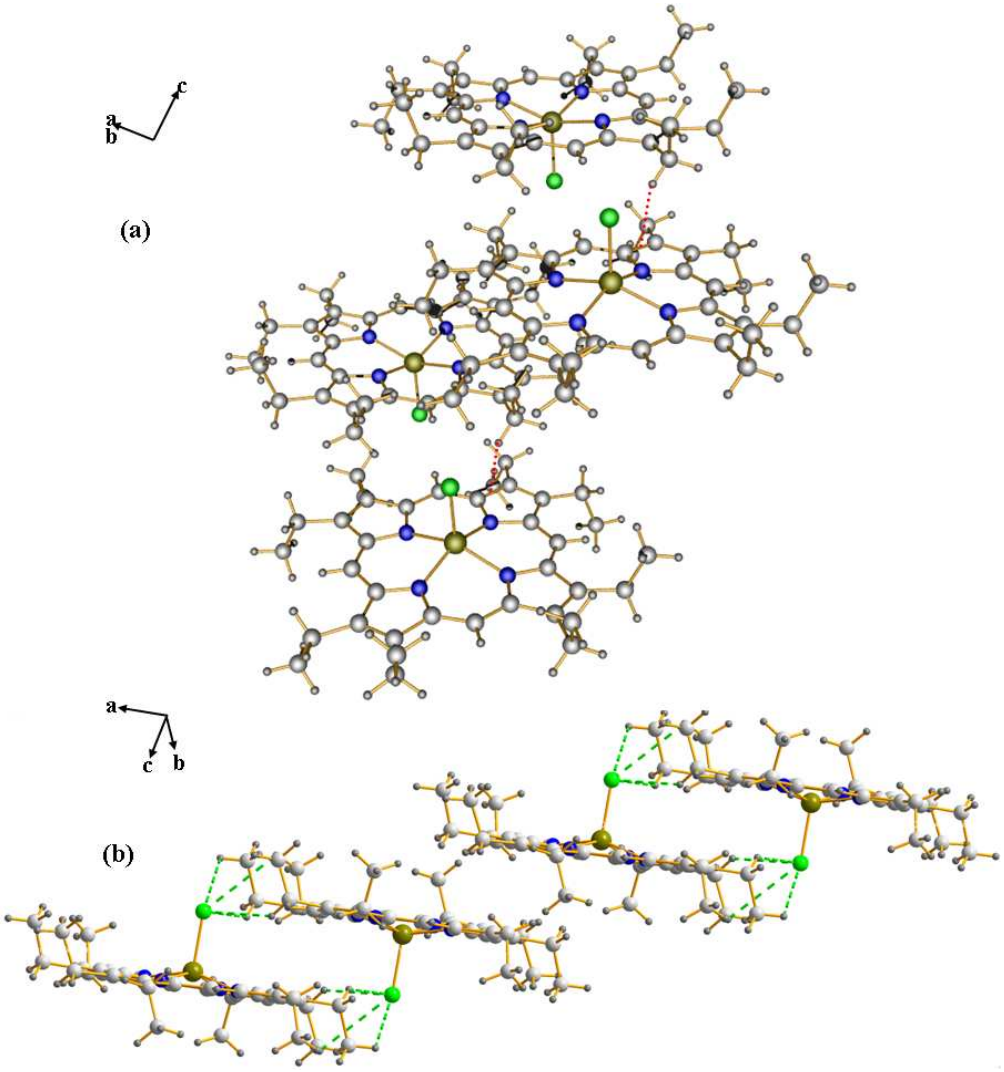

Figure 9
238x255mm (96 x 96 DPI)

Supporting Information

Ratchadaporn Puntharod[1,2], Grant T. Webster[2], Mehdi Asghari-Khiavi[2], Keith R. Bambery[2], Feryal Safinejad[2], Kenneth J. Haller[1,] and Bayden R. Wood[2,*]*

1. School of Chemistry, Institute of Science, Suranaree University of Technology, Nakhon Ratchasima 30000, Thailand

2. Centre for Biospectroscopy and School of Chemistry, Monash University, Victoria 3800, Australia

Email_bayden.wood@sci.monash.edu.au. and [redacted]

Table S1. Observed Raman bands (cm^{-1}), assignments, local coordinates, symmetry modes and relative enhancement factors for of Fe(TPP)Cl and $[Fe(TPP)]_2O$ at 413, 514, 633, 782 and 830 nm.

Fe(TPP)Cl					$[Fe(TPP)]_2O$					assignment	symmetry	local coordinate
413	**514**	**633**	**782**	**830**	**413**	**514**	**633**	**782**	**830**			
	1595(1)		1597(2)	1597(2)	1599(1)	1597(2)		1597(3)	1602(4)	F_4	A_{1g}	ph, ?(C–C)$_{sym}$
	1571(3)	1574(10)		1575(1)						F_4'	B_{2g}	ph, ?(C–C)$_{sym}$
						1565(7)	1565(8)			ν_{10}	B_{1g}	$\nu(C_aC_m)_{asym}$
1556(10)	1553(10)	1556(8)	1552(6)	1556(4)	1555(4)	1553(10)	1556(10)	1553(10)	1557(10)	ν_2	A_{1g}	$\nu(C_\beta C_\beta)$
	1515(2)	1518(9)					1515(3)			ν_{19}	A_{2g}	$\nu(C_aC_m)_{asym}$
1496(1)	1495(3)	1496(5)	1495(2)	1497(5)	1497(1)	1495(6)	1496(3)	1495(3)	1498(3)	ν_{11}	B_{1g}	$\nu(C_\beta C_\beta)$
								1464(2)	1469(2)	ν_{28}	B_{2g}	$\nu(C_aC_m)_{sym}$
1453(3)		1453(2)	1450(2)	1453(3)	1453(4)	1462(2)	1455(1)			ν_3	A_{1g}	$\nu(C_aC_m)_{sym}$
1363(6)	1362(5)	1365(6)	1362(10)	1365(8)	1362(10)	1361(5)	1361(8)	1361(8)	1365(8)	ν_4	A_{1g}	ν(pyr half-ring)$_{sym}$
	1335(1)	1335(6)					1335(2)			ν_{20}	A_{2g}	ν(pyr quarter-ring)
								1294(3)	1299(2)	ν_{12}	B_{1g}	ν(pyr half-ring)$_{sym}$
1273(2)	1268(1)	1271(3)				1268(2)				ν_{27}	B_{2g}	$\nu(C_m–X)$
1236(2)	1235(2)	1231(5)	1232(5)	1234(10)	1239(3)	1236(3)	1237(3)	1236(6)	1239(8)	ν_1	A_{1g}	$\nu(C_m–X)$
1182(1)	1182(1)	1183(0)	1182(0)	1174(1)		1181(1)	1183(1)	1182(1)	1183(1)	ν_{34}	B_{2g}	$d(C_\beta C1)_{asym}$
1076(1)	1074(2)	1077(2)	1073(2)	1075(2)	1078(1)	1081(2)	1079(2)	1077(2)	1078(3)	ν_{17}	B_{1g}	$d(C_\beta C1)_{sym}$
			1029(1)	1030(2)						F_7	A_{1g}	ph, ν(C–C)
		1014(3)					1015(4)	1014(3)	1017(2)	ν_{30}	B_{2g}	ν(pyr half-ring)$_{asym}$
1009(2)	1003(2)		1004(3)	1006(8)	1005(1)	1003(5)		1004(4)	1006(8)	ν_6	A_{1g}	ν(pyr breathing)
887(0)	886(1)	889(1)	885(1)	886(3)	888(1)	888(1)	875(1)	886(0)	889(1)	ν_7	A_{1g}	δ(pyr def)$_{sym}$
850(1)						847(1)	846(1)	840(1)	833(3)	ν_{32}	B_{2g}	d(pyr def)$_{asym}$
		832(1)	833(1)	833(1)						ν_{24}	A_{2g}	d(pyr def)$_{asym}$
780(1)	779(2)									$2\nu_8$	A_{1g}	
724(1)			723(1)		722(0)	723(1)	727(1)	726(1)	727(2)	$?_{26}$	E_g	?($C_\beta C1)_{asym}$
			666(1)					666(1)	667(2)	F_9''	E_u	ph ip
	638(1)	638(1)	636(1)	637(3)	640(1)	638(1)			639(2)	F_9	A_{1g}	ph ip
573(1)	570(1)		570(0)	569(1)	572(0)					$\nu_8+\nu_{18}$	B_{1g}	ν(Fe–N)
								543(1)		$?_{13}$	B_{1u}	?(C_aC_m)
							497(1)		501(2)	p_5		ph ip
391(3)	389(8)	388(10)	388(4)	388(4)	394(2)	389(2)	392(3)	393(3)	394(6)	s_3''	E_g	ph op, ring twisting
	366(1)	374(4)	375(2)	375(7)								ν(Fe–Cl)
						366(4)	365(5)	366(1)	366(3)		A_{1g}	ν(Fe–O–Fe)$_{sym}$
257(1)	256(1)	256(1)	255(2)	254(5)				257(1)	258(1)	$?_{16}$	B_{2u}	d(pyr tilt)

Table S2. Observed Raman bands (cm^{-1}), assignments, local coordinates, symmetry modes and relative enhancement factors for of Fe(TPP)Cl, $[Fe(TPP)]_2O$, Fe(OEP)Cl and $[Fe(OEP)]_2O$ at 413, 514, 633, 782 and 830 nm.

Fe(OEP)Cl					$[Fe(OEP)]_2O$					assignment	symmetry	local coordinate
413	**514**	**633**	**782**	**830**	**413**	**514**	**633**	**782**	**830**			
1632(4)	1628(10)	1630(10)	1629(6)	1631(2)	1625(1)	1624(8)	1626(7)	1624(4)	1628(4)	ν_{10}	B_{1g}	$\nu(C_aC_m)_{asym}$
1581(8)			1582(5)	1583(4)	1588(3)	1585(5)		1586(3)	1590(3)	ν_2	A_{1g}	$\nu(C_\beta C_\beta)$
	1563(7)	1562(10)	1560(10)	1561(5)	1567(2)	1562(7)	1563(10)	1560(10)	1565(10)	ν_{19}	A_{2g}	$\nu(C_aC_m)_{asym}$
	1563(7)	1562(10)	1560(10)	1561(5)	1567(2)	1562(7)	1563(10)	1560(10)	1565(10)	ν_{11}	B_{1g}	$\nu(C_\beta C_\beta)$
1494(5)				1495(0)	1494(9)	1492(2)				ν_3	A_{1g}	$\nu(C_aC_m)_{sym}$
	1453(1)	1454(3)	1453(1)	1454(0)		1452(1)	1452(1)	1447(1)	1453(1)	ν_{28}	B_{2g}	$\nu(C_aC_m)_{sym}$
	1402(2)	1404(6)				1402(3)	1403(2)			ν_{29}	B_{2g}	ν(pyr quarter-ring)
							1389(2)	1386(1)	1388(1)	ν_{20}	A_{2g}	ν(pyr quarter-ring)
1376(10)	1372(6)	1373(3)	1375(5)	1376(10)	1378(10)	1376(3)				ν_4	A_{1g}	$\nu(\text{pyr half-ring})_{sym}$
1313(1)	1308(3)	1308(5)	1312(1)	1311(1)	1313(1)	1313(3)	1314(2)	1315(1)	1317(1)	ν_{21}	A_{2g}	$d(C_mH)$
		1275(1)	1275(2)	1277(1)			1274(1)	1274(1)	1276(1)			ethyl
1262(2)				1262(1)	1263(1)	1257(3)				$\nu_5+\nu_9$	A_{1g}	$d(C_\beta C1)_{sym}$
1213(2)	1210(2)	1211(4)	1210(5)	1211(3)	1219(1)	1210(3)	1212(4)	1210(4)	1213(5)	ν_{13}	B_{1g}	$d(C_mH)$
	1155(2)	1157(3)				1160(1)	1162(1)			ν_{30}	B_{2g}	$\nu(\text{pyr half-ring})_{asym}$
1134(2)	1134(1)	1134(3)	1136(2)		1135(2)	1135(4)	1136(2)	1135(2)	1137(2)	$\nu_6+\nu_8$	A_{1g}	$\nu(C_a-C_\beta)_{sym} + \nu(Fe-N)$
		1124(3)		1127(2)						ν_{22}	A_{2g}	$\nu(\text{pyr half-ring})_{asym}$
		1054(1)	1054(1)	1055(1)	1055(1)		1058(0)	1056(1)	1059(1)	ν_{23}	A_{2g}	$\nu(C_\beta C1)_{asym}$
1024(1)	1024(2)	1026(4)	1024(4)	1026(2)	1024(1)	1023(2)	1024(3)	1023(3)	1025(3)	ν_5	A_{1g}	$\nu(C_\beta C1)_{sym}$
959(1)	962(1)	962(1)	961(1)	962(1)	964(1)	960(0)	960(1)	959(1)	960(1)	$\nu_{32}+\nu_{35}$	A_{1g}	d(porph def) + d(pyr transl)
	873(0)		874(0)	875(0)	887(1)							ethyl
			800(3)	801(2)	804(3)	802(1)	803(1)	802(1)	804(2)	ν_6	A_{1g}	ν(pyr breathing)
		779(1)					782(1)	781(1)	783(1)	ν_{32}	B_{2g}	$d(\text{pyr def})_{asym}$
			765(2)	766(2)	767(2)			765(1)	767(1)	ν_{47}	E_u	ν(pyr breathing)
753(2)	751(1)	752(3)	751(4)	752(2)		752(2)	753(3)	752(2)	753	ν_{15}	B_{1g}	ν(pyr breathing)
				735(1)	732(1)					$?_5$	A_{2u}	$d(\text{pyr fold})_{sym}$
672(2)		673(1)	670(3)	671(3)	671(1)	672(2)	673(0)	672(1)	673(1)	ν_7	A_{1g}	$d(\text{pyr def})_{sym}$
454(1)		464(1)	466(1)	464(1)	487(1)							d(pyr fold)?
					387(1)	391(1)		387(2)	386(1)		A_{1g}	$\nu(Fe-O-Fe)_{sym}$
353(2)	350(1)	345(2)	353(4)	352(4)								ν(Fe–Cl)
					342(1)	338(3)	341(1)	337(2)	338(2)			ν(Fe–N)
		280(1)	281(1)	278(1)								?
						269(1)	270(0)	269(1)	270(1)	ν_9	A_{1g}	$d(C_\beta C1)_{sym}$
244(1)		251(1)			252(1)					$?_{23}$	E_g	d(pyr tilt)

Table S3. Assignment of the UV-vis absorption spectra of [Fe(TPP)(Cl)].

(1) Ridley, R. G. *Nature* **2002**, *415*, 686–693.

(2) Brown, W. H. *J. Exp. Med.* **1911**, *13*, 290–299.

(3) Oliveira, M. F.; Silva, J. R.; Dansa-Petretski, M.; de Souza, W.; Lins, U.; Braga, C. M. S.; Masuda, H.; Oliveira, P. L. *Nature* **1999**, *400*, 517–518.

(4) Pagola, S.; Stephens, P. W.; Bohle, D. S.; Kosar, A. D.; Madsen, S. K. *Nature* **2000**, *404*, 307–310.

(5) Solomonov, I.; Feldman, I.; Baehtz, C.; Kjaer, K.; Robinson, I. K.; Webster, G. T.; McNaughton, D.; Wood, B. R.; Weissbuch, I.; Leiserowitz, L. *J. Am. Chem. Soc.* **2006**, *129*, 2615–2627.

(6) Bohle, D. S.; Conklin, B. J.; Cox, D.; Madsen, S. K.; Paulson, S.; Stephens, P. W.; Yee, G. T. *Am. Chem. Soc. Symp. Ser.* **1994**, *572*, 497–515.

(7) Francis, S.; Sullivan, D. J.; Goldberg, D. *Annu. Rev. Micobiol.* **1997**, *51*, 97–123.

(8) Tilley, L.; Loria, P.; Foley, M.; Ingram, V. M. In *Antimalarial Chemotherapy*; Rosenthal, P. J., Ed.; Humana Press: Totowa, N. J., 2001, pp. 87–122.

(9) Webster, G. T.; Tilley, L.; Deed, S.; McNaughton, D.; Wood, B. R. *FEBS Lett.* **2008**, *582*, 1087–1092.

(10) Wood, B. R.; Langford, S.; Cooke, B. M.; Lim, J.; Glenister, F. K.; Duriska, M.; Unthank, J.; McNaughton, D. *J. Am. Chem. Soc.* **2004**, *126*, 9233–9239.

(11) Wood, B. R.; Langford, S. J.; Cooke, B. M.; Lim, J.; Glenister, F. K.; McNaughton, D. *FEBS Lett.* **2003**, *554*, 247–252.

(12) Spiro, T. G. *Biological Applications of Raman Spectroscopy*; Wiley: New York, 1988; Vol. 3.

(13) Abe, M.; Kitagawa, T.; Kyogoku, K. *J. Chem. Phys.* **1978**, *69*, 4526–4534.

(14) Hu, S.; Smith, K. M.; Spiro, T. G. *J. Am. Chem. Soc.* **1996**, *118*, 12638–12646.

(15) Spiro, T. G.; Strekas, T. C. *J. Am. Chem. Soc.* **1974**, *96*, 338–345.

(16) Yamamoto, T.; Palmer, G. *J. Biol. Chem.* **1973**, *248*, 5211–5213.

(17) Strekas, T. C.; Packer, A. J.; Spiro, T. G. *J. Raman Spectrosc.* **1973**, *1*, 197–206.

(18) Strekas, T. C.; Spiro, T. G. *J. Raman Spectrosc.* **1973**, *1*, 387–392.

(19) Kramers, H. A.; Heisenberg, W. *Z. Phys.* **1925**, *31*, 681–707.

(20) Dirac, P. A. M. *Proc. Roy. Soc. (London)* **1927**, *114*, 710–728.

(21) (a) Spaulding, L. D.; Chang, C. C.; Yu, N.-T.; Felton, R. H. *J. Am. Chem. Soc.* **1975**, *97*, 2517–2525. (b) Adar, F.; Srivastava, T. S. *Proc. Nat. Acad. Sci. USA* **1975**, *72*, 4419–4424. (c) Kitagawa, T.; Abe, M.; Kyogoku, Y. *J. Phys. Chem.* **1976**, *80*, 1181–1186. (d) Burke, J. M.; Kincaid, J. R.; Spiro, T. G. *J. Am. Chem. Soc.* **1978**, *100*, 6077–6083. (e) Burke, J. M.; Kincaid, J. R.; Peters, S.; Gagne, R. R.; Collman, J. P.; Spiro, T. G. *J. Am. Chem. Soc.* **1978**, *100*, 6083–6088. (f) Hofmann, J. A.; Bocian, D. F. *J. Phys. Chem.* **1984**, *88*, 1472–1479. (g) Kowalewski, P.; Merlin, J. C.; Bremard, C.; Moreau, S. *J. Mol. Struct.* **1988**, *175*, 55–60. (h) Fidler, V.; Ogura, T.; Sato, S.; Aoyagi, K.; Kitagawa, T. *Bull. Chem. Soc. Jpn*. **1991**, *64*, 2315–2322. (i) Brémard, C.; Kowalewski, P. Merlin, J. C.; Moreau, S. *J. Raman Spectrosc*. **1992**, *23*, 325–333. (j) Shantha, P. K.; Thanga, H. H.; Verma, A. L. *J. Raman Spectrosc*. **1998**, *29*, 997–1001.

(22) Hoard, J. L.; Cohen, G. H.; Glick, M. D. *J. Am. Chem. Soc.* **1967**, *89*, 1992–1996.

(23) Scheidt, W. R.; Finnegan, M. G. *Acta Cryst. C.* **1989**, *45*, 1214–1216.

(24) Hoffman, A. B.; Collins, D. M.; Day, V. W.; Fleischer, E. B.; Srivastava, T. S.; Hoard, J. L. *J. Am. Chem. Soc.* **1972**, *94*, 3620–3626.

(25) Swepston, P. N.; Ibers, J. A. *Acta Cryst. C.* **1985**, *41*, 671–673.

(26) Senge, M. O. *Acta Cryst. E.* **2005**, *61*, 399–400.

(27) Cheng, B.; Hobbs, J. D.; Debrunner, P. G.; Erlebacher, J.; Shelnutt, J. A.; Scheidt, W. R. *Inorg. Chem.* **1995**, *34*, 102–110.

(28) Burnett, M. N.; Johnson, C. K. *ORTEP-III: Oak Ridge Thermal Ellipsoid Plot Program for Crystal Structure Illustrations*, Report ORNL-6895, Oak Ridge National Laboratory, Oak Ridge TN. **1996**.

(29) Cambridge Structural Database Version 5.27 Updates August 2006.

(30) Sadasivan, N.; Eberspaecher, H. I.; Fuchsman, W. H.; Caugey, W. S. *Biochem.* **1969**, *8*, 534–541.

(31) Fleischer, E. B.; Srivastava, T. S. *J. Am. Chem. Soc.* **1969**, *91*, 2403–2405.

(32) Rush, T. S. I.; Kozlowski, P. M.; Piffat, C. A.; Kumble, R.; Zgierski, M. Z.; Spiro, T. G. *J. Phys. Chem. B.* **2000**, *104*, 5020–5034.

(33) Ozaki, Y.; Mizuno, A.; Sato, H.; Kawaguchi, K.; Muraishi, S. *Appl. Spectrosc.* **1992**, *46*, 533–535.

(34) Wood, B. R.; Tait, B.; McNaughton, D. *Biochim. Biophys. Acta* **2001**, *1539*, 58–70.

(35) Kincaid J. R. *The Porphyrin Handbook*, vol. 7; Kadish K. M.; Smith K. M.; Guillard R. (Eds); Academic Press, **1999**, pp. 225–291.

(36) Zerner, M.; Gouterman, M.; Kobayashi, H. *Theoret. Chim. Acta* **1966**, *6*, 363–399.

(37) Paulat, F.; Lehnert, N. *Inorg. Chem.* **2008**, *47*, 4963–4976.

(38) Selensky, R.; Holten, D.; Windsor, M. W; Paine, J. B.; Doplin, D. *Chemical Physics* **1981**, *60*, 33–46.

(39) Webster, G. T.; McNaughton, D.; Wood, B. R. *J. Phys. Chem. B.* **2009**, Accepted pending revision.

(40) Crystal Impact. *DIAMOND*. Version 3.1. Crystal Impact GbR, Bonn, Germany, **2006**.

(41) Fuchsman, W. H.; Smith, Q. R.; Stein, M. M. *J. Am. Chem. Soc.* **1977**, *99*, 4190–4192.

(42) Eaton, S. S.; Eaton, G. R. *J. Am. Chem. Soc.* **1975**, *97*, 3660–3666.

(43) Tsubaki, M.; Srivastava, R. B.; Nai-Teng, Y. *Biochem.* **1982**, *21*, 1132−1140.

(44) Scheidt, W. R.; Geiger, D. K.; Hayes, R. G.; Laing, G. *J. Am. Chem. Soc.* **1983**, *105*, 2625−2632.

(45) Scheidt, W. R.; Geiger, D. K.; Haller, K. J. *J. Am. Chem. Soc.* **1982**, *104*, 495−499.

(46) Shelnutt, J. A.; Cheung, L. D.; Chang, R. C. C.; Yu, N.; Felton, R. H. *J. Phys.Chem.* **1977**, *66*, 3387−3398.

(47) Warshel, A.; Dauber, P. *J. Phys.Chem.* **1977**, *66*, 5477−5488.

(48) Bhuiyan, A. A.; Seth, J.; Yoshida, N.; Osuka, A.; Bocian, D. F. *J. Phys.Chem. B.* **2000**, *104*, 10757−10764.

(49) Akins, D. L. *J. Phys.Chem*. **1986**, *90*, 1530−1534.

(50) Akins, D. L.; Zhu, H. -R; Guo, C. *J. Phys.Chem*. **1996**, *100*, 5420−5425.

(51) Akins, D. L.; Zelik, S.; Zhu, H. -R.; Guo, C. *J. Phys.Chem*. *A.* **1997**, *101*, 3251−3259.

Supporting Information:

Density Functional Theory Calculations

The structure of Fe(TPP)Cl was optimized at the B3LYP/TZVP level of theory using the program package Gaussian 03 (Revision E.01)[1] starting from a X-ray crystallography structure derived from Scheidt *et al*.[2] The optimization was followed by frequency calculation at the corresponding level to assure finding the local minimum on the potential energy surface. Excited state calculations were performed using time-dependent density functional theory (TD-DFT) at the same level of theory. The number of excited states was limited to 50 which cover the energy states up to 361 nm.

(1) Frisch, M. J.; Trucks, G. W.; Schlegel, H. B.; Scuseria, G. E.; Robb, M. A.; Cheeseman, J. R.; Montgomery, Jr., J. A.; Vreven, T.; Kudin, K. N.; Burant, J. C.; Millam, J. M.; Iyengar, S. S.; Tomasi, J.; Barone, V.; Mennucci, B.; Cossi, M.; Scalmani, G.; Rega, N.; Petersson, G. A.; Nakatsuji, H.; Hada, M.; Ehara, M.; Toyota, K.; Fukuda, R.; Hasegawa, J.; Ishida, M.; Nakajima, T.; Honda, Y.; Kitao, O.; Nakai, H.; Klene, M.; Li, X.; Knox, J. E.; Hratchian, H. P.; Cross, J. B.; Bakken, V.; Adamo, C.; Jaramillo, J.; Gomperts, R.; Stratmann, R. E.; Yazyev, O.; Austin, A. J.; Cammi, R.; Pomelli, C.; Ochterski, J. W.; Ayala, P. Y.; Morokuma, K.; Voth, G. A.; Salvador, P.; Dannenberg, J. J.; Zakrzewski, V. G.; Dapprich, S.; Daniels, A. D.; Strain, M. C.; Farkas, O.; Malick, D. K.; Rabuck, A. D.; Raghavachari, K.; Foresman, J. B.; Ortiz, J. V.; Cui, Q.; Baboul, A. G.; Clifford, S.; Cioslowski, J.; Stefanov, B. B.; Liu, G.; Liashenko, A.; Piskorz, P.; Komaromi, I.; Martin, R. L.; Fox, D. J.; Keith, T.; Al-Laham, M. A.; Peng, C. Y.; Nanayakkara, A.; Challacombe, M.; Gill, P. M. W.; Johnson, B.; Chen, W.; Wong, M. W.; Gonzalez, C.; and Pople, J. A.; Gaussian, Inc., Wallingford CT, 2004.

(2) W. Robert Scheidt, Michael G. Finnegan, Acta Crystallogr. 1988, 45, 1214

Table S3. Assignment of the UV-visible absorption spectrum of Fe(TPP)Cl

Exp (nm)	Calc (nm)	f	Assignment
367*	361	0.0387	$\mathbf{a_{2u}\rightarrow d_{\pi}}$, $b_{2u}\rightarrow\pi^*$
377 st	370	0.0057	$p_x,p_y\rightarrow d_{\pi}$, $p_z\rightarrow dz^2$
"	376	0.0256	$p_x,p_y\rightarrow d_{\pi}$, $b_{2u}\rightarrow dz^2$, $a_{2u}\rightarrow d_{\pi}$, $b_{2u}\rightarrow\pi^*$
"	379	0.4553	$b_{2u}\rightarrow d_{\pi}$, $\pi\rightarrow\pi^*$, $a_{2u}\rightarrow d_{\pi}$
-	389	0.0132	$b_{2u}\rightarrow\pi^*$
415 vst	411	0.1543	$\boldsymbol{\pi\rightarrow\pi^*}$, $b_{2u}\rightarrow\pi^*$
460 sh	426, 432	0.0778	$b_{2u}\rightarrow d_{\pi}$
"	444	0.0004	$p_x,p_y\rightarrow d_{\pi}$
509	513	0.0154	$\boldsymbol{\pi\rightarrow\pi^*}$, $a_{2u}(\pi)\rightarrow d_{\pi}$
575	571	0.009	$\boldsymbol{\pi\rightarrow\pi^*}$, $a_{1u}(\pi)\rightarrow d_{\pi}$
-	641	0.0026	$a_{2u}(\pi)\rightarrow dz^2$
660, 690	676, 688, 734, 746	0.0046	$\mathbf{a_{1u}(\pi)\rightarrow d_{\pi}}$, $a_{2u}(\pi)\rightarrow\pi^*$
875* w br	882, 906	0.0013	$a_{2u}(\pi)\rightarrow d_{\pi}$

Exp, experimental results; Calc, calculated data; f, oscillator strength; st, strong; v, very; w, weak; *, shoulder; br, broad; p_x,p_y, p_z, chloride orbitals

Table S4. The *ORTEP* calculated interactions of Fe(TPP)Cl.

D–H···A	D–H (Å)	H···A (Å)	D···A (Å)	<D–H···A>	Type of interaction
C15_ii–H7_ii···Cl	0.948	2.953	3.826	153.68	C–H···Cl
C42_i–H26_i···Cl	0.945	3.040	3.734	131.60	C–H···Cl
C24_iv–H11_iv···Cl	0.951	3.146	3.773	125.02	C–H···Cl
C40_ii–H24_ii···(N1–C2)	0.950	2.802	3.660	150.79	C–H···π
C40_ii–H24_ii···N1	0.950	2.926	3.825	158.32	C–H···π
C41_ii–H25_ii···(N2–C3)	0.953	2.725	3.492	138.12	C–H···π
C41_ii–H25_ii···(N2–C4)	0.953	2.847	3.760	160.77	C–H···π
C41_ii–H25_ii···N2	0.953	2.791	3.635	148.13	C–H···π
C41_ii–H25_ii···(C3–C11)	0.953	2.921	3.586	127.95	C–H···π
C31_iii–H17_iii···(N4–C7)	0.950	2.750	3.550	142.45	C–H···π
C31_iii–H17_iii···N4	0.950	3.002	3.759	137.61	C–H···π
C31_iii–H17_iii···(C7–C15)	0.950	2.668	3.561	156.88	C–H···π
C31_iii–H17_iii···(C15–C16)	0.950	2.984	3.933	178.01	C–H···π
C9_iii–H1_iii···(C30–C31)	0.945	2.887	3.497	121.85	C–H···π

Table S5. The *ORTEP* calculated interactions of $[Fe(TPP)]_2O$.

D–H···A	D–H (Å)	H···A (Å)	D···A (Å)	<D–H···A>	Type of interaction
C43f_i–H27f_i···N1	0.964	2.943	3.578	124.54	C–H···π
C43f_i–H27f_i···(N1–C4)	0.964	2.982	3.455	111.59	C–H···π
C44f_i–H28f_i···N2	0.970	2.870	3.318	109.21	C–H···π
C44f_i–H28f_i···(N2–C9)	0.970	2.786	3.362	118.79	C–H···π
C31f_ii–H17f_ii···N3	0.971	3.085	3.846	136.21	C–H···π
C31f_ii–H17f_ii···(N3–C14)	0.971	2.894	3.755	148.37	C–H···π
C32f_i–H18f_i···(N4–C16)	0.979	2.986	3.555	118.19	C–H···π
C32f_i–H18f_i···N4	0.979	3.118	3.590	111.25	C–H···π
C32f_i–H18f_i···(C16–C17)	0.979	2.970	3.754	137.90	C–H···π
C29f_ii–H15f_i···(C41–C42)	0.959	2.832	3.686	148.93	C–H···π
C26f_i–H13f_i···(C40–C41)	0.955	2.816	3.757	168.80	C–H···π
C26f_i–H13f_i···(C41–C42)	0.955	2.851	3.711	150.40	C–H···π
C43_i–H27_i···N1f	0.964	2.943	3.578	124.54	C–H···π
C43_i–H27_i···(N1f–C4f)	0.964	2.982	3.455	111.59	C–H···π
C44_i–H28_i···N2f	0.970	2.870	3.318	109.21	C–H···π
C44_i–H28_i···(N2f–C9f)	0.970	2.786	3.362	118.79	C–H···π
C31_ii–H17_ii···N3f	0.971	3.085	3.846	136.21	C–H···π
C31_ii–H17_ii···(N3f–C14f)	0.971	2.894	3.755	148.37	C–H···π
C32_i–H18_i···(N4f–C16f)	0.979	2.986	3.555	118.19	C–H···π
C32_i–H18_i···N4f	0.979	3.118	3.590	111.25	C–H···π
C32_i–H18_i···(C16f–C17f)	0.979	2.970	3.754	137.90	C–H···π
C29_iii–H15_iii···(C41f–C42f)	0.959	2.832	3.686	148.93	C–H···π
C26_ii–H13_ii···(C40f–C41f)	0.955	2.816	3.757	168.80	C–H···π
C26_ii–H13_ii···(C41f–C42f)	0.955	2.851	3.711	150.40	C–H···π

Table S6. The *ORTEP* calculated interactions of Fe(OEP)Cl.

D–H···A	D–H (Å)	H···A (Å)	D···A (Å)	<D–H···A>	Type of interaction
C33_i–H39_i···Cl	0.990	2.864	3.664	138.43	C–H···Cl
C13_ii–H15_ii···Cl	0.981	2.887	3.706	141.62	C–H···Cl
C24_iv–H28_iv···Cl	0.991	3.108	3.657	116.34	C–H···Cl
C3_i–H2_i···Cl	0.989	2.979	3.790	139.88	C–H···Cl
C33_iii–H39_iii···(N1–C1)	0.990	2.786	3.593	139.14	C–H···π
C33_iii–H39_iii···N1	0.990	2.849	3.701	144.76	C–H···π
C33_iii–H39_iii···(N1–C8)	0.990	2.880	3.623	132.53	C–H···π
C33_iii–H39_iii···(C1–C2)	0.990	2.963	3.530	117.42	C–H···π
C12_ii–H13_ii···(N3–C19)	0.990	2.968	3.622	124.49	C–H···π
C12_ii–H13_ii···N3	0.990	3.116	3.898	136.82	C–H···π
C12_ii–H13_ii···(C19–C20)	0.990	2.904	3.347	108.10	C–H···π
C12_ii–H13_ii···(C20–C23)	0.990	2.995	3.512	113.64	C–H···π
C3_ii–H2_ii···(N4–C28)	0.989	2.979	3.820	143.45	C–H···π
C3_ii–H2_ii···N4	0.989	3.075	3.986	153.62	C–H···π
C3_ii–H2_ii···(C28–C29)	0.989	2.998	3.610	121.08	C–H···π

Table S7. The *ORTEP* calculated interactions of triclinic $[Fe(OEP)]_2O$.

D–H···A	D–H (Å)	H···A (Å)	D···A (Å)	<D–H···A>	Type of interaction
C53_i–H34_i···(N1–C1)	0.949	2.886	3.576	130.54	C–H···π
C53_i–H34_i···N1	0.949	2.979	3.757	140.16	C–H···π
C66_i–H69_i···N3	0.948	3.032	3.349	101.25	C–H···π
C66_i–H70_i···(N3–C5)	0.949	2.938	3.377	109.59	C–H···π
C66_i–H70_i···N3	0.949	3.047	3.349	100.27	C–H···π
C41_i–H10_i···N7	0.949	3.197	3.741	118.23	C–H···π

Table S8. The *ORTEP* calculated interactions of monoclinic $[Fe(OEP)]_2O$.

D–H···A	D–H (Å)	H···A (Å)	D···A (Å)	<D–H···A>	Type of interaction
C62_i–H16_i···(N1–C1)	0.949	2.999	3.561	119.32	C–H···π
C62_i–H16_i···N1	0.949	3.096	3.524	109.21	C–H···π
C57_i–H88_i···N3	0.946	2.997	3.599	122.81	C–H···π
C53_i–H80_i···N5	0.945	3.106	3.932	146.82	C–H···π
C53_i–H80_i···(N5–C10)	0.945	2.958	3.704	136.75	C–H···π
C50_i–H73_i···N7	0.948	3.161	3.671	115.53	C–H···π

Table S9. The *ORTEP* calculated interactions of *β*-hematin.

D–H···A	D–H (Å)	H···A (Å)	D···A (Å)	<D–H···A>	Type of interaction
C19_i–H···O36			3.949		C–H···O
C31_i–H···O36			3.778		C–H···O
C33_i–H···O36			3.959		C–H···O
O36–H···O37_iii			2.830		O–H···O
O36–H···O40_i			3.802		O–H···O
C31–H···O37			3.214		C–H···O
C30_i–H···O40			3.207		C–H···O
C38_i–H···O40			3.191		C–H···O
C13_i–H···O40			3.667		C–H···O
C18_ii–H···O40			3.651		C–H···O
C19_ii–H···O40			3.543		C–H···O
C21_ii–H···O40			3.973		C–H···O
C29_i–H···O40			3.884		C–H···O
C34_i–H···O40			3.146		C–H···O
C35_i–H···O40			3.733		C–H···O
C13_i–H···O41			3.841		C–H···O
C29_i–H···O41			3.464		C–H···O
C30_i–H···O41			3.570		C–H···O
C34_i–H···O41			3.592		C–H···O
C29–H···(N2–C6)			3.252		C–H···π
C29–H···(N2–C3)			3.450		C–H···π
C29–H···N2			3.418		C–H···π
C29–H···(C3–C4)			3.532		C–H···π
C29–H···(C4–C5)			3.413		C–H···π
C29–H···(C5–C6)			3.210		C–H···π
C30_iii–H···(N20–C21)			3.349		C–H···π
C30_iii–H···(N20–C24)			3.574		C–H···π
C30_iii–H···N20			3.566		C–H···π
C30_iii–H···(C21–C22)			3.207		C–H···π
C30_iii–H···(C22–C23)			3.388		C–H···π
C30_iii–H···(C23–C24)			3.583		C–H···π
C43_i–H···(N20–C21)			3.477		C–H···π
C43_i–H···(N20–C24)			3.615		C–H···π
C43_i–H···N20			3.690		C–H···π
C43_i–H···(C21–C22)			3.201		C–H···π
C43_i–H···(C22–C23)			3.177		C–H···π
C43_i–H···(C23–C24)			3.430		C–H···π
C4_i–H···(N20–C24)			3.616		C–H···π
C4_i–H···N20			3.823		C–H···π
C4_i–H···(C23–C24)			3.817		C–H···π
C26_i–H···(N20–C21)			3.806		C–H···π
C26_i–H···(N20–C24)			3.571		C–H···π
C26_i–H···N20			3.482		C–H···π

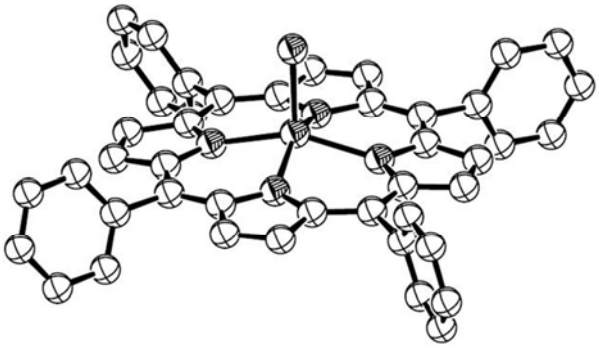

Figure S1. *ORTEP* diagrams showing molecular structure of Fe(TPP)Cl.

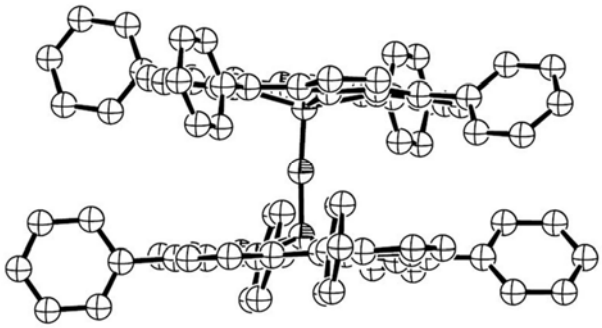

Figure S2. *ORTEP* diagrams showing molecular structure of $[Fe(TPP)]_2O$.

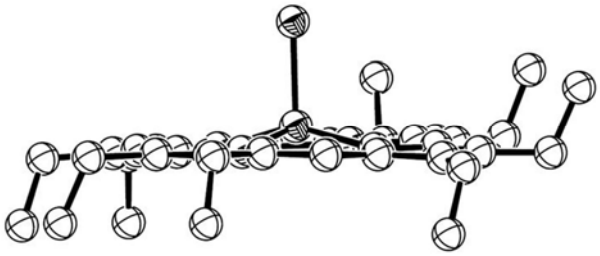

Figure S3. *ORTEP* diagrams showing molecular structure of Fe(OEP)Cl.

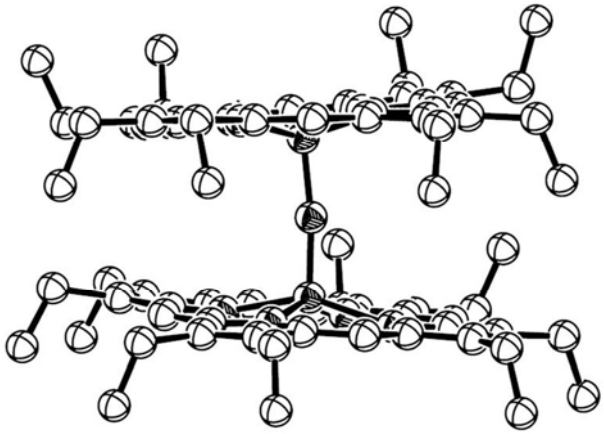

Figure S4. *ORTEP* diagrams showing molecular structure of triclinic $[Fe(OEP)]_2O$.

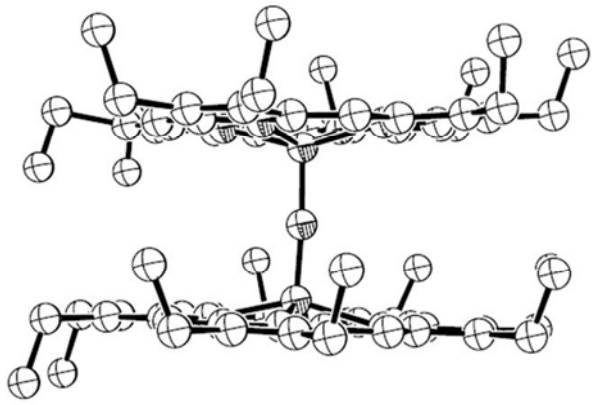

Figure S5. *ORTEP* diagrams showing molecular structure of monoclinic $[Fe(OEP)]_2O$.

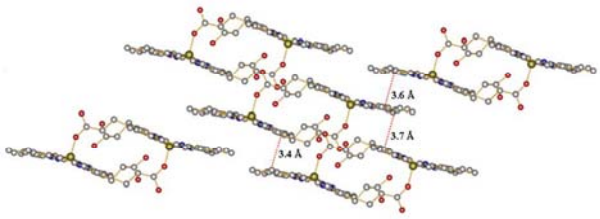

Figure S6. β-hematin molecules in the crystal structure show the closest porphyrin plane to porphyrin plane contact distance.

Figure S7. Contour plots of important molecular orbitals of [Fe(TPP)Cl]

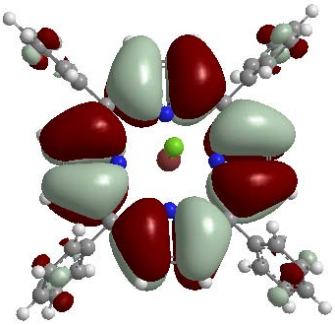

$a_{1u}(\pi)$

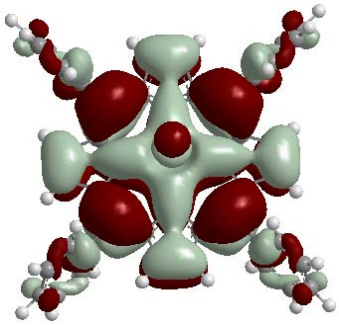

$a_{2u}(\pi)$

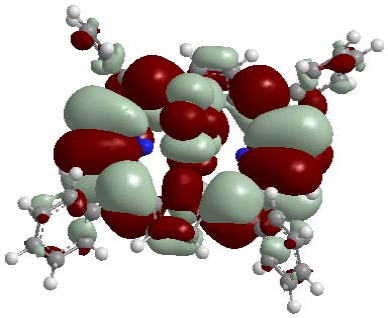

e_g

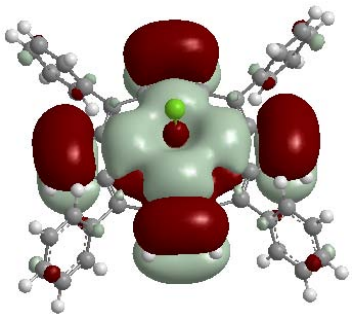

a_{2u}

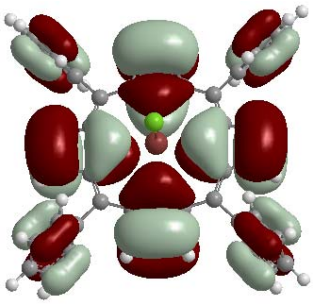

b2u

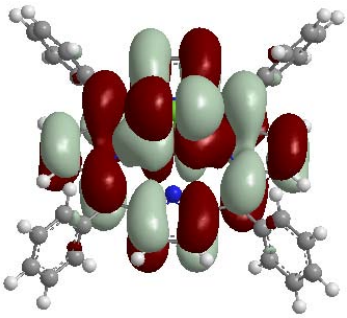

d_{xz}

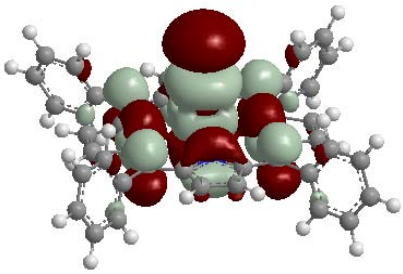

d_z^2

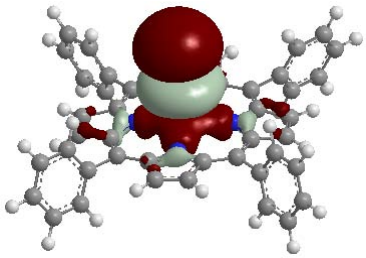

p_z

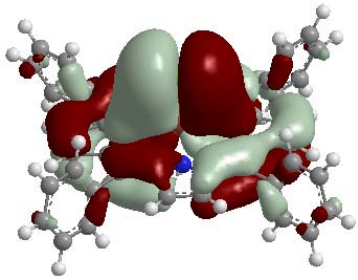

p_x

Chapter 6

Conclusions and Future Directions

This dissertation reports on some applications of resonance Raman and infrared microspectroscopy in malaria research. The powerful combination of spectroscopic data and multivariate statistical analysis has allowed the development of Raman and FTIR based techniques to analyse the *Plasmodium falciparum* strain of malaria parasite within human erythrocytes. Three major scientific areas have been addressed. Firstly, the potential of FTIR microspectroscopy to be used as a diagnostic tool for discriminating between the different stages of the malaria parasite lifecycle based on changes in lipid composition within the cell has been explained. Secondly, resonance Raman microscopy has been used to analyse the putative drug target, haemozoin, which develops in the late feeding stage (trophozoite) of the parasite. It was found the addition of chloroquine (CQ) can affect the molecular environment of haemozoin. Thirdly, Raman wavelength dependent investigations into the aggregation of Fe(III)PPIX molecules in solution as a function of concentration have demonstrated the process of CQ interaction with haemozoin through binding by supramolecular interactions to the unligated faces of Fe(III)PPIX-OH/H_2O monomers and μ-oxo-dimers. This later study discovered the important role CQ non-covalent binding has in reducing excitonic effects in monomeric or dimeric precursors of haemozoin and in the haemozoin dimer unit directly, which ultimately inhibits the growth of the biomineral.

The application of FTIR spectroscopy in combination with PCA and ANN to discriminating the different stages of the *Plasmodium falciparum's* intra-erythrocytic lifecycle in fixed single erythrocytes and to investigating the formation of haemozoin has been discussed in this dissertation (Chapter 3). Bands assigned to the haemozoin moiety are observed in FTIR difference spectra between uninfected erythrocytes and infected trophozoites. PCA identified that these bands are important contributors in separating the trophozoite spectra from the uninfected cell spectra. Excellent

spectroscopic discrimination between *Plasmodium falciparum* infected cells and the control cells became possible by training of an ANN. FTIR difference spectra indicated a change in the production of unsaturated fatty acids as the parasite matures, where different phases of its intra-erythrocytic lifecycle are characterised by different lipid compositions giving rise to distinct spectral profiles in the C-H stretching region.

Looking to practical applications for this research, it can be seen that although the FTIR instrument is expensive, the actual cost per test can be very cheap especially if one uses inexpensive IR substrates such as Kevley slides. In addition, a synchrotron source for a clinical environment is impractical. Therefore the development of cheaper and more realistic techniques is necessary. Hence, with the continued development of confocal FTIR imaging spectrometers with powerful globar sources and improved sensitivity FPA detectors, one can imagine conventional FTIR instruments becoming the instrument of choice when diagnosing malaria.

To more fully determine the applicability of FTIR spectroscopy to clinically diagnosing the different stages of malaria infection, future research is needed into the study of live infected erythrocytes and the effects antimalarial drugs have on lipid composition at the different developmental stages of the parasite. To effectively analyse live infected erythrocytes at the different stages, preliminary experiments by the group have shown that spectra can be taken of cells placed between two CaF_2 windows with thin sized spacers (*ca* 7 – 12 μm) fabricated onto one of the CaF_2 windows. To keep them positioned and parallel they can be placed into a compression cell and FTIR spectra can be taken in transmission mode.

Within the field of malaria research, the value of using FTIR spectroscopy lies in its ability to detect haemozoin and discriminate between the intra-erythrocytic lifecycle stages of the parasite based on the specific lipid signature from each individual stage

and in the near future the technique can potentially provide a cheaper diagnostic alternative.

On the other hand, FTIR spectroscopy cannot detect structural changes in haemozoin within trophozoite infected erythrocytes following quinoline drug treatment. The results of the synchrotron FTIR study to identify and discriminate the different stages of the parasite's intra-erythrocytic lifecycle and detect changes in the amount of haemozoin formed by the parasite after incubation with CQ within RBCs directed research towards investigating the applications of resonance Raman spectroscopy to malaria research.

Initially, FTIR-ATR and Raman measurements (**II**) were taken of β-haematin treated with quinoline drugs to monitor the direct effects quinoline drugs have on the molecular environment of synthetic malaria pigment. The results showed changes in the surface propionic acid groups (1744 cm^{-1}) of the haemozoin biomineral when CQ was present, which would be hidden in FTIR spectra of trophozoite infected RBCs by the superposition of the ester carbonyl band. Furthermore, the Raman spectra of β-haematin show changes in A_{1g} and B_{1g} modes in the presence of quinoline drugs. This lends support to a model involving a π-π stacked drug binding complex.

However, the true value of using Raman spectroscopy lies in its ability to detect haemozoin as well as the CQ interactions with haemozoin within the digestive vacuole of live trophozoite infected erythrocytes (**III**). Raman spectroscopy can also detect drug interactions with haemozoin precursors (Fe(III)PPIX-OH/H_2O monomer, μ-oxo dimers and π-π dimers).

There are many drug target sites located in the malaria parasite, of which some are the apicoplast, mitochondrion, cytosol and digestive vacuole. However, the application of Raman spectroscopy focuses on the analysis of constituents within the

digestive vacuole of the malaria parasite in particular because it is the site of haem accumulation and haemozoin formation, which are large Raman scatterers. Haemozoin precursors and the haemozoin dimer unit are drug targets within the digestive vacuole. Through the use of resonance Raman spectroscopy to analyse these Fe(III)PPIX molecules, one can detect structural changes in haemozoin as a result of drug interactions.

It was found that a number of bands assigned to A_{1g} and B_{1g} modes characteristic of the haemozoin biomineral are reduced in intensity in CQ-treated cells. However, no bands from CQ itself are observed as the drug concentration is too low and CQ is a weaker Raman scatterer. The intensity changes are attributable to intermolecular drug binding of CQ in a sandwich type complex between Fe(III)PPIX dimer units. It is postulated that CQ binds via supramolecular interactions between adjacent and oriented porphyrins thereby disrupting the haemozoin aggregate and reducing excitonic interactions between adjacent Fe(III)PPIX units.

Tip enhanced Raman scattering (TERS) is an alternative technique on the forefront of malaria research that can be used to analyse haemozoin growth within functional erythrocytes. Future research into the use of TERS to analyse single haemozoin biominerals at nano-scale spatial resolution (*ca* 20 nm) could also produce spectra showing the interaction of antimalarial drugs with haemozoin biominerals within infected erythrocytes, and also the location of those drugs directly on the haemozoin biominerals. Preliminary studies performed by my supervisor Dr. Bayden Wood show that TERS spectra display bands that are characteristic of haemozoin, which can be correlated to a precise position on the biomineral by comparison with the corresponding atomic force microscopy (AFM) image.

TERS enhancement occurs when a metal tip with dimensions smaller than that of the wavelength of light is irradiated.[1] A local enhancement of Raman scattering (*ca* 10^6-10^7) occurs in the vicinity of the electromagnetic near-field, when the tip apex (usually a silver nano-particle) interacts with a small portion of molecules.

The TERS experiment, although promising, still has some major challenges to overcome. Firstly, the reproducibility and yield of good tips is difficult, due to the tips picking up fractions of sample during a scan or simply breaking.[1] Ideally, TERS tip production will be made commercially available in the near future to combat this problem. Secondly, to obtain quality TERS spectra of haemozoin within trophozoite infected erythrocytes, the cells must be sectioned. Preparing quality samples of sectioned infected erythrocytes that are thin enough to allow laser light to pass through and interact with the tip, yet still preserve the structural integrity of the internal matrix of the cell, is challenging. However, these challenges aside, the TERS technique could be used in the foreseeable future as a new antimalarial drug screening tool for detecting the surface attachment of drugs to the haemozoin biomineral within the digestive vacuole of trophozoite infected erythrocytes.

The question still remains as to the mode in which CQ non-covalently associates with the haemozoin dimer unit. The results of Chapter 5 suggest that CQ can non-covalently bind to the unligated faces of Fe(III)PPIX-OH/H_2O monomer and μ-oxo dimers before haemozoin is formed within the digestive vacuole. This caps the faces of the haemozoin dimer unit and reduces the amount of haemozoin formed.

Resonance Raman spectra of haematin and haemin solutions are reported for 413 nm and 514 nm wavelengths. Enhancement of A_{1g} modes (1569 cm^{-1} and 1370 cm^{-1}) and B_{1g} modes (1124 cm^{-1} and 755 cm^{-1}) as a function of increased concentration are observed when irradiating with 514 nm laser excitation but not 413 nm. This can be

rationalised by considering an excitonic coupling mechanism. As the concentration of haematin increases there is an increased probability of supramolecular interactions such as π-π and other dispersion forces between Fe(III)PPIX units occurring. Resonance Raman spectra recorded using 514 nm excitation show that CQ acts as a molecular spacer and binds non-covalently through supramolecular interactions, most likely π-π interactions, between μ-oxo dimer units of Fe(III)PPIX. This is evinced by the decrease in intensity of ν_4 in the Raman spectrum as a function of increasing CQ mole ratio.

In comparison, UV-Visible spectra show that CQ can bind to the unligated face of Fe(III)PPIX-OH/H_2O monomers, potentially reducing the formation of π-π dimers. The discovery that CQ can bind to the monomeric and dimeric precursors of haemozoin or directly to the haemozoin dimer unit has important implications for the development of future antimalarial compounds that could exert effectiveness by binding through supramolecular interactions to the unligated faces of Fe(III)PPIX-OH/H_2O monomers and μ-oxo dimers.

Future research into using Raman spectroscopy could involve analysing the effects of other antimalarial drugs within live infected erythrocytes and observing for similar CQ-type drug binding effects. Previous work by de Villiers *et al.*[2] examined the crystal structure of a halofantrine-Fe(III)PPIX complex by single crystal X-ray diffraction. It was shown that halofantrine can exert its antimalarial activity by interacting with Fe(III)PPIX through coordination to the Fe(III) center by means of its alcohol functionality, π-stacking of the phenanthrene ring over porphyrin and other hydrogen bonding interactions.

Other antimalarial drugs include artemisinin and its derivatives, which could be analysed in future research involving Raman spectroscopy to determine the effects they have on Fe(III)PPIX and haemozoin. Previous work undertaken by the candidate as a

component of his Honours thesis investigated the effects artemisinin had on haemozoin within trophozoite infected erythrocytes using 633 nm and 782 nm excitation wavelength lasers. Spectra taken using the 782 nm excitation laser showed small changes in haemozoin bands are caused by the presence of artemisinin. These were similar to the haemozoin bands that are affected by the non-covalent binding of CQ.

In light of these findings, further research is needed to draw solid conclusions about the mode of attachment of artemisinin antimalarial drugs. Furthermore, the use of Raman spectroscopy to analyse supramolecular drug interactions make it an appropriate and powerful technique to monitor other antimalarial drugs (such as halofantrine, artemisinin and artemisinin derivatives) and the antimalarial activity they exert on haemozoin precursors and haemozoin dimer units.

References

(1) Bailo, E.; Deckert, V. *Chem. Soc. Rev.* **2008**, *37*, 921-930.

(2) de Villiers, K. A.; Marques, H. M.; Egan, T. J. *J. Inorg. Biochem.* **2008**, *102*, 1660-1667.